



HAL
open science

Characterization by nanoindentation of the local mechanical properties of superelastic titanium-based magnetron-sputtered films in connection to their microstructures

Ying Zhou

► **To cite this version:**

Ying Zhou. Characterization by nanoindentation of the local mechanical properties of superelastic titanium-based magnetron-sputtered films in connection to their microstructures. Material chemistry. INSA de Rennes, 2021. English. NNT : 2021ISAR0006 . tel-03738144

HAL Id: tel-03738144

<https://theses.hal.science/tel-03738144>

Submitted on 25 Jul 2022

HAL is a multi-disciplinary open access archive for the deposit and dissemination of scientific research documents, whether they are published or not. The documents may come from teaching and research institutions in France or abroad, or from public or private research centers.

L'archive ouverte pluridisciplinaire **HAL**, est destinée au dépôt et à la diffusion de documents scientifiques de niveau recherche, publiés ou non, émanant des établissements d'enseignement et de recherche français ou étrangers, des laboratoires publics ou privés.

THESE DE DOCTORAT DE

L'INSTITUT NATIONAL DES SCIENCES
APPLIQUEES RENNES

ECOLE DOCTORALE N° 596

Matière, Molécules, Matériaux

Spécialité : Science des Matériaux

Par

Ying ZHOU

Characterization by nanoindentation of the local mechanical properties of superelastic titanium-based magnetron-sputtered films in connection to their microstructures

Thèse présentée et soutenue à Rennes, le 05. 07. 2021

Unité de recherche : ISCR UMR 6226

Thèse N : 21ISAR 20 / D21 - 20

Rapporteurs avant soutenance :

Pierre Olivier RENAULT - Professeur des Universités - Université de Poitiers

Frédéric SANCHETTE - Professeur des Universités - Université de Technologie de Troyes

Composition du Jury :

Président : **Etienne PATOOR** - Professeur des Universités - Georgia Tech Lorraine

Examineurs : **Pierre Olivier RENAULT** - Professeur des Universités - Université de Poitiers

Frédéric SANCHETTE - Professeur des Universités - Université de Technologie de Troyes

Dir. de thèse : **Thierry GLORiant** - Professeur des Universités - INSA Rennes

Co-dir. de thèse : **Amélie FILLON** - Maître de Conférences - INSA Rennes

Invité :

Denis LAILLE - Assistant Ingénieur - INSA Rennes

Characterization by nanoindentation of the local mechanical properties of superelastic titanium-based magnetron-sputtered films in connection to their microstructures

Caractérisation par nanoindentation des propriétés mécaniques locales de films superélastiques à base de titane obtenus par pulvérisation magnétron en lien avec leurs microstructures

Ying ZHOU



Acknowledgements

First and foremost, I should acknowledge the China Scholarship Council (CSC) for the financial support, and I also acknowledge the laboratory of Chemical-Metallurgy ISCR UMR6226 in INSA de Rennes and University of Rennes 1 for providing access to various facilities. Then, I would like to thank the following people, without whom I would not have been able to complete this research, and without whom I would not have made it through my PhD degree.

I would like to express my deep and sincere gratitude to my supervisor Prof. Thierry Gloriant, for giving me the opportunity to do research and providing invaluable guidance throughout this research. His expertise was invaluable in formulating the research questions and methodology. His insightful feedback pushed me to sharpen my thinking and brought my work to a higher level. It was a great privilege and honor to work and study under his supervision.

I would like to extend my great thanks to Amélie Fillon for her dedicated involvement in every step during my entire study. She continuously provided encouragement and was always willing and enthusiastic to assist in any way she could. She provided me extensive personal and professional guidance and taught me a great deal about both scientific research and life in general. All time spent with her has become a valuable and inspiring experience for me. I am extending my heartfelt thanks to her husband, James CARRET, and her whole family for their kindness, acceptance and generosity and for taking me in as one of their member.

I would like to thank Philippe CASTANY who offered me great help and suggestions on the TEM manipulations and analyses. His immense knowledge and plentiful experience inspired my interest in the crystallography and materials. The assistance provided by Denis LAILLE and Sandrine GEFFROY are greatly appreciated. I greatly benefited from their abilities of operating various devices in the lab and keeping them running smoothly. Specially, Denis LAILLE provided immediate support for any computer problems I encountered, participated in most of my experiments and presentations, and offered me many technical suggestions. I also received generous support from our secretary Nadine BRIE who offered much needed assistance with administrative documents and kept our lab perfectly organized so that we could work efficiently. Also many thanks to Doïna GORDIN, Isabelle THIBON, Henri

FRANCILLETTE, Marilyne CORNEN and Yvan BEDOUIN for useful feedback and insightful comments on my work when I needed. I owe a debt of gratitude to all my colleagues with whom I worked together, Hamza JABIR, JingJun GAO, Gaëtan CABON, Hugo SCHAAL, and Thibaud CHOQUET. They provided a friendly and cooperative atmosphere at work and we counted on each other to move on.

I would like to thank the jury members of my thesis defense, Prof. Pierre Olivier RENAULT from Université de Poitiers, Prof. Frédéric SANCHETTE from Université de Technologie de Troyes, and Prof. Etienne PATOOR from Georgia Tech Lorraine. Their encouraging words and professional feedbacks have motivated me to continue the research work in my future career. Also many thanks to my committee members, Maryline GUILLOUX-VIRY and Gérard MAUVOISIN, who ensured consistency of my thesis work with the professional project. My sincere thanks also goes to my Master supervisors FaQin Xie and XiangQing Wu for stimulating my initial interest in research and for providing me opportunities to grow professionally, also many thanks to the colleagues from this group for always being there for me. I also would like to thank my new friends I met in France in the past four years, HaiYun Huang, HaoRan Li, Jin GENG and her husband, Cai Hu, LiPing CHEN, YaoDong LU, Fei FAN, PengZhi Wang, MiaoRan LIU, ZhiHang AN, LiMiao SHI, Rajaa BENCHOUAIA and Alphonsine Ngo NDIMBA, who endured this long process with me and always offered me happy distractions to rest my mind out of research.

My deepest appreciation goes to my parents and my younger brother, whose unconditional supports are with me in whatever I pursue, and whose unequivocal love keeps me motivated and confident. My special thanks must be offered to my boyfriend, ZhiPeng SUN, who I am extremely lucky to have met in France. His encouragement and understanding when the times got rough are much appreciated, and the caring and love from his family are duly noted. This accomplishment would not have been possible without them.

Ying ZHOU

September 8, 2021

Caractérisation par nanoindentation des propriétés mécaniques locales de films superélastiques à base de titane obtenus par pulvérisation magnétron en lien avec leurs microstructures

Résumé étendu en français

Dans ce travail de thèse, des alliages biomédicaux à base de titane du type β métastable et de compositions Ti-20Zr-3Mo-3Sn (Ti2033, at.%), Ti-16Zr-13Nb-2Sn (Ti16132, at.%) et Ti-24Nb-4Zr-8Sn (Ti2448, mass.%) ont été synthétisés en alliages massifs par fusion et en couches minces par pulvérisation magnétron. Les investigations se sont focalisées sur leurs caractérisations microstructurales et leurs propriétés mécaniques avec une attention particulière portée sur leurs propriétés superélastiques qui ont été sondées à l'échelle locale par nanoindentation en utilisant quatre types d'indenteurs: trois indenteurs sphériques de rayons 10 μm (Sp10), 50 μm (Sp50) et 200 μm (Sp200) et la pointe diamantée Berkovich modifiée (Bkv).

Pour confirmer la faisabilité de la technique de nanoindentation pour caractériser la propriété superélastique induite par une transformation martensitique réversible, des essais de nanoindentation ont été réalisés sur l'alliage massif Ti2033 et les résultats obtenus sont présentés et discutés au chapitre III. Ces mesures de nanoindentation ont été combinées avec des analyses EBSD pour examiner l'anisotropie cristallographique de la réponse en indentation à l'échelle des grains individuels dans la microstructure polycristalline. Les nombreuses mesures réalisées pour évaluer la dureté d'indentation H_{IT} , le module d'indentation E_{IT} , le taux de recouvrement en profondeur η_h et le taux de recouvrement du travail η_w sur une large gamme de directions cristallographiques ont permis d'investiguer avec une bonne statistique l'ensemble du triangle fondamental des orientations cristallographiques de la phase β . Les résultats, présentés judicieusement sous forme de cartes de distribution en figures de pôles inverses (IPF): $\eta_h - IPF$, $\eta_w - IPF$, $E_{IT} - IPF$ et $H_{IT} - IPF$, ont montré que les valeurs de η_h et η_w étaient fortement affectées par la direction cristallographique des grains atteignant un maximum pour la direction $\langle 001 \rangle_\beta$ et un minimum pour la direction $\langle 111 \rangle_\beta$ (voir figure 1). De plus, les distributions $\eta_h - IPF$ et $\eta_w - IPF$ se sont révélées être en bon accord avec la distribution IPF des distorsions de maille en compression, calculées à partir du modèle

cristallographique de la transformation martensitique, ce qui permet de mettre en évidence que l'anisotropie des taux de recouvrement découle bien de la nature superélastique de l'alliage. Il a également été montré que la nanoindentation sphérique est plus appropriée pour sonder l'anisotropie cristallographique de la superélasticité, en raison du champ de distribution des contraintes générées sous l'indenteur qui est plus favorable à la réversion de la transformation martensitique par rapport à celui généré sous l'indenteur Berkovich. Les mesures ont également montré une dépendance de l'orientation sur le module d'indentation E_{IT} et la distribution $E_{IT} - IPF$ obtenue est qualitativement similaire à celle prédite par les calculs du module d'Young à partir des constantes élastiques mesurées. Par contre, aucune anisotropie cristallographique de la dureté d'indentation H_{IT} n'a été détectée en raison des multiples systèmes de glissement activés dans le cristal β bcc.

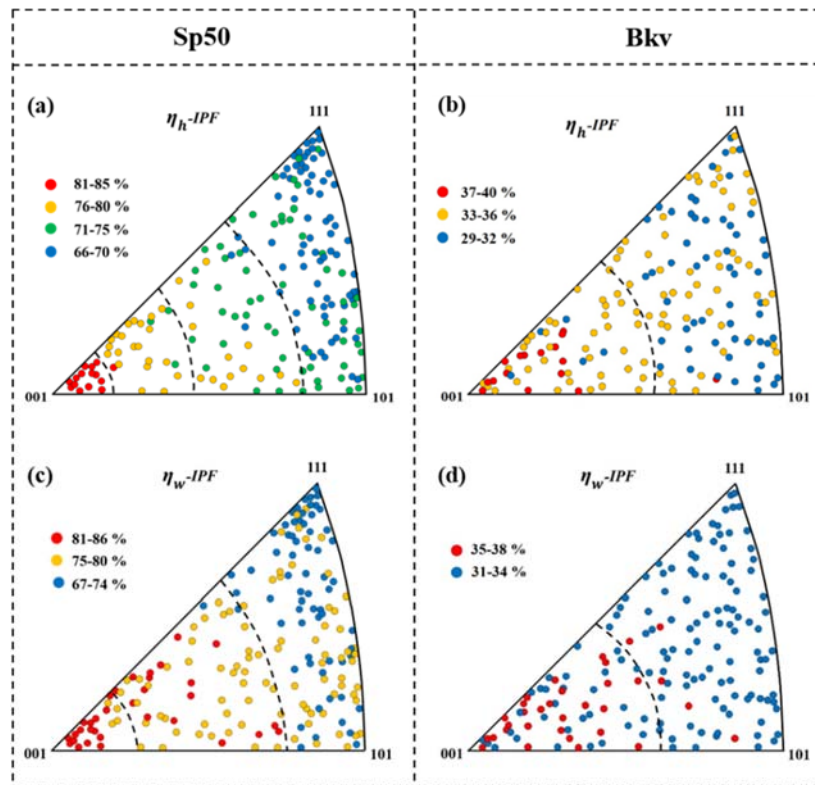


Fig. 1. Cartes des distributions en figures de pôles inverses des taux de recouvrement: $\eta_h - IPF$ avec l'indenteur sphérique Sp50 (a) et l'indenteur Berkovich Bkv (b) et $\eta_w - IPF$ avec l'indenteur sphérique Sp50 (c) et l'indenteur Berkovich Bkv (d).

Par conséquent, on peut conclure que l'anisotropie cristallographique des réponses en nanoindentation est gouvernée par l'anisotropie des réponses élastiques et superélastiques dans cet alliage β métastable. En revanche, la dépendance à l'orientation est perdue lorsque la déformation plastique devient trop importante. La technique de nanoindentation est ainsi capable de détecter la superélasticité à l'échelle locale et peut être de ce fait mise en œuvre pour la caractérisation de films superélastiques.

Un nouveau film quaternaire (composition Ti16132) a été obtenu par pulvérisation magnétron à température ambiante à partir d'une seule cible pré-alliée réalisée par fusion (chapitre IV). Les observations MET et les analyses DRX révèlent que le film consiste en une microstructure composée de nanograins β colonnaires qui s'étirent le long de la direction de croissance avec quelques nano-domaines martensitiques α'' qui sont également détectés. Les représentations en figures de pôles pour la structure bcc β montrent une texture de fibre $\langle 110 \rangle_\beta$ très marquée dans la direction de croissance (voir fig. 2).

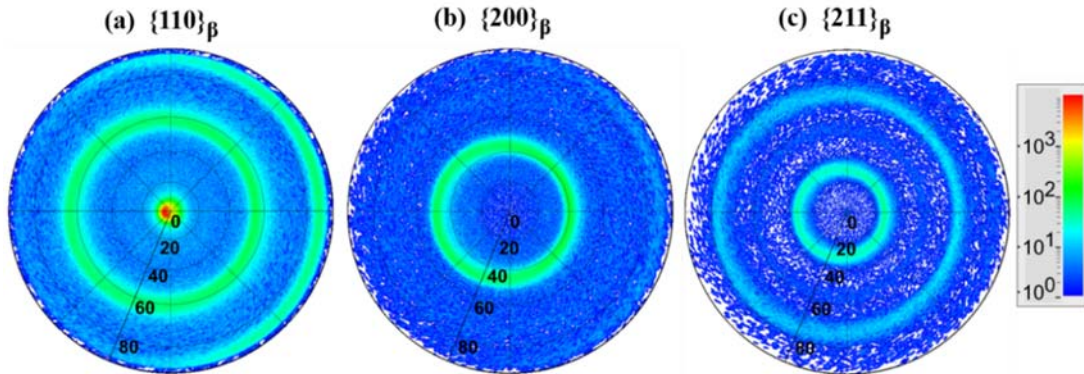


Fig. 2. Figures de pôles DRX montrant la texture de la phase β dans le film Ti16132: (a) $\{110\}_\beta$, (b) $\{200\}_\beta$, (c) $\{211\}_\beta$.

La réponse superélastique du film Ti16132 a été sondée par nanoindentation en évaluant les taux de recouvrement en profondeur et du travail (η_h et η_w) à partir des courbes charge-déplacement obtenues pour différentes profondeurs de pénétration. A partir de ces résultats, la déformation représentative (ϵ_r) du film a été calculée pour chaque indenteur. Il a ainsi été observé que la déformation représentative varie continuellement de 0,4% à 4,3% lorsque les trois pénétrateurs sphériques 200 μm (Sp200), 50 μm (Sp50) et 10 μm (Sp10) sont utilisés et qu'elle atteint 7% avec le pénétrateur Berkovich (Bkv). Ainsi, le comportement en nanoindentation du film Ti16132 est significativement affecté par la géométrie des pointes en raison des grandes différences d'amplitude et de distribution spatiale des contraintes induites sous chaque indenteur. En utilisant la pointe Bkv, presque aucune dépendance de la profondeur sur les taux de recouvrement n'a été observée. La déformation représentative constante et élevée ($\sim 7\%$) se situe au-delà du niveau de la déformation superélastique, ce qui a pour conséquence d'observer des taux de recouvrement très restreints ($\sim 40\%$) avec la pointe Bkv du fait d'une plastification intense. Ainsi, l'indentation Berkovich génère une densité élevée de dislocations qui contribuent à la fois à limiter la formation de la martensite et à inhiber sa réversion en phase β parente. Par contre, dans le cas de l'indentation sphérique, la déformation représentative dépend à la fois de la profondeur et du rayon du pénétrateur utilisé, ce qui permet de balayer les différents régimes de déformation. Des taux de recouvrement de près de 100% ont été mesurés avec le pénétrateur sphérique à grand rayon (Sp200) qui impose une

déformation représentative relativement faible (entre 0,4% et 1%) sondant ainsi une déformation principalement élastique. Des taux de recouvrement importants allant de 95% à 60% ont été mesurés avec les pénétrateurs Sp50 et Sp10 pour des déformations représentatives (ϵ_r) se situant entre 1% et 4,3%. Avec ces deux pointes sphériques, la déformation plastique est minorée tandis que la déformation superélastique, conséquence de la transformation martensitique réversible, est le mécanisme de déformation prédominant. La figure 3 résume les différents taux de recouvrement obtenus associés aux différents régimes de déformation pour chaque pointe utilisée.

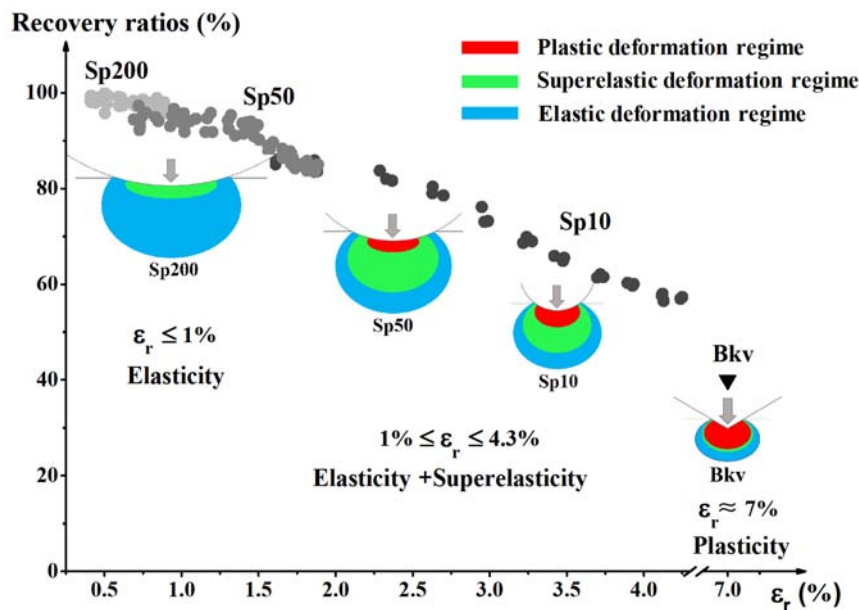


Fig.3. Taux de recouvrement et représentation schématique des mécanismes de déformation prédominants en fonction de la déformation représentative (ϵ_r) pour chaque pointe utilisée.

Les propriétés superélastiques étant très sensibles au niveau de déformation appliqué, cette étude montre l'importance de déterminer la fenêtre de profondeur d'indentation appropriée associée au rayon de la pointe du pénétreur pour révéler le comportement superélastique à l'échelle locale. Dans le cas présent, l'indentation avec les pointes sphériques intermédiaires Sp50 et Sp10, s'avère être une stratégie viable pour révéler la réponse superélastique dans le film Ti16132 étudié.

La propriété de superélasticité du film Ti2448 obtenu par pulvérisation magnétron a également été caractérisée dans ce travail de thèse (chapitre V.). Le film est constitué d'un mélange de phase β et de phase α'' et présente une texture de fibre $\langle 110 \rangle_\beta$ avec une distribution homogène de nanocristallites α'' dans la matrice β (voir sur la figure 4 un exemple d'observation MET en coupe transversale).

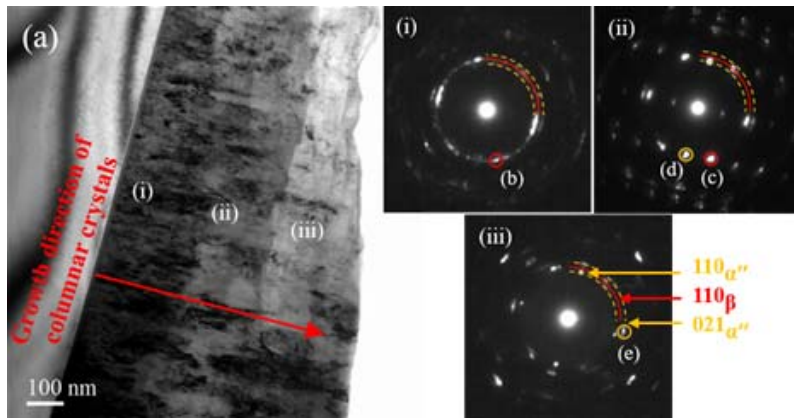


Fig.4. (a) Image en champs clair du film Ti2448 en coupe transverse, (i-iii) Clichés de diffraction électronique correspondant à différentes zones du champ clair.

Les réponses en nanoindentation avec les différents indenteurs ont été déterminées et corrélées aux calculs de la déformation représentative (ϵ_r) et de la distribution normalisée de la pression de contact (σ_z/p_m) évaluées sous indenteurs. Il a été observé que plus le rayon de la pointe du pénétrateur était petit, plus ϵ_r était élevé. La pression de contact normalisée atteint un maximum au centre de contact, puis diminue graduellement jusqu'à zéro au bord du cercle de contact pour les pénétrateurs sphériques et Bkv. Cependant, une concentration de contrainte relativement faible a été observée pour les pointes sphériques par rapport au pénétrateur Bkv, pour lequel la contrainte est particulièrement élevée au centre de l'empreinte. La concentration de contrainte élevée se produisant sous le pénétrateur Bkv se traduit par une déformation plastique plus intense par rapport au cas des pénétrateurs sphériques et une déformation résiduelle plus importante subsiste après la libération de la charge. Les modes de déformation dans les différentes zones sous les différents pénétrateurs ont été déterminés et discutés en comparant la contrainte équivalente de Von Mises aux contraintes critiques induisant la transformation martensitique.

La dépendance en profondeur de la dureté d'indentation (H_{IT}) et du module élastique d'indentation (E_{IT}) ainsi que l'influence des taux de recouvrement superélastique (η_h et η_w) sur ces deux grandeurs ont également été investiguées dans cette étude. On a observé que les valeurs de H_{IT} et E_{IT} n'étaient pas constantes. En effet, H_{IT} et E_{IT} présentent une dépendance à la profondeur qui diminue avec la profondeur dans le cas du pénétrateur Bkv et qui augmente avec la profondeur dans le cas des pénétrateurs sphériques. D'autre part, les valeurs H_{IT} et E_{IT} ont également été observées dépendantes au rayon de la pointe utilisée. H_{IT} augmente avec la diminution du rayon de la pointe du pénétrateur, tandis que E_{IT} diminue avec la diminution du rayon de la pointe du pénétrateur. La figure 5 montre bien l'influence de la géométrie des pointes et de la transformation martensitique (par l'évaluation des taux de recouvrement) sur

le module élastique d'indentation E_{IT} (a) et sur la dureté d'indentation H_{IT} (b).

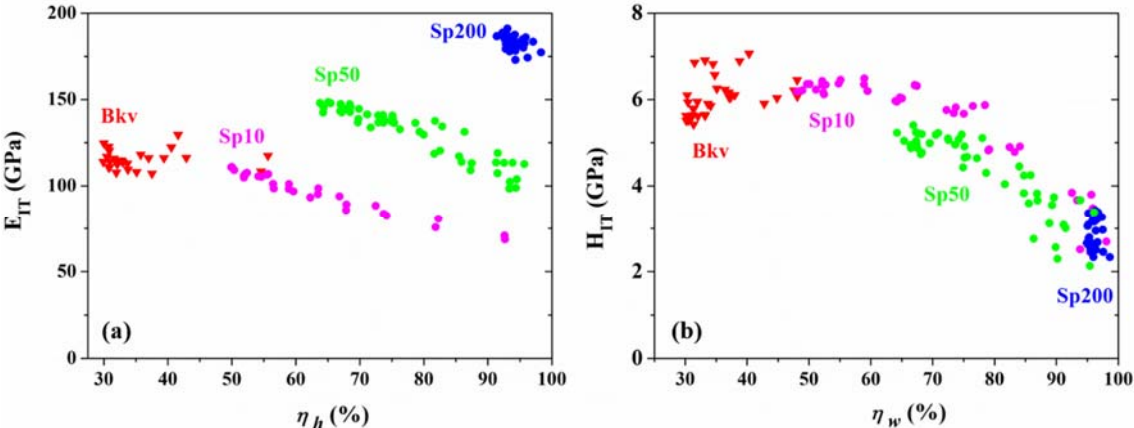


Fig.5. Module élastique d'indentation E_{IT} (a) et dureté d'indentation H_{IT} (b) en fonction du type d'indenteur et du taux de recouvrement pour le film Ti2448 superélastique.

Table of Contents

General introduction	1
Chapter I: Bibliography	5
I.1 Introduction	7
I.2 Titanium and its alloys.....	9
I.2.1 Allotropic phases in pure Ti.....	9
I.2.2 Ti alloys	11
I.2.2.1 Element additions in titanium alloys	11
I.2.2.2 Classification of Ti alloys.....	12
I.2.2.2.1 α alloys:	13
I.2.2.2.2 $\alpha + \beta$ alloys:	14
I.2.2.2.3 β alloys.....	14
I.2.3 Non-equilibrium phases in β -metastable Ti alloys	15
I.2.3.1 Martensite α'' phase	15
I.2.3.2 Athermal omega phase.....	17
I.2.4 NiTi alloys	20
I.3 Superelastic effect in Ti alloys.....	22
I.3.1 Generalities about martensitic transformation.....	22
I.3.2 Factors influencing superelastic response of Ti alloys	24
I.3.2.1 Chemical composition	24
I.3.2.2 Thermo-mechanical treatment.....	27
I.3.2.3 Texture	28
I.3.2.4 Grain size.....	30

I.4 Magnetron sputtered superelastic Ti-based alloy films	32
I.4.1 Magnetron sputtering technique	32
I.4.2 NiTi-based alloy films	34
I.4.3 Ni-free β -Ti alloy films.....	39
I.5 Conclusion.....	48
References.....	49
Chapter II: Elaboration and Characterization methods	55
II.1 Elaboration	57
II.1.1 Elaboration of Ti-based bulk alloys	57
II.1.1.1 Cold crucible levitation melting Furnace	57
II.1.1.2 Thermo-mechanical treatments	58
II.1.2 Elaboration of Ti-based alloy films	59
II.1.2.1 Magnetron sputtering technique.....	59
II.1.2.2 Deposition conditions.....	62
II.2 Characterization methods	64
II.2.1 Microstructural characterization	64
II.2.1.1 Optical microscopy	64
II.2.1.2 Surface topography and roughness measurements.....	64
II.2.1.3 X-ray diffraction analyses	65
II.2.1.4 Electron microscopy and analyses	67
II.2.2 Mechanical characterization.....	69
II.2.2.1 Tensile tests	69
II.2.2.2 Nanoindentation	70
References:.....	75

Chapter III: Characterization of the superelasticity and mechanical properties of the Ti-20Zr-3Mo-3Sn bulk alloy at the grain scale by nanoindentation 77

III.1 Introduction.....	79
III.2 Materials and methods	80
III.3 Results and discussion	82
III.3.1 Structural characterizations.....	82
III.3.2 Nanoindentation load-displacement curves along the three principal crystallographic directions of β phase	83
III.3.3 Anisotropy of indentation depth and work recovery ratios.....	86
III.3.4 Theoretical anisotropy of the martensitic transformation strain	88
III.3.5 Anisotropy of the indentation modulus.....	93
III.3.6 Indentation hardness	97
III.4 Conclusion	97
References.....	99

Chapter IV: Investigation of the superelastic behavior of Ti-16Zr-13Nb-2Sn sputtered film by nanoindentation 103

IV.1 Introduction	105
IV.2 Materials and methods	107
IV.2.1 Materials synthesis	107
IV.2.2 Microstructural and superelastic characterizations	108
IV.3 Results	110
IV.3.1 Microstructural properties	110
IV.3.2 Superelastic properties	116
IV.4 Discussion	120
IV.5 Conclusion.....	126
References:.....	129

Chapter V: Microstructure and local mechanical properties in superelastic Ti-24Nb-4Zr-8Sn film	133
V.1 Introduction	135
V.2 Experimental protocol	137
V.3 Results and discussion	138
V.3.1 Microstructural analyses.....	138
V.3.1.1 Chemical composition	138
V.3.1.2 Morphology	139
V.3.1.3 Phase composition	140
V.3.1.4 Texture analysis	142
V.3.1.5 TEM observations.....	147
V.3.2 Characterization of the superelastic response.....	149
V.3.2.1 Depth recoverability and work recoverability	150
V.3.2.2 Strain and Stress distributions under tips	152
V.3.2.2.1 Strain fields.....	152
V.3.2.2.2 Stress fields.....	153
V.3.2.3 Microstructure evolutions during indentation process	154
V.3.3 Mechanical properties	156
V.3.3.1 Elastic modulus	156
V.3.3.2 Indentation hardness	159
V.4 Conclusion	165
References:.....	166
General conclusion.....	171

General introduction

Titanium alloys are widely used as biomaterials due to their low density, adapted mechanical properties and good biocompatibility. A good biomedical titanium alloy needs to be optimized as the function of the targeted applications (hip prosthesis, dental implants, cardiovascular stents, orthopedic staples, orthodontic arches...). Such optimization depends on the chemical composition, the phase constitution and the microstructure. Research on the β -types Ti-based alloys with non-cytotoxic and non-allergenic elements such as Zr, Nb and Mo has increased rapidly during the past decade, especially with the aim to enhance their mechanical properties and more particularly their superelastic performances.

To our knowledge, the research work on Ni-free superelastic β Ti-based films deposited through physical vapor deposition methods has not been explored intensively. Film technology is promising for further miniaturization and design possibilities for nanometer-sized functional tools and devices for biomedicine. In the field of superelastic films, most activities have focused on the superelastic response of magnetron sputtered NiTi-based alloy films since the 1990s, basically for the development of miniature systems (micro-sensors, -actuators, -pumps and -valves). In addition to the suspected toxicity and carcinogenicity of nickel, a major drawback is the amorphous nature of as-deposited NiTi films at room temperature which require suitable heat treatments to obtain the crystalline phase responsible of the superelastic effect. Much less work has investigated superelastic response in Ni-free metastable β Ti-based alloy films deposited by magnetron sputtered. The aim of the present thesis is to investigate whether titanium-based alloys sputtered films can display superelastic behaviors as their bulk ingot counterparts. In the present work, β -Ti alloy compositions, namely Ti-20Zr-3Mo-3Sn (Ti2033, at.%), Ti-16Zr-13Nb-2Sn (Ti16132, at.%), and Ti-24Nb-4Zr-8Sn (Ti2448, wt.%) have been studied.

In the first chapter, a bibliographic study on the general properties for Ti and Ti-based alloys were carried out, and the interest was mainly in superelastic Ni-free metastable β titanium alloys as promising candidates for biomedical applications. Then, the superelastic property associated with a reversible martensitic transformation was reviewed in view of the responses to mechanical loads. Finally, the magnetron sputtered films were reviewed in cases of NiTi-based system and Ni-free β -Ti system. On the basis of this literature review, our investigative choices focused on four superelastic alloys from two quaternary systems (Ti-Zr-Mo-Sn and Ti-Nb-Zr-Sn) from bulk to film geometry.

In the second chapter, all elaboration procedures and experimental characterization techniques were presented. The bulks were elaborated by cold crucible levitation melting (CCLM) and a series of thermo-mechanical treatments. The films were deposited on Si substrates by magnetron sputtering technique. The morphological, crystallographic and microstructural characteristics of the bulks and films were studied by optical microscopy (OM), scanning electron microscopy (SEM), atomic force microscope (AFM), X-ray diffraction (XRD), electron backscatter diffraction (EBSD) and transmission electron microscopy (TEM). Conventional and cyclic tensile tests were used to evaluate the mechanical properties including the superelasticity in bulk alloys. In this work, the nanoindentation technique has been widely used to probe local mechanical properties in sputtered films and in bulk alloys with the aim of characterizing the superelastic response.

The following three chapters concern the results obtained and are written like articles. Note that chapter IV was the subject of an article published in the journal *Surface & Coatings Technologies* 450 (2021) 126690.

In the chapter III, the crystallographic anisotropy of indentation responses was studied at the scale of individual grains in superelastic Ti2033 polycrystalline bulk alloy by the combined application of nanoindentation and electron backscattered diffraction (EBSD) analysis. From the results obtained, it has been shown that nanoindentation is an effective technique for probing a superelastic response in this kind of alloy. In chapter IV, nanoindentation technique was used to characterize the superelasticity of magnetron-sputtered Ti16132 films. Four indenters with different geometries (spherical and Berkovich indenters) were used to study the nanoscale indentation behaviors of Ti16132 superelastic films through different deformation regimes. The representative strain was introduced to present the evolution of the deformation mechanisms during nanoindentation with increasing depths and increasing tip radii.

In chapter IV, nanoindentation technique was used to characterize the superelasticity of magnetron-sputtered Ti16132 films. Four indenters with different geometries (spherical and Berkovich indenters) were used to study the nanoscale indentation behaviors of Ti16132 superelastic films through different deformation regimes. The representative strain was introduced to present the evolution of the deformation mechanisms during nanoindentation with increasing depths and increasing tip radii.

In chapter V, nanoindentation measurements were performed to systematically characterize the superelasticity in the magnetron-sputtered Ti2448 thin films. The evolution of superelastic recovery as a function of indentation depths was presented and discussed in

terms of indentation stress and strain field distributions underneath the indenter tips. For this, the representative strain and normalized contact pressure distribution were calculated for spherical and Berkovich indenters, and the microstructure evolution during nanoindentation was illustrated. The indentation size effect and the tip radius effect on indentation hardness and elastic modulus in Ti₂448 films were investigated with a specific attention on the influence of martensitic transformation induced by indentation.

Chapter I: Bibliography

I.1 Introduction

Titanium (Ti) is a transition metal belonging to group 4 of the periodic table of elements. Ti is widely distributed throughout the whole universe such as stars and interstellar dust. After Al, Fe and Mg, titanium is the fourth most abundant of structural metals and is the ninth most abundant element on the earth. Titanium exists in most minerals such as ilmenite (FeTiO_3); rutile (TiO_2); arizonite ($\text{Fe}_2\text{Ti}_3\text{O}_9$); perovskite (CaTiO_3) and titanite (CaTiSiO_5). Titanium offers attractive property owing to the combination of high strength, stiffness, toughness, low density, and good corrosion resistance. As Ti is a transition metal with an incomplete d shell, various Ti alloys may form by alloying with interstitial and substitutional elements (Nb, Mo, Zr, O, etc.).

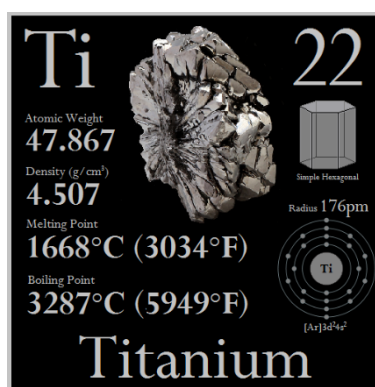


Fig. I-1 Physical and chemical properties of Titanium

The interest in the metal Ti and Ti-based alloys has gained momentum from the late 1940s in view of their suitability for being used as structural materials in certain rapidly developing industries, particularly, in the aerospace and chemical industries [1, 2]. During the last decade, titanium and titanium alloy production practices have matured rapidly, due to low elastic modulus, good biocompatibility, excellent corrosion resistance and their high specific strength. Fig. I-2 provides examples of the growth in the use of Ti in widely differing applications, and with a range of engineering demands, that in many cases impact human safety and well-being.

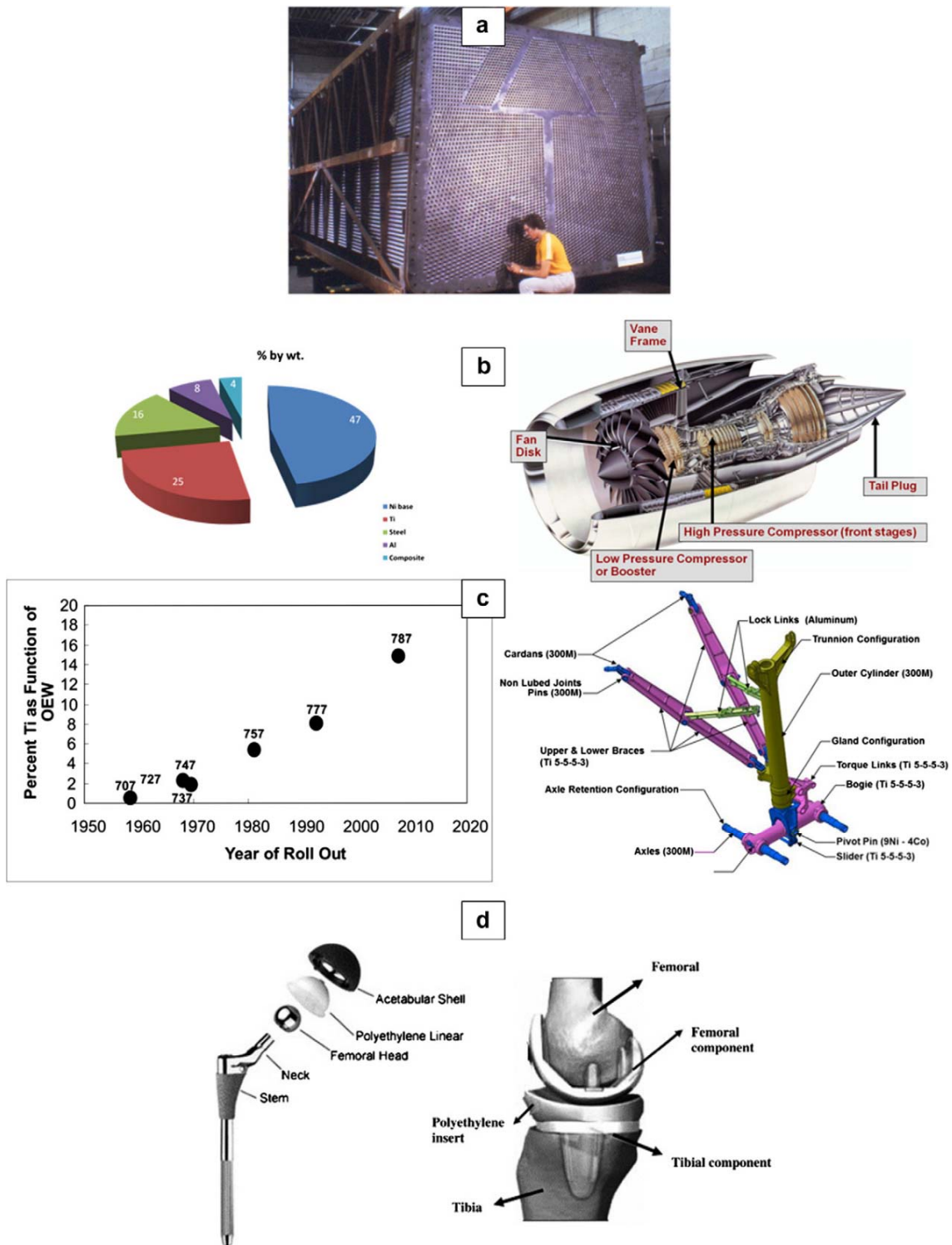


Fig. I-2 Some examples of applications of Ti and its alloys: (a) alpha Ti alloy in tubing for heat exchangers (courtesy JA Hall), (b) near alpha and alpha + beta Ti alloys in aeroengines, (c) high strength metastable beta Ti alloys in airframes, as percentage of overall aircraft weight and in landing gear of the Boeing 787, and (d) a titanium hip replacement [3].

I.2 Titanium and its alloys

I.2.1 Allotropic phases in pure Ti

Pure Ti exhibits two allotropic crystalline structures at atmospheric pressure: the low temperature phase termed as the α -Ti phase, and the high temperature phase termed as the β -Ti phase.

According to Fig. I-3, α -Ti phase has a hexagonal close packed (hcp) structure belonging to the space group of 194 $P6_3/mmc$, and the lattice parameters are: $a_\alpha = 0.295$ nm, $c_\alpha = 0.468$ nm and the ratio $c/a = 1.587$ [4, 5]. The β -Ti phase has a body centered cubic (bcc) structure belonging to the space group of 229 $Im\bar{3}m$, and the lattice parameter is: $a_\beta = 0.332$ nm [4].

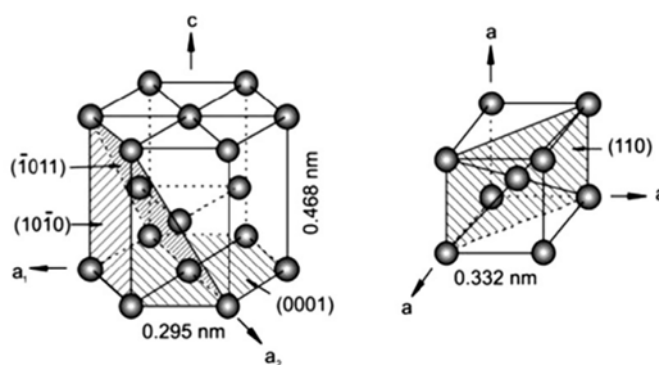


Fig. I-3 Crystallographic structures of α -Ti phase and β -Ti phase.

An allotropic transformation takes place between α -Ti and β -Ti at 882°C in pure Ti. The allotropic transformation temperature is the so-called β transus (T_β). The transformation can either occur by displacive transformation (martensitic transformation) or by a diffusion-controlled nucleation and growth process depending on thermal path.

Fig. I-4 shows the lattice arrangement of α and β phases. Allotropic transformation α -Ti \leftrightarrow β -Ti proceeds in strict agreement with crystallographic orientation relationship between α - and β - phases which has first been studied for zirconium described by W. G. Burgers [6] and is therefore called the Burgers relationship:

$$\{110\}_\beta \parallel (0001)_\alpha \text{ and } \langle 111 \rangle_\beta \parallel \langle 11\bar{2}0 \rangle_\alpha$$

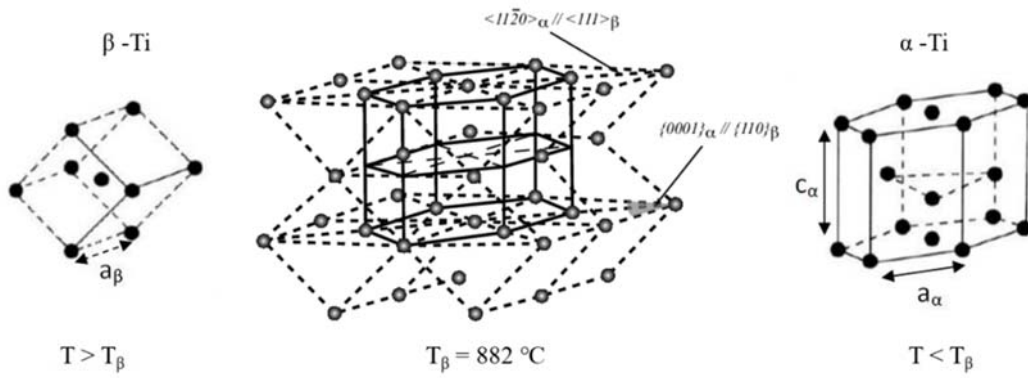


Fig. I-4 Arrangement of bcc β into hcp α lattice during the allotropic transformation [6, 7].

Lattice reconstructing process during the allotropic transformation can be schematically shown as a complex displacement of atoms in various directions (Fig. I-5). Generally, it was found that the unit cells reconstruction in crystal lattice during phase transformation α -Ti \leftrightarrow β -Ti is based on atoms displacement along $\{112\}$ surface and $\langle 111 \rangle$ direction with concurrent unit cell expansion in two directions and compression in the third direction.

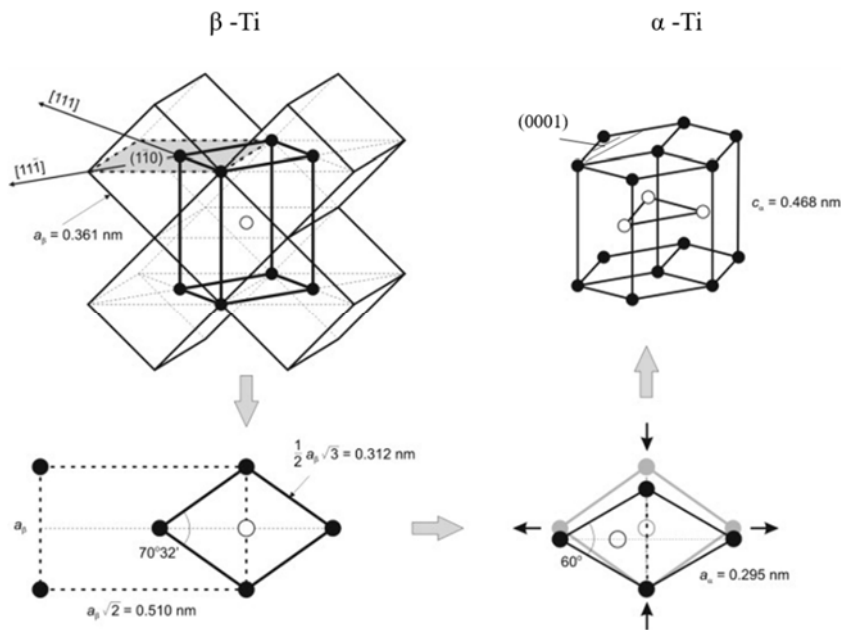


Fig. I-5 Scheme of the allotropic transformation [8].

According to the Burgers relationship and the crystal symmetry of α and β phases, a bcc β crystal can transform to 12 possible hexagonal α -variants, having different orientations with regard to the parent β crystal, as summarized in Table I-1.

Table I-1 Orientation variants resulting from $\beta \rightarrow \alpha$ phase transformation [9, 10].

Variant No.	Corresponding plane $(hkl)_\beta (hkil)_\alpha$	Corresponding direction $[uvw]_\beta [uvtw]_\alpha$
1	$(011)_\beta (0001)_\alpha$	$[\bar{1}\bar{1}1]_\beta [2\bar{1}\bar{1}0]_\alpha$
2		$[1\bar{1}1]_\beta [2\bar{1}\bar{1}0]_\alpha$
3	$(\bar{1}01)_\beta (0001)_\alpha$	$[1\bar{1}1]_\beta [2\bar{1}\bar{1}0]_\alpha$
4		$[111]_\beta [2\bar{1}\bar{1}0]_\alpha$
5	$(0\bar{1}1)_\beta (0001)_\alpha$	$[111]_\beta [2\bar{1}\bar{1}0]_\alpha$
6		$[\bar{1}11]_\beta [2\bar{1}\bar{1}0]_\alpha$
7	$(101)_\beta (0001)_\alpha$	$[\bar{1}11]_\beta [2\bar{1}\bar{1}0]_\alpha$
8		$[\bar{1}\bar{1}1]_\beta [2\bar{1}\bar{1}0]_\alpha$
9	$(\bar{1}\bar{1}0)_\beta (0001)_\alpha$	$[\bar{1}\bar{1}1]_\beta [2\bar{1}\bar{1}0]_\alpha$
10		$[111]_\beta [2\bar{1}\bar{1}0]_\alpha$
11	$(110)_\beta (0001)_\alpha$	$[1\bar{1}1]_\beta [2\bar{1}\bar{1}0]_\alpha$
12		$[\bar{1}11]_\beta [2\bar{1}\bar{1}0]_\alpha$

I.2.2 Ti alloys

I.2.2.1 Element additions in titanium alloys

In Ti-based alloys, the effect of an alloying element pertains significantly to the manner in which its addition alters the β transus temperature (T_β). Elements which, on being dissolved in Ti, raise the T_β are defined as α -stabilizers. These elements are generally non-transition metals or interstitial elements, such as Al, C, N and O (Fig. I-6a). Elements which, on alloying with Ti, bring down the T_β are termed as β -stabilizers. These elements are generally divided into β -isomorphous elements (such as the transition metals V, Nb, Ta and Mo in Fig. I-6b) and β eutectoid forming elements (such as Cr, Cu and Ni in Fig. I-6c), depending on whether intermetallic compounds are formed through eutectoid decomposition of β -phase. Elements which change the T_β only slightly are named as neutral elements such as Zr, Hf and Sn in Fig. I-6d.

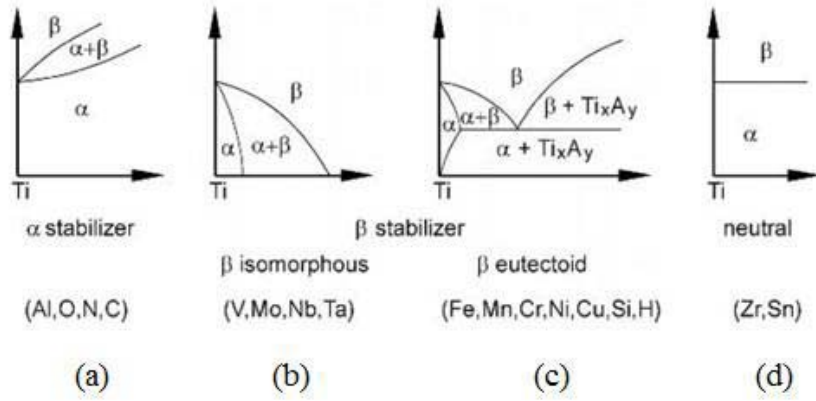


Fig. I-6 Effect of alloying elements on the T_{β} of Ti alloys (schematically).

I.2.2.2 Classification of Ti alloys

According to the alloying additions and the phases present at room temperature, Ti alloys are broadly grouped into three major categories: α alloys, $\alpha + \beta$ alloys and β alloys. Their properties are dependent on microstructure, which is connected to the chemical composition and thermomechanical processing. The corresponding phase fields are delineated in temperature-composition phase diagram of Ti alloys in Fig. I-7.

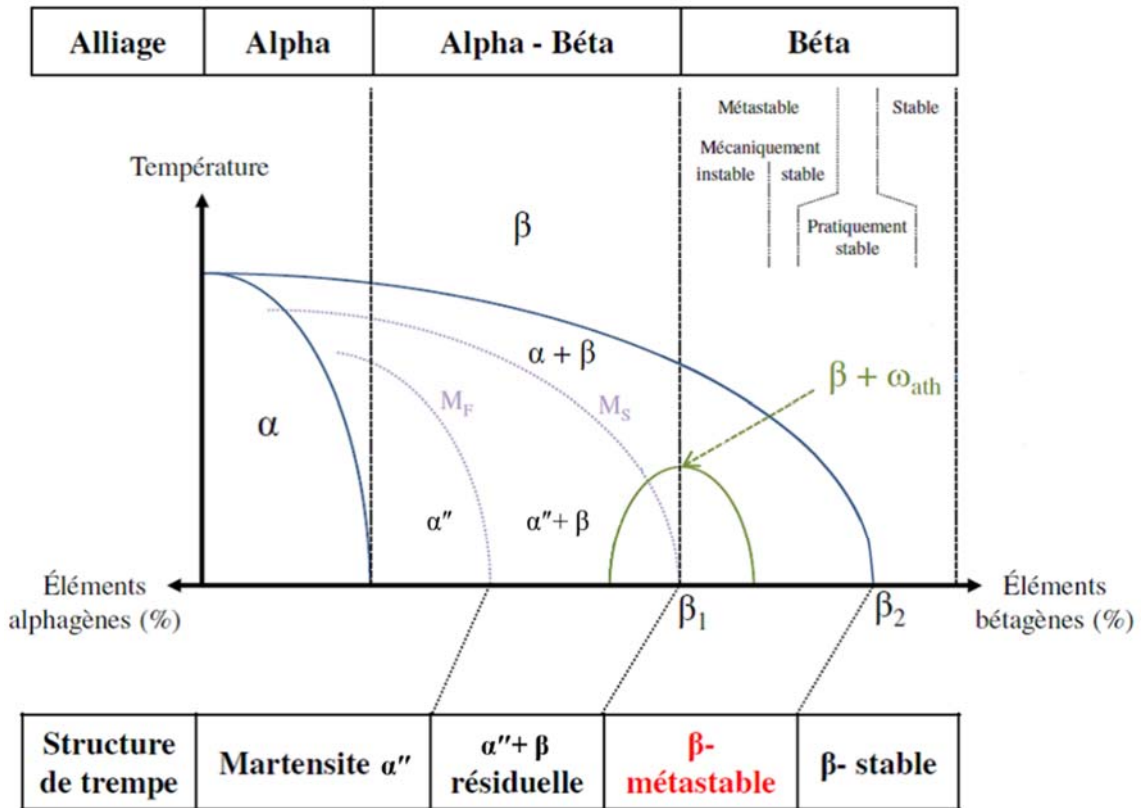


Fig. I-7 Classification of Ti-alloys based on different alloying concentrations and present phases in the microstructures at room temperature (schematically) [11].

Table I-2 lists the more frequently used β -stabilizers and their respective β_1 values. It shows that the β -isomorphous stabilizers have high β_1 values and decompose to form only $\alpha + \beta$ phases (i.e. no compound formation), while the β -eutectoid stabilizers have lower β_1 values and are less efficient in decreasing the T_β , tend to form $\alpha +$ intermetallic compound upon decomposition of β -phase.

Table I-2 β -stabilizers and their respective β_1 values [12, 13]

β -Stabilizer	Type	β_1 (wt.%) ^a	β_1 Suppression (°C) ^b
Mo	Isomorphous	10.0	-8.3
V		15.0	-5.5
W		22.5	-13.8
Nb		36.0	-10.6
Ta		45.0	-15.6
Fe	Eutectoid	3.5	0.0
Cr		6.5	-2.8
Cu		13.0	-5.6
Ni		9.0	4.4
Co		7.0	3.3
Mn		—	21.1

^a Approximate wt.% needed to retain 100% beta upon quenching.

^b Approximate amount of beta transus reduction per wt.% of addition.

There is a convenient manner in which to consider the overall stability of β phase in an alloy with various alloying additions. By arbitrarily using Mo as a baseline, a “moly equivalent” (Mo Eq.) has been defined as follows [12]:

$$\text{Mo Eq.} = 1.0 \text{ Mo(wt.\%)} + 0.22 \text{ Ta(wt.\%)} + 0.28 \text{ Nb(wt.\%)} + 0.44 \text{ W(wt.\%)} + 0.67 \text{ V(wt.\%)} \\ + 1.6 \text{ Cr(wt.\%)} + 2.9 \text{ Fe(wt.\%)}$$

The constants before each alloying elements are associated with the ratio of β_1 for molybdenum divided by β_1 for the particular element. In general, the β transus temperature (T_β) tends to decrease as the Mo Eq. increases [13].

The metallurgy of β alloys enables the development of compositions and processing routes that can satisfy diverse requirements of high strength with adequate toughness and fatigue resistance required in airframe applications (Fig. I-2c) or meeting requirements of low modulus and biocompatibility with shape memory response and fatigue strength for use in biomedical applications (Fig. I-2d).

1.2.2.2.1 α alloys:

Ti alloys with one or more α -stabilizer additions present a single α -Ti phase (hexagonal structure) at room temperature, known as α alloys. Depending on the cooling rates, the

microstructure can be composed of equiaxed α , widmanstatten lath-like α phase or martensitic α' phases. These alloys are non-heat treatable alloys having moderate strength, good fracture toughness, superior high temperature creep, oxidation resistance and weldability [1]. The α alloys are extensively used in applications that are not particularly demanding in terms of strength but focus more on the attractive corrosion resistance of titanium (an example can be seen from Fig. I-2a). α -type alloys can tolerate a small amount of β phase (2-5%) upon cooling from the β phase field with addition of Mo and V, which are called near- α alloys. The small amount of β phase in the near- α alloys is useful for better controlling the recrystallized α grain size and improving mechanical properties.

1.2.2.2.2 $\alpha + \beta$ alloys:

The $\alpha + \beta$ alloys are such that at room temperature they contain a mixture of the α - and β - phases. The relative proportions of the constituent phases are determined by the nature (α - or β -stabilizers) and the amounts of the alloying elements, as well as the heat treatment. The mechanical properties of $\alpha + \beta$ alloys depend on the relative amount and distribution of α and β phases [14]. Two-phase $\alpha + \beta$ alloys offer a range of combinations of strength, toughness and high temperature properties that make them attractive in wide ranging aerospace products. This category of alloys represent the majority of Ti alloys on the market, the most known one being Ti-6Al-4V (an example in Fig. I-2b). Seen from the phase diagram in Fig. 1-7, the range for $\alpha + \beta$ alloys show the presence of the M_s line above room temperature. Therefore, the $\alpha + \beta$ alloys have a α'' martensitic transformation upon fast cooling from the β phase field to room temperature.

1.2.2.2.3 β alloys

The β alloys are defined as alloys that retain 100% β phase when quenched to room temperature from above the β transus. These alloys contain enough β -stabilizing elements to avoid passing through the martensite start line (M_s) when quenched to room temperature, consequently precluding the formation of martensite at room temperature. Within the β alloys group, there are the subclasses of metastable β and stable β alloys, with respect to the stability of β phase obtained at room temperature.

The **β -metastable alloys** are alloys that lie between the β_1 critical minimum content of β -stabilizers and the β_2 point and within the two-phase $\alpha + \beta$ region at room temperature (see Fig. I-7). A fully β phase microstructure can be retained by quenching from the β phase field in such alloys, the obtained β phase is metastable at room temperature. Non-equilibrium

phases (such as α'' martensite, isothermal or athermal ω phase) can appear in these β -metastable alloys. In such case, the superelastic property can be achieved via stress-induced martensitic phase transformation and will be detailed later in section I.3.

The **β -stable alloys** are alloys to the right of β_2 concentration (see Fig. I-7). Thus, for these alloys, more content of β stabilizing elements is added decreasing the β transus below the room temperature. A fully β -stable phase microstructure is obtained at room temperature and for any cooling conditions. The β -phase is ductile, and therefore β -Ti alloys exhibit attractive cold and hot workability, which enables creating specialized β -Ti alloys for specific applications. β alloys are prone to ductile-brittle transformation, and thus are not used for cryogenic applications.

I.2.3 Non-equilibrium phases in β -metastable Ti alloys

Phase transformations in crystalline materials can be classed generally under two headings: (a) replacement-type transformations in which atoms of a given species are replaced at or near lattice sites by atoms of a different species (including vacancies); (b) displacement-type transformations in which atoms, regardless of their nature move in a cooperative way by distances which are fractions of lattice translation vectors. The former transformations, being diffusion-controlled, occur slowly except at high temperatures, the latter, controlled by local atomic shuffles, can occur very rapidly below a certain critical temperature, even at low temperatures. The phases formed during diffusion-controlled transformation are equilibrium phases, such as α -Ti and β -Ti phases mentioned above, and the phases formed by displacive transformation are non-equilibrium phases, such as martensite α'' phase and ω_{ath} phase observed in β -metastable Ti alloys.

I.2.3.1 Martensite α'' phase

The martensitic α'' phase presents a C-centered orthorhombic structure belonging to the space group of $N^\circ 63$, Cmc m . The atom positions are:

$$(0, y, 1/4) \quad (1/2, 1/2+y, 1/4) \quad (0, \bar{y}, 3/4) \quad (1/2, 1/2-y, 3/4)$$

where the value of y is determined by the atom positions in the (002) plane of the orthorhombic crystal structure, depending on the alloy composition [15].

Fig. I-8a shows a schematic illustration exhibiting the crystal structures of the β , α'' , and α phases and their lattice correspondences. The orthorhombic α'' martensite is an intermediate structure between the body centered cubic structure of β -Ti phase and the hexagonal structure of α -Ti phase. The lattice parameters (a' , b' , c') of the martensitic α'' phase depend significantly on the β -stabilizer content, varying between two extreme situations, one corresponding to the hexagonal structure of α -Ti phase (for which $y=1/6$; $b'/a'=\sqrt{3}$ and $c'/a'=\sqrt{8/3}$), the other corresponding to the body centered cubic structure of β -Ti phase (for which $y=1/4$ and $b'/a' = c'/a' = \sqrt{2}$), as illustrated in Fig. I-8b.

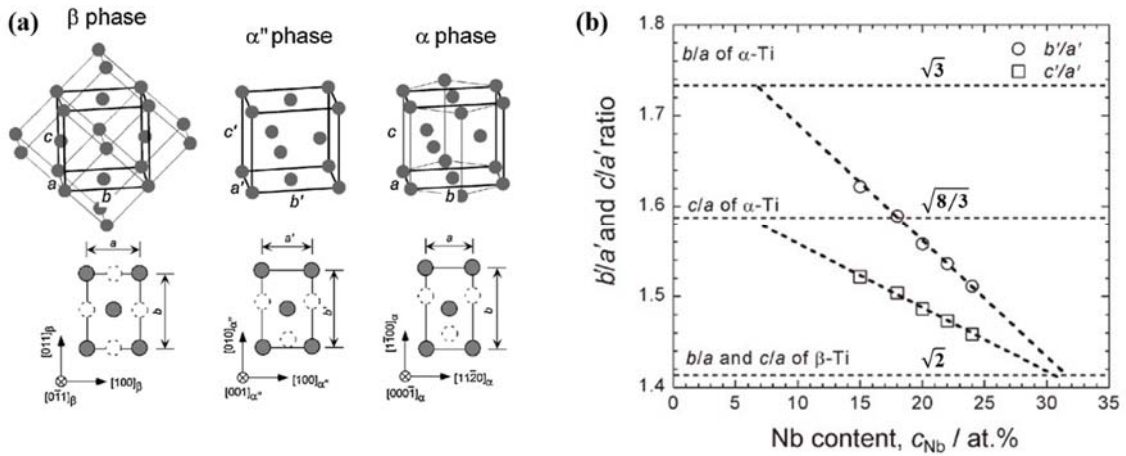


Fig. I-8 (a) Crystal structures of the β , α'' , and α phases and their lattice correspondences. (b) Nb dependence of b'/a' and c'/a' of the orthorhombic martensite α'' - phase [16].

During the martensitic transformation, the orientation relationship between β phase and α'' orthorhombic martensite follows the relations below [17]:

$$(110)_{\beta} // (001)_{\alpha''} \quad [111]_{\beta} // [101]_{\alpha''}.$$

The lattice correspondences between β and α'' phases are expressed as follows [16]:

$$[100]_{\alpha''} - \langle 100 \rangle_{\beta}, \quad [010]_{\alpha''} - \langle 011 \rangle_{\beta}, \quad [001]_{\alpha''} - \langle 0-11 \rangle_{\beta}.$$

Hence, there are six different ways to orientate the three principal axes of orthorhombic crystal in the body centered cubic crystal while respecting the orientation relationship between β and α'' phases. The six equivalent rotary permutations are called variants. The six lattice correspondence variants are designated as V1, V2, V3, V4, V5 and V6, are given in Table I-3.

Table I-3 Lattice correspondence variants derived from the β/α'' orientation relationship [18].

Variant	$[100]_{\alpha''}$	$[010]_{\alpha''}$	$[001]_{\alpha''}$
V1	$[100]_{\beta}$	$[011]_{\beta}$	$[0\bar{1}1]_{\beta}$
V2	$[100]_{\beta}$	$[0\bar{1}1]_{\beta}$	$[01\bar{1}]_{\beta}$
V3	$[010]_{\beta}$	$[101]_{\beta}$	$[10\bar{1}]_{\beta}$
V4	$[010]_{\beta}$	$[10\bar{1}]_{\beta}$	$[\bar{1}01]_{\beta}$
V5	$[001]_{\beta}$	$[110]_{\beta}$	$[\bar{1}10]_{\beta}$
V6	$[001]_{\beta}$	$[\bar{1}10]_{\beta}$	$[1\bar{1}0]_{\beta}$

The α'' phase in metastable β alloys with various variants can be observed as shown in Fig. I-9.

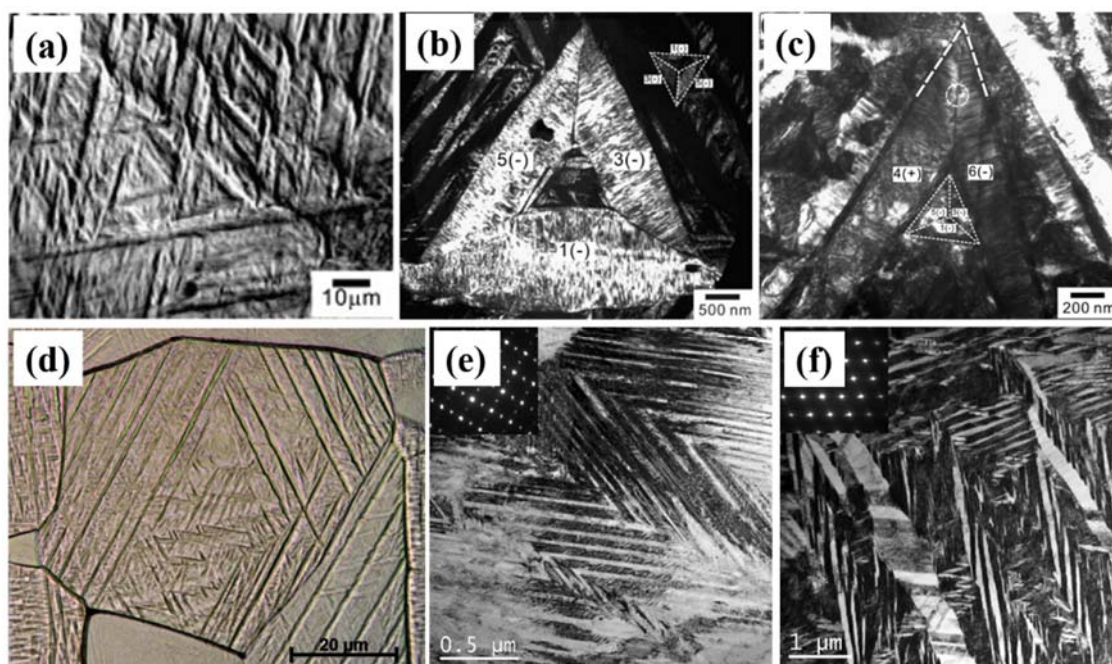


Fig. I-9 Optical micrograph (a) and dark-field TEM images (b-c) showing the morphology of α'' martensite variants in quenched Ti-20Nb alloys [18]; (d-f) Optical micrograph (d) and bright-field TEM images (e-f) of V-shaped α'' martensite morphology in quenched Ti-25Ta-20Nb alloys [19].

I.2.3.2 Athermal omega phase

ω -phase is the high-pressure equilibrium phase for chemical elements such as Ti, Zr and Hf belonging to column IVB of the periodic table, and can be formed at atmosphere pressure by rapidly cooling the bcc structure [20]. ω -phase was firstly identified in β -type Ti-Cr alloys by Frost et al. in 1954 [21]. Since then, the ω -phase has been observed in numerous Ti-, Ta-, Hf- and Zr- based alloys containing appropriate β -stabilizing elements and many other β -metastable alloys [2, 22, 23]. Depending on the formation condition, ω phase can be formed as a non-equilibrium phase by rapid cooling (athermal ω_{ath} phase), by aging in the temperature range of 373-773K (isothermal ω_{iso} phase) or stress-induced from applied stress. The ω -phase

presents a hexagonal structure (space group: N°191 P6/mmm) with three atomic positions [24]:

$$(0, 0, 0), (1/3, 2/3, 1/2), \text{ and } (2/3, 1/3, 1/2).$$

The ω_{ath} phase can form upon water quenching from the β -phase region over a limited composition range (Fig. I-10). The orientation relationships between ω_{ath} and β resulting from displacive transformation were reported to be [20, 24, 25]:

$$[111]_{\beta} // [0001]_{\omega_{\text{ath}}} \text{ and } (1-10)_{\beta} // (11-20)_{\omega_{\text{ath}}}.$$

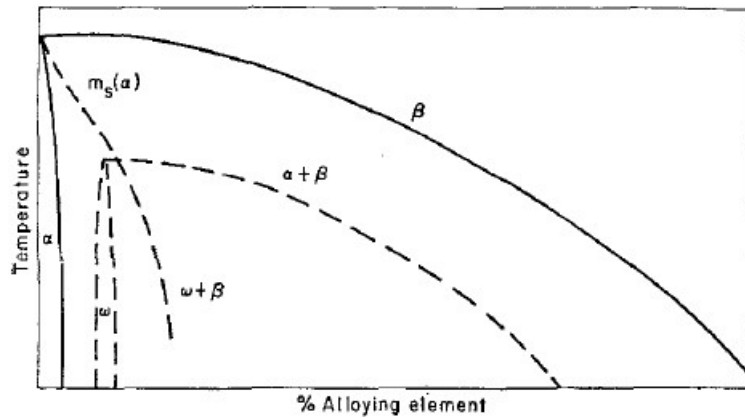


Fig. I-10 Metastable phase diagram for omega formation in β -isomorphous systems [24].

Frost [21] and De Fontaine [26] have proposed the $(111)_{\beta}$ plane collapse model to explain the $\beta \rightarrow \omega_{\text{ath}}$ displacive transformation: the ω_{ath} lattice can be obtained by collapsing one pair of (111) planes to the intermediate position leaving the adjacent (111) planes unaltered, involving a diffusionless process (Fig. I-11). Lin et al. [27] demonstrated that the athermal ω -phase formation was caused by an atom collapse from the $(110)_{\beta}$ plane to the $(111)_{\beta}$ plane along the $\langle 111 \rangle_{\beta}$ direction (Fig. I-12). The model also suggests that the rigid atom clusters originated from athermal ω phase can be directly developed to the perfect α phase with the help of vacancies.

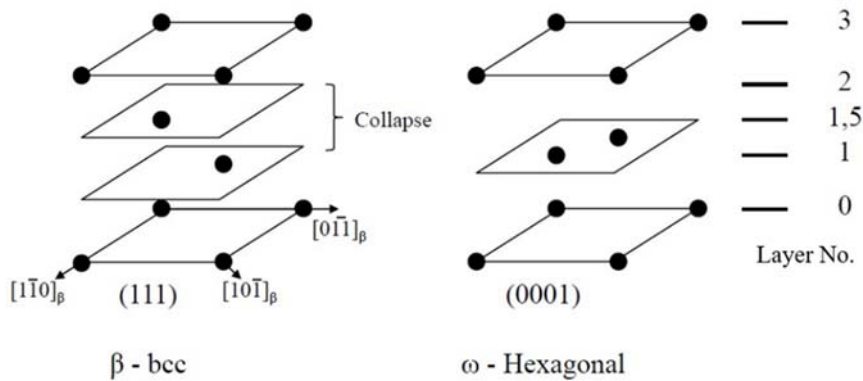


Fig. I-11 (111) planes in a bcc lattice. (b) Collapsed planes to generate hexagonal omega [20].

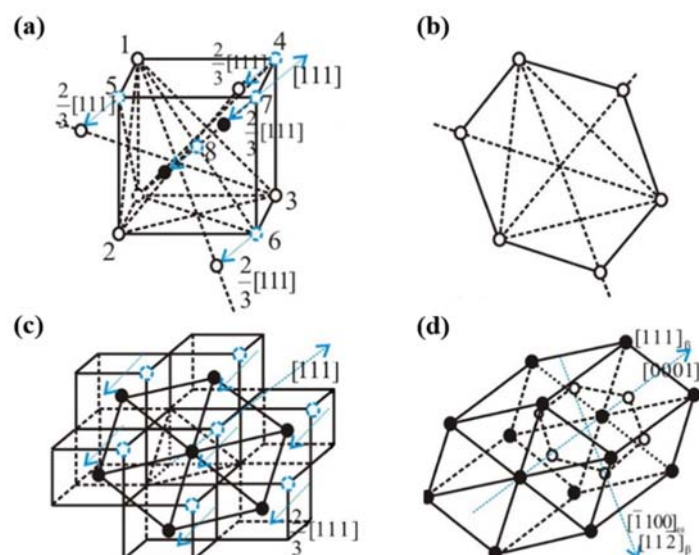


Fig. I-12 Formation model of ω_{ath} phase. (a) the atom movement pathways of β phase, showing the atom movement from the (110) plane to (111) plane; (b) the formed (0002) crystal plane in ω phase, associated with atoms marked with empty circle; (c) the formed (0001) crystal plane in ω phase, associated with atoms marked with solid circle; (d) the ω_{ath} phase formed by two sets of atom movement, exhibiting $[111]_{\beta} // [0001]_{\omega}$, and $[11-2]_{\beta} // [-1100]_{\omega}$ [27].

ω phase appears as nanosized coherent precipitates with a typical size range of 2–10 nm dispersed in β -phase matrix. Fig. I-13 shows the morphology of ω_{ath} phase in the dark field TEM images of Ti-Mo-Sn-Zr alloys. In the corresponding SADPs, in addition to the primary diffraction spots from the β matrix, diffused scattering at $1/3$ and $2/3\{1\ 1\ 2\}_{\beta}$ positions corresponding to the ω_{ath} phase were observed. The intensity of diffuse scattering of the ω_{ath} phase decreased with increasing Sn content, suggesting that the addition of Sn can suppress the formation of ω_{ath} phase. Similarly, the addition of Ta is effective in suppressing the formation of ω_{ath} phase [28].

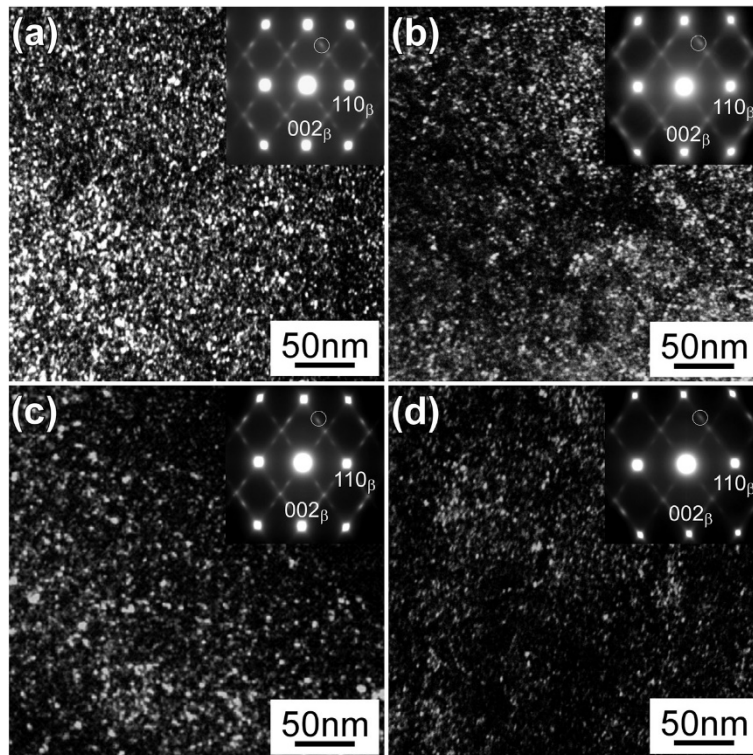


Fig. I-13 Dark field TEM images of the ω_{ath} phase and the corresponding selected area diffraction patterns (SADPs) taken from the zone axis of $[110]_{\beta}$ in water quenched specimens of (a) Ti-3Mo-5.5Sn-9Zr, (b) Ti-3Mo-6Sn-7Zr, (c) Ti-3Mo-6.5Sn-5Zr, and (d) Ti-3Mo-7Sn-3Zr alloys [29].

I.2.4 NiTi alloys

The discovery in the 1960's of shape memory properties in the Ni-Ti system led to the rapid growth of interest in the shape memory phenomenon. Nitinol is commonly used when referring to NiTi based shape memory alloys: Ni for Nickel, Ti for Titanium and NOL for Naval Ordnance Laboratory, the place where Buehler and his coworker discovered this alloy. From the phase diagram in Fig. I-14, NiTi is an ordered intermetallic compound with near an equiatomic composition of Ti and Ni, and it exists as the stable phase down to room temperature. At low temperature the stoichiometric range of NiTi is rather narrow and it often contains precipitates of a secondary intermetallic phases, such as $NiTi_2$, Ni_3Ti and Ni_4Ti_3 . These secondary phase precipitations influence the mechanical properties of NiTi alloys.

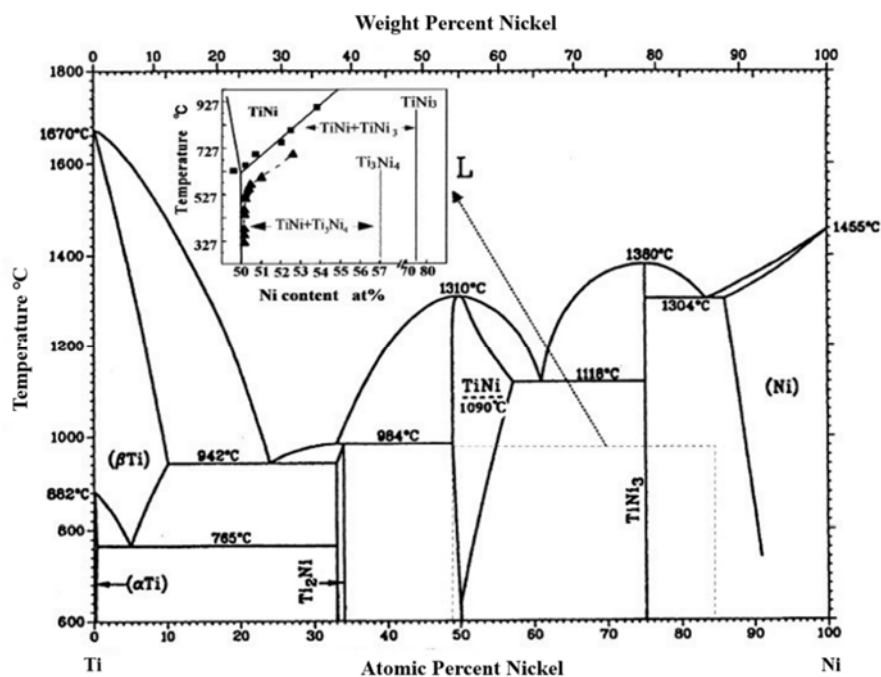


Fig. I-14 Phase diagram for NiTi system [30].

Within the composition range at which NiTi phase exists at room temperature, martensite start temperature M_s depends strongly on composition, particularly on the Ni-rich side (Fig. I-15). Thus precise composition control is required when elaborating NiTi alloys.

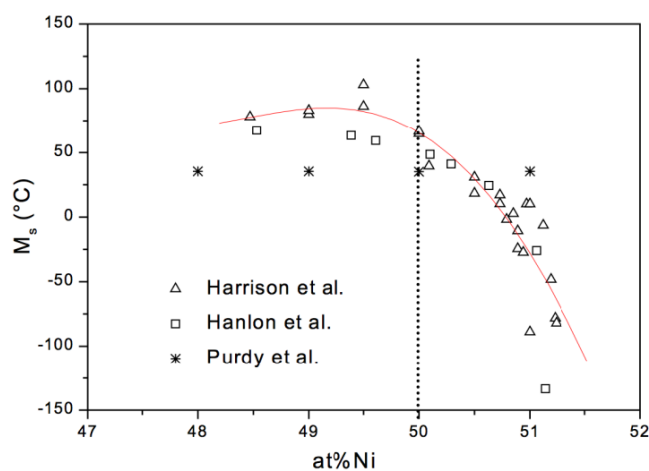


Fig. I-15 Evolution of the transformation temperature M_s as a function of the Ni content [31].

NiTi austenite phase has a CsCl (B2) type ordered cubic structure with the space group of $N^{\circ}221$, $Pm-3m$ and lattice parameter $a = 0.3015$ nm at room temperature [32]. Martensitic phase observed in NiTi alloy has a monoclinic B19' structure with the space group of $N^{\circ}11$, $P2_1/m$ and the lattice parameters: $a = 0.2884$ nm, $b = 0.411$ nm, $c = 0.4665$ nm, and $\beta = 98.1^{\circ}$ [33]. The crystal structures of B2 and B19' phases are presented in Fig. I-16. The lattice correspondence between B2 phase and B19' phase is expressed as:

$$[100]_{B19'} - [-100]_{B2}, [010]_{B19'} - [01-1]_{B2}, [001]_{B19'} - [0-1-1]_{B2}.$$

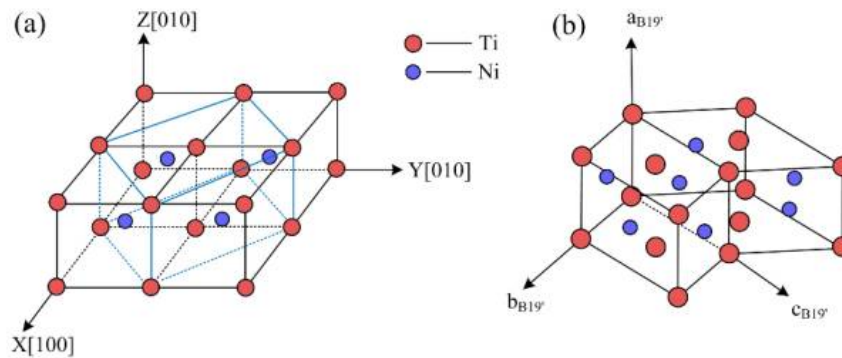


Fig. I-16 Crystal structures of NiTi: (a) B2 parent phase; (b) monoclinic B19' martensite [34].

NiTi alloys became attractive for medical applications particularly because of shape memory and superelastic properties. Ability of NiTi devices to recover an original shape after being deformed up to almost 10 % offers a considerable improvement and new possibilities for numerous medical and surgical interventions. In addition to memory properties, NiTi alloys exhibit significantly better mechanical compatibility with tissues compared to other alloys and ceramics used in medicine. NiTi alloys are now being used in many biomedical applications, including archwire [35, 36], self-expandable stents [37], abdominal wall lift devices [38], vascular ligation clips [39], staples for foot surgery [40] etc. However, concerns related to nickel release from NiTi biomaterials into body fluids and tissues exist, since Ni hypersensitivity represents a significant problem.

I.3 Superelastic effect in Ti alloys

I.3.1 Generalities about martensitic transformation

Martensitic transformation is a phase transformation accompanied with shear deformation (shape change) resulting from diffusionless cooperative movement of atoms. In a shape memory routine, the parent high-temperature phase called austenite transforms to the low temperature phase - martensite and vice versa. Martensite has an athermal nature - it nucleates and grows progressively upon cooling and is characterized by a balance of thermal and elastic energy during growth.

The formation of martensite can be isothermally induced from the parent austenitic phase by the application of external mechanical load. This type of martensite is known as stress-induced martensite (SIM). The formation of SIM yields a dominant shape change in the direction of applied load. If the plastic regime deformation has not been reached, the SIM progressively disappears when the applied load is removed and deformation is recovered. This

behavior is called superelastic effect or superelasticity.

Owing to mechanical instability of β phase, the superelasticity in metastable β -Ti alloys is associated with the reversible stress-induced martensitic transformation between the parent β phase (bcc structure) and the α'' martensite phase (orthorhombic structure) [41, 42]. Upon loading, the material transforms from metastable β phase to α'' phase. Once the load is removed, the material returns to its original shape as α'' phase completely transforms back to parent β phase.

In NiTi alloys, the reversible stress-induced martensitic transformation takes place between austenite B2 phase and martensite B19' phase [30, 33, 43].

The reversible stress-induced martensite transformation process can be describes through the following sequences:

- (1) The initial applied stress leads to the elastic deformation of austenite.
- (2) When loaded up to a certain critical stress (σ_{Ms}), austenite transforms to martensite, resulting in a plateau in the stress-strain curve as shown in Fig. I-17c.
- (3) At the end of plateau, when the critical stress σ_{Mf} has been reached, martensitic deforms elastically.
- (4) Upon unloading, the elastic deformation of martensite can be totally recovered.
- (5) When the load is released to σ_{As} , the martensitic variants transforms inversely to the parent austenite phase, leading to a full recovery of transformation strain in an ideal scenario (Fig. I-17f).

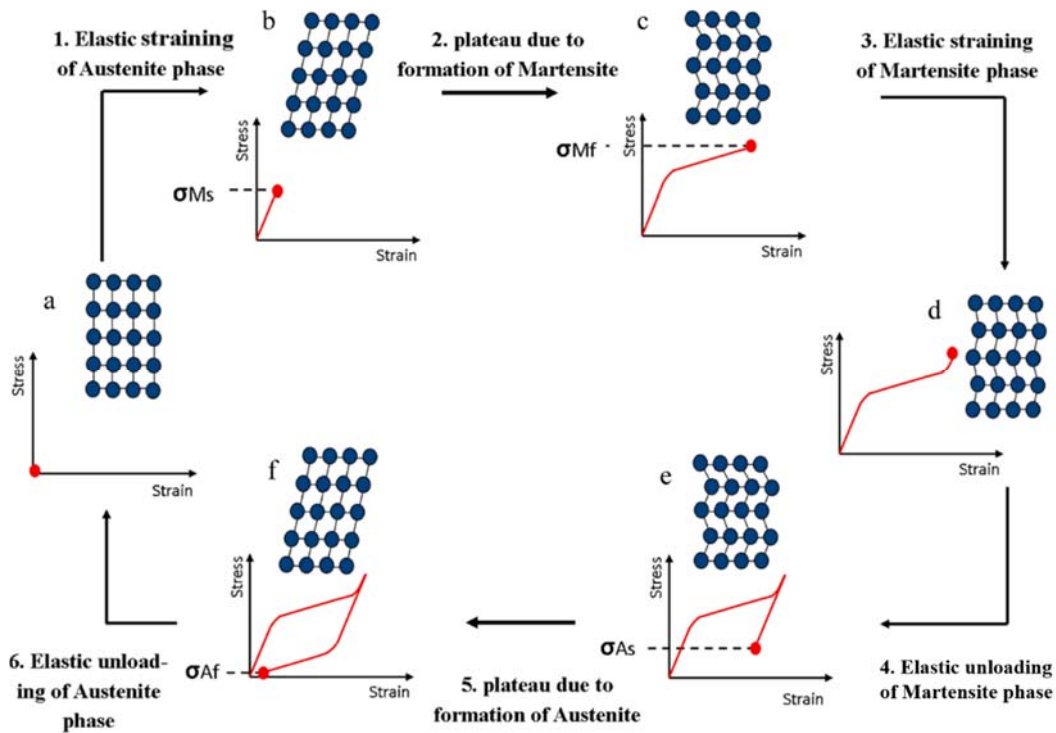


Fig. I-17 Schematic representation of superelasticity driven by reversible and stress-induced martensitic transformation [44].

I.3.2 Factors influencing superelastic response of Ti alloys

I.3.2.1 Chemical composition

It has been confirmed that superelasticity is sensitive to alloy composition. For binary Ti-Nb alloys, the superelastic behavior is observed in Ti-(25.5-27)at.% Nb [45]. However, the recovery strain is as small as about 3% even including elastic strain, which is quite smaller than those of practical NiTi superelastic alloys [46]. This is due to the small lattice distortion strain associated with the martensitic transformation from parent β phase to martensite α'' phase: the maximum transformation strain calculated for Ti-27Nb is only 2.5% [16]. Addition of a third or more alloying elements has been proven to be an efficient way for improving superelastic properties. The selection of alloying elements is crucial since alloy composition affects both martensitic transformation temperature (M_s), lattice parameters of β phase and α'' phase and thus transformation strain, formation of precipitates and stress inducing plastic deformation.

According to literatures, additions of alloying elements regardless of β -stabilizers or α -stabilizers decrease M_s of Ti-Nb based alloy: M_s decreases by 40 K with 1 at.% increase in Nb content for Ti-(20-28) at.% Nb alloys [45]; M_s decreases by about 30-35 K with 1 at.% increase of Ta and Zr content [47]; addition of Sn, from 4 to 5 at.% , decreases M_s by 150K

[48]; noble alloying element Pt decreases M_s by 160K with 1 at.% increase [49]; 1 at.% Mo addition reduces M_s by 120 K [50]. Interstitial alloying elements such as O and N significantly suppress the martensitic transformation of Ti-Nb alloys: 1 at.% O or N addition in Ti-Nb alloys decreases M_s by about 160 K [51] or 200 K [52] respectively. The addition of interstitial alloying elements (such as O, N) is very effective in increasing the yield strength. The martensite can be induced for stress range below the plasticity threshold.

The addition of alloying elements affects not only M_s transformation temperature but also the transformation strain. The greater the transformation strain, the more important the superelastic recovery strain. In the Ti-22Nb based alloy, the transformation strain decreases by about 0.34% or 0.13% with 1 at% increase of Nb or Zr content, respectively, while M_s decreases by about 40K or 35K with 1 at.% increase of Nb or Zr content, respectively [47]. This indicates that the addition of Zr as a substitute of Nb, with keeping M_s similar, is effective to increase the transformation strain.

Addition of Mo in Ti-Nb based alloys is very effective at increasing superelastic recovery strain due to the solid-solution strengthening effect of Mo and the increase in transformation strain [50]. However, excess addition of Mo in the Ti-Nb-Mo system adversely affects the superelasticity due to the formation of athermal ω precipitates. Sn is effective in increasing the superelastic recovery strain since it can both decrease M_s and reduce the athermal ω phase formation. Another interesting point with Sn addition is that the stress for inducing martensitic transformation (σ_{M_s}) decreases with increasing Sn content up to 1 at.%, then it increases on/with further addition [53].

Therefore, the superelasticity in Ti-based alloys is closely dependent on the nature and content of alloying elements. Fig. I-18 illustrates the composition dependence of the superelastic effect and transformation strain in Ti-Nb-Zr system. Superelasticity is observed only for a narrow and well-defined composition range in Ti, Nb and Zr, and the Zr content improves transformation strain. Similar composition dependence triangles have been reported in the literature for Ti-Nb-Ta system [54], Ti-Nb-Mo system [50], and Ti-Nb-Pt system [49].

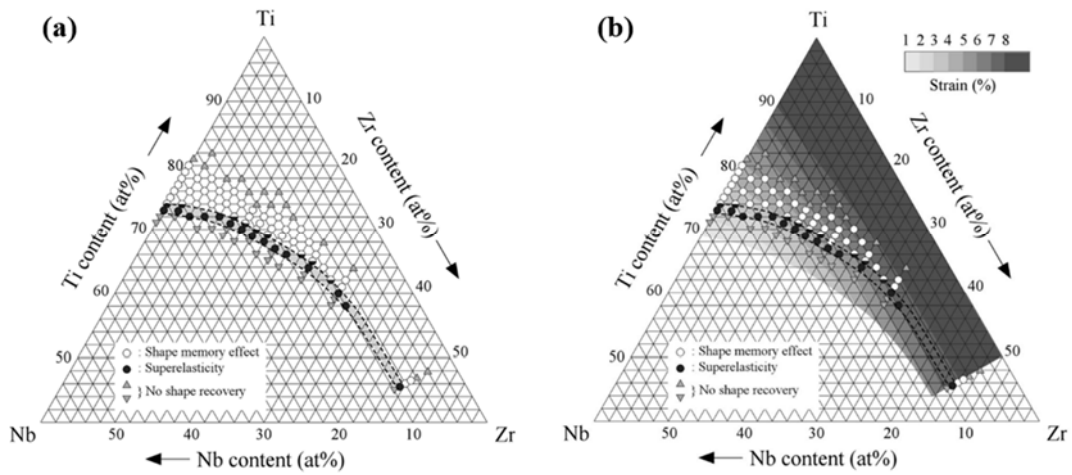


Fig. I-18 Composition dependences of shape memory and superelastic properties (a) and the transformation strain along the $[011]_{\beta}$ direction(b) for Ti-Nb-Zr system [54].

Fig. I-19 shows the influences of alloying elements on the superelastic behaviors of β -Ti alloys. Fig.I-19a presents cyclic stress-strain curves of Ti-27Nb, Ti-22Nb-7Ta, Ti-22Nb-6Zr, Ti-21Nb-2Mo and Ti-19Nb-2Pt alloys performed at room temperature. All of these alloys have similar M_s and exhibit superelastic response at room temperature. Maximum recovery strains of 3.5%, 3.2% and 3.0% are obtained respectively in the Ti-22Nb-6Zr, Ti-21Nb-2Mo and Ti-19Nb-2Pt alloys, which are larger than that of the 2.0 % observed in Ti-27Nb binary alloy. The addition of a ternary element Zr, Mo or Pt contributes to increase effectively the transformation strain while keeping transformation temperature in a similar level so as to maintain superelasticity at room temperature. Systematic investigations of superelasticity with special attention to the nature and content of alloying elements have been successfully achieved in various alloy systems such as, for example, in Ti-Mo-Zr-Sn and Ti-Zr-Nb-Sn systems in, showing excellent superelastic recovery (Fig. I-19 b-c).

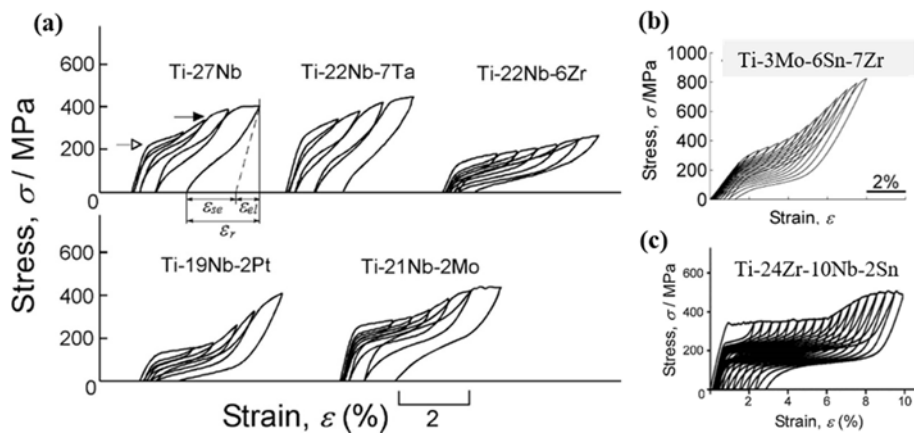


Fig. I-19 Effect of different alloying elements on the superelastic behavior of (a) Ti-Nb based alloy systems [55]; (b) Ti-Mo-based alloy system [29] and (c) Ti-Zr-based alloy system [56].

I.3.2.2 Thermo-mechanical treatment

Superelastic strain recovery performance is also extremely sensitive to the thermo-mechanical treatment of the alloy. The superelastic capability can be also evaluated from the ratio between the critical stress to initiate slip deformation (σ_{CSS}) and the critical stress to induce martensite formation (σ_{Ms}). σ_{CSS} can be defined as the stress inducing 0.5% plastic strain. In Ti-Nb alloys, it has been demonstrated that, the higher the critical stress for slip deformation compared to critical stress for inducing martensite transformation ($\sigma_{\text{CSS}}/\sigma_{\text{Ms}}$), the better superelastic recovery. Thus, it may be valuable to increase the critical stress for slip deformation. Previous investigations [57, 58] showed that fine-grained microstructures coupled or not with appropriate ω phase precipitation could induce large increase in the critical stress for the dislocation slip mechanism resulting in a significant improvement of the superelastic properties. A multistep thermo-mechanical approach, combining intermediate temperature annealing (873 K) with a followed-by aging treatment for ω precipitation (573 K), conducted in the Ti-27 at.% Nb alloy resulted in a better superelastic behavior than the solution treated specimen, as shown in Fig. I-20.

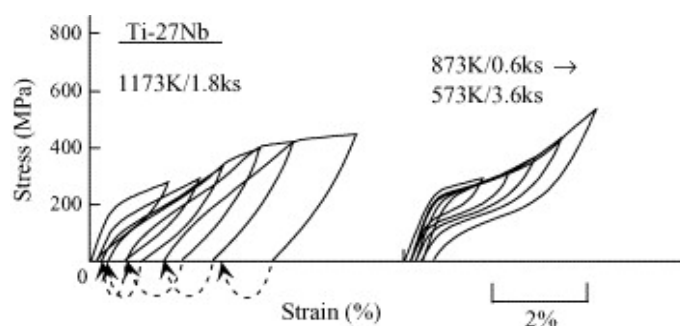


Fig. I-20 Influence of thermal treatments on the stress-strain curves obtained by cyclic loading–unloading tensile tests for the Ti-27 at.% Nb alloy [47].

Fan et al [59] proposed a strategy based on a short aging treatment following by quenching (= solution treating) carried out on heavily cold-rolled metastable β Ti-20Nb-6Zr (at.%) alloys. Fig. I-21 presents the tensile stress-strain curves for three different metallurgical states: a cold-rolled specimen, a cold-rolled and solution-treated specimen and a cold-rolled and rapidly solution-treated specimen. Superelastic performances of the rapidly solution-treated alloy are significantly improved compared with the as-rolled and the conventional solution-treated ones. A superelastic recovery strain of 3.2 % with a maximum applied stress of 750 MPa is obtained upon progressive cyclic loading-unloading for the rapidly solution-treated alloy. No significant superelasticity is visible on the stress-strain curve of the as-rolled specimen, due to the important plastic strain stored in the material. In the conventional

solution-treated alloy, the low critical stress for dislocation slip is assumed to be responsible for the limited superelastic recovery, since martensite is partially prevented by the early accumulation of dislocations.

The rapidly treated specimen shows optimized combination of superelasticity and high strength when compared to the as-rolled alloy and to as-quenched alloy. This is attributed to the resulting microstructure induced by the short solution treatment. The combined effect of grain refinement (1 μm in size) and the fine and dense isothermal ω nanoprecipitation contributed greatly to delay the formation and movement of dislocations, resulting in a significant increase in the critical stress for dislocation slip. Moreover, the short thermal treatment enabled very small volume fraction of α to be kept and guaranteed a small amplitude of solute partitioning between α and β phases. Those combined effects result in keeping the M_s temperature at a level that promotes the promising combination of superelastic behavior and high strength at room temperature.

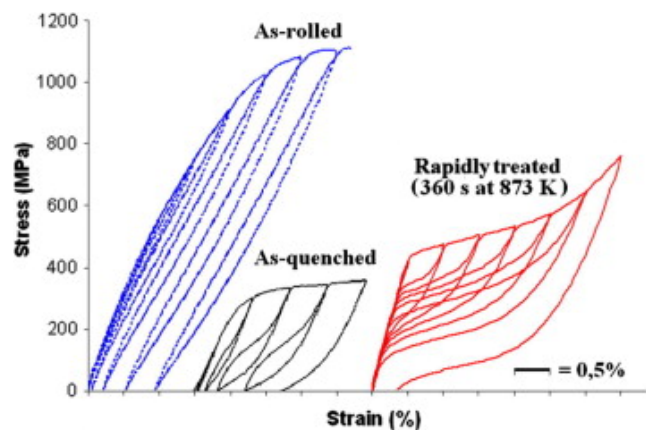


Fig. I-21 Incremental loading-unloading tensile tests from 0% to 3.5% strain on Ti-20Nb-6Zr specimens after heavy cold-rolling, after conventional solution treatment and after fast solution-treatment respectively [59].

I.3.2.3 Texture

Since the martensitic transformation strain is strongly anisotropic, texture control is another way to improve superelastic recovery. In β titanium alloys, there are 6 equivalent lattice correspondence variants (Tab. I.3) which can be formed when the bcc crystal of β phase transforms into the orthorhombic crystal of α'' martensite with respect of the $\{110\}_\beta // (001)_{\alpha''}$ and $\langle 111 \rangle_\beta // [110]_{\alpha''}$ orientation relationships. Martensitic transformation strains induced by the lattice distortions between β and α'' phases can be calculated from the lattice parameters and the lattice correspondences of both phases. When martensite is stress-induced, the variant selection operates to form the variant that would best accommodate the imposed deformation.

It is commonly assumed that the preferentially activated variant in each grain is the one that would give the maximum transformation strain, so the one that would produce maximum driving force for the martensitic transformation. In a previous work, maximum lattice distortion strains that can be accommodated under tension, regardless of the variants, have been calculated along different crystallographic loading directions of the β crystal for Ti-20Zr-3Mo-3Sn alloy and reported in a standard stereographic triangle (Fig. I-22). Maximum transformation strain under tension decreases significantly with changing the crystallographic loading direction from $[101]_{\beta}$ toward $[001]_{\beta}$ and $[111]_{\beta}$, for which transformation strain values are 7.3%, 3.8% and 2.5%, respectively. It indicates that greater superelastic recovery can be reached when all grains present the $[101]_{\beta}$ direction oriented along the tensile loading direction.

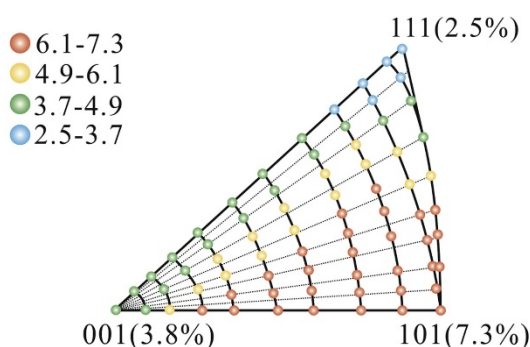


Fig. I-22 Inverse pole figure distribution of maximum lattice distortion strains accommodated from martensitic transformation in single β grains under tension for Ti-20Zr-3Mo-3Sn [60].

Three Ti-20Zr-3Mo-3Sn specimen subjected to three different temperatures (700 °C, 800 °C and 900 °C) during solution treatments in single β -phase domain develop different texture and exhibit different superelastic responses [60]. As it can be seen from the cyclic stress-strain curves in Fig. I-23, maximum recovery strains measured from the cycle marked in bold are 3.5%, 2.7% and 2.5% for specimens treated at 700 °C, 800 °C and 900 °C, respectively. The different textures are responsible for these different superelastic responses. Specimen solution-treated at 700 °C, exhibits a dominant $\langle 011 \rangle_{\beta} \{ 100 \}_{\beta}$ texture (Fig. I-23d). Specimen solution-treated at 800 °C, shows a strong $\langle 100 \rangle_{\beta} \{ 011 \}_{\beta}$ texture (Fig. I-23e) and for the specimen solution treated at 900 °C, a dominant $\langle 113 \rangle_{\beta} \{ 110 \}_{\beta}$ texture is obtained (Fig. I-23f).

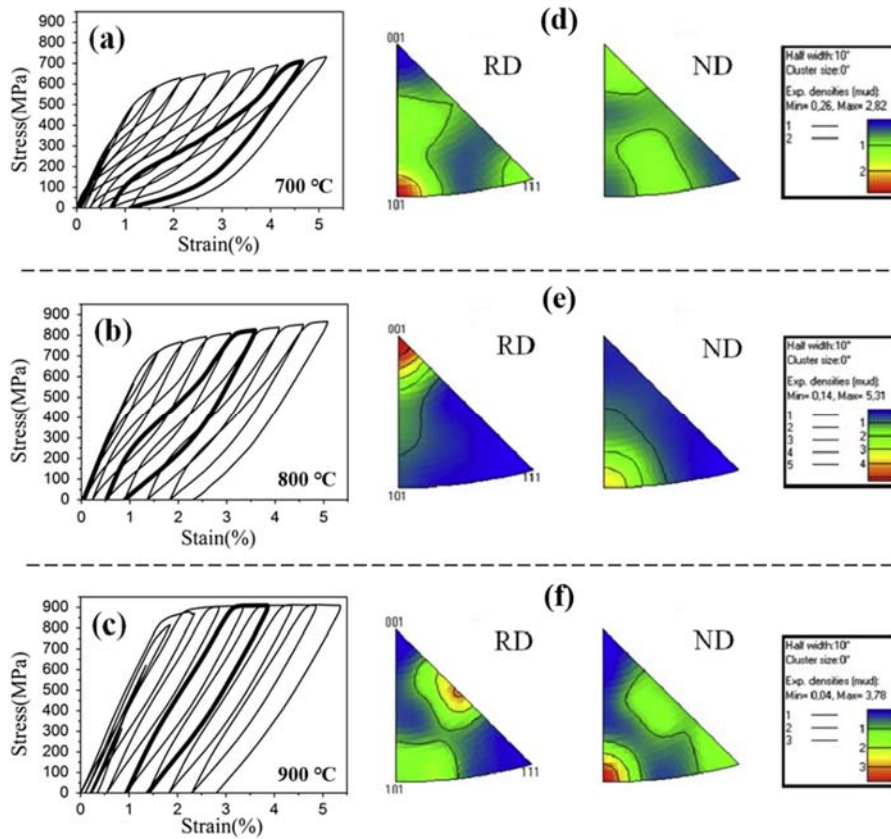


Fig. I-23 Stress-strain curves obtained from cyclic tensile tests at room temperature (a-c) and inverse pole figures (d-f) for Ti-20Zr-3Mo-3Sn alloys solution treated during 30 min at: 700 °C (a, d), 800 °C (b, e) and (c, f) 900 °C, respectively. RD for rolling direction and ND for normal direction [60].

Thus, the high recovery strain of 3.5% obtained in Ti-20Zr-3Mo-3Sn alloy after a solution treatment at 700 °C for 30 min is related to the dominant $\langle 011 \rangle_{\beta} \{100\}_{\beta}$ recrystallization texture and to the fact that the tensile loading direction is applied along the favorable $\langle 011 \rangle_{\beta}$ direction allowing to reach the highest maximum transformation strain calculated from the crystallographic model of martensitic transformation.

I.3.2.4 Grain size

Grain size is another factor that affects the superelasticity. In a previous work, Ti-20Zr-12Nb-2Sn alloy specimens were subjected to three different recrystallization temperatures and times to tailor the grain size. Tensile stress-strain curves obtained at room temperature in Fig. I-24 reveal a superelastic behavior for the three specimens of Ti-20Zr-12Nb-2Sn alloy: a stress plateau is clearly visible, which is associated with the presence of hysteresis between loading and unloading curves due to the occurrence of reversible SIM transformation between β and α'' phases. The critical stress for slip, σ_{css} , is defined as the stress beyond which permanent deformation occurs. σ_{css} and the corresponding fully reversible strain are indicated by dash lines for all specimens. The short-treated specimen (FT-560-02) with a very refined grain size

($0.4 \pm 0.3 \mu\text{m}$) and the highest $\sigma_{\text{css}} = 800 \text{ MPa}$ exhibits a remarkable recovery strain of 4.5%, as compare to the other two conditions.

It is seen from the EBSD analyzes in Fig. I-24 that the three specimens exhibit the same strong $\{111\}_{\beta} \langle 101 \rangle_{\beta}$ recrystallization texture but different average grain sizes, which allows to discuss the influence of the grain size on the superelastic properties. According to the Hall-Petch law, the grain size refinement increases drastically the critical stress for slip (σ_{css}). High σ_{css} delays the formation of dislocations and, in turn, preclude the trapping of martensitic phase by dislocations favoring reversion of the martensite into parent β phase, resulting in high recovery strain. In this study, grain size refinement improves the superelastic response of Ti-20Zr-12Nb-2Sn alloy. For similar textures, the smaller grains favor the greater recoverable strain.

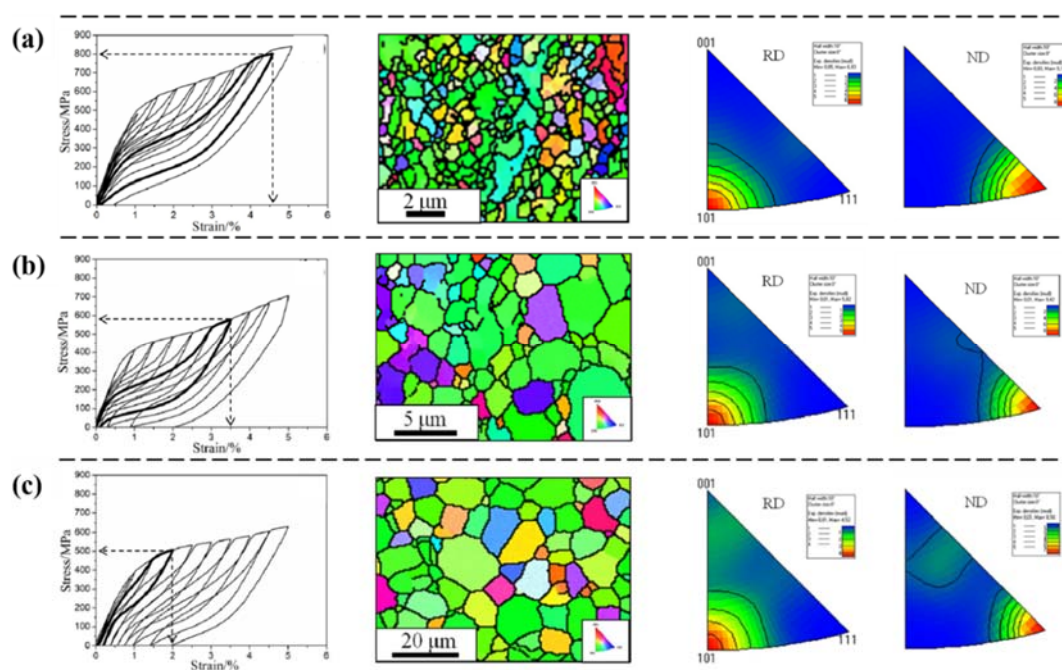


Fig. I-23 Stress-strain curves, EBSD maps along RD (Rolling Direction) and inverse pole figures of the solution-treated Ti-20Zr-12Nb-2Sn specimens: (a) flash-treated at 560 °C for 2 min (FT-560-02); (b) solution-treated at 560 °C for 30 min (ST-560-30); (c) solution-treated at 700 °C for 30 min (ST-700-30) [61].

The grain size dependence of the superelasticity in nanostructured polycrystalline NiTi alloys has been observed by Sun et al. [62]. Fig. I-24 shows the tensile stress-strain curves and the surface morphology for specimens with grain size of 10, 32, 64, 80, 1500 nm. It is seen that SIM transformation occurs for all specimens as evidenced by the hysteresis loop and the reversible deformation cycle (no residual strain) with almost full recovery strains in the range of 5% - 7%. In this study, in-situ XRD during loading-unloading confirm that martensite can still be induced by stress in grains as small as 10 nm. When the grain size decreases below 60

nm, the typical plateau-type tensile stress strain curve of coarse-grained NiTi sample (with macroscopic domain nucleation and propagation) gradually becomes hardening and eventually tends to be elastic and reversible with homogeneous deformation. With the decrease of grain size, the critical stress for phase transition σ_{SIM} increases significantly and superelastic hysteresis loop area decreases monotonically.

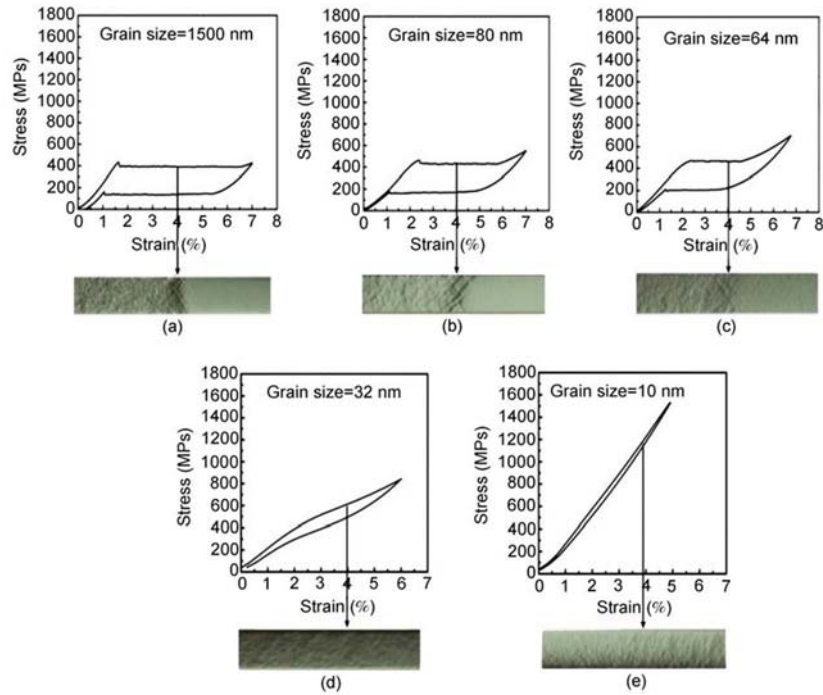


Fig. I-24 Grain size effects on the tensile stress-strain responses and the macroscopic deformation mode of dog-bone NiTi polycrystalline specimen with different average grain size (a) 1500 nm (b) 80 nm (c) 64 nm (d) 32 nm (e) 10 nm.

Therefore, it is concluded that the superelasticity of Ti-based alloys can be influenced by alloying elements, thermo-mechanical treatment, texture and grain size. It is worth noting that these parameters are interdependent and cannot be controlled independently. For instance, thermo-mechanical treatments influence grain size, texture, and the phase stability. The predominant factors that determine the superelasticity should be analyzed in details according to the specific cases.

I.4 Magnetron sputtered superelastic Ti-based alloy films

I.4.1 Magnetron sputtering technique

Magnetron sputtering is one of the more widely used techniques of physical vapor deposition (PVD). This technique is based on the sputtering of a solid target by energetic ionic

species from a magnetically enhanced glow discharge. The magnetic field produced by magnets changes the trajectory of the electrons near the target, producing more collisions and therefore higher ionization of the plasma. This allows a reduction in the working pressure, which is usually beneficial for the growth of dense films, but also increases deposition rates.

The deposition rate of the films depends on different variables, including the power applied to the cathode (direct current (DC), radio frequency (RF), pulsed DC), the gas source, the working pressure and the target composition. The dependence of the deposition rate on the target composition is represented in the sputtering yield, which is an index of the efficiency of the sputtering process (number of atoms ejected from the target by each incident ion) [63]. Besides, magnetron sputtering involves a series of deposition parameters and variables that can be controlled for tailoring the microstructural and physical properties of the growing coatings [64-66].

However, deposition of an alloy film with a given composition is often problematic due to different sputtering yields of depositing elements which causes compositional deviation between alloy target and deposited film. For example, sputtering equiatomic NiTi alloy target to obtain NiTi alloy films invariably leads to Ni-rich films because the sputtering yield for Ni is higher than that for Ti [67]. This problem is exacerbated in ternary and quaternary alloy films deposited from a single alloy target. The simplest and most common solution to this composition problem is to place small pieces of pure Ti onto the wear track of the NiTi target to compensate for the increased Ni sputtered flux. Alternatively, this can be achieved by using an alloy target enriched in deficient component [68], or by the co-sputtering of multiply pure metal targets [69], or by co-sputtering of the alloy target with the required element as an additional target. The latter issue was employed in the present thesis work for the growth of Ti-20Mo-3Zr-3Sn alloy films for which a Ti-20Mo-3Zr-3Sn alloy target was coupled with a compensatory pure Mo target.

The phase transformations and physical properties related to sputtered alloy films might be different from their bulk counterparts. In general, thin films demonstrate fast cooling rates due to their higher surface/volume ratio and their substantial increase in heat transfer rate in comparison to bulk materials [67, 70]. Phase transformations in thin films are generally accompanied by significant changes in physical, thermal, optical, electrical and mechanical properties. Properties of sputtered films are dependent on the microstructure developed during thin film growth which often takes place especially in nanocrystalline regime whereas bulks exhibit a wide range of grain size, generally in the micrometric scale.

In the field of superelastic films, magnetron sputtering has been employed to deposit superelastic NiTi films with good adhesion, reproducibility and flexibility [71-73], since the 1990s, basically for the development of microactuators [74-76]. Magnetron sputtering has also been used for the deposition of multi-component β -Ti alloy films, such as Ti-Nb [68, 77-79], Ti-Nb-Zr [80-83], Ti-Nb-Hf [84], Ti-Nb-Zr-Ta [85]. Contrary to NiTi alloy films, superelastic properties of these β -Ti alloy films have not been subject to systematic studies.

I.4.2 NiTi-based alloy films

Since 1990, most investigations have focused on the superelastic response of magnetron sputtered NiTi-based alloy films, basically for the development of miniature systems (micro-sensors, -actuators, -pumps and -valves) [71, 74, 86-88]. The use of superelastic films has the advantage not only for small size applications but also for improving the response speed. Fig. I-25 shows various functional microdevices made with NiTi-based thin films. Further applications are focused on the use of NiTi-based interlayers as self-healing superelastic films to improve interface adhesion and tribological properties of hard and super-hard coatings (Cr-N, Ti-C-N, ...) on soft substrate [89-91]. Soft substrates have poor support characteristics which severely degrade hard coating performance. It is shown that the superelastic NiTi interlayer introduced between the CrN hard coating and Al soft metallic substrate effectively decreases the friction coefficient and the wear loss (by a factor 100 for the latter) of the composite coating. In other studies, the superelastic TiNiCu interlayer introduced between a functional lubricant W-S-C top layer and substrate improve significantly the resistance to adhesion damage of the coating [92, 93]. The interlayer relaxes stress in a reversible manner, due to stress induced martensitic transformation, which causes a mitigation of the stress on the top layer. The magnetron sputtered thin films of superelastic NiTi interlayer improve hard-coating performance on soft substrates by limiting asperity contact stresses and mitigating the effects of compliance and thermal expansion coefficient mismatches between base metal and coating.

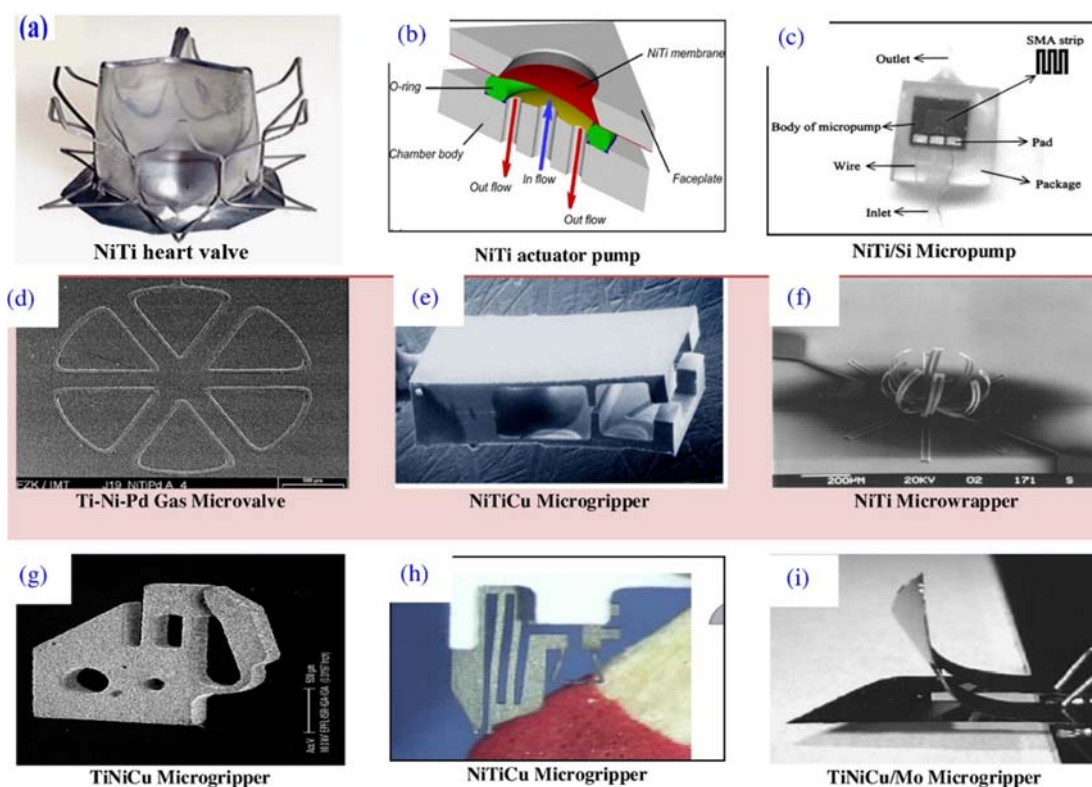


Fig. I-25 (a-i) Various microdevices made of NiTi-based thin films for MEMS applications [94].

The as-deposited NiTi films are known to be amorphous when the substrate (glass or quartz) temperature is lower than 473 K during sputtering deposition, while films deposited at elevated temperature are crystalline [30]. In general, there are two types of methods to obtain the superelasticity in sputter-deposited TiNi-based thin films: (1) sputter-deposition of crystalline thin films on a substrate at high temperature, or (2) sputter-deposition of amorphous thin films on a substrate at room temperature followed by crystallization process through post-thermal treatment.

Kumar et al. [95] deposited NiTi thin films on Si (100) substrate at various substrate temperatures (room temperature to 923 K) using magnetron sputtering and investigated the effect of substrate temperature on the microstructure, mechanical properties and phase transformation behavior of NiTi thin films. Fig. I-26a shows the XRD pattern of NiTi thin films for different deposition temperatures. Film deposited at 623 K was amorphous while films deposited at 723 K and 823 K were crystalline with the growth direction highly oriented along (110) plane of the B2 austenite phase. With further increase in deposition temperature to 923 K, a dominance of B19' martensite phase peaks was observed in as-deposited NiTi films. HRTEM images (Fig. I-26b) of NiTi films deposited at 823 K and 923 K clearly confirm the formation of austenite phase and mixed (austenite + martensite) phase, respectively. The mechanical properties were studied by nanoindentation, and revealed that the fully austenitic

film exhibited relatively high hardness, high reduced elastic modulus and better wear behavior in comparison to that with mixed (martensite + austenite) structure in Fig. I-26c.

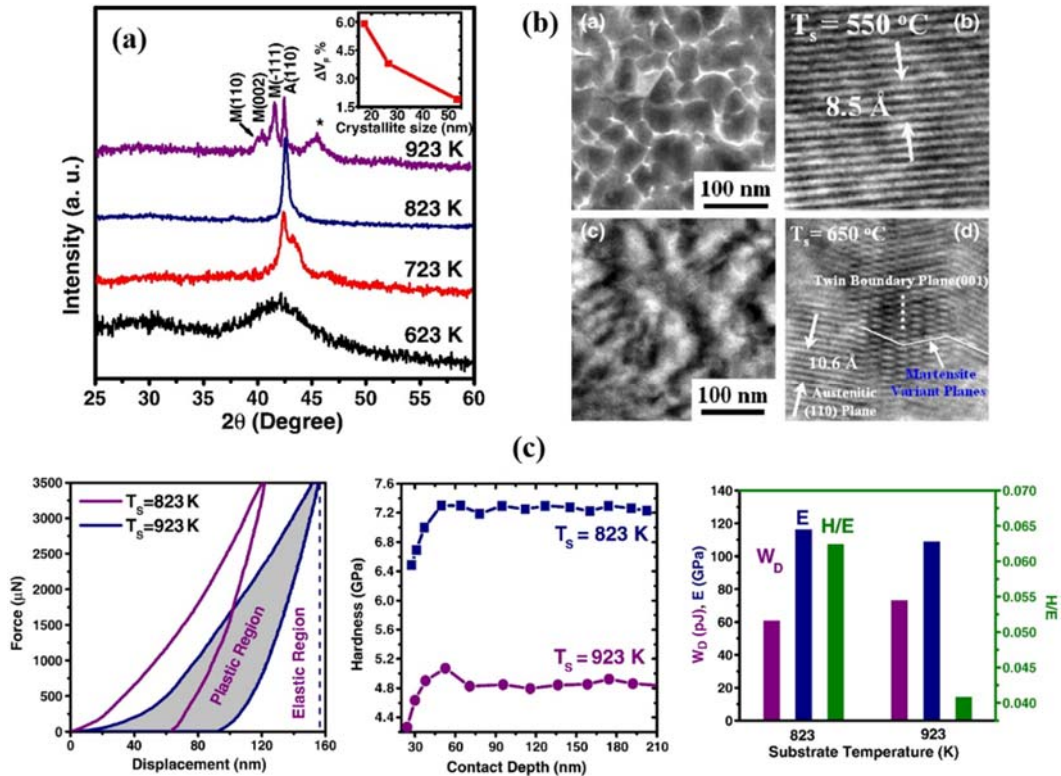


Fig. I-26 (a) XRD patterns of NiTi films deposited at different substrate temperatures (b) HRTEM images showing the single austenite phase and the austenite + martensite phases in NiTi films deposited at 823 K and 923 K, respectively. (c) Nanoindentation load–displacement curves, hardness, Dissipation energy (W_D), reduced modulus (E_r) and hardness to reduced modulus ratio (H/E) of NiTi films deposited at 823 K and 923 K [95].

Li et al. [96] studied the phase transformation behavior of post-annealed $\text{Ni}_{41.7}\text{Ti}_{38.8}\text{Nb}_{19.5}$ (at%) films using a four probe electrical resistivity method, by cooling the austenitic specimen from room temperature down to -270°C using liquid helium. It was found that the thermal hysteresis is highly dependent on the grain size, which can be controlled through the post-annealing process (Fig. I-27a). The extent of crystallization and grain size progressively increase with annealing temperature (Fig. I-27b). It was observed that the ultrafine nanograined austenite crystalline microstructure favors the martensitic transformation due to the high volume fraction of grain boundary defects. A narrow thermal hysteresis was obtained in films with grain size of less than 50 nm (Fig. I-27c). The thermal hysteresis in the martensitic transformation originates from the friction energy in the interfacial movement during the shear process. It was found that the reduction in grain size reduces the energy dissipation in transformation friction by shortening the interfacial movement distance and weakens the lattice distortions between the parent phase and the martensite phase, which reduces the energy barriers and facilitates the process of phase transformation.

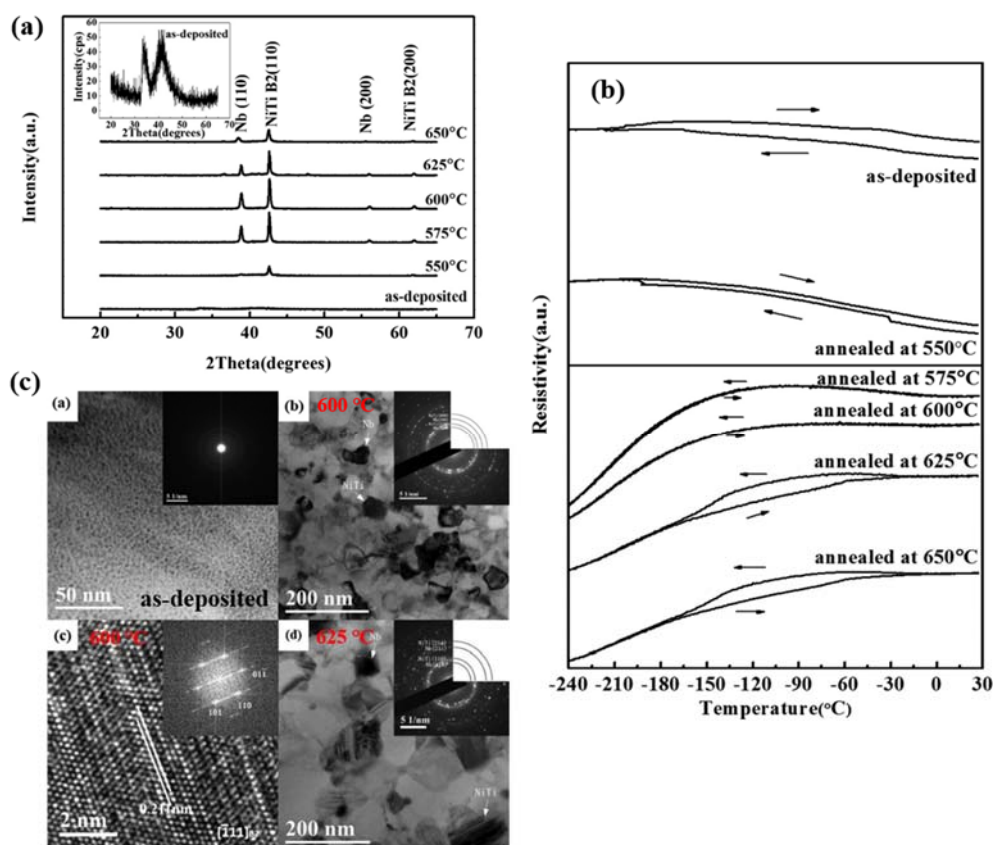


Fig. I-27 XRD patterns (a) and Electrical resistance-temperature (ER-T) curves (b) of the as-deposited NiTi-Nb film and post-annealed films at 550 °C, 575 °C, 600 °C, 625 °C and 650 °C, respectively. (c) TEM images and corresponding diffraction patterns of the as-deposited film and post-annealed films at 600 °C and 625 °C [96].

Pan et al. [97] studied the mechanical response of superelastic NiTi thin films subjected to nanoindentation tests using two types of indenters: spherical and Berkovich. Due to the shape difference of two indenters, obvious differences in nanoindentation load-displacement ($F-h$) curves and deformation behaviors were observed (Fig. I-28). It is shown that Berkovich indenter produced much deeper penetration depth than spherical one under the same load. Spherical indentations always exhibit much higher depth recovery ratio η_h than Berkovich ones for both cases of similar loading force or similar maximum penetration depth. Under the peak load of 500 μN , the depth recovery ratios are 100% and 68% determined by spherical and Berkovich indentations, respectively. For similar maximum penetration depth (around 37 nm), the depth recovery ratios are 100% and 57% determined by spherical and Berkovich indentations, respectively.

The nanoindentation $F-h$ curves were converted into nominal stress-strain curves from which the deformation behavior of NiTi thin films under different indenter tips was discussed. For spherical indentations, the whole deformation was divided into three stages: elastic deformation of austenite, austenite to martensite transformation and elastic deformation of

martensite. Hence, as shown in Fig. I-28c, a phase transition strain of 2.6 % was obtained corresponding to the strain range for which the phase transformation occurs, namely from the forward phase transition start stress σ_f^s (first change in slope) to the phase transition end stress σ_f^e (second change in slope). For Berkovich indentations, phase transition cannot be clearly distinguished (Fig. I-28d), due to the fully plastic flow which developed early in the loading stage.

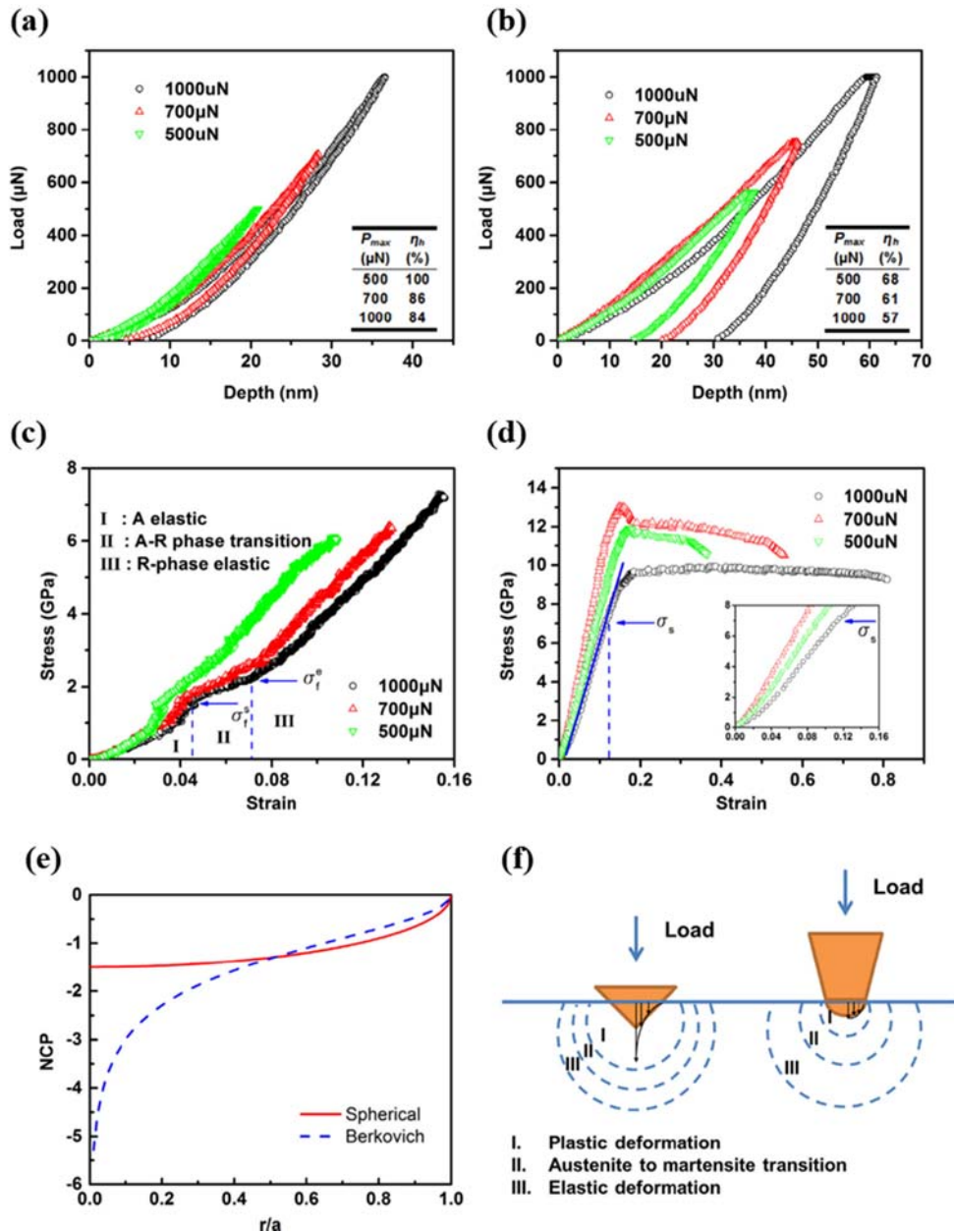


Fig. I-28 Nanoindentation load-displacement curves of 1 μm -thick NiTi film using: (a) spherical tip; (b) Berkovich tip. Corresponding stress-strain curves obtained from nanoindentation experimental data: (c) for the spherical indentation; (d) for the Berkovich indentation. (e) Normalized contact pressure (NCP) distribution $\sigma z/p_m$ for spherical and Berkovich indenters, r and a denote the radial coordinate and the contact radius, respectively, and (f) Schematic representation of the deformation volume area underneath the indenter.

The considerable difference in NiTi film responses for the two indenters under the same load is due to the varied stress distribution beneath two indenters during indentation process, as schematically shown in Fig. I-28e. For spherical indenter, no stress concentration is observed, while for Berkovich indenter, the stress considerably increases as r approaches to zero (i.e., the region right underneath the indenter tip). That means, severe stress concentration occurs beneath sharper Berkovich indenter, resulting in larger plastic zone than that under spherical indenter. The stress-gradient induced deformation under the indenter that can be divided into three deformation zones: plastic deformation zone, austenite to martensite transition (superelastic) zone and elastic deformation zone, as shown in Fig. I-28f. Upon unloading, the elastic deformation zone and the deformation zone accommodated by martensitic transformation (superelastic effect) are expected to be fully recovered. Only the plastic deformation is left behind in the residual indent. It is noticed that the plastic zone proportion induced by Berkovich nanoindentation is much larger than that produced by spherical one, causing much more permanent deformation after unloading.

Nanoindentation testing can be employed to reveal the different elastic and plastic deformation behaviors of austenite and martensite, which is promising for characterization of superelasticity, phase transition and mechanical properties of constrained thin film.

I.4.3 Ni-free β -Ti alloy films

Magnetron sputtering offers the possibility to synthesize alloy films outside thermodynamic equilibrium enabling the formation of metastable phases in film geometries. Musil et al. [98] found that the metastable β -Ti phase can be obtained in Ti-14 wt.% Cr and Ti-10 wt.% Fe films when sputtered onto unheated substrates or at a substrate temperature (T_s) considerably lower than the β transus temperature T_β ($T_{\beta, Ti-Cr} \geq 667$ °C, $T_{\beta, Ti-Fe} \geq 595$ °C), which should be necessary overcome for the formation of the high-temperature β stable phase in an equilibrium process. This result shows a promising route to form metastable β -Ti alloy films at low T_s ($T_s < T_\beta$), even at room temperature.

Different groups reported that in magnetron sputtered Ti-Nb films, the phase growth is closely dependent on Nb content, as illustrated in Fig. I-29. The structure is fully α -phase when the Nb content is not high enough to stabilize the β -phase. The increasing Nb content into the films tends to suppress the $(100)_\alpha$ and $(101)_\alpha$ diffraction peaks and slowly transform the $(002)_\alpha$ into $(111)_{\alpha'}$ and eventually $(110)_\beta$. Noteworthy, for 15 at.% Nb content, the α phase (hexagonal structure) is changing into α' martensite (orthorhombic structure). Generally, the

kinetic energy provided by magnetron sputtering can generate enough momentum to stabilize the β -phase at even lower Nb contents and temperatures when compared with equivalent results on bulk specimens. For binary Ti-Nb bulk alloys, metastable β phase can be stabilized at room temperature after quenching process from the high temperature phase field for Nb content between 25.5-27at.% Nb whereas α'' martensite phase can be obtained for Nb content ranging from 20 to 25 at% Nb [55].

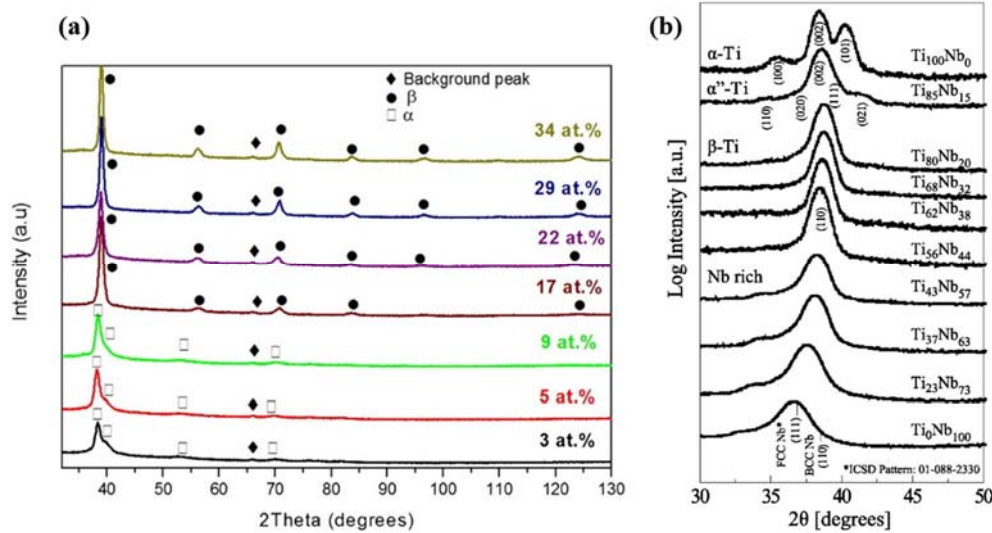


Fig. I-29 XRD patterns for magnetron-sputtered Ti-Nb films showing the phase evolution as a function of Nb content, referring to (a) Achache et al. [78] and (b) Photiou et al. [99].

The influence of Nb content on texture has also been studied in Ti-Nb films. The texture changes from $\{110\}_\beta$ to $\{111\}_\beta$ as the Nb content increases from 17 at.% to 34 at.%, as presented in Fig. I-30. This can be explained by the competition between (i) surface and strain energies and (ii) anisotropy collision effect. The detailed explanations are below as following:

(i) Surface and strain energy effect. The intrinsic stress in magnetron sputtering coatings was introduced due to the extremely non-equilibrium deposition process associated to the rapid condensation of the oversaturated metallic vapor onto the substrate at a very fast cooling rate [100]. Subsequently, the intrinsic stresses induce a significant amount of strain energy into the films. For Ti-17Nb film, the strain energy is low, and the film growth is determined by the surface energy, so the preferential orientation corresponds to the planes with the lowest surface energy, i.e. the $\{110\}_\beta$ densest planes parallel to the substrate surface. In the case of Ti-34Nb film, the film growth is predominantly controlled by strain energy, so its preferential orientation corresponds to the plane $\{111\}_\beta$ with the lowest elastic strain energy parallel to the substrate surface.

(ii) Anisotropy collision effect. Dense planes are more susceptible to atomic

bombardments during deposition process and have lower probability to survive [101]. The increase of atomic bombardment on the Ti-34Nb film causes $\{110\}_\beta$ planes to disappear in favor of the growth of $\{111\}_\beta$ planes parallel to the substrate surface.

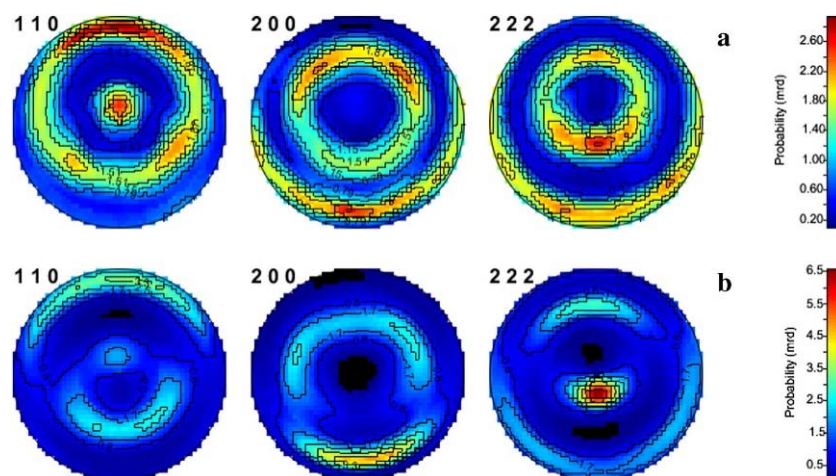


Fig. I-30 Texture of β -phase in Ti-Nb films containing (a) 17 at.% Nb and (b) 34 at.% Nb [78].

Similar observations of texture modification with increasing Nb concentration in magnetron sputtered Ti-Nb films have been reported by Gonzalez et al.[81, 102]. The film texture and crystallographic orientation of individual grain have been characterized at the nanometric scale by TEM coupled with the technique of automatic crystal orientation mapping (ACOM-TEM). This technique provides information of ultra-fine crystalline features with a spatial resolution of approximately 2 nm [103].

Fig. I-31 displays the crystallographic orientation mappings for $\text{Ti}_{85}\text{Nb}_{15}$, $\text{Ti}_{80}\text{Nb}_{20}$, $\text{Ti}_{70}\text{Nb}_{30}$, and $\text{Ti}_{60}\text{Nb}_{40}$ films (at.%) showing the local textures of the β phase (bcc structure) indexed along the film growth direction. The morphology of the films changes with the increase in the Nb content: starting with a zone I structure of the structure zone diagram with high rate of grain nucleation in the direction of the plasma flux and going towards a characteristic T zone structure with the formation of larger grain sizes and columnar growth structures. The nucleation and growth process depend on the surface and strain energies and are affected by the temperature. The texture of the films also changes with the increase in the Nb content going from $\{110\}_\beta$ to a competitive growth dominated mainly by $\{113\}_\beta$ and $\{111\}_\beta$. Since Nb has a higher atomic mass compared to Ti, the presence of Nb species favors the diffusion process at the surface, modifying the texture and growth modes for the growth direction (plasma flux) in a more noticeable way [103, 104]. For a lower Nb content, the process is dominated by Ti species, the mobility is not high enough, and a zone I growth mode is generated. For higher Nb content, the system receives more energy from the heavier Nb species, favoring adatom mobility on the growing surface producing larger grains having

different orientations. The texture is then dominated by the Nb species yielding a high strain energy (high intensity of the bombardment caused by the Nb species) that generates a T zone. This texture change may be responsible for the behavior of elastic modulus: it increases with the Nb content from 15 up to 30 at.% Nb, and presents a slight decrease for 40 at.% Nb [104].

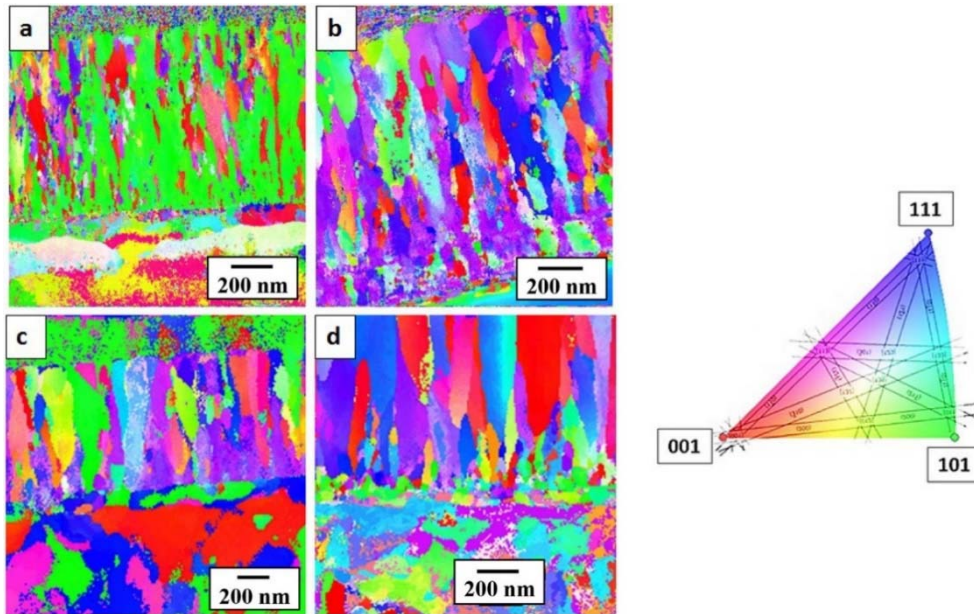


Fig. I-31 Fig. I-37 Crystallographic orientation mappings for: (a) $\text{Ti}_{85}\text{Nb}_{15}$, (b) $\text{Ti}_{80}\text{Nb}_{20}$, (c) $\text{Ti}_{70}\text{Nb}_{30}$, and (d) $\text{Ti}_{60}\text{Nb}_{40}$ coatings deposited on stainless steel, showing the textures along the film growth direction. [102].

Achache et al. [78] studied the superelastic response of binary Ti-Nb films by nanoindentation. Fig. I-32 shows the spherical nanoindentation load-displacement ($F-h$) curves for different maximum loads and the calculated depth-recovery ratio (the ratio of recovery depth to the total depth) as a function of maximum applied loads to assess the superelastic effect. The depth-recovery ratio decreases with the increasing load due evolution of the strain field below the indenter tip with increasing indentation depth. Low indentation loads are associated with relatively small strains that can be largely accommodated by the elastic deformation and the stress-induced martensitic transformation. The reverse transformation upon unloading results in superelastic recovery and the depth-recovery ratio is high. At high indentation loads, the superelastic response decreases, due to the increase of strain level and also to an increased volume fraction of dislocations underneath the indented surface which promotes the stabilization of martensite in the deeper zone.

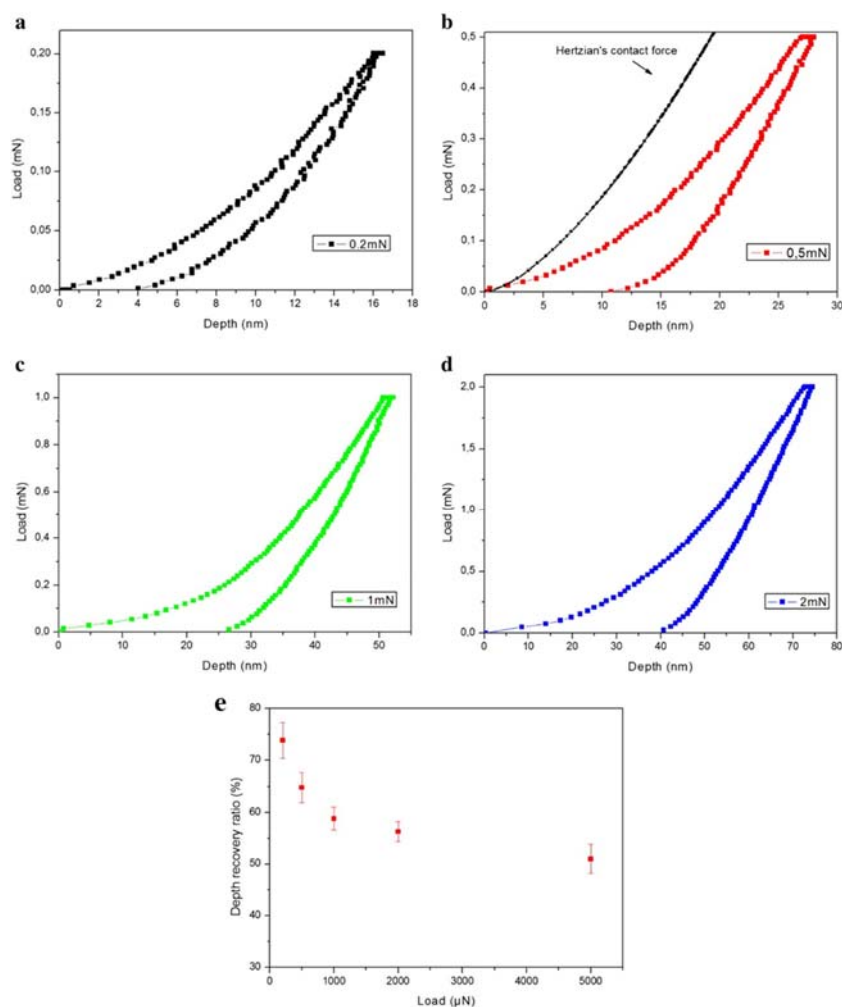


Fig. I-32 Nanoindentation load-displacement (F-h) curves of Ti-34 at.% Nb films measured at different maximum applied loads: 200 μN (a), 500 μN (b), 1000 μN (c), 2000 μN (d); and (e) depth-recovery ratio as a function of maximum applied loads [78].

Meng et al. studied the superelastic response of magnetron sputtered Ti-18 at.% Nb films after different heat treatment conditions [68]. The as-deposited films were peeled off their Si substrates and then annealed in a vacuum furnace at different temperatures between 550°C and 900°C for 3 min. The tensile loading-unloading stress-strain curves of Ti-18 at.% Nb films exposed to different heat treatment conditions are shown in Fig. I-33. The specimens were firstly deformed to 2%, and then the stress was removed. The measurement is repeated via increasing the maximum strain by 0.5% for a same specimen. The magnitude of recovered strain is shown in Fig I-33d. It is observed that 2.5% total strain recovery can be obtained in the 650 °C annealed film. The superelasticity of the annealed Ti-18 at.% Nb thin films is equal to that of the Ti-26at%Nb bulk materials after thermal–mechanical treatment. The as-deposited and most of the annealed Ti-18Nb films consist of β and α'' dual phases at room temperature. TEM observations reveal that fine spherical ω phase particles about dozens of nanometers in size embed in the β phase matrix. The martensitic transformation is supposed to be limited by the presence of the ω phase.

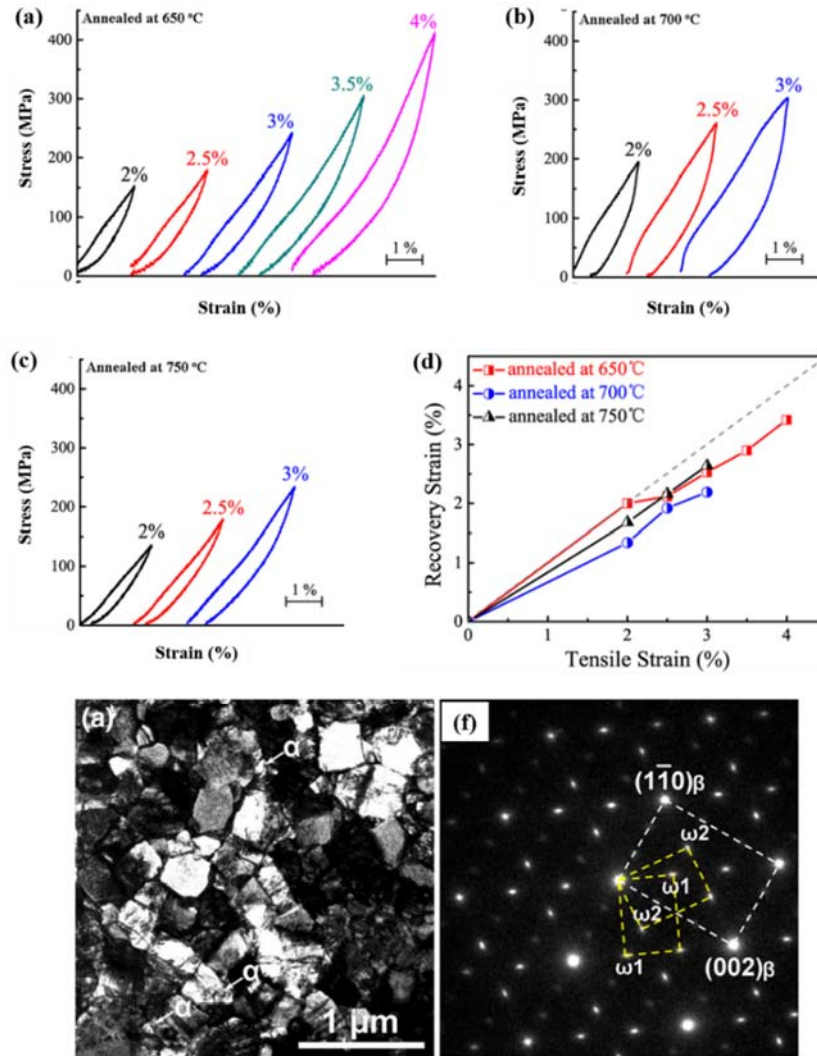


Fig. I-33 Tensile loading-unloading stress-strain curves obtained at 80 °C for Ti-18at%Nb film annealed at different temperatures for 3 min: (a) 650°C, (b) 700°C, (c) 750°C. (d) Recovery strain as a function of the maximum applied strain for the different annealing conditions. (e) Bright field TEM image and corresponding diffraction pattern of the 650°C annealed Ti-18Nb film [68].

Several groups have spread the researches on ternary Ti-Nb-Zr system films [69, 81-83]. Frutos et al. [83] studied magnetron-sputtering Ti-22Nb-10Zr (wt.%) films with focus on the effect of bias voltage on the microstructure evolutions and mechanical properties. Figs. I-34 a-d show the phase evolutions of α , α'' and β -phases as a function of bias voltage. It can be observed that with increasing the bias voltage, the peak intensities of α and β -phases decrease progressively, whereas the peak intensity of α'' -phase increases. This is due to that the increase in bias voltage induced the stress-induced martensitic (SIM) transformation. The higher bias voltage introduced more ion bombardments during deposition process, and produced higher compressive stress. When the compressive stress level exceeded the martensitic start stress σ_s , SIM transformation occurred. The higher the accumulated compression stresses magnitude, the higher the α'' martensite percentage induced by SIM transformation ($\beta \rightarrow \alpha''$) and the lower

the β phase content is. Besides, the strong presence of a $(111)\alpha''$ texture arise from the $\{110\}_\beta$ fiber texture as a consequence of well-known lattice correspondence between β -phase and α'' martensite is: $[100]_{\alpha''} // [100]_\beta$, $[010]_{\alpha''} // [110]_\beta$ and $[001]_{\alpha''} // [110]_\beta$.

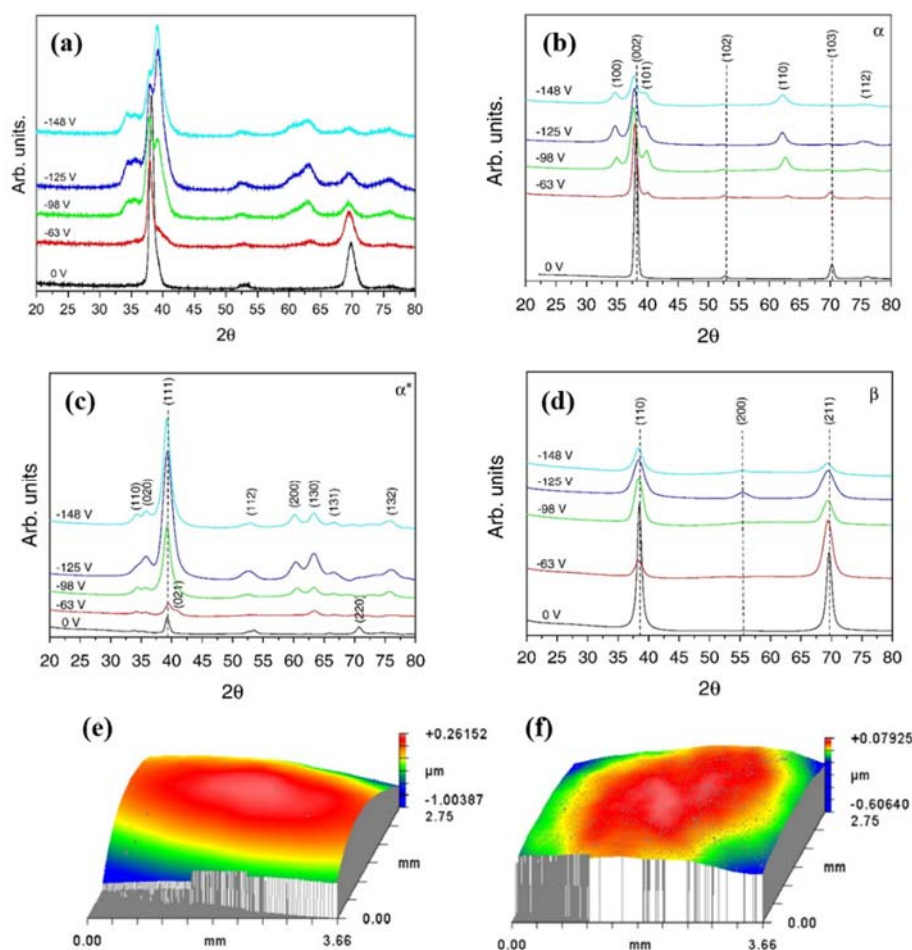


Fig. I-34 (a) X-Ray diffractions patterns of magnetron-sputtering Ti-22Nb-10Zr (wt.%) films as a function of increasing bias voltage. Evolution of the phases as a function of the increasing bias voltage: (b) hexagonal close-packed α phase, (c) orthorhombic α'' phase, (d) body centered cubic β phase; the peaks were deconvoluted from the XRD pattern in (a). The concave curvature of the Ti-22Nb-10Zr (wt.%) films obtained at a bias voltage value of -63 V (a) and -148 V (b), respectively. As the bias voltage increase, the curvature radius, R , decrease.

From the Figs. I-34 e and f, the curvature radius decrease with increasing bias voltage. The calculated compressive residual stresses were -700 MPa for bias -63 V and -100 MPa for bias -148 V, respectively. Such result is expected, since the compressive stresses was accommodated as a consequence of the induction of the martensitic transformation ($\beta \rightarrow \alpha''$), resulting in the reduced magnitude of residual stress. This decrease in the magnitude of the compressive residual stresses present has a direct impact on hardness values in the coating.

Achache et al. [85] have proposed another β -type superelastic film, the Ti-Nb-Ta-Zr (TNTZ) “Gum metal” film deposited by magnetron sputtering, and have investigated the effect

of deposition pressure and negative substrate bias voltage, on the morphology, texture, and superelastic behavior in TNTZ films.

Fig. I-35 shows the fractured cross-sectional and the surface SEM images of TNTZ films deposited at different working pressures and bias voltages. It is clearly seen that the film structure becomes more compact when the deposition pressure is reduced due to the fact that the mean free path in the plasma increases and thus, adatoms energy and mobility increase with reduction of the pressure, resulting in the filling of the voids between the grains and in an increase of the film density. From the surface SEM images, the film deposited with bias voltage have a crater-like surface structure indicating that high bias voltage induces argon ions etching of the growing surface.

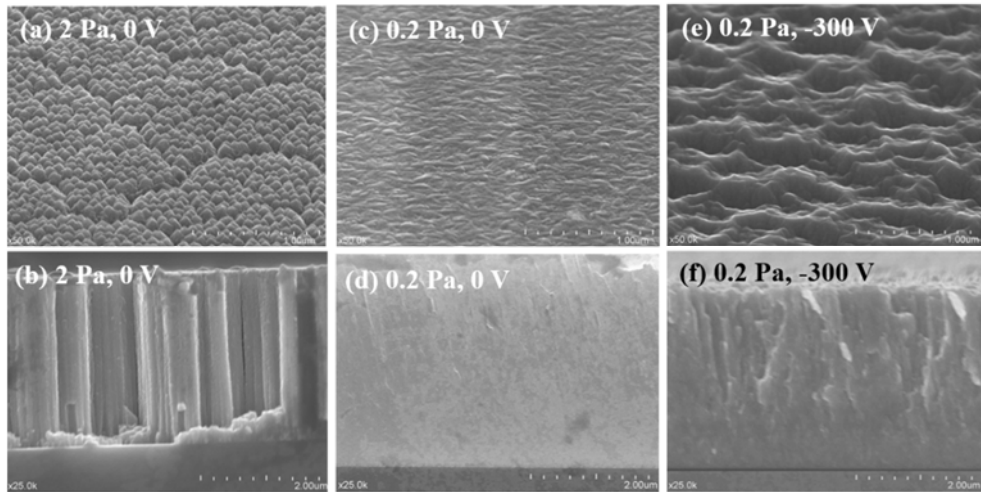


Fig. I-35 Surface and cross-sectional SEM images of TNTZ films deposited at (a, b) 2 Pa, 0 V; (c, d) 0.2 Pa, 0 V; (e, f) 0.2 Pa, -300 V.

Fig. I-36 shows the film textures for the different deposition pressure and bias voltage conditions. The texture changes from a mixture of $\{111\}_\beta$ and $\{100\}_\beta$ to $\{110\}_\beta$ with the reduction of the deposition pressure for the same reasons already discussed earlier. Applying negative bias voltage leads to the disappearance of $\{110\}_\beta$ texture and promotes the presence of $\{100\}_\beta$ and $\{111\}_\beta$ textures. It is suggested that the strong ion bombardment due to high applied bias voltage favors the resputtering of the densest $\{110\}_\beta$ planes while $\{100\}_\beta$ and $\{111\}_\beta$ planes with open channeling directions have a higher probability of surviving.

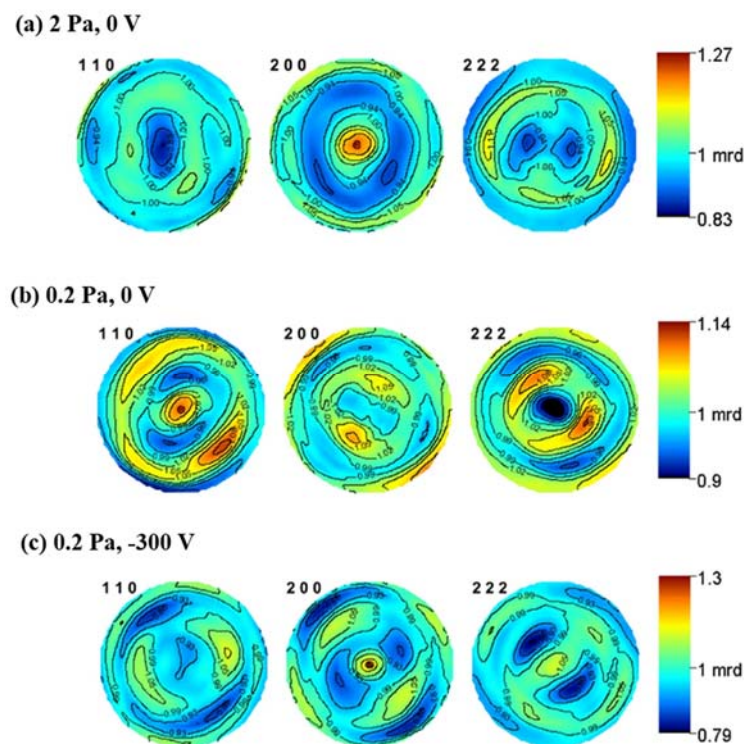


Fig. I-36 Recalculated poles figures of TNTZ films deposited at (a) 2 Pa, 0 V; (b) 0.2 Pa, 0 V and (c) 0.2 Pa, -300 V.

The evolution of depth recovery ratios measured during spherical nanoindentations of TNTZ films is presented as a function of the deposition pressure and negative substrate bias voltage in Fig. I-37. It is noticed that the superelastic effect depends strongly on the deposition pressure and negative bias voltage, and the film deposited at 0.2 Pa without bias voltage presents the greatest depth recovery ratio (81%). It is due to the fact that the film structure is dense with a $\{110\}_\beta$ fiber texture.

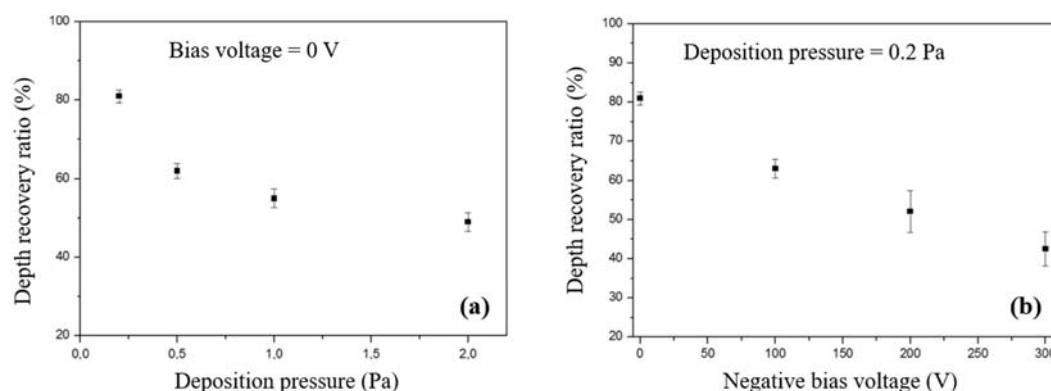


Fig. I-37 Evolution of depth recovery ratio of TNTZ films as a function of deposition pressure (a) and negative bias voltage (b).

I.5 Conclusion

In the first chapter, a bibliographic study on the general properties for Ti and Ti-based alloys were carried out, and the focus was mainly on β -metastable titanium alloys composed of biocompatible alloying elements as promising candidates for biomedical applications to replace the currently used NiTi alloys which present a risk of Ni allergy and hypersensitivity. Then, the superelasticity associated with a reversible martensitic transformation was elucidated in view of the response reacting to mechanical loads. Finally, the magnetron sputtered thin films were reviewed in cases of NiTi-based system and Ni-free β -Ti system. The aim of the present thesis was elucidated to investigate the superelasticity of Ti-Nb-Zr-Sn and Ti-Zr-Mo-Sn alloys from bulk to film geometry. Elaboration procedures and experimental characterization techniques were presented in the next chapter.

References

- [1] R.R. Boyer, An overview on the use of titanium in the aerospace industry, *Materials Science and Engineering: A*, 213 (1996) 103-114.
- [2] S. Banerjee, P. Mukhopadhyay, *Phase transformations: examples from titanium and zirconium alloys*, 1st ed., Elsevier Science, 2010.
- [3] M. Geetha, A.K. Singh, R. Asokamani, A.K. Gogia, Ti based biomaterials, the ultimate choice for orthopaedic implants – A review, *Progress in Materials Science*, 54 (2009) 397-425.
- [4] G. Welsch, R. Boyer, E. Collings, *Materials properties handbook: titanium alloys*, ASM International, 1993.
- [5] C. Leyens, M. Peters, *Titanium and titanium alloys: fundamentals and applications*, John Wiley & Sons, 2003.
- [6] W.G. Burgers, On the process of transition of the cubic-body-centered modification into the hexagonal-close-packed modification of zirconium, *Physica*, 1 (1934) 561-586.
- [7] H. Jabir, *Local scale characterisation of the superelastic properties of titanium alloys (bulk and coatings)*, PhD thesis, INSA de Rennes, 2018.
- [8] M. Motyka, K. Kubiak, J. Sieniawski, W. Ziąja, 2.02 - Phase Transformations and Characterization of $\alpha + \beta$ Titanium Alloys, in: S. Hashmi, G.F. Batalha, C.J. Van Tyne, B. Yilbas (Eds.) *Comprehensive Materials Processing*, Elsevier, Oxford, 2014, pp. 7-36.
- [9] J. Fan, *Microstructural study of the $\beta \rightarrow \alpha$ phase transformation induced by thermo-mechanical treatments in metastable β Ti-5553 alloy*, PhD thesis, INSA de Rennes, 2016.
- [10] T. Furuhashi, S. Takagi, H. Watanabe, T. Maki, Crystallography of grain boundary α precipitates in a β titanium alloy, *Metallurgical and Materials Transactions A*, 27 (1996) 1635-1646.
- [11] Y. Combres, *Traitements thermiques des alliages de titane*, (2013).
- [12] P.J. Bania, Beta titanium alloys and their role in the titanium industry, *JOM*, 46 (1994) 16-19.
- [13] R.P. Kolli, A. Devaraj, A review of metastable beta titanium alloys, *Metals*, 8 (2018) 506.
- [14] S. Semiatin, V. Seetharaman, I. Weiss, The thermomechanical processing of alpha/beta titanium alloys, *Jom*, 49 (1997) 33-39.
- [15] J.P. Morniroli, M. Gantois, Study of the conditions under which the omega phase forms in titanium-niobium and titanium-molybdenum alloys, *Memoires Scientifiques de la Revue de Metallurgie*, 70 (1973) 831-842.
- [16] H. Kim, Y. Ikehara, J.I. Kim, H. Hosoda, S. Miyazaki, Martensitic transformation, shape memory effect and superelasticity of Ti-Nb binary alloys, *Acta Materialia*, 54 (2006) 2419-2429.
- [17] T. Duerig, J. Albrecht, D. Richter, P. Fischer, Formation and reversion of stress induced martensite in Ti-10V-2Fe-3Al, *Acta Metallurgica*, 30 (1982) 2161-2172.
- [18] Y. Chai, H. Kim, H. Hosoda, S. Miyazaki, Self-accommodation in Ti-Nb shape memory alloys, *Acta materialia*, 57 (2009) 4054-4064.
- [19] E. Bertrand, P. Castany, Y. Yang, E. Menou, T. Gloriant, Deformation twinning in the full- α' martensitic Ti-25Ta-20Nb shape memory alloy, *Acta Materialia*, 105 (2016) 94-103.

- [20] S.K. Sikka, Y.K. Vohra, R. Chidambaram, Omega phase in materials, *Progress in Materials Science*, 27 (1982) 245-310.
- [21] P. Frost, W. Parris, L. Hirsch, J. Doig, C. Schwartz, Isothermal transformation of titanium-chromium alloys, *Trans. Asm*, 46 (1954) 231-256.
- [22] S. Sikka, Y. Vohra, R. Chidambaram, Omega phase in materials, *Progress in Materials Science*, 27 (1982) 245-310.
- [23] S.L. Sass, The structure and decomposition of Zr and Ti bcc solid solutions, *Journal of the Less Common Metals*, 28 (1972) 157-173.
- [24] B.S. Hickman, The formation of omega phase in titanium and zirconium alloys: A review, *Journal of Materials Science*, 4 (1969) 554-563.
- [25] F. Prima, P. Vermaut, G. Texier, D. Ansel, T. Gloriant, Evidence of α -nanophase heterogeneous nucleation from ω particles in a β -metastable Ti-based alloy by high-resolution electron microscopy, *Scripta Materialia*, 54 (2006) 645-648.
- [26] D. De Fontaine, N. Paton, J. Williams, The omega phase transformation in titanium alloys as an example of displacement controlled reactions, *Acta Metallurgica*, 19 (1971) 1153-1162.
- [27] C. Lin, G. Yin, A. Zhang, Y. Zhao, Q. Li, Simple models to account for the formation and decomposition of athermal ω phase in titanium alloys, *Scripta Materialia*, 117 (2016) 28-31.
- [28] H.Y. Kim, S. Hashimoto, J.I. Kim, T. Inamura, H. Hosoda, S. Miyazaki, Effect of Ta addition on shape memory behavior of Ti-22Nb alloy, *Materials Science and Engineering: A*, 417 (2006) 120-128.
- [29] K. Endoh, M. Tahara, T. Inamura, H. Hosoda, Effect of Sn and Zr content on superelastic properties of Ti-Mo-Sn-Zr biomedical alloys, *Materials Science and Engineering: A*, 704 (2017) 72-76.
- [30] K. Otsuka, X. Ren, Physical metallurgy of Ti-Ni-based shape memory alloys, *Progress in Materials Science*, 50 (2005) 511-678.
- [31] T.W.D. Duerig, T. W., K.N. Melton, D. Stöckel, *Engineering aspects of shape memory alloys.*, Butterworth-heinemann, London, 1990.
- [32] R. Plietsch, K. Ehrlich, Strength differential effect in pseudoelastic NiTi shape memory alloys, *Acta Materialia*, 45 (1997) 2417-2424.
- [33] Y. Kudoh, M. Tokonami, S. Miyazaki, K. Otsuka, Crystal structure of the martensite in Ti-49.2 at.%Ni alloy analyzed by the single crystal X-ray diffraction method, *Acta Metallurgica*, 33 (1985) 2049-2056.
- [34] M. Wang, S. Jiang, Y. Zhang, Phase Transformation, Twinning, and Detwinning of NiTi Shape-Memory Alloy Subject to a Shock Wave Based on Molecular-Dynamics Simulation, *Materials (Basel, Switzerland)*, 11 (2018) 2334.
- [35] A. Teramoto, *Sentalloy, the story of superelasticity*, Dentsply GAC, Bohemia, New York, USA, (2010).
- [36] T. Duerig, A. Pelton, D. Stöckel, An overview of nitinol medical applications, *Materials Science and Engineering: A*, 273 (1999) 149-160.
- [37] C.T. Dotter, R. Buschmann, M.K. McKinney, J. Rösch, Transluminal expandable nitinol coil stent grafting: preliminary report, *Radiology*, 147 (1983) 259-260.
- [38] C. Song, P. Campbell, T. Frank, A. Cuschieri, Thermal modelling of shape memory alloy fixator for medical application, *Smart Materials and Structures*, 11 (2002) 312.

- [39] Y. Ng, C. Song, D. McLean, S. Shimi, T. Frank, A. Cuschieri, P. Campbell, Optimized deployment of heat-activated surgical staples using thermography, *Applied Physics Letters*, 83 (2003) 1884-1886.
- [40] T. Mereau, T. Ford, Nitinol Compression Staples for Bone Fixation in Foot Surgery, *Journal of the American Podiatric Medical Association*, 96 (2006) 102-106.
- [41] L. Héraud, P. Castany, D. Lailllé, T. Gloriant, In Situ Synchrotron X-ray Diffraction of the Martensitic Transformation in Superelastic Ti-27Nb and NiTi Alloys: A Comparative Study, *Materials Today: Proceedings*, 2 (2015) S917-S920.
- [42] E. Bertrand, P. Castany, T. Gloriant, Investigation of the martensitic transformation and the damping behavior of a superelastic Ti-Ta-Nb alloy, *Acta Materialia*, 61 (2013) 511-518.
- [43] W.-N. Hsu, E. Polatidis, M. Šmíd, S. Van Petegem, N. Casati, H. Van Swygenhoven, Deformation and degradation of superelastic NiTi under multiaxial loading, *Acta Materialia*, 167 (2019) 149-158.
- [44] A. Ramezannejad, W. Xu, W. Xiao, K. Fox, D. Liang, M. Qian, New insights into nickel-free superelastic titanium alloys for biomedical applications, *Current Opinion in Solid State and Materials Science*, 23 (2019) 100783.
- [45] H.Y. Kim, S. Hashimoto, J.I. Kim, H. Hosoda, S. Miyazaki, Mechanical properties and shape memory behavior of Ti-Nb alloys, *Materials Transactions*, 45 (2004) 2443-2448.
- [46] S. Miyazaki, T. Imai, Y. Igo, K. Otsuka, Effect of cyclic deformation on the pseudoelasticity characteristics of Ti-Ni alloys, *Metallurgical Transactions A*, 17 (1986) 115-120.
- [47] S. Miyazaki, H.Y. Kim, H. Hosoda, Development and characterization of Ni-free Ti-base shape memory and superelastic alloys, *Materials Science and Engineering: A*, 438 (2006) 18-24.
- [48] E. Takahashi, T. Sakurai, S. Watanabe, N. Masahashi, S. Hanada, Effect of heat treatment and Sn content on superelasticity in biocompatible TiNbSn alloys, *Materials Transactions*, 43 (2002) 2978-2983.
- [49] H.Y. Kim, N. Oshika, J.I. Kim, T. Inamura, H. Hosoda, S. Miyazaki, Martensitic transformation and superelasticity of Ti-Nb-Pt alloys, *Materials Transactions*, 48 (2007) 400-406.
- [50] Y. Al-Zain, H.Y. Kim, H. Hosoda, T.H. Nam, S. Miyazaki, Shape memory properties of Ti-Nb-Mo biomedical alloys, *Acta Materialia*, 58 (2010) 4212-4223.
- [51] J.I. Kim, H.Y. Kim, H. Hosoda, S. Miyazaki, Shape memory behavior of Ti-22Nb-(0.5-2.0) O (at%) biomedical alloys, *Materials Transactions*, 46 (2005) 852-857.
- [52] M. Tahara, H.Y. Kim, H. Hosoda, S. Miyazaki, Shape memory effect and cyclic deformation behavior of Ti-Nb-N alloys, *Functional Materials Letters*, 2 (2009) 79-82.
- [53] M.F. Ijaz, H.Y. Kim, H. Hosoda, S. Miyazaki, Effect of Sn addition on stress hysteresis and superelastic properties of a Ti-15Nb-3Mo alloy, *Scripta Materialia*, 72 (2014) 29-32.
- [54] H.Y. Kim, J. Fu, H. Tobe, J.I. Kim, S. Miyazaki, Crystal structure, transformation strain, and superelastic property of Ti-Nb-Zr and Ti-Nb-Ta alloys, *Shape memory and Superelasticity*, 1 (2015) 107-116.
- [55] H.Y. Kim, S. Miyazaki, Martensitic transformation and superelastic properties of Ti-Nb base alloys, *Materials Transactions*, 56 (2015) 625-634.
- [56] L. López Pavón, H.Y. Kim, H. Hosoda, S. Miyazaki, Effect of Nb content and heat treatment temperature on superelastic properties of Ti-24Zr-(8-12)Nb-2Sn alloys, *Scripta Materialia*, 95 (2015) 46-49.
- [57] H.Y. Kim, J.I. Kim, T. Inamura, H. Hosoda, S. Miyazaki, Effect of thermo-mechanical treatment on

mechanical properties and shape memory behavior of Ti-(26–28)at.% Nb alloys, *Materials Science and Engineering: A*, 438-440 (2006) 839-843.

[58] H.Y. Kim, T. Sasaki, K. Okutsu, J.I. Kim, T. Inamura, H. Hosoda, S. Miyazaki, Texture and shape memory behavior of Ti–22Nb–6Ta alloy, *Acta Materialia*, 54 (2006) 423-433.

[59] F. Sun, S. Nowak, T. Gloriant, P. Laheurte, A. Eberhardt, F. Prima, Influence of a short thermal treatment on the superelastic properties of a titanium-based alloy, *Scripta Materialia*, 63 (2010) 1053-1056.

[60] J.J. Gao, I. Thibon, D. Laillé, P. Castany, T. Gloriant, Influence of texture and transformation strain on the superelastic performance of a new Ti–20Zr–3Mo–3Sn alloy, *Materials Science and Engineering: A*, 762 (2019) 138075.

[61] J.J. Gao, I. Thibon, P. Castany, T. Gloriant, Effect of grain size on the recovery strain in a new Ti–20Zr–12Nb–2Sn superelastic alloy, *Materials Science and Engineering: A*, 793 (2020) 139878.

[62] Q. Sun, A. Aslan, M. Li, M. Chen, Effects of grain size on phase transition behavior of nanocrystalline shape memory alloys, *Science China Technological Sciences*, 57 (2014) 671-679.

[63] J. Musil, S. Kadlec, Reactive sputtering of TiN films at large substrate to target distances, *Vacuum*, 40 (1990) 435-444.

[64] J. Musil, Recent advances in magnetron sputtering technology, *Surface and Coatings Technology*, 100 (1998) 280-286.

[65] J. Musil, J. Vlček, Magnetron sputtering of films with controlled texture and grain size, *Materials Chemistry and Physics*, 54 (1998) 116-122.

[66] J. Musil, J. Vlček, Magnetron sputtering of alloy and alloy-based films, *Thin Solid Films*, 343 (1999) 47-50.

[67] K.S.S.E. Raju, S. Bysakh, M.A. Sumesh, S.V. Kamat, S. Mohan, The effect of ageing on microstructure and nanoindentation behaviour of dc magnetron sputter deposited nickel rich NiTi films, *Materials Science and Engineering: A*, 476 (2008) 267-273.

[68] X.L. Meng, B. Sun, J.Y. Sun, Z.Y. Gao, W. Cai, L.C. Zhao, Microstructure and shape memory behavior of Ti-Nb shape memory alloy thin film, *Shape Memory and Superelasticity*, 3 (2017) 230-237.

[69] X.-H. Yan, J. Ma, Y. Zhang, High-throughput screening for biomedical applications in a Ti-Zr-Nb alloy system through masking co-sputtering, *Science China Physics, Mechanics & Astronomy*, 62 (2019) 1-9.

[70] S.K. Sharma, S. Mohan, Influence of annealing on structural, morphological, compositional and surface properties of magnetron sputtered nickel-titanium thin films, *Applied Surface Science*, 282 (2013) 492-498.

[71] A. Ishida, M. Sato, S. Miyazaki, Mechanical properties of Ti-Ni shape memory thin films formed by sputtering, *Materials Science and Engineering: A*, 273 (1999) 754-757.

[72] X. Cao, X. Cao, Q. Zhang, Nanoscale indentation behavior of pseudo-elastic Ti–Ni thin films, *Journal of Alloys and Compounds*, 465 (2008) 491-496.

[73] X.G. Ma, K. Komvopoulos, Nanoscale pseudoelastic behavior of indented titanium–nickel films, *Applied Physics Letters*, 83 (2003) 3773-3775.

[74] S. Miyazaki, A. Ishida, Martensitic transformation and shape memory behavior in sputter-deposited TiNi-base thin films, *Materials Science and Engineering: A*, 273 (1999) 106-133.

[75] R.L. de Miranda, C. Zamponi, E. Quandt, Fabrication of TiNi thin film stents, *Smart Materials and*

Structures, 18 (2009) 104010.

[76] H. Rumpf, T. Walther, C. Zamponi, E. Quandt, High ultimate tensile stress in nano-grained superelastic NiTi thin films, *Materials Science and Engineering: A*, 415 (2006) 304-308.

[77] D. Photiou, N.T. Panagiotopoulos, L. Koutsokeras, G.A. Evangelakis, G. Constantinides, Microstructure and nanomechanical properties of magnetron sputtered Ti– Nb films, *Surface and Coatings Technology*, 302 (2016) 310-319.

[78] S. Achache, S. Lamri, M.A.P. Yazdi, A. Billard, M. François, F. Sanchette, Ni-free superelastic binary Ti– Nb coatings obtained by DC magnetron co-sputtering, *Surface and Coatings Technology*, 275 (2015) 283-288.

[79] M. Baatarsukh, J. Bae, S. Huh, H. Jeong, B. Choi, G. Cho, T. Nam, J. Noh, Composition Dependence of the β Phase Stability and Mechanical Properties of Ti–Nb Thin Films, *Journal of Nanoscience and Nanotechnology*, 19 (2019) 3627-3630.

[80] D. Tallarico, A. Gobbi, P. Paulin Filho, M.M. da Costa, P. Nascente, Growth and surface characterization of TiNbZr thin films deposited by magnetron sputtering for biomedical applications, *Materials Science and Engineering: C*, 43 (2014) 45-49.

[81] E.D. Gonzalez, N.K. Fukumasu, C.R.M. Afonso, P.A.P. Nascente, Impact of Zr content on the nanostructure, mechanical, and tribological behaviors of β -Ti–Nb–Zr ternary alloy coatings, *Thin Solid Films*, (2021) 138565.

[82] J. Yang, M. Baatarsukh, J. Bae, S. Huh, H. Jeong, B. Choi, T. Nam, J. Noh, Phase stability and properties of Ti–Nb–Zr thin films and their dependence on Zr addition, *Materials*, 11 (2018) 1361.

[83] E. Frutos, M. Karlík, J.A. Jiménez, H. Langhansová, J. Lieskovská, T. Polcar, Development of new β/α'' -Ti–Nb–Zr biocompatible coating with low Young's modulus and high toughness for medical applications, *Materials & Design*, 142 (2018) 44-55.

[84] J.J. Gutiérrez Moreno, N.T. Panagiotopoulos, G.A. Evangelakis, C.E. Lekka, Electronic Origin of α'' to β Phase Transformation in Ti–Nb–Based Thin Films upon Hf Microalloying, *Materials (Basel, Switzerland)*, 13 (2020) 1288.

[85] S. Achache, S. Lamri, A. Alhussein, A. Billard, M. François, F. Sanchette, Gum Metal thin films obtained by magnetron sputtering of a Ti–Nb–Zr–Ta target, *Materials Science and Engineering: A*, 673 (2016) 492-502.

[86] A. Ishida, A. Takei, M. Sato, S. Miyazaki, Stress-strain curves of sputtered thin films of Ti– Ni, *Thin Solid Films*, 281 (1996) 337-339.

[87] Y. Fu, H. Du, RF magnetron sputtered TiNiCu shape memory alloy thin film, *Materials Science and Engineering: A*, 339 (2003) 10-16.

[88] P. Krulevitch, A.P. Lee, P.B. Ramsey, J.C. Trevino, J. Hamilton, M.A. Northrup, Thin film shape memory alloy microactuators, *Journal of Microelectromechanical Systems*, 5 (1996) 270-282.

[89] W. Ni, Y.-T. Cheng, M. Lukitsch, A.M. Weiner, L.C. Lev, D.S. Grummon, Novel layered tribological coatings using a superelastic NiTi interlayer, *Wear*, 259 (2005) 842-848.

[90] W. Tillmann, S. Momeni, Deposition of superelastic composite NiTi based films, *Vacuum*, 104 (2014) 41-46.

[91] Y. Zhang, Y.-T. Cheng, D.S. Grummon, The influence of superelastic NiTi interlayers on tribological properties of CrN hard coatings, *Materials Science and Engineering: A*, 438 (2006) 710-713.

- [92] M. Callisti, T. Polcar, The role of Ni-Ti-(Cu) interlayers on the mechanical properties and nano-scratch behaviour of solid lubricant W-S-C coatings, *Surface and Coatings Technology*, 254 (2014) 260-269.
- [93] M. Callisti, T. Polcar, Stress-induced martensitic transformation in Ni-Ti (-Cu) interlayers controlling stress distribution in functional coatings during sliding, *Applied Surface Science*, 325 (2015) 192-202.
- [94] N. Choudhary, D. Kaur, Shape memory alloy thin films and heterostructures for MEMS applications: A review, *Sensors and Actuators A: Physical*, 242 (2016) 162-181.
- [95] A. Kumar, D. Singh, D. Kaur, Grain size effect on structural, electrical and mechanical properties of NiTi thin films deposited by magnetron co-sputtering, *Surface and Coatings Technology*, 203 (2009) 1596-1603.
- [96] K. Li, Y. Li, K. Yu, C. Liu, D. Gibson, A. Leyland, A. Matthews, Y.Q. Fu, Crystal size induced reduction in thermal hysteresis of Ni-Ti-Nb shape memory thin films, *Applied Physics Letters*, 108 (2016) 171907.
- [97] G. Pan, Z. Cao, J. Shi, M. Wei, L. Xu, X. Meng, Different mechanical response of TiNi film induced by the shape of indenter during nanoindentation, *Sensors and Actuators A: Physical*, 217 (2014) 75-80.
- [98] J. Musil, A. Bell, J. Vlček, T. Hurkmans, Formation of high temperature phases in sputter deposited Ti-based films below 100° C, *Journal of Vacuum Science & Technology A: Vacuum, Surfaces, and Films*, 14 (1996) 2247-2250.
- [99] D. Photiou, N.T. Panagiotopoulos, L. Koutsokeras, G.A. Evangelakis, G. Constantinides, Microstructure and nanomechanical properties of magnetron sputtered Ti-Nb films, *Surface and Coatings Technology*, 302 (2016) 310-319.
- [100] F. Sanchette, L. Tran Huu, A. Billard, C. Frantz, Structure—properties relationship of metastable Al-Cr and Al-Ti alloys deposited by r.f. magnetron sputtering: role of nitrogen, *Surface and Coatings Technology*, 74-75 (1995) 903-909.
- [101] S. Mahieu, D. Depla, Reactive sputter deposition of TiN layers: modelling the growth by characterization of particle fluxes towards the substrate, *Journal of Physics D: Applied Physics*, 42 (2009) 053002.
- [102] E.D. Gonzalez, C.R.M. Afonso, P.A.P. Nascente, Nanostructural characterization of sputter deposited Ti-Nb coatings by automated crystallographic orientation mapping, *Thin Solid Films*, 661 (2018) 92-97.
- [103] F. Sun, J.Y. Zhang, M. Marteleur, C. Brozek, E.F. Rauch, M. Veron, P. Vermaut, P.J. Jacques, F. Prima, A new titanium alloy with a combination of high strength, high strain hardening and improved ductility, *Scripta Materialia*, 94 (2015) 17-20.
- [104] E. Gonzalez, C.R. Afonso, P.A. Nascente, Influence of Nb content on the structure, morphology, nanostructure, and properties of titanium-niobium magnetron sputter deposited coatings for biomedical applications, *Surface and Coatings Technology*, 326 (2017) 424-428.

Chapter II: Elaboration and Characterization methods

II.1 Elaboration

II.1.1 Elaboration of Ti-based bulk alloys

In this thesis work, investigated alloys were elaborated from pure raw metals. The elaboration procedure for the Ti-based bulk alloys is presented in Fig. II-1. Ultra-pure raw metals were melted into button-shaped alloy ingots by the cold crucible levitation melting (CCLM) technique. The followed thermo-mechanical treatments were applied to tailor the mechanical and functional properties of alloys. Raw materials were cleaned by acid solutions: 50 vol.% HF + 50 vol.% HNO₃ for titanium and 20 vol.% HF + 40 vol.% HNO₃ + 5 vol.% H₂SO₄ + 35 vol.% H₂O for other alloying metals. After each thermal treatment, alloy ingots were cleaned in the acid solution of 50 vol.% HF + 50 vol.% HNO₃ to remove oxide layer.

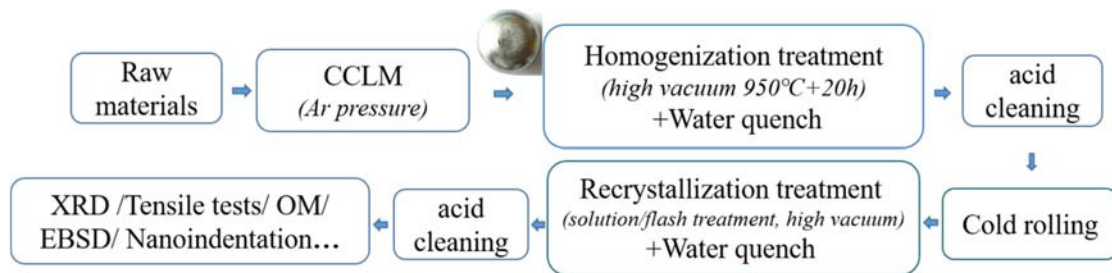


Fig. II-1 Elaboration procedure for alloy bulks.

II.1.1.1 Cold crucible levitation melting Furnace

Cold crucible levitation melting (CCLM) is a type of induction melting furnace and is a specific melting method from the viewpoint of metals being levitated in a crucible and alloyed by diffusion mixing effect of strong stirring by an electromagnetic force [1]. The CCLM apparatus is illustrated in Fig. II-2. A water-cooled crucible is made from oxygen-free, high-purity copper segments. Two coils are wrapped around the crucible and connected separately to a high frequency inverter power supply ($U=220$ V, $I=70$ A, $P=20$ KW, $f=215$ kHz). High-frequency current flows through the coils. Eddy currents are induced in the crucible and in the metals to be melted. The metals in the crucible are levitated with electromagnetic repulsion forces (Laplace forces induced by current loops). The eddy currents generate joule heat in the crucible and metals, and the metals melt. The CCLM is proceeded in a high vacuum furnace under Ar atmosphere.

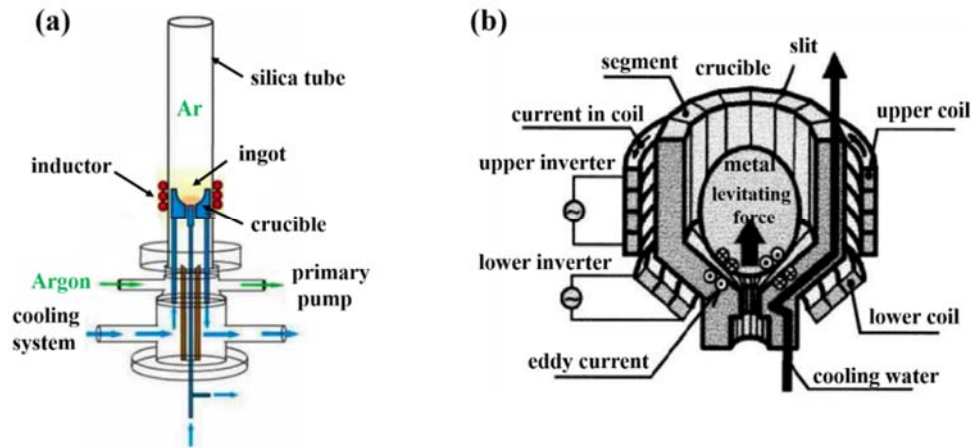


Fig. II-2 Cold crucible levitation melting furnace: (a) the schematic and (b) the principles [1].

CCLM has several advantages as follows:

- (i) It can melt metals with high melting point.
- (ii) It can create an alloy with homogeneous composition due to strong stirring effect by an electromagnetic force.
- (iii) It enables metals to be melted without contamination because the molten metals are levitated by electromagnetic repulsion forces over the crucible.

The above features enable a solid alloy to be composed uniformly, independent of differences in melting point and specific gravity without contamination.

II.1.1.2 Thermo-mechanical treatments

The thermo-mechanical treatment procedures are presented in Fig. II-3, in three steps: homogenization treatment, cold rolling and recrystallization treatment.

The button-shaped alloy ingots were homogenized at 950 °C for 20h in a high vacuum of 10^{-7} mbar, and quenched into water. Then they were subjected to cold rolling up to a define thickness reduction. Recrystallization treatments were carried out on cold rolled specimens. For instance, Ti-20Zr-3Mo-3Sn (Ti2033, at.%) alloys were solution-treated at 850°C for 30 min. The homogenization treatment and solution treatment were performed in the vacuum furnace in Fig. II-4.

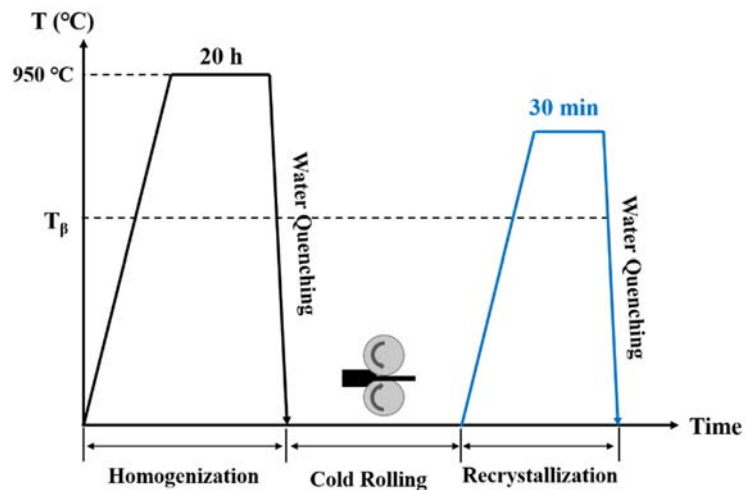


Fig. II-3 Thermo-mechanical procedures for β -Ti alloys.

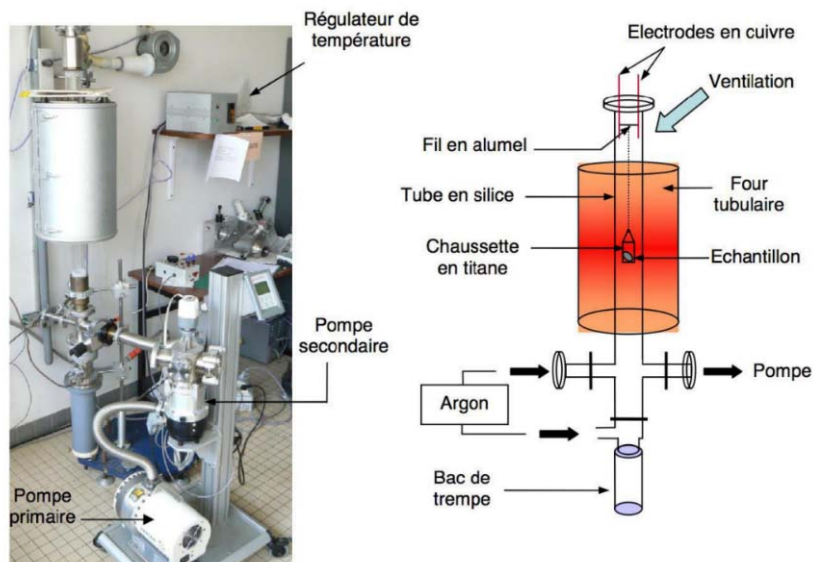


Fig. II-4 Vacuum furnace for thermal treatments: (a) general view and (b) schematic view [2].

II.1.2 Elaboration of Ti-based alloy films

II.1.2.1 Magnetron sputtering technique

Sputtering deposition is a process belonging to the physical vapor deposition (PVD) techniques. The sputtering process is an energy and momentum exchange procedure through a series of collisions between species (neutral atoms, ions, electrons), during which target surface is bombarded by energetic ions (e.g., Ar^+). These ions are generated in a glow discharge plasma and accelerated towards the target by an electric field. Fig. II-5 shows the bombardment process of incident ions causing ejection of target atoms, which may then condense on substrate as thin film. The energy of incident ions needs to be high enough to

create collision cascades, in which the primary knock-on atoms cause a series of collisions and eventually lead to the ejection of a surface atom (Fig. II-5b). Secondary electrons are also emitted from the target surface as a result of the ion bombardment, and these electrons are needed to create new ions by collision to maintain the plasma. The most important quantity describing the sputter process is the sputter yield Y , which corresponds to the number of sputtered target atoms/number of incident ions ratio.

The sputtering yield depends strongly on the mass of incident and sputtered atoms as well as on the energy transferred by the collisions. However, the basic sputtering process is limited by low deposition rates, low ionization efficiencies in the plasma, and high substrate heating effects.

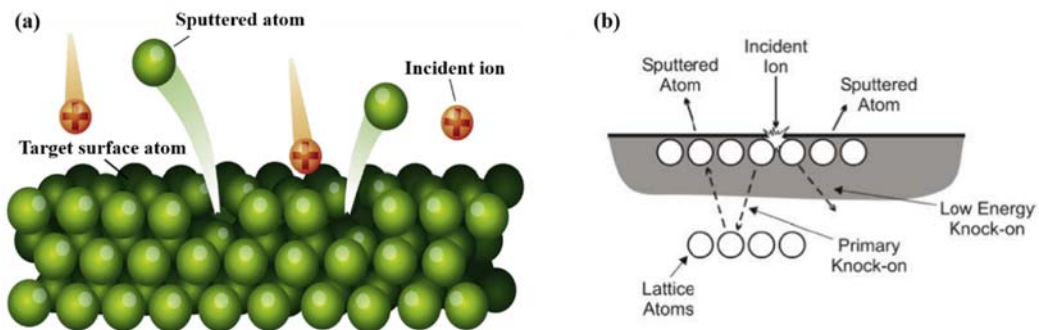


Fig. II-5 (a) The principle of sputtering [3]; (b) Momentum transfer process during sputtering [4].

These limitations have been overcome by the development of the magnetron sputtering technique. Magnetron sputtering has become the most common process for growing thin films by sputter deposition. The distinctive feature of the magnetron sputtering is the application of a magnetic field [5]. Fig. II-6 illustrates a planar circular magnetron configuration, where permanent magnets are arranged in such a way that one pole is positioned at the central axis of the target and the second pole is formed by a ring of magnets around the outer edge of the target, forming a magnetic field in a circular symmetry. The magnetic field is configured in a region near the target surface, and serves to constrain the motions of secondary electrons to the vicinity of the target. Meanwhile, the electric field is established between the cathode subjected to a negative electric bias and the anode. The substrate or the reactor walls are usually grounded. For planar magnetrons, it is reasonable to assume the electric field to be normal to the target or cathode surface.

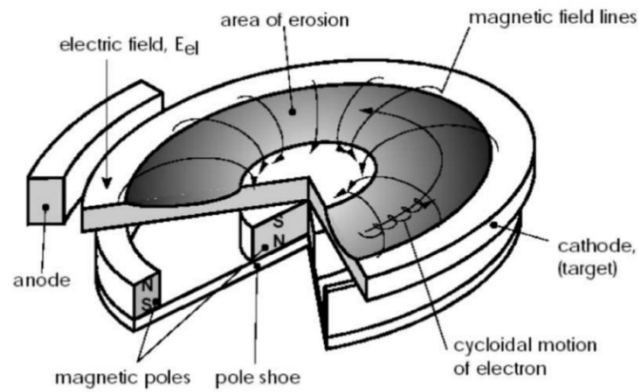


Fig. II-6 Schematic illustration of a planar circular magnetron configuration [6].

It is worth mentioning that the electrons move in a spiral trajectory in the orthogonal electromagnetic field (circling around the magnetic flux lines in the region near the target) and their paths are prolonged significantly, which favors the improved ionization efficiency, resulting in a local and denser plasma that can be sustained at a lower working gas pressure [7]. The magnetic field only affects electrons but not ions, since they exhibit a higher mass than electrons while the positively charged ions are accelerated by the electric field. The strong confinement of the plasma near the target surface leads to high sputtering rates in the area of the drift loops. As a consequence, the erosion of the target material is localized and non-uniform.

According to the difference of working power supplies, there are two types of sputtering: direct current (DC) sputtering and radio frequency (RF) sputtering. A DC magnetron sputtering system, which basically consists of two electrodes, is shown schematically in Fig. II-7. The negative potential of the DC power supply is applied to the cathode or target to generate a glow discharge (plasma). Positive ions of the plasma are accelerated towards the target, knocking off or sputtering atoms from the target surface. In the case of RF magnetron sputtering, the electrical potential of the current is alternated at radio frequencies to avoid a charge building up on the sputtered target which over time can result in arcing into the plasma and can even lead to the complete cessation of the sputtering of atoms terminating the process.

Sputtering is a non-equilibrium process, consequently thin films prepared by sputtering deposition exhibit quite different microstructures as compared to their bulk counterparts [8].

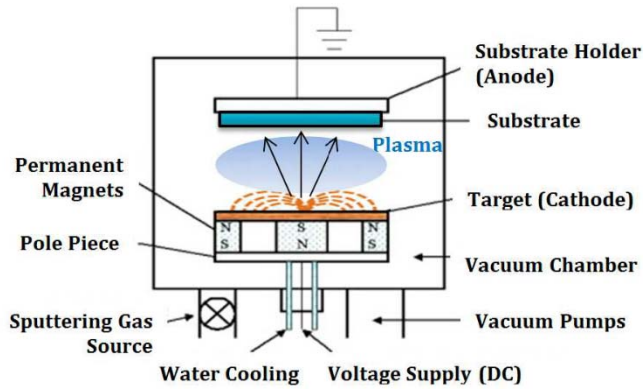


Fig. II-7 Schematic of a DC magnetron sputtering system [9].

II.1.2.2 Deposition conditions

In the present thesis work, the Ti-16Zr-13Nb-2Sn (at. %, Ti16132 for short) and Ti-24Nb-4Zr-8Sn (wt%, Ti2448 for short) films were deposited on Si substrates oriented (100) (with their native surface oxide layer) by RF magnetron sputtering from single alloyed targets using the deposition machine shown in Fig. II-9. This deposition machine presents a face-on-face sputter geometry (substrate holder above, target below) and was originally used for sputtering deposition. The deposition machine was upgraded at the beginning of my thesis work and notably a magnetron cathode system was implemented in the deposition chamber. The rotation of the specimen holder was not possible in this deposition machine with a face-on-face sputter geometry.



Fig. II-9 RF magnetron sputtering machine and the alloy targets for Ti16132 and Ti2448 films.

The investigated alloy films were elaborated from homemade quaternary alloyed target, i.e., Ti16132 and Ti2448 alloy targets. The procedure for the elaboration of homemade sputtering targets was presented in Fig. II-11. Ultra-pure raw metals of titanium (>99.6 wt%), zirconium (>99.078 wt%), niobium (>99.9 wt%), molybdenum (>99.99 wt%) and tin (>99.99 wt%) were used to synthesize the alloy by cold crucible levitation melting (CCLM)

technique. The ingots were then cold-rolled and surface-machined to obtain a perfect flat surface with the size of 75 mm diameter and 3 mm thick. The targets were finally cleaned in HF/HNO₃ solution (1/1 ratio).

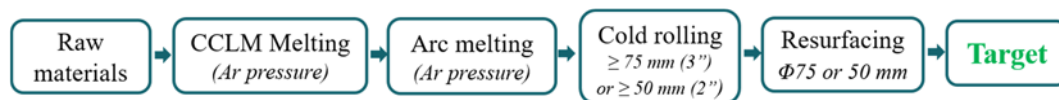


Fig. II-11 Preparation procedure of sputtering targets

The chemical compositions of the targets were measured by EDS analyses and were listed in Table II-1. Note that the name given to the Ti16132 target differs from its original composition measured by EDS. Indeed the assigned name reflects the final concentration of the obtained film investigated in the present work when this single target is employed during the deposition process.

Table II-1 Chemical compositions of the targets

Targets	Zr	Nb	Sn	Ti
Ti-24Nb-4Zr-8Sn (Ti2448, wt. %)	4.0	24.1	8.4	-
Ti-16Zr-13Nb-2Sn (Ti16132, at. %)	20.1	11.9	2.1	-

Table II-2 presents the deposition conditions for the magnetron sputtering Ti-based films investigated in the present work.

Table II-2 Deposition conditions for magnetron sputtering Ti-based films

Films	Vacuum (mbar)	Pressure (Pa)	Power (W)	Target bias (V)	Target-substrate distance (mm)	Duration (min)
Ti16132	3.3E-7	0.2	300	385	55	50
Ti2448	3.4E-7	0.2	300	440	55	50

Here, we describe the deposition process for example, in the case of the Ti16132 film. The Ti16132 alloy target was placed in the deposition chamber. Si substrate was ultrasonically cleaned in acetone and ethanol for 5 min in each, and dried under compressed air gas, then mounted on the sample holder at a distance of 5.5 cm from the target. The deposition chamber was evacuated to a base pressure of 3.4×10^{-5} Pa. High purity argon was used as the sputtering gas and the working pressure was maintained at 0.2 Pa during the entire sputtering process. Before each deposition, the target was pre-sputtered in Ar plasma for 10 min to clean the target surface and to equilibrate thermally. During this stabilizing period the substrate was protected by a large shutter. During deposition at room temperature, the sputtering RF power of the

target was fixed at 300 W and the negative voltage on the target was recorded as 385 V. Deposition was carried out for 50 min.

Plane-view TEM specimen were also prepared by depositing thin film layer on a Cu TEM grid within very short time leading to a film thickness of 30 nm. Films were studied in their as-deposited state without any post-treatment.

II.2 Characterization methods

II.2.1 Microstructural characterization

II.2.1.1 Optical microscopy

Metallographic observations of grain structure on alloy bulks were realized on inverted Metallurgical OLYMPUS Microscope (Fig. II-12a). Specimens were mechanically polished with SiC abrasive papers on an automatic polishing machine (double rotation, speed control, force control). In order to obtain a mirror-like surface, each specimen was electrochemically polished in an electrolyte composed of perchloric acid (4 vol.%) and methanol (96 vol.%) with a controlled temperature of $-14 \sim -16$ °C and a controlled electric current of $0.15 \sim 0.2$ A for 45 s. The electrochemical polishing machine is as shown in Fig. II-12b. Optical microstructural observations were also conducted on the Anton Paar platform equipped with an optical microscope coupled to other local mechanical characterizations.

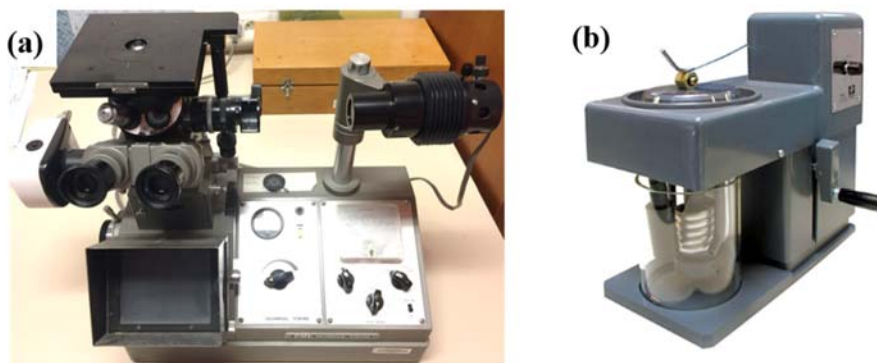


Fig. II-12 (a) Inverted Metallurgical OLYMPUS Microscope and (b) Polisecc C25 electrochemical polishing machine

II.2.1.2 Surface topography and roughness measurements

Atomic-force microscopy (AFM) is a powerful technique that offers both qualitative and

quantitative information on many physical properties including grain size, topography, and surface roughness. AFM is operated in two basic modes, contact and tapping. In the contact mode, the AFM tip is in continuous contact with the surface. In contrast, in the tapping mode, the AFM cantilever is vibrated above the sample surface such that the tip is only in intermittent contact with the surface. The contact mode is only used for specific applications, such as force curve measurements. The tapping mode is commonly recommended for AFM imaging.

In our work, 3D images on surface topographies and surface roughness were measured using a Bruker Nano GmbH AFM operating in the tapping mode. The surface profiling and features of as-deposited films and alloy bulks were checked before the fine structural characterization by EBSD and before the mechanical characterization by nanoindentation.

II.2.1.3 X-ray diffraction analyses

The principle of X-ray diffraction is based on Bragg's law: $2d_{hkl} \sin \theta = n\lambda$, where the variable d_{hkl} is the interplanar distance, the variable θ is the angle between the incident beam and the diffracting atomic planes, the variable λ is the wavelength of the incident X-ray beam and n is an integer. This law expresses a X-ray wave interference phenomenon, commonly known as X-ray diffraction (XRD), and is a direct evidence for the periodic atomic structure of crystals.

In the present work, the classic $\theta/2\theta$ Bragg-Brentano diffractograms were performed using a Bruker D8 Advance XRD system with Cu-K α_1 radiation ($\lambda_{K\alpha_1} = 0.154060$ nm) and working power fixed at 40 kV and 40 mA. Through identification of position for each reflection peak, the phase composition in the alloy bulks can be known. However, due to the strong crystallographic texture of the as-deposited alloy films along the growth direction, the peak broadness (related to the nanogained microstructure of films) and the very close d-spacing of the multiple phases (α , β , α'') co-existing in our films, additional θ - 2θ scans for different χ inclinations (angles of the sample surface normal with respect to the diffraction vector) were performed in order to look for specific ($h k l$) reflections to identify properly the present phases in the films. For these additional measurements a four-angle diffractometer was required. In the present thesis, the Rigaku SmartLab 5 circle X-rays diffraction system was used with Cu-K α_1 radiation and working power fixed at 40kV and 50mA. Besides, omega scanning is an efficient way to get the information about the misorientation of crystalline planes from a same family in the film. During the measurements, the X-ray source and the detector are fixed and the sample is tilted. The width of the peak around the ideal position

$(2\theta/2)$ of the peak reveals how disperse is the orientation of the corresponding planes: a perfect crystal produces a very narrow and shape peak, and a wide peak indicates a large dispersion.

In a polycrystalline material, the crystallographic orientation of the grains can be distributed randomly with respect to each other, or they can be oriented to a certain preferential direction. If there is a preferred orientation, then we say that the material has a crystallographic texture. The preferred crystalline orientation, or texture, is a fundamental property of a polycrystalline film. Many important physical properties such as magnetic, mechanical, and electrical properties of films depend on the developed texture. There are several ways for representing texture, like pole figure (PF), inverse pole figure (IPF) and orientation distribution function (ODF), those can be transformed mutually into another. In the thesis work, in-plane pole figure measurements were employed for characterizations of textures in our films by XRD on Rigaku SmartLab system using Cu- $K_{\alpha 1}$ radiation at 40kV and 50 mA.

Pole figure measurement is an XRD measurement technique where the detector is fixed at a particular 2θ position for the lattice plane of interest, scattering vector represents the normal vector of the diffracted lattice planes, and the diffracted intensity is collected by varying two geometrical parameters, such as the α angle (tilt angle of scattering vector from sample surface normal direction, $0^\circ - 90^\circ$) and the β angle (ϕ rotation angle of scattering vector around sample surface normal direction, $0^\circ - 360^\circ$), resulting in data collection of an entire hemisphere of reciprocal space (Fig. II-13a). In-plane pole figure measurement is a pole figure measurement performed using the in-plane arm, as shown in Fig. II-13b. It is possible to control the α , β , 2θ angles by the combination of four axes: $2\theta_\chi$, ϕ , 2θ and ω , where χ is fixed to 0 all through the measurement [10]. In particular, the control of α axis is equivalent of the tilt angle of sample. Due to the geometrical constraint, 2θ is generally applied below 90° .

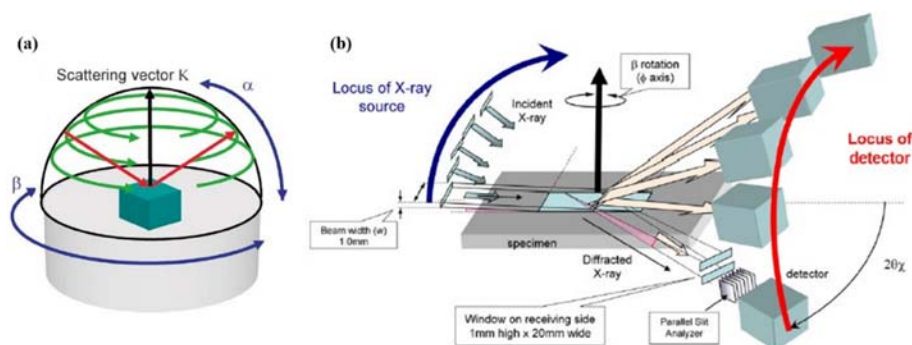


Fig. II-13 (a) Schematic illustration of pole figure measurement [10] and (b) Goniometer motion for in-plane pole figure measurement [11].

The In-plane pole figure measurement has two advantages. First, this method allows a

complete pole figure to be recorded from $\alpha = 0^\circ$ to $\alpha = 90^\circ$ because the goniometer used can detect diffraction lattice planes perpendicular to the sample surface (in-plane diffraction). Second, this method does not require the sample to be tilted. The sample is only rotated about the φ axis, maintaining a horizontal condition in the case of a horizontal sample goniometer.

The recorded diffracted intensity distribution of in-plane pole figures is plotted as a function of α and β . Fig. II-14 demonstrates the definition of α and β . These two parameters can be compared to the latitude and longitude of the Earth, respectively. In general, the center of the pole figure is defined as $\alpha = 0^\circ$ and the outer end is defined as $\alpha = 90^\circ$. $\alpha = 0^\circ$ means that the scattering vector is parallel to the sample surface normal, and denotes the condition for classic θ - 2θ measurements, and $\alpha = 90^\circ$ means that the scattering vector is perpendicular to the sample surface normal. Rotation angle β is relative to a certain reference position, such as the top of the figure, and is circularly coordinated with a counter clockwise rotation.

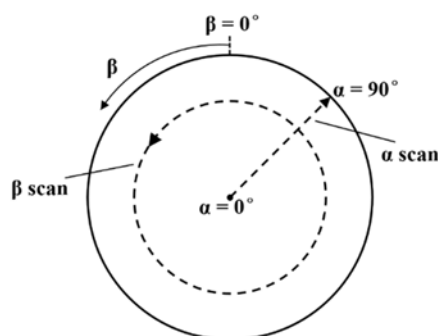


Fig. II-14 Definition of α and β in in-plane pole figures [10].

II.2.1.4 Electron microscopy and analyses

Morphological and microstructural analyses were carried out on a JEOL JSM 6400 SEM operated at 10 kV. The cross-sectional specimens were freshly cut just before inserting into the SEM chamber. The film thicknesses were measured from the cross-section SEM image. The chemical compositions of bulks, alloy targets and films were assessed by energy dispersive X-ray spectroscopy (EDS) coupled with the SEM.

Electron backscatter diffraction (EBSD) is to correlate Kikuchi bands generated from individual grains of a material to their crystal structure and their orientation. It is an extremely useful analytical approach to analyzing microstructure in the following three aspects: (a) grain size of materials and crystal orientation, (b) texture in microstructure and its relationship with individual grains, and (c) grain boundary misorientation [12]. EBSD analyses were conducted to characterize the grain size and the texture of bulks in SEM equipped with an Oxford HKL EBSD system. The specimen preparations for bulks follow the same procedures and

parameters of electrochemical polishing method as described in section II.2.2.1. Note that no Kikuchi bands can be observed in our films probably mainly because of the so fine nanograined structure.

TEM analyses were performed on the plane-view and cross-sectional specimens of films with a JEOL 2100 microscope operating at 200 kV. Conventional TEM analyses were performed to characterize the very fine nanograined microstructure of films and their phase compositions, through bright-field (BF) imaging, dark-field (DF) imaging and selected area electron diffraction (SAED). Plane-view TEM specimens were obtained by depositing a ~30 nm thick layer on a Cu TEM grid. Cross-sectional TEM specimens were treated in procedures as shown in Fig. II-15 [13]: cut two small pieces of film/substrate using a sharp diamond pensile, glued them together film-to-film using a Gatan epoxy resin (10:1 ratio of epoxy resin to epoxy hardener), sliced it normally to the film-film layer into 600 μm wide \times 3 mm long using a diamond wire saw (WELL 3241) in Fig. II-16a, mounted onto a stub of Pyrex using Gatan mounting wax and mechanically polishing the cross-sectional surface to a thickness of 30-50 μm with a tripod polisher, centered and then stuck the thin foil specimen on a TEM Cu ring, final thinning by ion milling to electron transparency with a PIPS II Gatan precision ion-polishing system in Fig. II-16b.

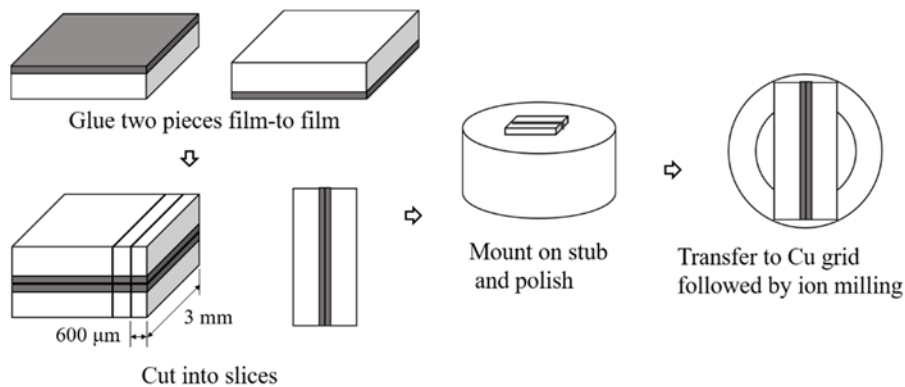


Fig. II-15 A schematic illustration for the preparation of cross-sectional TEM specimen.

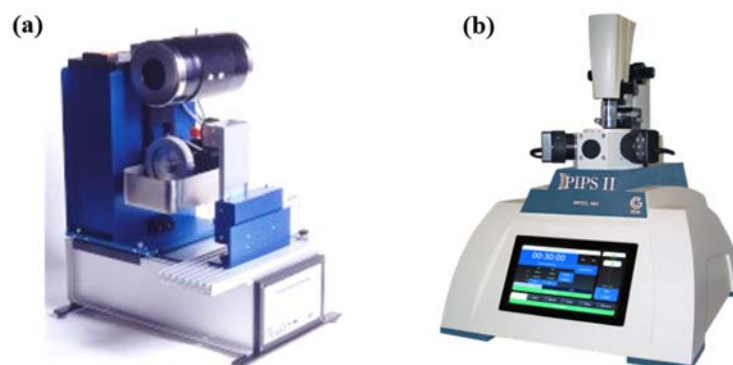


Fig. II-16 (a) Diamond wire saw WELL 3241; (b) PIPS II System Precision ion polishing system.

II.2.2 Mechanical characterization

II.2.2.1 Tensile tests

The mechanical properties and the superelasticity of alloy bulks were characterized by conventional tensile tests (single loading) and cyclic loading-unloading tensile tests with the constant strain rate of 10^{-4} s^{-1} on INSTRON 3369 tensile machine shown in Fig. II-17. For cyclic tests, the tensile strain was incremented by steps of 0.5% for each loading and the stress was completely released for each unloading. An extensometer was employed to record the real strain. Normalized flat tensile specimen with gauge dimensions of $3 \times 15 \times 0.5 \text{ mm}$ were used, as shown in Fig. II-18. The tension direction is parallel to the cold rolling direction.

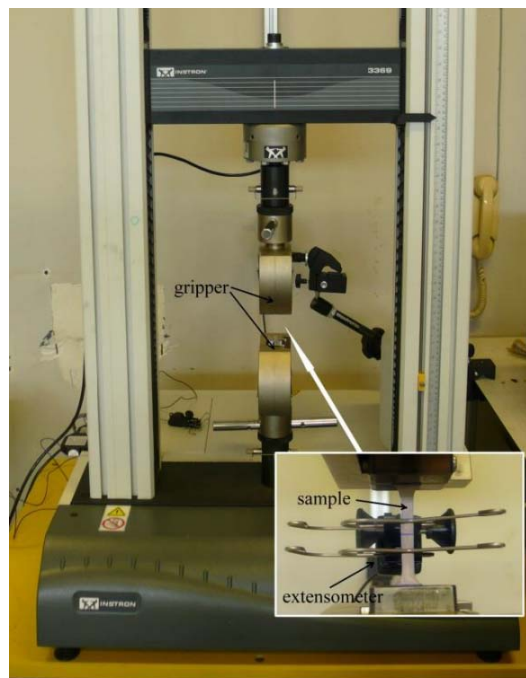


Fig. II-17 Tensile test machine (INSTRON 3369) [14].

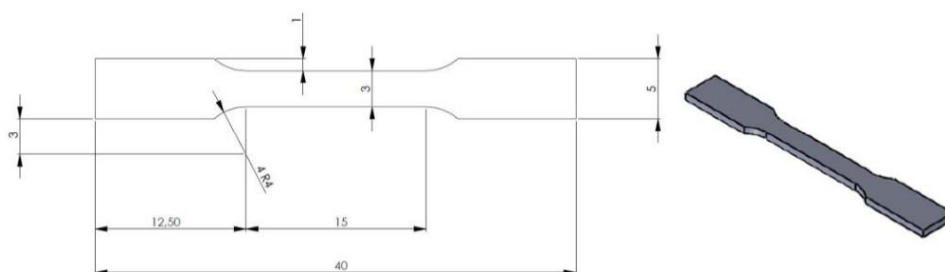


Fig. II-18 The gauged dimensions of the specimens for tensile test [15].

The superelasticity evaluated by the magnitude of recoverable strain on every cycle of cyclic tensile tests. Fig. II-19 shows one loading-unloading cycle from a cyclic tensile curve

for which the total applied strain can be decomposed as follows: the elastic recoverable strain ϵ_e , the superelastic recoverable strain due to the reversible SIM transformation ϵ_{se} and the residual strain after discharge ϵ_{res} [16]. Note that the recoverable strain ϵ_{rec} commonly used to characterize the superelasticity is the sum of pure elastic strain and superelastic strain: $\epsilon_{rec} = \epsilon_e + \epsilon_{se}$.

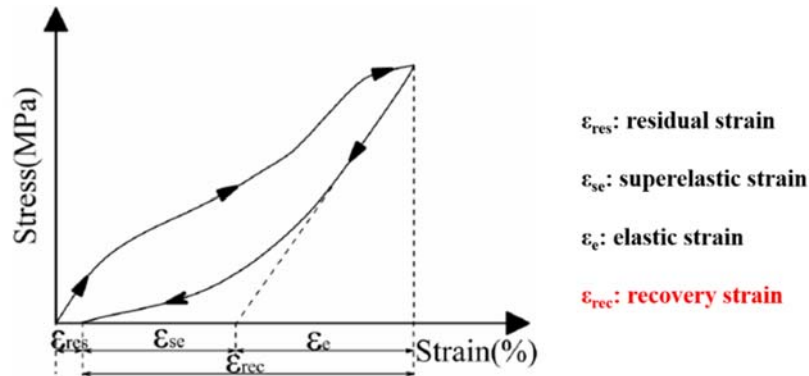


Fig. II-19 Illustration of one loading-unloading cycle from a cyclic tensile curve to interpret different strains occurring during deformation of superelastic alloys.

II.2.2.2 Nanoindentation

Nanoindentation is considered as a suitable and efficient technique to characterize the locally nanoscale deformation behavior and mechanical properties of materials because of its ability for characterizing mechanical response of small volume materials. In the present thesis, nanoindentation technique was used to characterize the local mechanical properties and superelastic responses of alloy films and bulks at the sub-micrometer scale. The Anton Paar TriTec mechanical platform, shown in Fig. II-20, combines multiple systems for surface and mechanical characterizations which are organized as follows (from the left to the right): the scratch test machine, the instrumented Nano Hardness Tester (NHT), the confocal microscope, the AFM microscope and optical microscope.



Fig. II-20 Anton Paar TriTec mechanical platform for surface and mechanical characterizations.

Load controlled nanoindentation tests were performed along the surface normal direction of alloy films and bulks with the instrumented NHT system, at room temperature. For alloy films, the penetration depth was kept in the first 10% of the film thickness to minimize the influence of the substrate material in the characterization of superelasticity.

Nanoindentation refers to a depth-sensing indentation (DSI) technique, with high-resolution load control and precise indent location [17]. Depth sensing indentation technique is widely recognized as one of the most common method for testing thin film and surface mechanical properties at micrometer or nanometer scale. During a nanoindentation experiment an external load applied to the indenter tip enables the tip to be pushed into the sample creating a nanoscale impression on the surface. Unlike conventional indentation or microindentation tests where the analysis uses optical imaging of the indentation impression, instrumented nanoindentation methods continuously record the load, displacement, and time as the indenter is pressed into and removed from the sample, resulting in a load-displacement curve. Analysis of these data is then used to obtain the mechanical properties of the sample without using optical imaging of the indentation impression. The NHT system includes a loading system for which the continuous applied force is controlled via an electrostatic actuator and the displacement of the indenter is continuously measured via a capacitive sensor. Load-displacement curves provide a lot of information about the elastic modulus, hardness, small scale deformation processes. To illustrate the related parameters used for the data analysis, a schematic representation of the load versus indenter displacement ($F-h$ curve) and a schematic representation of a section through an indentation impression showing quantities used for the analysis are presented in Fig. II-21.

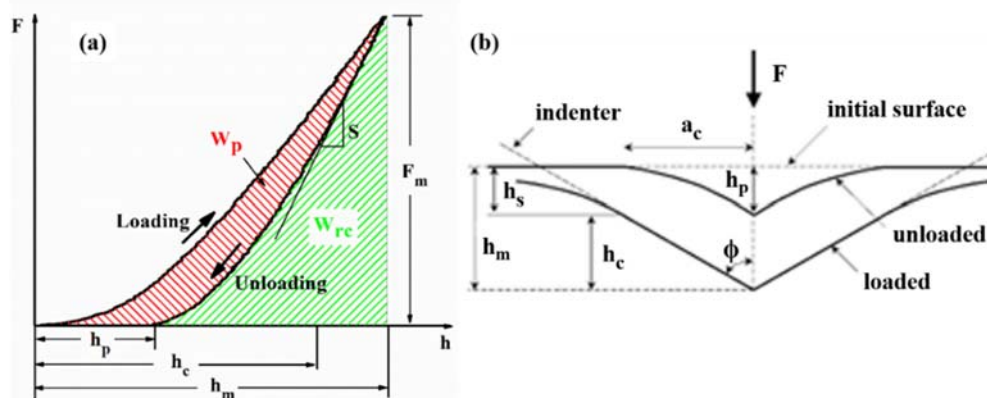


Fig. II-21 Schematic representations of various parameters used for the analysis by (a) Nanoindentation $F-h$ curve and (b) a schematic indentation process [17].

In the case of superelastic alloys, it is recognized that recoverable depth after nanoindentation test, which is defined as the difference between h_{max} , the depth at maximum

load (F_{\max}), and h_p , the permanent depth upon complete unloading (Fig. II. 21a), is associated with the sum of usual elastic recovery and superelastic recovery [18, 19]. Ma et al. [20] firstly used nanoindentation experiments in films to reveal the nanoscale superelasticity of NiTi films. The hysteresis loop of load-displacement indentation cycles was interpreted as the result of the occurrence of reversible and stress-induced martensitic phase transformation (i.e. superelastic behavior). Wood and Clyne [21] demonstrated that nanoindentation, using the remnant depth ratio (unloaded depth /peak depth) as a detection parameter, was suitable for local testing whether or not superelastic deformation was occurring in NiTi alloys. To characterize the superelastic effect in the present thesis work, the recovery ratio under nanoindentation is evaluated from the force-displacement curve by measuring the depth recovery ratio η_h and work recovery ratio η_w following the relations [22]:

$$\eta_h = \frac{h_m - h_p}{h_m} \quad (\text{II} - 1)$$

$$\eta_w = \frac{W_{rc}}{W_t} = \frac{\int_{h_p}^{h_m} F \cdot dh}{\int_0^{h_m} F \cdot dh} \quad (\text{II} - 2)$$

The total energy W_t is the sum of W_p and W_{rc} , and is represented by the area enclosed by the loading curve and the maximum penetration depth. The integration is performed along the loading curve. The recoverable work W_{rc} is represented by the area enclosed by the unloading curve and the maximum penetration depth, as indicated by green slashed line. The integration is performed along the unloading curve. The value of W_{rc} represents the capability of a superelastic material to absorb the deformation energy during indentation without damage [23]. Dissipated work W_p is represented by the area enclosed by the loading curve and unloading curve, as indicated by the red slashed line. The value of W_p represents the dissipated energy due to the plastic deformation and the reversible movement of austenite/martensite boundaries (i.e., internal friction) during nanoindentation experiment.

It is commonly accepted that higher the recovery ratio, the greater the superelastic effect [18, 19]. Based on the studies of Liu et al. [23], Ni et al. [22], Achache et al. [24, 25] and Yang et al. [26], the work recovery ratio and depth recovery ratio extracted from indentation load-displacement ($F-h$) curves were able to display the superelastic effect in alloy bulks and films. The higher values of work and depth recovery ratios especially during spherical indentations reflected the greater capability of the material to accommodate deformations and to behave more superelastically.

In the present thesis work, four indenters with different geometries were used: three spherical diamond indenters with tip radii of 10 μm (Sp10), 50 μm (Sp50) and 200 μm (Sp200) and a modified Berkovich diamond tip ($\alpha \approx 65.31^\circ$), in order to study the nanoscale indentation behavior of superelastic films through different deformation regimes. There is a special interest in indenting with different indenter geometries for characterizing the superelasticity, because not all geometries developed strain states that predominantly induced the martensitic phase transformation. Finite element method (FEM) simulations of the evolving strain fields under conical tip (which is considered to represent a good approximation to the Berkovich tip) and under spherical tip showed that peak strain levels are much higher under Berkovich indenter [21]. Different indenter geometries make material exhibits different indentation responses. Nanoindentation experiment generates complex loading conditions necessitating considerable care in the interpretation of the nanoindentation responses. It is necessary to clarify which tip geometries and loading conditions are suitable to probe superelastic recovery.

According to Oliver-Pharr model [17], indentation hardness and modulus can be deduced from the nanoindentation $F-h$ curves. The parameters needed to determine hardness and modulus are also schematically shown in Fig. II-21. The indentation hardness H_{IT} is defined as the load divided by the projected contact area A_p .

$$H_{IT} = \frac{F_m}{A_p} \quad (\text{II} - 3)$$

Note that because this definition of hardness is based on the contact area under load, it may deviate from the traditional hardness measured from the area of the residual hardness impression if there is significant elastic/superelastic recovery during unloading. The indentation modulus of the specimen is determined by:

$$E_{IT} = \frac{1 - \nu_s^2}{(1/E_r) - ((1 - \nu_i^2)/E_i)} \quad (\text{II} - 4)$$

where ν_s is Poisson's ratio of the specimen, ν_i and E_i are respectively Poisson's ratio and the elastic modulus of the indenter. For the diamond indenter, $\nu_i = 0.07$, $E_i = 1141$ GPa. E_r is the reduced elastic modulus calculated through the relation:

$$E_r = \frac{\sqrt{\pi}}{2\beta} \frac{S}{\sqrt{A_p}} \quad (\text{II} - 5)$$

where β is a constant that determined by the geometry of the indenter, S is the contact stiffness,

and A_p is the projected contact area function. $\beta = 1$ for a spherical indenter, and $\beta = 1.034$ for a Berkovich indenter [17]. The contact stiffness S is the experimentally measured stiffness of the upper portion of the unloading curve, $S = dF/dh$. This relationship holds for any indenter that can be described as body of revolution of a smooth function and is thus not limited to a specific geometry. The projected contact area function A_p is a key parameter for the determination of indentation hardness H_{IT} and elastic modulus E_{IT} . The contact area function is a critical quantity to evaluate, especially in nanoindentation tests with pyramidal indenters, where the influence of the blunted indenter tip can be very important, especially for small displacements. The projected contact area function A_c , also commonly called the indenter shape function, must carefully be calibrated by independent measurements so that geometrical imperfections of the real shape of indenters, i.e., the tip bluntness, are taken into considerations, and thus is described as:

$$A_p = \sum_{n=0}^6 C_n (h_c)^{2-n} = C_0 h_c^2 + C_1 h_c + C_2 h_c^{1/2} + \dots + C_8 h_c^{1/16} \quad (\text{II} - 6)$$

where C_0 - C_6 are geometrical constants determined by the indenter calibration procedure, and h_c is the contact depth defined as the vertical distance along which contact is made between the indenter and the specimen at maximum load F_m :

$$h_c = h_m - \epsilon \frac{F_m}{S} \quad (\text{II} - 7)$$

where ϵ is the geometric constant: $\epsilon = 0.72$ for a Berkovich indenter and $\epsilon = 0.75$ for a spherical indenter [27]. The contact penetration depth h_c changes according to the predominant deformation mode. Oliver and Pharr suggested in their model a sink in deformation mode.

To determine the C_0 - C_6 constants, nanoindentation measurements over a wide range of depths are performed on fused silica and fitted in Oliver & Pharr formula. Table II-3 presents the C_0 - C_6 constants for Sp200, Sp50, Sp10 and Bkv indenters.

Table II-3 C_0 - C_6 constants for the four tips used in the present study

Indenters	C_0	C_2	C_3	C_4	C_5	C_6
Sp200	24.5	-1.23E5	2.27E7	-2.82E8	7.79E8	-5.25E8
Sp50	24.5	5.49E4	1.21E6	-8.07E6	7.61E6	
Sp10	24.5	6.81E4	-4.33E6	5.13E7	-1.31E8	8.36E7
Bkv	24.5	-1.57E4	2.41E6	-3.17E7	8.94E7	-6.09E7

References:

- [1] A. Morita, H. Fukui, H. Tadano, S. Hayashi, J. Hasegawa, M. Niinomi, Alloying titanium and tantalum by cold crucible levitation melting (CCLM) furnace, *Materials Science and Engineering: A*, 280 (2000) 208-213.
- [2] M. Besse, Elaboration et caractérisation d'alliages à base de titane de type Gum Metals en vue d'adapter leurs propriétés superélastiques aux applications biomédicales, PhD thesis, INSA de Rennes, 2010.
- [3] G. Bräuer, 4.03 - Magnetron Sputtering, in: S. Hashmi, G.F. Batalha, C.J. Van Tyne, B. Yilbas (Eds.) *Comprehensive Materials Processing*, Elsevier, Oxford, 2014, pp. 57-73.
- [4] T. Jörg, Oxidation and wet etching behavior of sputtered ternary molybdenum alloy thin films, PhD thesis, Montanuniversität Leoben, Austria, 2014.
- [5] O. Baranov, M. Romanov, M. Wolter, S. Kumar, X.X. Zhong, K. Ostrikov, Low-pressure planar magnetron discharge for surface deposition and nanofabrication, *Physics of Plasmas*, 17 (2010) 053509.
- [6] P.H. Mayrhofer, Materials science aspects of nanocrystalline PVD hard coatings, PhD thesis, Montanuniversitaet Leoben, Austria, 2001.
- [7] X. Wen, Q. Zhang, Z. Shao, Magnetron sputtering for ZnO: Ga scintillation film production and its application research status in nuclear detection, *Crystals*, 9 (2019) 263.
- [8] P. Martin, Introduction to surface engineering and functionally engineered materials, John Wiley & Sons, 2011.
- [9] H. Guo, J. Zhang, F. Li, Y. Liu, J. Yin, Y. Zhou, Surface strengthening of Ti_3SiC_2 through magnetron sputtering Cu and subsequent annealing, *Journal of the European Ceramic Society*, 28 (2008) 2099-2107.
- [10] K. Nagao, E. Kagami, X-ray thin film measurement technique VII. Pole figure measurement, *The Rigaku Journal*, 27 (2011).
- [11] K. Inaba, S. Kobayashi, Various pole figure measurement techniques with Smartlad, assisting thin film characterization, *The Rigaku Journal*, 34 (2018).
- [12] M. Yan, Microstructural characterization of as-sintered titanium and titanium alloys, in: M. Qian, F.H. Froes (Eds.) *Titanium Powder Metallurgy*, Butterworth-Heinemann, Boston, 2015, pp. 555-578.
- [13] L. Weaver, Cross-section TEM sample preparation of multilayer and poorly adhering films, *Microscopy Research and Technique*, 36 (1997) 368-371.
- [14] F. Sun, Alliages nanostructurés : à base d'aluminium et des beta-métastables à base de titane, PhD thesis, INSA de Rennes, 2009.
- [15] E. Bertrand, Elaboration et caractérisation d'alliages biocompatibles Ti-Ta-Nb présentant des propriétés superélastiques et à mémoire de forme, PhD thesis, INSA de Rennes, 2011.
- [16] T. Grosdidier, M.-J. Philippe, Deformation induced martensite and superelasticity in a β -metastable titanium alloy, *Materials Science and Engineering: A*, 291 (2000) 218-223.
- [17] W.C. Oliver, G.M. Pharr, Measurement of hardness and elastic modulus by instrumented indentation: Advances in understanding and refinements to methodology, *Journal of Materials Research*, 19 (2004) 3-20.
- [18] R.D. Dar, Y. Chen, Nanoindentation studies of small-scale martensitic transformations and ductile

precipitate effects in dual-phase polycrystalline shape memory alloys, *Acta Materialia*, 91 (2015) 112-127.

[19] W. Ni, Y.-T. Cheng, D.S. Grummon, Microscopic superelastic behavior of a nickel-titanium alloy under complex loading conditions, *Applied Physics Letters*, 82 (2003) 2811-2813.

[20] X.-G. Ma, K. Komvopoulos, Pseudoelasticity of shape-memory titanium–nickel films subjected to dynamic nanoindentation, *Applied Physics Letters*, 84 (2004) 4274-4276.

[21] A.J.M. Wood, T.W. Clyne, Measurement and modelling of the nanoindentation response of shape memory alloys, *Acta Materialia*, 54 (2006) 5607-5615.

[22] W. Ni, Y.-T. Cheng, D.S. Grummon, Microscopic shape memory and superelastic effects under complex loading conditions, *Surface and Coatings Technology*, 177-178 (2004) 512-517.

[23] R. Liu, D.Y. Li, Y.S. Xie, R. Llewellyn, H.M. Hawthorne, Indentation behavior of pseudoelastic TiNi alloy, *Scripta Materialia*, 41 (1999) 691-696.

[24] S. Achache, S. Lamri, M.A.P. Yazdi, A. Billard, M. François, F. Sanchette, Ni-free superelastic binary Ti-Nb coatings obtained by DC magnetron co-sputtering, *Surface and Coatings Technology*, 275 (2015) 283-288.

[25] S. Achache, S. Lamri, A. Alhussein, A. Billard, M. François, F. Sanchette, Gum Metal thin films obtained by magnetron sputtering of a Ti-Nb-Zr-Ta target, *Materials Science and Engineering: A*, 673 (2016) 492-502.

[26] J. Yang, M. Baatarsukh, J. Bae, S. Huh, H. Jeong, B. Choi, T. Nam, J. Noh, Phase stability and properties of Ti-Nb-Zr thin films and their dependence on Zr addition, *Materials*, 11 (2018) 1361.

[27] W.C. Oliver, G.M. Pharr, An improved technique for determining hardness and elastic modulus using load and displacement sensing indentation experiments, *Journal of Materials Research*, 7 (1992) 1564-1583.

Chapter III : Characterization of the superelasticity and mechanical properties of the Ti-20Zr-3Mo-3Sn bulk alloy at the grain scale by nanoindentation

III.1 Introduction

Crystal orientation, and thus crystallographic texture, is known to be one of the important factors influencing mechanical properties and superelastic responses of Ti alloys [1-6]. A good understanding of orientation-dependent mechanical response in superelastic Ti alloys is highly desirable to determine preferential structural features to approach the optimum performance for a specific application. The uniaxial deformation behavior of single crystals of metastable β Ti alloys was studied during tensile tests carried out along the three main directions of the bcc crystal structure [7]. The results display a clear crystallographic anisotropy of the mechanical responses: (i) regarding superelasticity, crystals along the $\langle 101 \rangle_{\beta}$ direction provide the highest recoverable strain and crystals along $\langle 111 \rangle_{\beta}$ the lowest one during tensile testing, (ii) the lowest elastic modulus is observed along the $\langle 001 \rangle_{\beta}$ direction and the highest one along $\langle 111 \rangle_{\beta}$. To broaden these experimental studies over all possible crystallographic directions of loading in the bcc β -crystal structure, many different oriented single crystals would be necessary. The cost and difficulty of producing single crystals with many different and defined crystal orientations, for macroscale mechanical testing prohibit extensive testing programs [8]. Over the last decade, micro- and nanoscale mechanical testing, including mostly micropillar compression tests and nanoindentation tests have become more widely employed in order to understand the local mechanical response of materials [9-14]. If smaller scale tests are employed, one could use a large-grained polycrystalline material to test a wide variety of orientations.

Nanoindentation is a suitable tool for the characterization of mechanical behavior of materials at micrometer or nanometer scale [15-22]. Recently, nanoindentation has been also used to investigate the superelastic effect [23-28]. When the nanoindentation platform is coupled with optical microscopy, the targeted indent locations can be chosen visibly and precisely [11]. As such, a large number of nanoindentations can be performed on individual grains with a wide variety of crystal orientations in polycrystalline materials, which is particularly feasible to investigate the anisotropic property of polycrystalline materials at grain scale [10, 29]. The information on anisotropic performance of the superelasticity, hardness and elastic modulus at grain scale can be of great interest to understand and predict the influences of texture on the macroscopic properties of engineering alloys. However, only a few concerned studies exist in literature.

The present study focuses on the polycrystalline metastable β -type Ti-20Zr-3Mo-3Sn

alloy (at.%; abbreviated as Ti2033). It was reported that a high strain recovery of 3.5% was obtained by tensile testing after solution-treated at 700 °C for 30 min, and the effect of texture on the superelasticity of Ti2033 has been studied during macroscale tensile test experiments [30].

In the present study, the anisotropic indentation responses in Ti2033 alloy were studied by the combined application of nanoindentation and electron backscattered diffraction (EBSD) analysis. Through an appropriate thermo-mechanical treatment, large-grained polycrystalline Ti2033 alloy was obtained covering a wide variety of crystal orientations. EBSD orientation mapping was used to identify grain orientations. A large number of nanoindentation measurements were performed on individual grains to explore their superelastic responses (depth recovery ratio η_h and work recovery ratio η_w) and mechanical properties (indentation hardness H_{IT} and indentation modulus E_{IT}). Measured results were presented in the [001]-[101]-[111] standard stereographic triangles based on the inverse pole figure (IPF) in surface normal direction (parallel to the indentation direction), in order to build the distribution maps (η_h - , η_w - , E_{IT} - and H_{IT} - IPF), which could correlate the mechanical properties with the crystallographic orientation of a given individual grain. The aim of the present study was to show the orientation-dependent indentation responses in the β -metastable Ti2033 alloy, with a sufficiently high statistic covering the whole crystallographic orientations.

III.2 Materials and methods

The Ti2033 alloy was synthesized by cold crucible levitation melting (CCLM) technique under argon atmosphere. The synthesized button-shape ingot was then homogenized at 950 °C for 20h under high vacuum (10^{-7} mbar) followed by quenching into water at room temperature (RT). Then, the ingot was cold-rolled to 90% in thickness reduction and subsequently solution-treated at 800 °C for 0.5 h followed by water quenching at RT, so as to retain the metastable β -phase with appropriate grain size and random texture having all possible crystal orientations.

After these series of thermo-mechanical treatments, Ti2033 alloy was subjected to experimental characterizations carried out in the rolling plane. The phase composition was analyzed by x-ray diffraction (XRD) using a Cu $K\alpha$ radiation. The grain structure was observed by optical microscopy and the crystallographic orientations of individual grains were identified by electron backscattered diffraction (EBSD). Individual grains with labeled orientations were located using an optical microscope coupled with the instrumented nanoindentation test system. The grains could be distinguished by the use of a microscope

with polarized light. Load controlled nanoindentation tests were performed along the surface normal direction of selected grains, at room temperature using two types of indenters: a spherical diamond tip with nominal radius of 50 μm (Sp50) and the modified Berkovich diamond tip (Bkv). The two indenters have been calibrated on fused silica. For the present study, each indentation experiment was carried out at a fixed maximum indentation load (F_m) of 60 mN for Sp50 and 10 mN for Bkv indenter. Grain sizes larger than 50 μm and 30 μm for the Sp50 and Bkv indenters, respectively were selected for this work. To minimize the influence of grain boundaries and neighboring grains, nanoindentation tests were limited to the central region of each targeted grains. Depending on the diameter of the targeted grain size, between 3 and 5 nanoindentation tests were conducted in the same grain to check the reproducibility of measurements.

Depth recovery ratio η_h , work recovery ratio η_w , indentation modulus E_{IT} and indentation hardness H_{IT} were measured during nanoindentation (see details in II.2.2.2) in individual grains of the polycrystalline metastable β Ti2033 alloy. By combining EBSD analysis for identifying grain orientations and nanoindentation measurements for exploring elastic and plastic responses of individual grains depending on their orientations, measured data were reported in inverse pole figures that have the advantage of displaying the value distribution of each measured property in a single representation for all possible crystallographic directions of loading. Fig. III-1 summarizes the experimental strategy initiated for the present study.

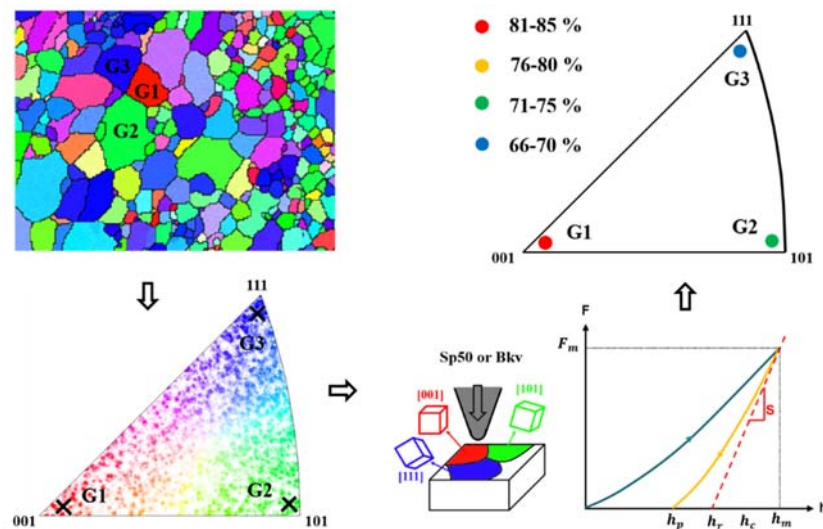


Fig. III-1 Experimental protocol.

In this way, results show a full experimental study of orientation-dependent indentation response in the metastable β Ti2033 alloy covering all crystallographic directions of loading and allowing a full evaluation of changes in superelastic and elastic responses. The values

were scaled in three or four ranges presented by different colors. The color of dots refers to the values and the position of dots in the standard stereographic triangle refers to the crystallographic orientation of the indented grain. As such, the distribution maps (η_h - , η_w - , E_{IT} - and H_{IT} - IPF) were built.

III.3 Results and discussion

III.3.1 Structural characterizations

XRD pattern of solution-treated Ti2033 alloy is shown in Fig. III-2a. The diffraction profile displays the (110), (200), (211), (220) and (310) reflections corresponding to the bcc β -Ti polycrystalline structure. The cyclic tensile stress-strain curve in Fig. III-2b presents the superelasticity in Ti2033 alloy.

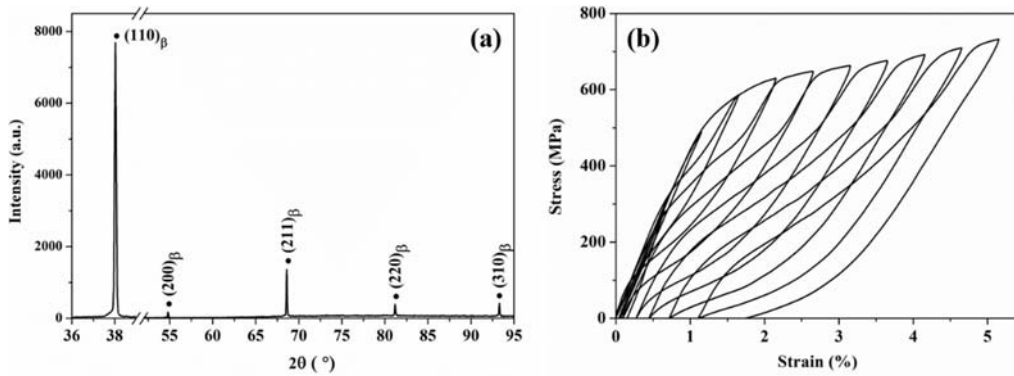


Fig. III-2 (a) XRD profile and (b) tensile stress-strain curve [30] for solution-treated Ti2033 alloy.

EBSDB analysis was carried out to identify the crystallographic orientation of each grain along the surface normal direction over a large area. Prior to EBSD analysis the sample surface was carefully prepared as described in section II.2.2.1 and a low surface roughness (R_a) of 8.4 nm was measured in the region of interest by atomic force microscopy evidencing the high quality surface finish, which is absolutely crucial for the fulfillment of both EBSD analysis and subsequent nanoindentation measurements. Fig. III-3a presents the EBSD orientation map for a selected region of solution-treated Ti2033 alloy in the normal surface direction (ND, parallel to the indentation loading direction) with the corresponding color code. It shows a typical equiaxed β -grain microstructure with average diameter of 70 μm . Fig. III-3b presents the corresponding orientation distribution of surface normal (also nanoindentation loading directions) of individual grains in the standard stereographic triangle for β phase showing a random distribution suggesting a polycrystalline and randomly textured bcc microstructure. The analyzed area consists of several hundreds of grains covering the entire inverse pole figure

(IPF), which allows a substantial study concerning the orientation dependence of the superelastic and mechanical properties during nanoindentation in metastable β Ti2033 alloy. Fig. III-3c shows the optical microstructural morphology where the grains and boundaries are evidently observed to carry out nanoindentation measurements on each individual grains.

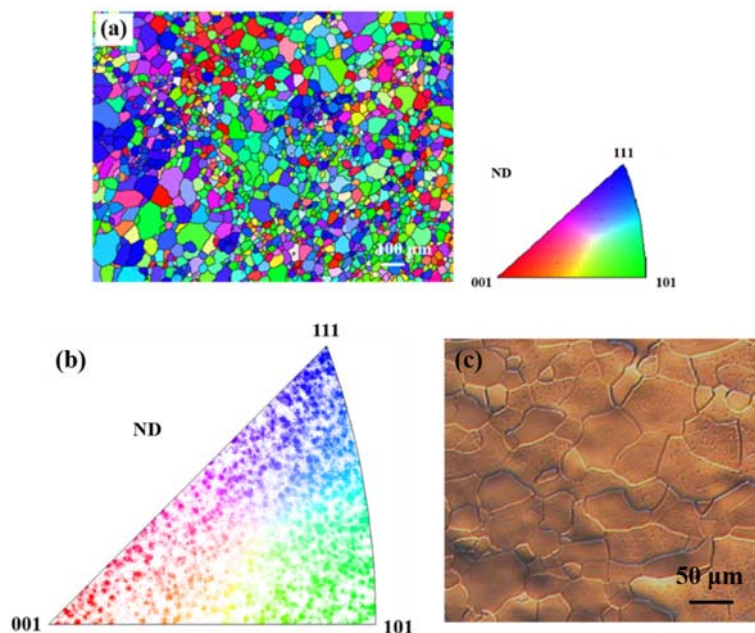


Fig. II-3 (a) EBSD orientation map with the corresponding orientation triangle, (b) inverse pole figures (IPF) along the surface normal direction (ND), and (c) Optical microstructural image prepared by electrochemical polishing in solution treated Ti2033 alloy. ND is also parallel to the indentation loading direction.

III.3.2 Nanoindentation load-displacement curves along the three principal crystallographic directions of β phase

Fig. III-4 shows nanoindentation load-displacement ($F-h$) curves measured into selected grains with surface normal directions close to the three principal directions of β crystal phase: $\langle 001 \rangle_{\beta}$, $\langle 101 \rangle_{\beta}$, and $\langle 111 \rangle_{\beta}$. Typical $F-h$ curves obtained with the spherical Sp50 tip are presented on the Fig. III-4a, and those measured with a Bkv tip on Fig. III-4b. The maximum load was fixed respectively at $F_m = 60$ mN for the Sp50 indenter and at $F_m = 10$ mN for the Bkv indenter, so as to obtain an approximately equivalent maximum indentation depth h_m for both indenters ($h_m \approx 300$ nm). Means values of permanent depth h_p and means values of maximum penetration depth h_m are provided in figures for each principal directions.

$F-h$ curves for the Sp50 indentations clearly show the very high depth-recoveries with low permanent depths $\langle h_p \rangle$ in the range of 55 - 83 nm (Fig. III-4a), when compared to those for the Bkv indentations showing restricted depth recoveries with large $\langle h_p \rangle$ in the range of

198 - 214 nm (in Fig. III-4b). Besides, the F - h curves for the Sp50 indentations show the crystallographic anisotropy of the depth recoverability: the depth-recovery in $\langle 001 \rangle_\beta$ direction is higher than that in $\langle 101 \rangle_\beta$ and $\langle 111 \rangle_\beta$ directions. In contrast, no evident crystallographic anisotropy of depth recoverability was observed in the case of Bkv indenter. In our measurement conditions, i.e. equivalent maximum penetration depth, the Sp50 indenter seems more sensitive to the crystallographic anisotropy of the depth recovery than the Bkv indenter.

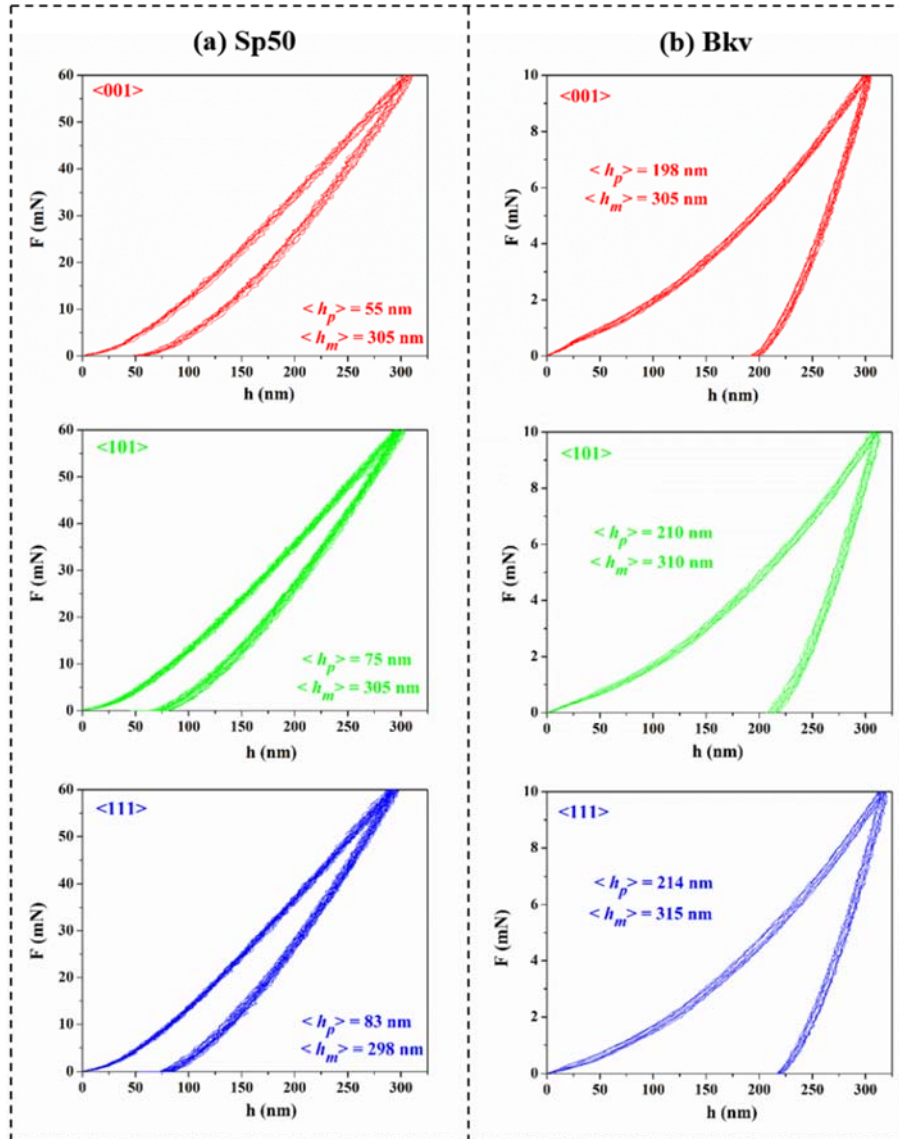


Fig. III-4 F - h nanoindentation curves measured into individual grains for which surface normal directions are close to $\langle 001 \rangle_\beta$, $\langle 101 \rangle_\beta$, and $\langle 111 \rangle_\beta$ crystallographic orientations: (a) with Sp50 indenter at $F_m = 60$ mN and (b) with Bkv indenter at $F_m = 10$ mN.

Fig. III-5 presents the normalized $F/F_m - h/h_m$ nanoindentation curves for which the load raw data F were divided by the maximum applied load F_m and the depth raw data h_m were divided by the maximum indentation depth h_m . This procedure was realized for each loading-unloading nanoindentation curves.

Normalized nanoindentation curves enable a direct reading of η_h values which correspond to the x-intercepts of unloading curves. The work recovery ratio η_w is represented by the area enclosed between the normalized unloading curve, the $y=1$ vertical line and the x axis. Means values of depth recovery ratio $\langle \eta_h \rangle$ and work recovery ratio $\langle \eta_w \rangle$ are provided in Fig. III-5 for both indenters and along each principal crystallographic direction (also the nanoindentation loading direction).

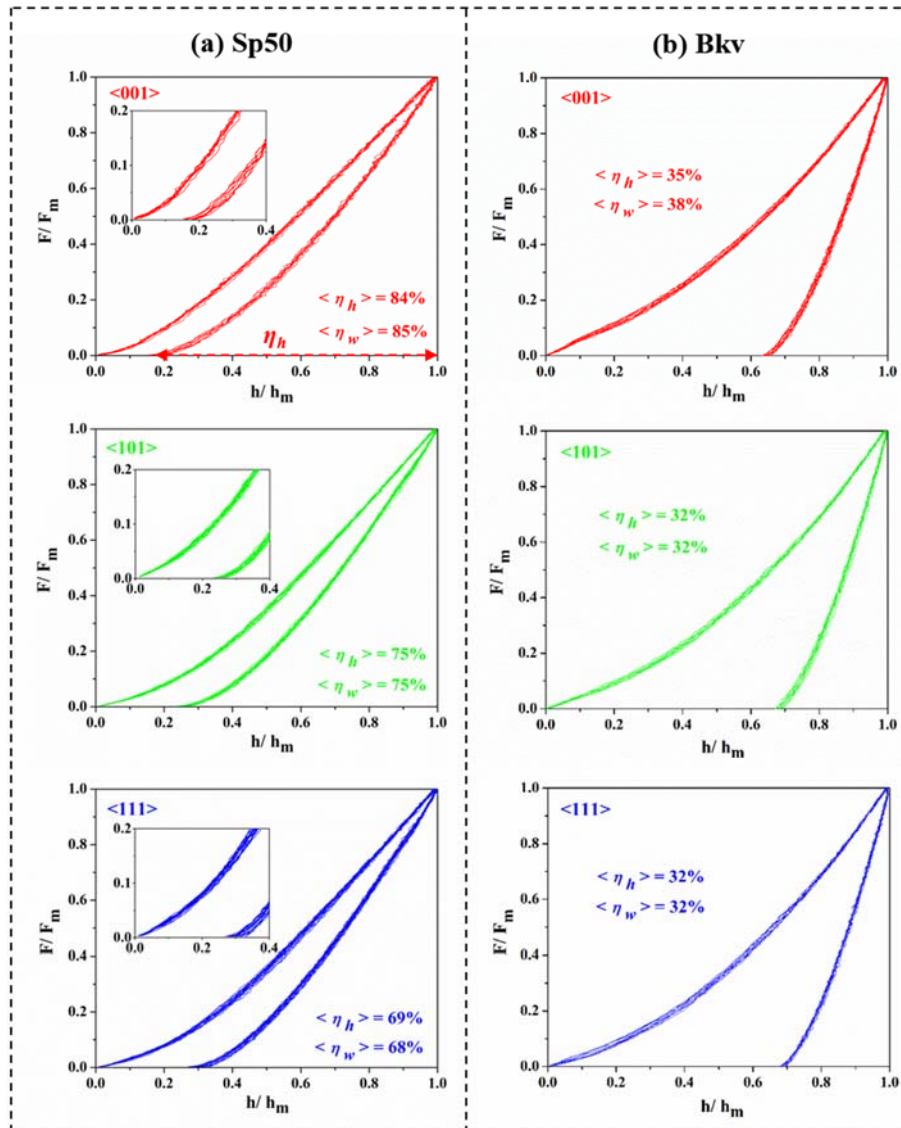


Fig. III-5 Normalized nanoindentation curves ($F/F_m - h/h_m$) corresponding to raw data of Fig. III-4: (a) for Sp50 indenter at $F_m = 60$ mN and (b) for Bkv indenter at $F_m = 10$ mN.

When indenting with the Sp50 indenter, the recoverability is highly dependent on the crystallographic orientation of the indented grain: the η_h and η_w for the grain orientated in the $\langle 001 \rangle_\beta$ direction, noted $\eta_h \langle 001 \rangle$ and $\eta_w \langle 001 \rangle$, have the largest values of 84% and 85%, respectively, as compared to $\eta_h \langle 101 \rangle$ and $\eta_w \langle 101 \rangle$ that present intermediate values of 75% and 75%, and $\eta_h \langle 111 \rangle$ and $\eta_w \langle 111 \rangle$ that display the lowest values of 69% and 68%. This tendency can clearly be seen on close-up views of Fig. III-5a. For the Bkv indenter, recovery ratios are

relatively low (~32%), with no significant orientation-dependence. The characteristic of unloading curves is closely associated with the recoverability and reflects the deformation mechanisms underneath the indenters. Bkv indenter produces sudden large stresses associated with sudden and immediate onset of plasticity causing extremely steep unloading curves [29], whereas the spherical indentations exhibit gentle and soft unloading curves, suggesting the occurrence of strain accommodation by reversible phase transformation.

It is noteworthy that measurements of recoverability (η_h and η_w) by nanoindentation demonstrate high reproducibility. For instance, using Sp50 indenter, the mean values of depth recovery ratio $\langle \eta_h \rangle$ for three principal directions show very small mean standard deviations of 1.04 %, 0.93 %, and 1.38% in Fig. III-5.

III.3.3 Anisotropy of indentation depth and work recovery ratios

To present the crystallographic anisotropy of the superelastic response in β metastable Ti2033 alloy, indentation depth- and work- recovery ratios measured in individual grains with Sp50 and Bkv indenters were reported in a standard stereographic triangle for a large and extended selection of crystallographic loading directions. Fig. III-6 shows $\eta_h - IPF$ and $\eta_w - IPF$ for the Sp50 indenter and the Bkv indenter. As a reminder, the position of each experimental point in stereographic triangle corresponds to the normal direction of the indented grain and its color refers to the measured value according to the provided color scale. Each colored point corresponds to the average of at least 5 measurements. With this representation, it is now clearly observed that η_h and η_w values are indeed influenced by the crystallographic orientation of the loading direction. For both indenters, grains orientated in the $\langle 001 \rangle_\beta$ direction exhibit the largest η_h and η_w values, and then the η_h and η_w values decrease with changing direction from the $\langle 001 \rangle_\beta$ towards the $\langle 101 \rangle_\beta$ and $\langle 111 \rangle_\beta$ directions. Besides, the η_h and η_w values for Sp50 indenter are higher than those for the Bkv indenter in all directions. Specifically, the values of η_h and η_w for the Sp50 indenter vary in the ranges of 66% - 85% and 67% - 86%, respectively, for which the ranges are approximately twice of those for the Bkv indenter varying from 29% to 40% and from 31% to 38%, respectively for η_h and η_w . The larger ranges (Δ (max-min)) of η_h and η_w values obtained with the Sp50 suggest that spherical indentations are more sensitive to the crystallographic loading direction when compared to the Bkv indentations. It is appropriate to conclude that the spherical nanoindentation is capable of characterizing the crystallographic anisotropy of the mechanical response.

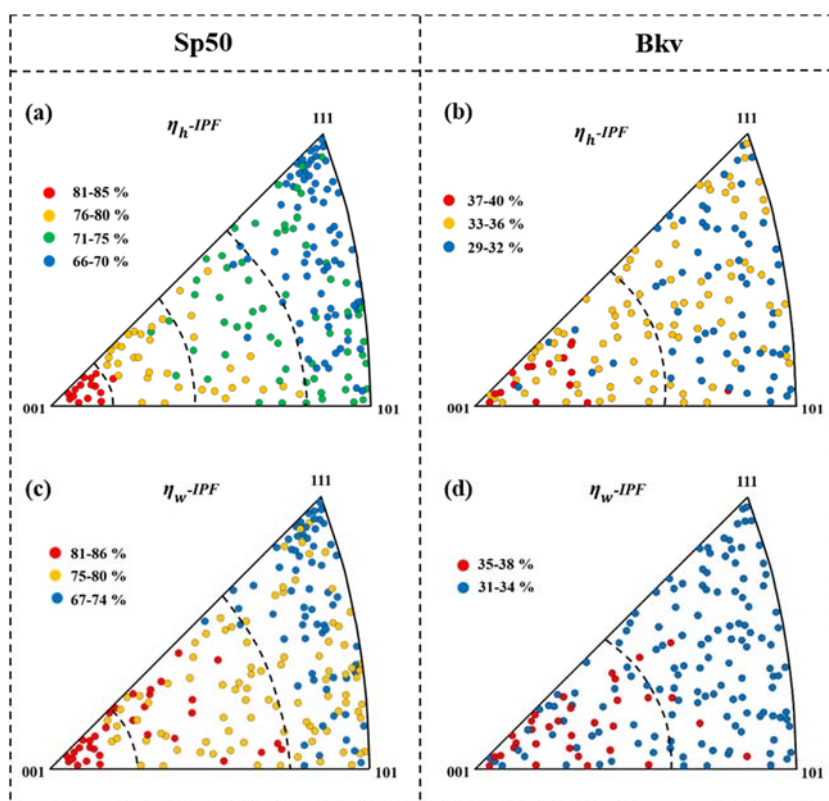


Fig. III-6 η_h - IPF and η_w - IPF measured with: (a, c) Sp50 indenter and (b, d) Bkv indenter.

The different nanoindentation behaviors probed using two different indenters can be explained from two aspects.

Firstly, the difference in the depth- and work- recoverability for the Sp50 indenter and Bkv indenter is strongly related to the geometry of the indenter tips. Indenting with the Sp50 indenter clearly displays higher recoverability, evidencing the superelasticity, whereas Bkv indentations result in more pronounced plastic deformation. The sharp Bkv indenter generates high strain which cannot be accommodated by elastic deformation and stress-induced martensitic transformation (superelastic deformation), so that plastic deformation through dislocation motions is the predominant deformation mechanism under Bkv indenter [31, 32]. At first sight, any noticeable change related to crystal directions in the case of Bkv indentations. At this step, it could be argued that plastic deformation of β phase seems not sensitive to crystallographic direction. This part will be discussed in section III.3.6. The SIM transformation competes with the dislocation motions. The generation of dislocations, on one hand, is not desirable for the occurrence of SIM transformation from β phase to α'' phase, and on the other hand, impedes the reverse transformation from α'' phase to the parent β phase, resulting in a low recoverability. In contrast, the strain field developed underneath the Sp50 indenter is more likely to probe larger martensitic transformation and capture the superelastic nature of metastable β Ti2033 alloy. To conclude on this first aspect, the large difference in the

magnitude of indentation recovery ratios between the spherical and Bkv indenters confirm that the relative amount of elastic and plastic deformation (strain distribution) induced beneath the indenter tip is very different for the two indenter geometries.

Secondly, $\eta_h - IPF$ and $\eta_w - IPF$ obtained with the spherical tip show a wide dispersion in the recovery ratios. Spherical nanoindentation offers a suitable means to probe the anisotropy of depth- and work- recoverability which is attributed to the crystallographic anisotropy of elastic recovery and superelastic recovery. Although recoverable deformation is only due to elastic deformation in conventional materials, while it is expected in superelastic alloys that an additional and important contribution from the stress-induced martensitic transformation participates in the reversible straining. This interpretation will be discussed in the later section.

III.3.4 Theoretical anisotropy of the martensitic transformation strain

The superelastic nature of the polycrystalline Ti2033 alloy is associated with the reversible martensitic transformation between the bcc structure of the parent β phase and the C-centered orthorhombic structure of the stress-induced α'' martensite [30]. In metastable β -Ti alloys, superelasticity is related to the mechanical instability of the metastable β phase. The superelastic part of the reversible straining arises from the strain accommodation during the reversible martensitic transformation. As explained in section I.2.3.1, six lattice correspondence variants can be derived from the orientation relationships: $\{100\}_\beta // (100)_{\alpha''}$, and $\langle 111 \rangle_\beta // [110]_{\alpha''}$, or alternatively $[100]_{\alpha''} - [100]_\beta$, $[010]_{\alpha''} - [011]_\beta$, $[001]_{\alpha''} - [0-11]_\beta$. Fig. III-7 shows six equivalent rotary permutations also called martensite variants V_i ($i = 1$ to 6).

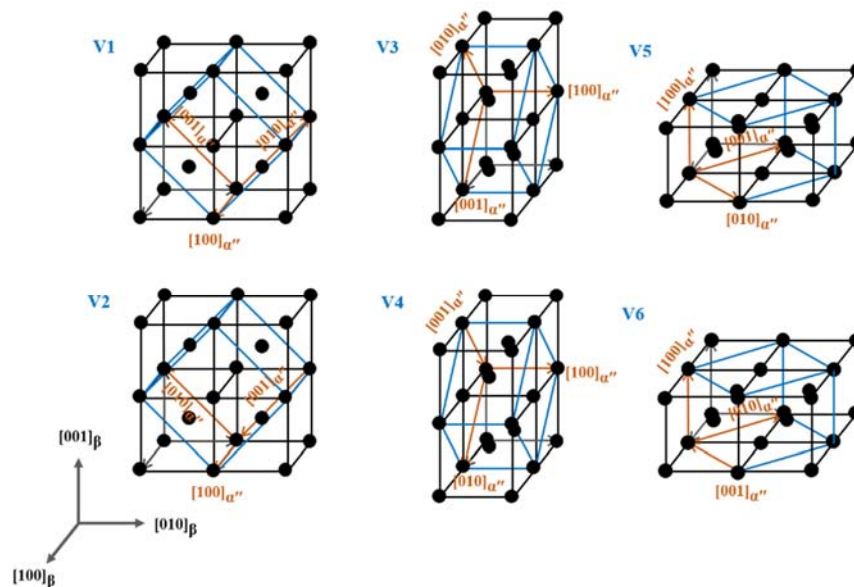


Fig. III-7 Lattice correspondences between the bcc structure of β phase and the six orthorhombic α'' martensite variants.

The superelastic recovery arises from the transformation strain which is driven by the lattice distortions that ensue from the geometric compatibilities between the β crystal and α'' crystal. It is commonly assumed that the variant that would accommodate maximum strain along the loading direction (including compression or tension) would produce maximum driving force for the martensitic transformation and would thus be preferentially formed in each grain [1, 4, 33]. It indicates that the formation of the favorable variants of stress-induced martensite is dependent on the loading direction. It also suggests that superelastic effect is orientation-dependent. The theoretical maximum value of transformation strain which can be obtained along a given crystallographic direction of the β phase is consisted with the maximum lattice deformation strain that can be obtained along this direction.

The transformation strain is associated with the lattice distortion between the bcc structure of β phase and the C-centered orthorhombic structure of α'' phase, and can be calculated using the lattice parameters of β and α'' phases, and their lattice correspondences. The orientation dependence of the theoretical transformation strains related to the six possible martensite variants is presented here for Ti2033 superelastic alloy.

Table III-1 presents the lattice parameters of the β phase (a_β) and α'' phase ($a_{\alpha''}$, $b_{\alpha''}$, and $c_{\alpha''}$) for Ti-Zr-Mo-Sn alloys. The first set of lattice parameters for β and α'' phases were calculated from laboratory XRD analysis of magnetron-sputtered Ti2033 film into which both phases co-exist in the as-deposited state (the details about these results will be presented in chapter V). The second set of lattice constants was measured in Ti2033 alloy bulk by in situ synchrotron XRD measurement during tensile tests [30]. The third set of lattice constants was calculated from laboratory XRD analysis of solution treated (thermal treatment + water quenching) (Ti-Zr)-2Mo-3Sn alloys for which both phases co-exist [34]. Differences between these sets of lattice constants reflect different stress-states. In the present work, the set of lattice parameters measured in the Ti2033 films were used for the theoretical calculations of transformation strain of Ti2033 bulks, because of the same composition and also because the martensite in films was compressively stress-induced in this case which tends more towards indentation loading conditions in bulks.

Table III-1 Lattice parameters for β phase (a_β) and α'' phase ($a_{\alpha''}$, $b_{\alpha''}$, $c_{\alpha''}$) for Ti-Zr-Mo-Sn alloys.

Composition	Lattice parameters (Å)				Formation of α'' -martensite	Ref.
	a_β	$a_{\alpha''}$	$b_{\alpha''}$	$c_{\alpha''}$		
Ti2033 film	3.395	3.219	5.008	4.874	magnetron-sputtered	-
Ti2033 bulk	3.364	3.122	5.104	4.766	Tensile stress-induced	[30]
(Ti-Zr)-2Mo-3Sn	3.435	3.144	5.289	4.896	cooling-induced	[34]

When a given vector X in the coordinates of the parent β phase is transformed to X' due to martensitic transformation (Fig. III-7), the transformation strain of each variant $\varepsilon_{\beta \rightarrow \alpha''}^{(Vi)}$ can be calculated as follows [35, 36]:

$$\varepsilon_{\beta \rightarrow \alpha''}^{(Vi)} = \frac{|X'^{(Vi)}| - |X|}{|X|} \quad (\text{III-1})$$

where $X'^{(Vi)} = T^{(Vi)}X$, and $T^{(Vi)}$ represents the lattice distortion matrix expressed in the coordinates of the parent β phase for each variant Vi . Table III-2 shows the six lattice distortion matrices for each of six lattice correspondence variants. In this way, the lattice distortion strain induced by martensitic transformation $\varepsilon_{\beta \rightarrow \alpha''}^{(Vi)}$ can be expressed for each martensite variant Vi along any X crystallographic direction in the coordinate of β phase.

Table III-2 Lattice distortion matrices $T^{(Vi)}$ for the six α'' martensite variants.

$T^{(V1)} = \begin{pmatrix} \frac{a_{\alpha''}}{a_{\beta}} & 0 & 0 \\ 0 & \frac{b_{\alpha''} + c_{\alpha''}}{2\sqrt{2} a_{\beta}} & \frac{b_{\alpha''} - c_{\alpha''}}{2\sqrt{2} a_{\beta}} \\ 0 & \frac{b_{\alpha''} - c_{\alpha''}}{2\sqrt{2} a_{\beta}} & \frac{b_{\alpha''} + c_{\alpha''}}{2\sqrt{2} a_{\beta}} \end{pmatrix}$	$T^{(V2)} = \begin{pmatrix} \frac{a_{\alpha''}}{a_{\beta}} & 0 & 0 \\ 0 & \frac{b_{\alpha''} + c_{\alpha''}}{2\sqrt{2} a_{\beta}} & \frac{-b_{\alpha''} + c_{\alpha''}}{2\sqrt{2} a_{\beta}} \\ 0 & \frac{-b_{\alpha''} + c_{\alpha''}}{2\sqrt{2} a_{\beta}} & \frac{b_{\alpha''} + c_{\alpha''}}{2\sqrt{2} a_{\beta}} \end{pmatrix}$
$T^{(V3)} = \begin{pmatrix} \frac{b_{\alpha''} + c_{\alpha''}}{2\sqrt{2} a_{\beta}} & 0 & \frac{b_{\alpha''} - c_{\alpha''}}{2\sqrt{2} a_{\beta}} \\ 0 & \frac{a_{\alpha''}}{a_{\beta}} & 0 \\ \frac{b_{\alpha''} - c_{\alpha''}}{2\sqrt{2} a_{\beta}} & 0 & \frac{b_{\alpha''} + c_{\alpha''}}{2\sqrt{2} a_{\beta}} \end{pmatrix}$	$T^{(V4)} = \begin{pmatrix} \frac{b_{\alpha''} + c_{\alpha''}}{2\sqrt{2} a_{\beta}} & 0 & \frac{-b_{\alpha''} + c_{\alpha''}}{2\sqrt{2} a_{\beta}} \\ 0 & \frac{a_{\alpha''}}{a_{\beta}} & 0 \\ \frac{-b_{\alpha''} + c_{\alpha''}}{2\sqrt{2} a_{\beta}} & 0 & \frac{b_{\alpha''} + c_{\alpha''}}{2\sqrt{2} a_{\beta}} \end{pmatrix}$
$T^{(V5)} = \begin{pmatrix} \frac{b_{\alpha''} + c_{\alpha''}}{2\sqrt{2} a_{\beta}} & \frac{b_{\alpha''} - c_{\alpha''}}{2\sqrt{2} a_{\beta}} & 0 \\ \frac{b_{\alpha''} - c_{\alpha''}}{2\sqrt{2} a_{\beta}} & \frac{b_{\alpha''} + c_{\alpha''}}{2\sqrt{2} a_{\beta}} & 0 \\ 0 & 0 & \frac{a_{\alpha''}}{a_{\beta}} \end{pmatrix}$	$T^{(V6)} = \begin{pmatrix} \frac{b_{\alpha''} + c_{\alpha''}}{2\sqrt{2} a_{\beta}} & \frac{-b_{\alpha''} + c_{\alpha''}}{2\sqrt{2} a_{\beta}} & 0 \\ \frac{-b_{\alpha''} + c_{\alpha''}}{2\sqrt{2} a_{\beta}} & \frac{b_{\alpha''} + c_{\alpha''}}{2\sqrt{2} a_{\beta}} & 0 \\ 0 & 0 & \frac{a_{\alpha''}}{a_{\beta}} \end{pmatrix}$

Fig. III-8a shows the coordinate system employed for calculations of transformation strain $\varepsilon_{\beta \rightarrow \alpha''}^{(Vi)}$ along different loading directions belonging to $(1\bar{1}0)_{\beta}$ plane of the β phase. The angle θ denotes the angle between $[001]_{\beta}$ direction and the loading direction. Thus, when

θ is equal to 0° , 54.74° or 90° , the loading direction refers to $[001]_\beta$, $[111]_\beta$, or $[110]_\beta$ crystallographic directions of the β phase, respectively. Fig. III-8b shows the transformation strain $\varepsilon_{\beta \rightarrow \alpha''}^{(Vi)}$, calculated for each variant as a function of θ angle.

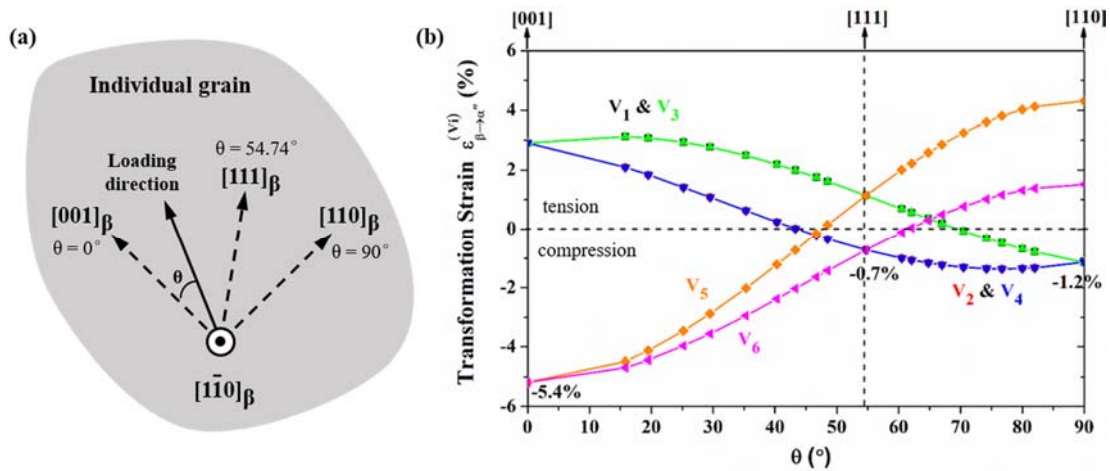


Fig. III-8 (a) Schematic illustration of the coordinate system employed for calculations of transformation strain. The angle θ denotes the angle between the loading direction and $[001]_\beta$ direction of the considered β grain. (b) Transformation strain $\varepsilon_{\beta \rightarrow \alpha''}^{(Vi)}$ of each variant along the indentation direction as a function of θ angle.

The sign of the transformation strain $\varepsilon_{\beta \rightarrow \alpha''}^{(Vi)}$ implies the strain states under which the $\beta \rightarrow \alpha''$ transformation occurs: positive values for tensile strain state and negative ones for compressive strain state. Calculations confirm the strong tension-compression asymmetry of the strain response observed during uniaxial tests in superelastic β titanium textured alloys [37] or single crystals [7]. Similar tendency was observed in NiTi alloys [5, 6, 38]. Asymmetry refers to difference in the magnitude of transformation strain between tension and compression for one loading direction.

More focus is placed on the negative values of $\varepsilon_{\beta \rightarrow \alpha''}^{(Vi)}$ (half- below x-axis) which represents the theoretical compressive strains that can be accommodated during compressive-stress-induced martensitic transformation in Ti2033 alloy. Although nanoindentation test is different as compared to compressive uniaxial tests, it is likely in the same sense that compressive strain field is developed when the indenter is pressed into the material surface. As can be seen from Fig. III-8b, when the compressive loading direction is along the $[001]_\beta$ ($\theta = 0^\circ$), V5 and V6 variants have the largest magnitude of $\varepsilon_{\beta \rightarrow \alpha''}^{(Vi)}$ (5.2%), and thus can be preferentially indentation-induced, showing the potential to obtain a large superelastic

recovery. When the compressive loading direction is along $[111]_{\beta}$ ($\theta = 54.74^{\circ}$) and $[110]_{\beta}$ ($\theta = 90^{\circ}$), the magnitudes of $\varepsilon_{\beta \rightarrow \alpha''}^{(Vi)}$ are comparable at 0.7% and 1.2%, respectively. Transformation strain calculations show the crystallographic anisotropy of martensitic transformation through the existence of 6 martensite variants. Anisotropy refers here to the transformation strain changes with the loading direction.

To comprehensively show the orientation dependence of the transformation strain, the $\varepsilon_{\beta \rightarrow \alpha''}^{(Vi)}$ were calculated for 85 representative orientations located in the $[001]$ - $[101]$ - $[111]$ standard stereographic triangle. Among the negative calculated $\varepsilon_{\beta \rightarrow \alpha''}^{(Vi)}$ values for a given direction, the one with the largest absolute value is recorded as the theoretical maximum transformation strain under compression for this considered direction and is reported in the standard stereographic triangle (Fig. III-9). The maximum transformation strain of 5.2% is obtained along the $[001]_{\beta}$ direction, and decreases with changing direction from $[001]_{\beta}$ direction to $[101]_{\beta}$ and $[111]_{\beta}$ directions, as indicated by the contour lines in Fig. III-9.

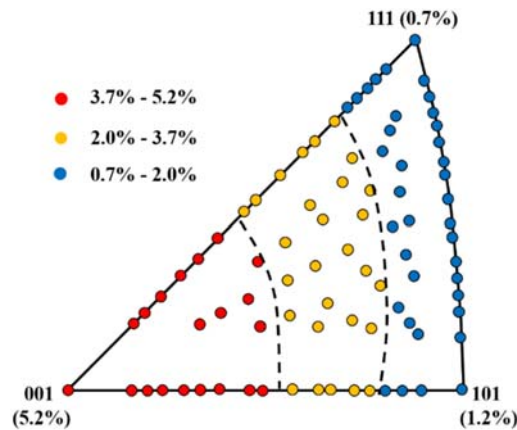


Fig. III-9 Orientation dependence of the calculated transformation strain associated with the indentation-induced martensitic transformation from the β to α'' phases in Ti2033 alloy.

These results indicate that the maximum strain accommodation from martensitic transformation is obtained when the indentation loading direction is parallel to the $[001]_{\beta}$ direction. In this way, it is clearly observed that our IPF distributions of indentation depth- and work- recovery ratios ($\eta_h - IPF$ and $\eta_w - IPF$) reflect the crystallographic anisotropy of the maximum transformation strain calculated under compression from the crystallographic model of the martensitic transformation in β -Ti alloys. It is reasonable to accept that the IPF distributions of η_h and η_w capture the orientation dependence of the superelastic effect. Transformation strain calculations and nanoindentation η_h and η_w measurements are in good

qualitative agreement following the same trend, especially when spherical indenter is used, which confirms that nanoindentation is a suitable technique to probe crystallographic anisotropy of superelastic response in β -Ti alloys. It appears that the strain induced under the spherical indenter is largely accommodated by the reversible stress-induced martensitic transformation, leading to a remarkable superelastic strain recovery upon unloading.

III.3.5 Anisotropy of the indentation modulus

Fig. III-10 shows the distribution of the indentation modulus, E_{IT} - IPF, measured with the Sp50 and Bkv indenters. Each colored point corresponds again to the average of at least five measurements and the mean standard deviation is 3 GPa. According to the distribution of E_{IT} values, each inverse pole figure was divided into 3 sections following the same model. The distribution of the indentation modulus measured from individual grains according to the crystallographic loading direction shows consistent values that change continuously through the fundamental triangle, suggesting the orientation dependence of E_{IT} : The same trend is observed for the two indenter geometries: the $\langle 001 \rangle_{\beta}$ and $\langle 111 \rangle_{\beta}$ crystallographic directions exhibiting the lowest and largest values, respectively, and $\langle 101 \rangle_{\beta}$ direction falling in the intermediates, for both indenters. For a given orientation, the E_{IT} value for Bkv indenter was observed to be lower than that for Sp50 indenter, which is consistent with the results reported for pure titanium [9] and Ti2448 alloy [29].

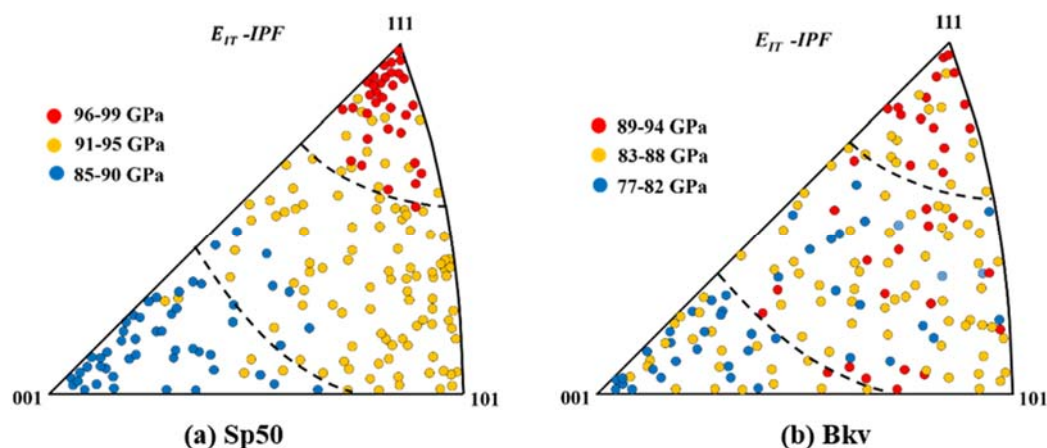


Fig. III-10 Indentation modulus distributions (E_{IT} - IPF) measured by: (a) Sp50 and (b) Bkv tips.

The orientation dependence of indentation modulus E_{IT} can be qualitatively analyzed from the crystallographic anisotropy of calculated Young's modulus. A cubic crystal can be characterized by only three independent elastic constants (c_{11} , c_{12} and c_{44}) due to the strong cubic symmetry. To ensure a positive energy change with any small distortion, the requirements for these three elastic constants are as follows [39]:

$$c_{11} + 2c_{12} > 0, c_{11} - c_{12} > 0, c_{44} > 0 \quad (\text{III-2})$$

For all classes of cubic crystals, Young's modulus E_{hkl} in any crystallographic direction $[h k l]$ can be calculated by the following equations [40-42]:

$$E_{hkl} = \left\{ s_{11} - 2 \left(s_{11} - s_{12} - \frac{1}{2} s_{44} \right) (m^2 n^2 + m^2 p^2 + n^2 p^2) \right\}^{-1} \quad (\text{III-3})$$

where s_{ij} are the three independent elastic compliances as defined for cubic structure:

$$s_{11} = \frac{c_{11} + c_{12}}{(c_{11} - c_{12})(c_{11} + 2c_{12})}; \quad s_{12} = \frac{-c_{12}}{(c_{11} - c_{12})(c_{11} + 2c_{12})}; \quad s_{44} = \frac{1}{c_{44}} \quad (\text{III-4})$$

and m, n, p are the direction cosines for the direction $[h k l]$ along which E_{hkl} is calculated:

$$m = \frac{h}{\sqrt{h^2 + k^2 + l^2}}; \quad n = \frac{k}{\sqrt{h^2 + k^2 + l^2}}; \quad p = \frac{l}{\sqrt{h^2 + k^2 + l^2}} \quad (\text{III-5})$$

By submitting equations (III 4-5) into the equation (III-3), the Young's modulus E_{hkl} can be expressed equivalently as:

$$E_{hkl} = \left\{ \frac{c_{11} + c_{12}}{(c_{11} - c_{12})(c_{11} + 2c_{12})} + \left(\frac{1}{c_{44}} - \frac{2}{c_{11} - c_{12}} \right) \frac{(h^2 k^2 + h^2 l^2 + k^2 l^2)}{(h^2 + k^2 + l^2)^2} \right\}^{-1} \quad (\text{III-6})$$

For the Young's moduli of the directions $\langle 100 \rangle$, $\langle 110 \rangle$, and $\langle 111 \rangle$ in cubic crystals, the above equations can be simplified as follows:

$$E_{[001]} = \frac{(c_{11} - c_{12})(c_{11} + 2c_{12})}{c_{11} + c_{12}} \quad (\text{III-7})$$

$$E_{[011]} = \left\{ \frac{c_{11} + c_{12}}{(c_{11} - c_{12})(c_{11} + 2c_{12})} + \frac{1}{4} \left(\frac{1}{c_{44}} - \frac{2}{c_{11} - c_{12}} \right) \right\}^{-1} \quad (\text{III-8})$$

$$E_{[111]} = \left\{ \frac{c_{11} + c_{12}}{(c_{11} - c_{12})(c_{11} + 2c_{12})} + \frac{1}{3} \left(\frac{1}{c_{44}} - \frac{2}{c_{11} - c_{12}} \right) \right\}^{-1} \quad (\text{III-9})$$

It is worth noting that the Young's modulus corresponds to uniaxial testing conditions while the indentation modulus is obtained from rather more complex loading conditions with triaxial stress state. The neglect of the triaxial stress state under the indenter introduces some difficulties to clearly determine the real local Young's modulus. Nevertheless, the objective of this work was focused on evolution tendency of elastic modulus with respect to the crystallographic orientations, rather than the determination of the absolute value of this local elastic property. Comparison of the values of the Young's and indentation moduli deserves

further research. Thus, indentation modulus evolution could be roughly correlated with the evolution of Young's modulus.

For a grain having its $\langle h k l \rangle$ direction aligned with the loading axis, the Young's modulus E_{hkl} can be deduced from Equation (III-6). Table III-3 presents the elastic constants c_{11} , c_{12} and c_{44} of bcc Ti-based alloys reported in the literature, as well as the anisotropy factor $A = 2c_{44}/(c_{11}-c_{12})$. The degree of elastic anisotropy increases with the deviation in factor A from 1. The elastic constants of Ti-22Zr alloy, $c_{11} = 109.2$ GPa, $c_{12} = 98.9$ GPa and $c_{44} = 14.3$ GPa [44], were used for the calculation of theoretical Young's modulus and were considered for discussion and comparison with indentation moduli measured in our Ti2033 alloy.

Table III-3 Elastic constants c_{11} , c_{12} and c_{44} (GPa) and anisotropy factor A of bcc Ti-based alloys

Composition	c_{11}	c_{12}	c_{44}	A	Methods	Ref.
Ti	97.7	82.7	37.5	5	RUS	[43]
Ti-22Zr (at.%)	109.2	98.9	14.3	2.78	ML	[44]
Ti-41Zr (at.%)	118.3	94.7	33.6	2.95	Calculation	[45]
Ti-24Nb-4Zr-8Sn (wt.%)	57.2	36.1	35.9	3.39	RUS	[7]
Ti-29Nb-Ta-Zr (mass%)	65.1	40.5	32.4	2.63	RUS + EMAR	[46]
Ti-25Nb-Ta-Zr (mass%)	90.8	55.9	35.8	2.05		
Ti-26.6Nb-6.7Al (at.%)	144.42	119.12	42.96	3.42	RPR	[47]
Ti-8Mo-3Zr-6Al (at.%)	135.1	104.2	46.2	2.99	RUS + EMAR	[48]
Ti-15Mo-3Nb-3Al (wt.%)	110	74	89	5	HEDM	[49]

* ML is Machine Learning methods;

RUS is Resonant Ultrasound Spectroscopy;

EMAR is Electromagnetic Acoustic Resonance method;

RPR is Rectangular Parallelepiped Resonance method.

HEDM is High-energy Diffraction Microscopy experiments and crystal-based finite element model.

Fig. III-11 shows the orientation dependence of calculated Young's modulus in directions between the $\langle 001 \rangle_{\beta}$ and $\langle 110 \rangle_{\beta}$ directions which were calculated by coordinate conversion of c_{ij} . The angle θ denotes the angle between the $[100]_{\beta}$ direction of the considered β crystal and the crystallographic loading direction belonging to $(1\bar{1}0)_{\beta}$ plane of the β crystal. Young's modulus of Ti2033 alloy shows anisotropy as a function of θ in Fig. III-11a. Young's moduli in the $\langle 100 \rangle_{\beta}$ direction $E_{\langle 100 \rangle}$ is approximately two times lower than Young's modulus in the $\langle 111 \rangle_{\beta}$ direction $E_{\langle 111 \rangle}$, where $E_{\langle 100 \rangle}$ and $E_{\langle 111 \rangle}$ are the lowest (15.1 GPa) and highest (40.9 GPa) values, respectively. The observed orientation dependence in Ti2033 is consistent with that calculated from the measured elastic stiffness in Ti-29Nb-Ta-Zr and Ti-25Nb-Ta-Zr single crystals [46] and shown in Fig. III-11b.

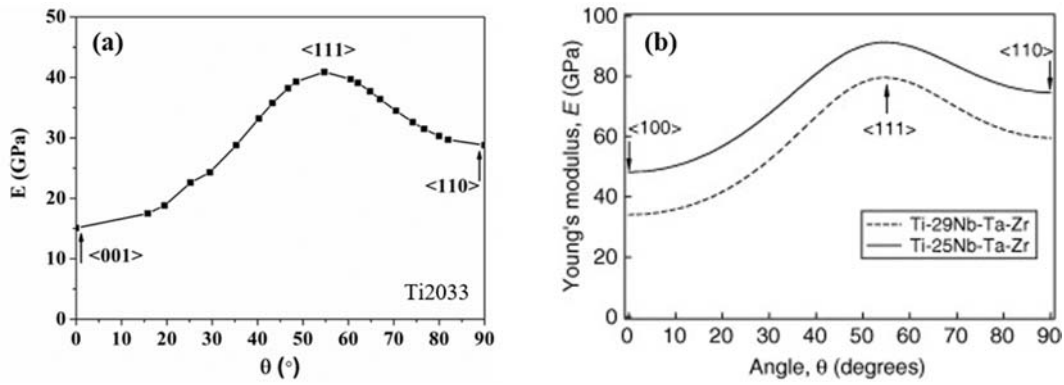


Fig. III-11 Orientation dependence of Young’s moduli as a function of θ angle, calculated by coordinate conversion of c_{ij} : (a) for Ti2033 β crystal; (b) for Ti-29Nb-Ta-Zr and Ti-25Nb-Ta-Zr β -crystals. The θ angle denotes the angle between the $[001]_{\beta}$ direction and the different loading directions belonging to the $(1\bar{1}0)_{\beta}$ plane of the β -crystal.

Fig. III-12 shows the inverse pole figure distribution of calculated Young’s modulus for Ti2033 β crystal. The crystallographic orientation dependence is obviously demonstrated as indicated by the ranges bounded by dashed lines, showing a decreasing trend with changing the crystallographic direction from $[111]_{\beta}$ toward the $[101]_{\beta}$ and $[001]_{\beta}$, which is in a good qualitative agreement with the nanoindentation measurements in Fig. III-10. Elastic moduli determined by nanoindentation appear overestimated compared to Young’s moduli calculated from measured elastic constants. This is explained by the fact that the true contact area can be underestimated during indentation leading to overestimation of the indentation modulus, which is consistent with the literature [50, 51]. Accurate determination of the contact area during post-experiment using imaging techniques can be used only if elastic recovery is negligible, which is not the present case.

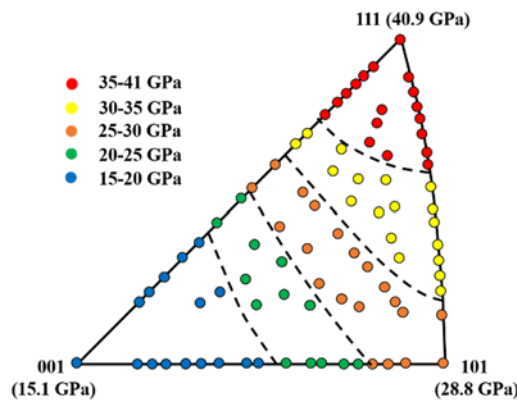


Fig. III-12 Orientation dependence of Young’s modulus calculated from the measured elastic stiffness constant in Ti-22Zr.

III.3.6 Indentation hardness

Fig. III-13 shows the inverse pole figure distribution of indentation hardness (H_{IT} -IPF) measured with the Sp50 and Bkv indenters. In contrast to the inverse pole figure distribution of η_h , η_w E_{IT} , no consistent and continuous change in nanoindentation hardness is found with the crystallographic orientation and for both indenters. No significant trend is found for H_{IT} values as a function of the crystallographic orientation, suggesting that H_{IT} is orientation-independent. Similar result has been reported in polycrystalline β Ti-Al alloys where no obvious change was identified for indentation hardness of β grains [52]. It is related to the bcc structure of the β grains which is prone to generate a high number of potential slip systems. In β Ti alloys, dislocation slip systems can be easily activated in the $\{110\}$ and $\{112\}$ planes, dislocation activity has been also found in the $\{123\}$ planes. Thus, dislocation slip is activated rather easily for any bcc crystallographic orientation and supports the isotropic distribution of hardness values usually observed in bcc alloys. It is different from the observations in pure α -Ti that indentation hardness varied significantly with crystal orientation: indentation hardness for individual grains orientated in $[0001]$ direction exhibited the highest value, then decreased as the orientations deviated from the $[0001]$ direction [8, 9, 53]. This is due to a strong anisotropy of slip systems in hcp α -Ti structure.

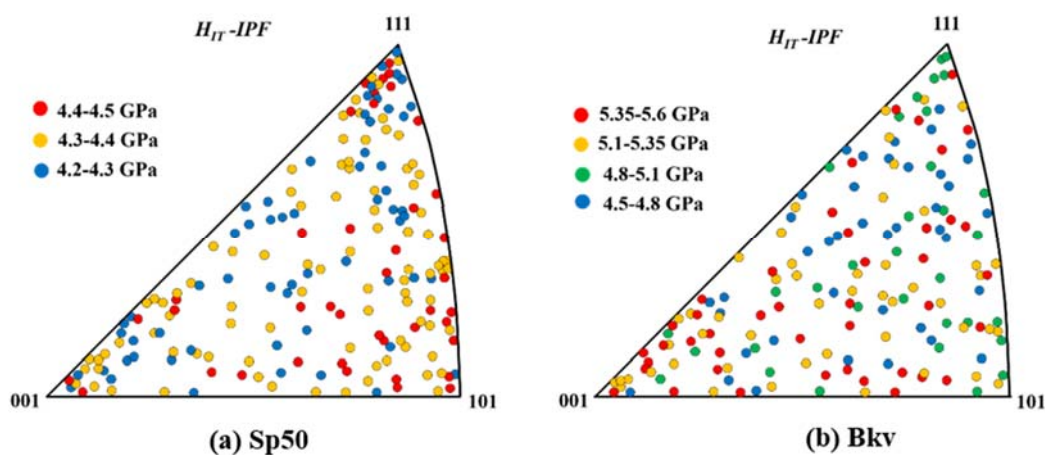


Fig. III-13 Indentation hardness inverse pole figures (H_{IT} -IPF) measured with: (a) the Sp50 indenter and (b) the Bkv indenter.

III.4 Conclusion

This chapter combines nanoindentation and electron backscatter diffraction (EBSD) to examine the crystallographic anisotropy of the indentation response in individual grains of β Ti2033 polycrystalline alloy. Nanoindentation, using spherical (Sp50) and Berkovich (Bkv)

indenters, was employed to probe small volumes of material within individual grains for which orientations were known from prior EBSD mapping. Indentation depth- and work- recovery ratios (η_h and η_w), indentation modulus E_{IT} and hardness H_{IT} were calculated from the nanoindentation force-displacement curves. For a better understanding, and a highlighted visual effect, results were presented as inverse pole figure distribution maps of $\eta_h - IPF$, $\eta_w - IPF$, $E_{IT} - IPF$ and $H_{IT} - IPF$. The high statistic of measurements carried out along a large range of crystallographic directions allowed an investigation through the entire fundamental stereographic triangle of the β phase.

Results showed that indentation recovery ratios were strongly affected by the loading direction and reached a maximum along the $\langle 001 \rangle_\beta$ direction and a minimum along the $\langle 111 \rangle_\beta$ direction. The IPF distributions of indentation recovery ratios were in good agreement with the IPF distribution of compressive lattice distortions calculated from the crystallographic model of martensitic transformation, which evidenced that anisotropy of indentation recovery ratios arose from the superelastic nature of our alloy. On the other hand, it was shown that spherical nanoindentation is more appropriate for probing crystallographic anisotropy of the superelasticity, due to the strain distribution field generated under the Sp50 indenter which is smoothly distributed and more favorable for the martensitic transformation (superelastic deformation), as compared to the case of sharp Bkv indenter.

Besides, orientation dependence in indentation modulus E_{IT} was also observed whereas in the case of indentation hardness H_{IT} no trend was seen, for both Sp50 and Bkv indenters. The IPF distributions of the indentation modulus were qualitatively similar to the one predicted by calculations of Young's modulus from the measured elastic constants. No crystallographic anisotropy of indentation hardness was detected, due to multiple slip systems activated in the bcc β crystal.

As a short conclusion, the present work showed that crystallographic anisotropy of the nanoindentation response was governed by anisotropy of elastic and superelastic responses in our β -metastable Ti2033 alloy and in contrast, orientation dependence was lost when plasticity took place.

References

- [1] T. Inamura, Y. Fukui, H. Hosoda, K. Wakashima, S. Miyazaki, Relationship between Texture and Macroscopic Transformation Strain in Severely Cold-Rolled Ti-Nb-Al Superelastic Alloy, *Materials Transactions*, 45 (2004) 1083-1089.
- [2] Y. Chai, H. Kim, H. Hosoda, S. Miyazaki, Self-accommodation in Ti-Nb shape memory alloys, *Acta Materialia*, 57 (2009) 4054-4064.
- [3] H.Y. Kim, S. Miyazaki, Martensitic transformation and superelastic properties of Ti-Nb base alloys, *Materials Transactions*, 56 (2015) 625-634.
- [4] H.Y. Kim, T. Sasaki, K. Okutsu, J.I. Kim, T. Inamura, H. Hosoda, S. Miyazaki, Texture and shape memory behavior of Ti-22Nb-6Ta alloy, *Acta Materialia*, 54 (2006) 423-433.
- [5] K. Gall, H. Sehitoglu, The role of texture in tension-compression asymmetry in polycrystalline NiTi, *International Journal of Plasticity*, 15 (1999) 69-92.
- [6] K. Gall, H. Sehitoglu, Y.I. Chumlyakov, I.V. Kireeva, Tension-compression asymmetry of the stress-strain response in aged single crystal and polycrystalline NiTi, *Acta Materialia*, 47 (1999) 1203-1217.
- [7] Y.W. Zhang, S.J. Li, E.G. Obbard, H. Wang, S.C. Wang, Y.L. Hao, R. Yang, Elastic properties of Ti-24Nb-4Zr-8Sn single crystals with bcc crystal structure, *Acta Materialia*, 59 (2011) 3081-3090.
- [8] T. Britton, H. Liang, F. Dunne, A. Wilkinson, The effect of crystal orientation on the indentation response of commercially pure titanium: experiments and simulations, *Proceedings of the Royal Society A: Mathematical, Physical and Engineering Sciences*, 466 (2010) 695-719.
- [9] C. Fizanne-Michel, M. Cornen, P. Castany, I. Péron, T. Gloriant, Determination of hardness and elastic modulus inverse pole figures of a polycrystalline commercially pure titanium by coupling nanoindentation and EBSD techniques, *Materials Science and Engineering: A*, 613 (2014) 159-162.
- [10] C. Tomas, J.-C. Stinville, C. Templier, P. Villechaise, Hardness and elastic modulus gradients in plasma-nitrided 316L polycrystalline stainless steel investigated by nanoindentation tomography, *Acta Materialia*, 60 (2012) 1965-1973.
- [11] C. Tomas, M. Arnoux, X. Milhet, Hardness cartography to increase the nanoindentation resolution in heterogeneous materials: Application to a Ni-based single-crystal superalloy, *Scripta Materialia*, 66 (2012) 77-80.
- [12] C.P. Frick, B.G. Clark, S. Orso, P. Sonnweber-Ribic, E. Arzt, Orientation-independent pseudoelasticity in small-scale NiTi compression pillars, *Scripta Materialia*, 59 (2008) 7-10.
- [13] C.P. Frick, T.W. Lang, K. Spark, K. Gall, Stress-induced martensitic transformations and shape memory at nanometer scales, *Acta Materialia*, 54 (2006) 2223-2234.
- [14] G. Laplanche, J. Pfetzinger-Micklich, G. Eggeler, Sudden stress-induced transformation events during nanoindentation of NiTi shape memory alloys, *Acta Materialia*, 78 (2014) 144-160.
- [15] J. Menčík, D. Munz, E. Quandt, E.R. Weppelmann, M.V. Swain, Determination of elastic modulus of thin layers using nanoindentation, *Journal of Materials Research*, 12 (2011) 2475-2484.
- [16] Y.-G. Jung, B.R. Lawn, M. Martyniuk, H. Huang, X.Z. Hu, Evaluation of elastic modulus and hardness of thin films by nanoindentation, *Journal of Materials Research*, 19 (2004) 3076-3080.

- [17] M. Xia, P. Liu, Q. Sun, Grain size dependence of Young's modulus and hardness for nanocrystalline NiTi shape memory alloy, *Materials Letters*, 211 (2018) 352-355.
- [18] W.C. Oliver, G.M. Pharr, Measurement of hardness and elastic modulus by instrumented indentation: Advances in understanding and refinements to methodology, *Journal of Materials Research*, 19 (2004) 3-20.
- [19] W. Wang, K. Lu, Nanoindentation measurement of hardness and modulus anisotropy in Ni₃Al single crystals, *Journal of Materials Research*, 17 (2002) 2314-2320.
- [20] G. Kang, W. Yan, Effects of phase transition on the hardness of shape memory alloys, *Applied Physics Letters*, 94 (2009) 261906.
- [21] A. Amini, C. Cheng, Nature of hardness evolution in nanocrystalline NiTi shape memory alloys during solid-state phase transition, *Scientific Reports*, 3 (2013) 2476-2476.
- [22] W. Yan, A. Amini, Q. Sun, On anomalous depth-dependency of the hardness of NiTi shape memory alloys in spherical nanoindentation, *Journal of Materials Research*, 28 (2013) 2031-2039.
- [23] S. Kumar, I.A. Kumar, L. Marandi, I. Sen, Assessment of small-scale deformation characteristics and stress-strain behavior of NiTi based shape memory alloy using nanoindentation, *Acta Materialia*, 201 (2020) 303-315.
- [24] A.M. Wood, J.-H. You, T. Clyne, Nanoindentation response of superelastic materials, in: *Smart Materials III*, International Society for Optics and Photonics, 2004, pp. 216-223.
- [25] H.-S. Zhang, K. Komvopoulos, Nanoscale pseudoelasticity of single-crystal Cu–Al–Ni shape-memory alloy induced by cyclic nanoindentation, *Journal of Materials Science*, 41 (2006) 5021-5024.
- [26] C.-Y. Nien, H.-K. Wang, C.-H. Chen, S. Ii, S.-K. Wu, C.-H. Hsueh, Superelasticity of TiNi-based shape memory alloys at micro/nanoscale, *Journal of Materials Research*, 29 (2014) 2717-2726.
- [27] J. Pfetzinger, A. Schaefer, C. Somsen, M.F.-X. Wagner, Nanoindentation of pseudoelastic NiTi shape memory alloys: thermomechanical and microstructural aspects, *International Journal of Materials Research*, 100 (2009) 936-942.
- [28] J. Pfetzinger-Micklich, M.F.X. Wagner, R. Zarnetta, J. Frenzel, G. Eggeler, A.E. Markaki, J. Wheeler, T.W. Clyne, Nanoindentation of a pseudoelastic NiTiFe shape memory alloy, *Advanced Engineering Materials*, 12 (2010) 13-19.
- [29] H. Jabir, A. Fillon, P. Castany, T. Gloriant, Crystallographic orientation dependence of mechanical properties in the superelastic Ti-24Nb-4Zr-8Sn alloy, *Physical Review Materials*, 3 (2019) 063608.
- [30] J.J. Gao, I. Thibon, D. Laillé, P. Castany, T. Gloriant, Influence of texture and transformation strain on the superelastic performance of a new Ti–20Zr–3Mo–3Sn alloy, *Materials Science and Engineering: A*, 762 (2019) 138075.
- [31] G. Pan, Z. Cao, J. Shi, M. Wei, L. Xu, X. Meng, Different mechanical response of TiNi film induced by the shape of indenter during nanoindentation, *Sensors and Actuators A: Physical*, 217 (2014) 75-80.
- [32] W. Ni, Y.-T. Cheng, D.S. Grummon, Microscopic superelastic behavior of a nickel-titanium alloy under complex loading conditions, *Applied Physics Letters*, 82 (2003) 2811-2813.
- [33] M. Tahara, H.Y. Kim, T. Inamura, H. Hosoda, S. Miyazaki, Lattice modulation and superelasticity in oxygen-added β -Ti alloys, *Acta Materialia*, 59 (2011) 6208-6218.
- [34] M.F. Ijaz, H.Y. Kim, H. Hosoda, S. Miyazaki, Superelastic properties of biomedical (Ti–Zr)–Mo–Sn

- alloys, *Materials Science and Engineering: C*, 48 (2015) 11-20.
- [35] H. Kim, Y. Ikehara, J.I. Kim, H. Hosoda, S. Miyazaki, Martensitic transformation, shape memory effect and superelasticity of Ti–Nb binary alloys, *Acta Materialia*, 54 (2006) 2419-2429.
- [36] H.Y. Kim, J. Fu, H. Tobe, J.I. Kim, S. Miyazaki, Crystal structure, transformation strain, and superelastic property of Ti–Nb–Zr and Ti–Nb–Ta alloys, *Shape memory and Superelasticity*, 1 (2015) 107-116.
- [37] Z. Zhang, Y. Hao, S. Li, R. Yang, Fatigue behavior of ultrafine-grained Ti–24Nb–4Zr–8Sn multifunctional biomedical titanium alloy, *Materials Science and Engineering: A*, 577 (2013) 225-233.
- [38] S.C. Mao, J.F. Luo, Z. Zhang, M.H. Wu, Y. Liu, X.D. Han, EBSD studies of the stress-induced B2–B19' martensitic transformation in NiTi tubes under uniaxial tension and compression, *Acta Materialia*, 58 (2010) 3357-3366.
- [39] X. Wang, L. Zhang, Z. Guo, Y. Jiang, X. Tao, L. Liu, Study of low-modulus biomedical β Ti–Nb–Zr alloys based on single-crystal elastic constants modeling, *Journal of the Mechanical Behavior of Biomedical Materials*, 62 (2016) 310-318.
- [40] L. Zhang, R. Barrett, P. Cloetens, C. Detlefs, M. Sanchez del Rio, Anisotropic elasticity of silicon and its application to the modelling of X-ray optics, *Journal of Synchrotron Radiation*, 21 (2014) 507-517.
- [41] J.-M. Zhang, Y. Zhang, K.-W. Xu, V. Ji, Young's modulus surface and Poisson's ratio curve for cubic metals, *Journal of Physics and Chemistry of Solids*, 68 (2007) 503-510.
- [42] J.J. Wortman, R.A. Evans, Young's Modulus, Shear Modulus, and Poisson's Ratio in Silicon and Germanium, *Journal of Applied Physics*, 36 (1965) 153-156.
- [43] H. Ledbetter, H. Ogi, S. Kai, S. Kim, M. Hirao, Elastic constants of body-centered-cubic titanium monocrystals, *Journal of Applied Physics*, 95 (2004) 4642-4644.
- [44] C.A. Salvador, B.F. Zornio, C.R. Miranda, Discovery of Low-Modulus Ti-Nb-Zr Alloys Based on Machine Learning and First-Principles Calculations, *ACS Applied Materials & Interfaces*, (2020).
- [45] W. Duan, X. Liang, X. Yang, Y. Wang, B. Luan, Lattice Stability and Elastic Properties of Zr-Ti-X Alloys (X= Al, V) by the First Principles Study, *Metals*, 10 (2020) 1317.
- [46] M. Tane, S. Akita, T. Nakano, K. Hagihara, Y. Umakoshi, M. Niinomi, H. Nakajima, Peculiar elastic behavior of Ti–Nb–Ta–Zr single crystals, *Acta Materialia*, 56 (2008) 2856-2863.
- [47] P. Wang, M. Todai, T. Nakano, Beta titanium single crystal with bone-like elastic modulus and large crystallographic elastic anisotropy, *Journal of Alloys and Compounds*, 782 (2019) 667-671.
- [48] S.H. Lee, M. Todai, M. Tane, K. Hagihara, H. Nakajima, T. Nakano, Biocompatible low Young's modulus achieved by strong crystallographic elastic anisotropy in Ti–15Mo–5Zr–3Al alloy single crystal, *Journal of the Mechanical Behavior of Biomedical Materials*, 14 (2012) 48-54.
- [49] C. Efstathiou, D.E. Boyce, J.S. Park, U. Lienert, P.R. Dawson, M.P. Miller, A method for measuring single-crystal elastic moduli using high-energy X-ray diffraction and a crystal-based finite element model, *Acta Materialia*, 58 (2010) 5806-5819.
- [50] R.A. Mirshams, R.M. Pothapragada, Correlation of nanoindentation measurements of nickel made using geometrically different indenter tips, *Acta Materialia*, 54 (2006) 1123-1134.
- [51] G.B. Viswanathan, E. Lee, D.M. Maher, S. Banerjee, H.L. Fraser, Direct observations and analyses of dislocation substructures in the α phase of an α/β Ti-alloy formed by nanoindentation, *Acta Materialia*, 53

(2005) 5101-5115.

[52] X. Lei, L. Dong, Z. Zhang, M. Hu, Z. Wang, Y. Hao, R. Yang, Microtexture and nanoindentation of α and β Phases in Ti-6Al-1.5 Cr-2.5 Mo-0.5 Fe-0.3 Si titanium alloy, *Science of Advanced Materials*, 9 (2017) 1476-1483.

[53] C. Zambaldi, Y. Yang, T.R. Bieler, D. Raabe, Orientation informed nanoindentation of α -titanium: Indentation pileup in hexagonal metals deforming by prismatic slip, *Journal of Materials Research*, 27 (2011) 356-367.

Chapter IV: Investigation of the superelastic behavior of Ti-16Zr-13Nb-2Sn sputtered film by nanoindentation

IV.1 Introduction

Superelasticity refers to the property of recovering large deformation strain when removing an applied load. In metastable β -Ti alloys, superelasticity is attributed to the stress-induced martensitic transformation from the parent bcc- β phase to the orthorhombic- α' martensite phase upon loading, and to the subsequent reverse transformation upon unloading resulting in remarkable accommodation of large reversible deformation strains [1]. Recently, the Ti-Zr-Nb-Sn bulk system has received much attention and appears promising alloy system for biomedical purpose because it offers opportunity to combine large transformation strains, low elastic modulus and high strength by adjusting alloy concentration and optimization of microstructure, and also shows excellent cyto- and hemo-compatibility with enhanced viability and proliferation of living cells. For instance, Ti-(1~5)Zr-(12~17)Nb-(2~6)Sn [2-4], Ti-18Zr-(9~16)Nb-(0~4)Sn [5, 6], Ti-20Zr-12Nb-2Sn [7], Ti-24Zr-(8~12)Nb-2Sn [8] and Ti-(40~50)Zr-8Nb-2Sn [9] (at.%) bulk alloys have been reported in literature and some of which have reached superelastic recovery strain up to 7.5% at room temperature.

To our knowledge, there has been no reported work related to the Ti-Zr-Nb-Sn system in film geometries. Film technology is promising for further miniaturization and design possibilities for nanometer-sized functional tools and devices for biomedicine. In the field of superelastic films, most activities have focused on the superelastic response of magnetron sputtered NiTi-base alloy films since the 1990s, basically for the development of miniature systems (micro-sensors, -actuators, -pumps and -valves) [10-13]. Beside the suspected toxicity and carcinogenicity of nickel, a major drawback is the amorphous nature of as-deposited NiTi films at room temperature which required suitable heat treatment to obtain the crystalline phase responsible of the superelastic effect. Much less work has investigated superelastic response in Ni-free metastable β -Ti alloy films deposited by magnetron sputtered. One can mention some studies related superelasticity in Ti-Nb binary films [14-16], in Ti-(3~13)Zr-(18~23)Nb ternary films (at.%) [17] and in Ti-Nb-Ta-Zr quaternary films [18]. As with bulk alloys, it has been confirmed that superelastic response of ternary Ti-Zr-Nb films is much higher than that of binary Ti-Nb films. Further studies were focused on microstructure and nanomechanical properties (elastic modulus and hardness) of magnetron sputtered Ni-free β -Ti alloy films, such as in Ti-Nb films [19-21] and in Ti-Nb-Zr films [22-24].

Magnetron sputtering offers the possibility to synthesize alloy films outside thermodynamic equilibrium enabling the formation of metastable phases in film geometries.

Studies have confirmed that the allotropic β phase of Ti can be stabilized under the β transus temperature, at room temperature, in β -Ti alloy films [25]. It has also been established that the addition of Zr as a substitute of Nb affects the lattice parameters of β phase and α'' martensite phase leading to an increase in the lattice deformation associated with the transformation strain during martensitic transformation which is beneficial for improving the accommodation of the deformation strain, and thus the superelastic response of alloys [17]. Meanwhile the decrease in Nb accelerates ω phase precipitation which affects superelasticity and increases drastically the elastic modulus and brittleness of alloys [21]. It has been observed that Sn addition suppresses ω phase formation and improves superelastic performances [26].

In the present work, we investigated if magnetron sputtered Ti-16Zr-13Nb-2Sn film could display superelastic properties as its bulk counterpart. In this Sn-added alloy film we suggested that full metastable β microstructure and large transformation strain could be obtained. For this purpose and considering previous work in bulk alloys [7], a new quaternary Ti-16Zr-13Nb-2Sn (in at.%) film was obtained by magnetron sputtering at room temperature and the morphological, crystallographic and microstructural characteristics of the films were investigated by scanning electron microscopy (SEM), atomic force microscope (AFM), X-ray diffraction (XRD), and transmission electron microscopy (TEM).

Relatively little information is known about the reversible and stress-induced superelastic deformation at the micro- and nano-meter length scale in Ni-free Ti-based alloy films. Nanoindentation is considered as an efficient technique to characterize the locally nanoscale deformation behavior and mechanical properties of films because of its ability for characterizing mechanical response of small volume materials. Ma et al. [12] firstly used nanoindentation experiments in films to reveal the nanoscale superelasticity of NiTi films. The hysteresis loop of load-displacement indentation cycles was interpreted as the result of the occurrence of reversible and stress-induced martensitic phase transformation (i.e. superelastic behavior). Wood and Clyne [27] demonstrated that nanoindentation, using the remnant depth ratio (unloaded depth / peak depth) as a detection parameter, was suitable for local testing whether or not superelastic deformation was occurring in NiTi alloys. A relatively low value for the remnant depth ratio was indicative that superelasticity was occurring. Moreover, the finite element method (FEM) simulations of the evolving strain fields under conical tip (which is considered to represent a good approximation to the Berkovich tip) and under spherical tip showed that peak strain levels are much higher under Berkovich indenter. Different indenter geometries make material exhibits different indentation responses. Nanoindentation experiment generates complex loading conditions necessitating considerable

care in the interpretation of the nanoindentation responses. It is necessary to clarify which tip geometries and loading conditions are suitable to probe superelastic recovery. Based on the studies of Liu et al.[28], Ni et al.[29], Jabir et al. [30] for superelastic bulks, and Achache et al.[14, 18] and Yang et al.[17] for superelastic films, the work recovery ratio and depth recovery ratio extracted from indentation load-displacement ($F-h$) curves were able to probe the superelastic effect in bulk and film alloys. The higher values of work and depth recovery ratios especially during spherical indentation reflected the greater capability of the material to accommodate deformations and to behave more superelastically. Shastry et al. [31] described the variation of the depth recovery ratio with the calculated representative strain with a physically-meaningful and simple function, and showed the importance of selecting the appropriate representative strain window to capture the differences in nanoindentation depth recovery ratio between superelastic and shape memory behaviors of Ti alloys. Indeed, in this study, the strain introduced into the material during Berkovich indentation was independent of penetration depth and caused significant plastic flow precluding a discriminating examination of the two different behaviors of Ti alloys. Spherical indentations, wherein the representative strain was varied systematically by changing the applied load, offered the advantage of investigating different deformation regimes from elastic to elasto-plastic to fully plastic regimes. Spherical indentations allowed to select the suitable representative strain window to reveal superelasticity and offered higher opportunity than Berkovich indentations to discern the discrepancies between the two close behaviors in Ti alloys. In the present chapter, nanoindentation technique was used to characterize the superelasticity of the obtained Ti-16Zr-13Nb-2Sn films, and four indenters with different geometry were used to study the nanoscale indentation behavior of Ti-16Zr-13Nb-2Sn superelastic films through different deformation regimes.

IV.2 Materials and methods

IV.2.1 Materials synthesis

The Ti-16Zr-13Nb-2Sn (at. %, Ti16132 for short) films were deposited on Si (100) substrates by radio frequency (RF) magnetron sputtering from a single target. Ultra-pure raw metals of titanium (>99.95 wt.%), zirconium (>99.078 wt.%), niobium (>99.9 wt. %) and tin (>99.99 wt. %) were used to synthesize the four-element ingot by the cold crucible levitation melting technique (CCLM). The ingot was next cold rolled and machined to obtain the alloyed target with perfect flat surface (76 mm diameter and 3 mm thick). The alloyed target was then

cleaned in HF/HNO₃ solution (1/1 ratio). Si substrate was ultrasonically cleaned in acetone and ethanol for 5 min in each, and dried under compressed air gas, then mounted on the sample holder at a distance of 5.5 cm from the target. The chamber was evacuated to a base pressure of 3.4×10^{-5} Pa. High purity argon was used as the sputtering gas and the working pressure was maintained at 0.2 Pa. Before each deposition, the target was pre-sputtered in Ar plasma for 10 min to clean the target surface and to equilibrate thermally. During this stabilizing period the substrate was protected by a large shutter. During deposition at room temperature, the sputtering RF power of the target was fixed at 300 W and the negative voltage on the target was recorded as 385 V. Deposition was carried out for 50 min. Plane-view TEM specimen were also prepared by depositing thin film layer on a Cu TEM grid within a reduced time leading to a film thickness of 30 nm. Ti16132 coatings were studied in their as-deposited state without any post-treatment.

IV.2.2 Microstructural and superelastic characterizations

Morphological and microstructural analyses were carried out on a JEOL JSM 6400 SEM operated at 10 kV. The chemical compositions of the composite target and films were assessed by energy dispersive X-ray spectroscopy (EDS) coupled with the SEM. Surface roughness and 3D images of surfacetopography were characterized using a Bruker Nano GmbH AFM operating in the tapping mode. Phase identification was performed using a Bruker D8 Advance XRD system in θ - 2θ Bragg-Brentano mode with Cu-K α radiation and power fixed at 40 kV and 40 mA. Pole figures and additional θ - 2θ scans at different χ inclinations (angles of the sample surface normal with respect to the diffraction vector) were performed by XRD on Rigaku SmartLab 5-circle diffraction system using Cu-K α radiation at 40kV and 50 mA. TEM analyses of the plane view specimen and cross section specimen were performed using a JEOL 2100 microscope operating at 200 kV. Details concerning sample preparation for these TEM specimens are described in section II.2.1.4.

Superelastic response of the Ti16132 film was investigated by nanoindentation using the instrumented NHT Anton Paar nanoindentation test system. Four indenter tips were used to explore the contribution of the superelastic response during the deformation of small volumes in our film: the Berkovich (Bkv) indenter and three spherical indenters with tip radii of 10 μ m (Sp10), 50 μ m (Sp50) and 200 μ m (Sp200). There is a special interest in indenting with different indenter geometries for characterizing the superelasticity, because not all geometries developed strain states that predominantly induced the martensitic phase transformation. The penetration depth was kept in the first 10% of the film thickness to minimize the influence of

the substrate material in the characterization of superelasticity. The depth recovery ratio η_h and work recovery ratio η_w were calculated from load-depth ($F-h$) nanoindentation curves (as described in section II.2.2.2) to evaluate the superelastic ability of Ti16132 film. As a short reminder, the depth recovery ratio η_h is defined as:

$$\eta_h = \frac{h_m - h_p}{h_m} \quad (\text{IV } -1)$$

where h_m is the maximum penetration depth at maximum applied load, and h_p is the permanent depth upon complete unloading [29]. The work recovery ratio η_w is defined as the ratio of recoverable work W_{rc} to the total work W_t :

$$\eta_w = \frac{W_{rc}}{W_t} = \frac{\int_{h_p}^{h_m} F.dh}{\int_0^{h_m} F.dh} \quad (\text{IV } -2)$$

where W_{rc} is represented by the area enclosed by the unloading curve and the maximum penetration depth and W_t is represented by the area enclosed by the loading curve and the maximum penetration depth [28]. Relatively high values for η_h and η_w indicate the occurrence of superelastic effect [27].

Both η_h and η_w ratios of Berkovich indentations were found largely depth independent in many studies and it was recognized that the imposed strain during nanoindentation with sharp indenters, such as Bkv indenter, was independent of indentation depth and solely dependent on the indenter geometry [33]. Indeed, for a pyramidal indenter like Bkv tip, the ratio of the length of contact diagonal to the depth of penetration remains constant for increasing indenter load. Thus for ideally sharp pyramidal, the representative strain ε_r introduced into the material is determined by the face angles, as given according to Tabor's theory by:

$$\varepsilon_r = 0.2 \cot(\beta) \quad (\text{IV } -3)$$

where β was the semi-apex angle of an axisymmetric equivalent cone [34]. For the Bkv indenter, $\beta = 70.3^\circ$ based on the equivalent displaced volumes in a single cone indenter [35]. Hence, a representative strain of ~ 0.07 is found for the Bkv indenter.

For spherical indentations, the radius of the circle of contact increases faster than the depth of penetration as the load increases. Therefore, for spherical indenter, the representative strain ε_r is not constant and increases continuously with the area of contact as given by:

$$\varepsilon_r = 0.2 a_c/R \quad (\text{IV } -4)$$

where a_c is the in-plane contact radius and R the indenter radius. The contact radius a_c is defined from the geometry of indentation of a plane surface with a spherical indenter as $a_c = \sqrt{2h_c R - h_c^2}$, where h_c is the contact depth (as represented in Fig. II-21) calculated from $F-h$ indentation curves with the following relation $h_c = h_m - 0.75(F_m / S)$, where F_m is the maximum load and S is the stiffness estimated from the unloading curve using the Oliver–Pharr method [36]. The same value of representative strain may be obtained with different radii of spherical indenters and different depths. Spherical indentations offer the opportunity to vary the representative strain by changing either h_m with fixed R or R at a fixed h_m , enabling exploration from elastic to elasto-plastic deformation regimes. It is therefore expected that both η_h and η_w ratios of spherical indentations are depth-dependent. In this work, the representative strain ε_r was used to present the evolution of the measured indentation response through different deformation regimes.

IV.3 Results

IV.3.1 Microstructural properties

The chemical compositions of the alloyed target and film are given in Table IV-1. The Zr concentration in film was observed to be lower to that of the target. Only 15.6 at.% of Zr was measured in the film whereas 19.7 at.% was found in the target. Compositions of the other elements of the film were observed to be very close to those of the target. The deviation in chemical composition between film and target is frequently attributed to the preferential sputtering effect. For film magnetron sputtered from an alloyed target, its composition depends greatly on the individual sputtering yields (the number of sputtered atoms per incident ion) of target components as well as their different masses [37]. Atoms of higher sputtering yield are removed preferentially from the bombarded surfaces resulting in surface segregation of one component. However, the reason for this depletion in Zr content in our film was not clear because it was expected that Zr and Nb elements which present similar sputtering yields, heats of sublimation and atomic weights would exhibit very close behaviors during the sputtering process [38, 39].

Table IV-1 Chemical compositions (in at. %) of the bulk target and the as-deposited film.

(at. %)	Zr	Nb	Sn	Ti
Target	20.1	11.9	2.1	balance
Film	15.6	13.5	1.7	balance

The cross-sectional SEM image and the 3D AFM image of surface morphology of the film are shown in Fig. IV-1. The film thickness measured from cross-sectional images was uniform and estimated to be $3.3\ \mu\text{m}$. The film appeared extremely compact with no discernible morphological features indicating sufficient adatom surface mobility in consistence with the low deposition pressure ($0.2\ \text{Pa}$). The surface morphology of the film observed by AFM displayed very small topographic features with uniform and fine needle shapes. The average roughness established from AFM images over a surface region of $5 \times 5\ \mu\text{m}$ was low at a value of $1.2\ \text{nm}$ for the R_a roughness and $1.5\ \text{nm}$ for the RMS roughness.

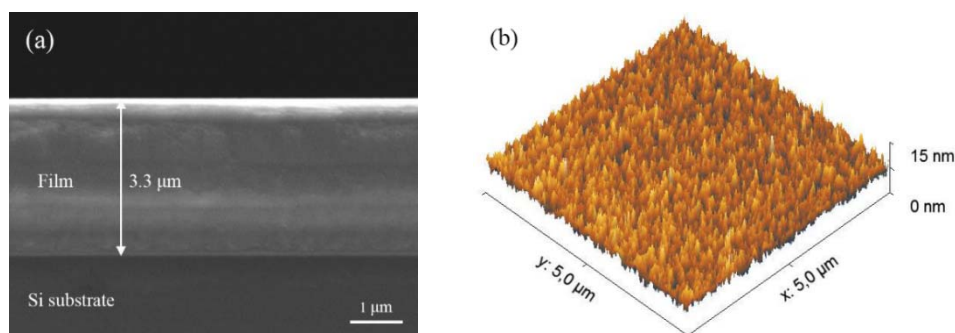


Fig. IV-1 (a) Cross sectional SEM image and (b) 3D AFM morphology of the Ti16132 film deposited on Si (100) substrate.

Fig. IV-2 shows the XRD pattern of Ti20163 film and the corresponding deconvolution profiles showing the contribution of β (bcc structure) and α'' (orthorhombic structure) phases to the XRD pattern. Formation of the high temperature β solid solution is common in Ti alloy films deposited via magnetron sputtering [14, 19, 21, 23]. Magnetron sputtering is a non-equilibrium process that leads to the formation of metastable phases due to abrupt changes in the energetic conditions of the system [40]. Only the $(110)_\beta$ and $(220)_\beta$ diffraction peaks are observed indicating a strong fiber texture associated to the preferential growth along the $[110]_\beta$ direction. There is a tendency for films grown by physical vapor deposition to develop specific preferred orientation which depends on the prevailing conditions during the deposition process including thermodynamic and kinetic considerations [41, 42]. The preferred orientation results from the competition between the strain and surface energies, and from the bombardment and mobility of incoming species at the film surface during growth process. In bcc alloys, $\{110\}$ planes are the densest planes and have the lowest surface energy. The development of the $[110]$ preferred orientation in our mainly bcc film is determined by the minimization of the total surface energy. $\{110\}_\beta$ densest planes are lengthened parallel to the substrate surface. This behavior has been reported in binary Ti-Nb [14], ternary Ti-Zr-Nb [21, 23, 24] and quaternary Ti-Nb-Zr-Ta [18] films.

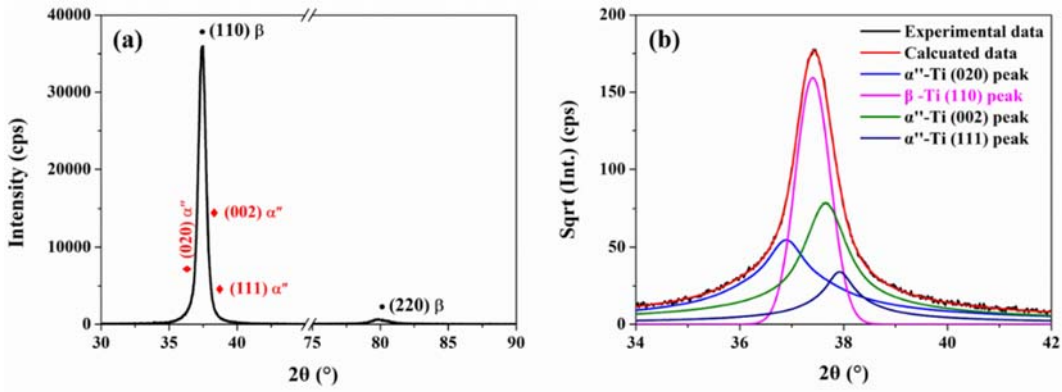


Fig. IV-2 (a) Classic θ - 2θ XRD pattern measured in the Ti16132 film and (b) Zoomed view of the deconvolution profile in the 2θ range of 34° - 42° in (a) with Y axis in square root scale.

Due to the strong crystallographic texture of the film along the growth direction, and the very close d-spacing of the β and α'' phases that likely co-exist in the film, additional θ - 2θ scan for χ inclination fixed at 29.16° was performed in order to look for specific (hkl) reflections of α'' phase and thus to confirm the co-existence of α'' phase in the Ti16132 film. Fig. IV-3 presents the θ - 2θ scan measured at $\chi = 29.16^\circ$ and the deconvolution profiles showing the $(111)_{\alpha''}$ and $(021)_{\alpha''}$ reflections. At χ around 29.16° , no reflections from β planes is expected in the 2θ range of 30 - 50° , which will be confirmed later from the pole figures measurements. The formation of some α'' phase in the as-deposited Ti16132 film is probably related to the extremely fast cooling rate environment and the compressive intrinsic stress state (low deposition pressure) both induced by the sputtering deposition process. Frutos et al. [43] showing that the β/α'' volume ratios can be designed by sputtering process in a single composition Ti-Zr-Nb film. In this work, the bias voltage was used during sputter deposition to increase the compressive residual stress state and the defect density in the Ti-13Nb-6Zr (at.%) film. Results showed that α'' phase forms at the expense of β phase as negative bias voltage is increased. Although bias voltage was not applied during sputter deposition of our Ti16132 film, we worked at a lower argon pressure (0.2 Pa), shorter target-substrate distance (5 cm) and with a face-on-face sputter geometry compared to the deposition conditions (0.4 Pa; 8 cm and 30° tilted angle between target normal and substrate normal) used by Frutos et al. [43], which, in our case, increase the energy of the deposited species favoring the incorporation of defects and development of compressive residual stress state during the film growth. Thus, it is not surprising that our deposition conditions enable the stabilization of some α'' phase in our Ti16132 film.

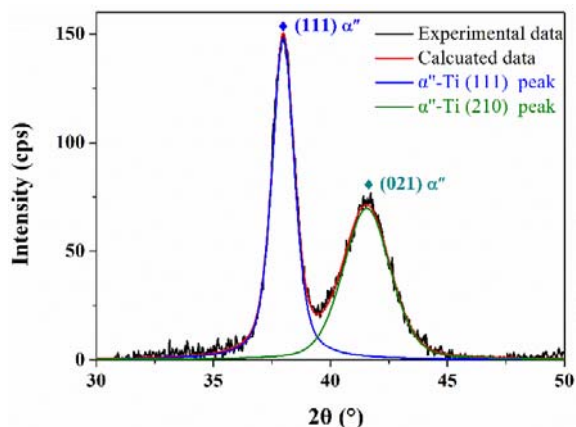


Fig. IV-3 XRD pattern in θ - 2θ scan at $\chi = 29.16^\circ$ of the Ti16132 film.

The number of identified reflections from XRD measurement is sufficient for the calculation of the lattice parameters for both β and α'' phases: $a_\beta = 3.39 \text{ \AA}$; $a_{\alpha''} = 3.29 \text{ \AA}$, $b_{\alpha''} = 4.88 \text{ \AA}$ and $c_{\alpha''} = 4.78 \text{ \AA}$. The calculated lattice parameters of the both β and α'' phase in Ti16132 film are very close to that calculated for bulk alloys with similar composition in literature (Fig. IV-4).

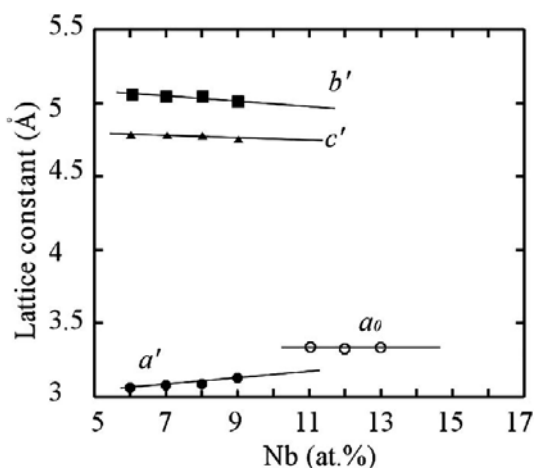


Fig. IV-4 Lattice parameters of α'' and β phases calculated from XRD profiles obtained in Ti-18Zr-(6-13)Nb-3Sn bulk alloys [5].

Fig. IV-5 shows the in-plane pole figures of $\{110\}_\beta$, $\{200\}_\beta$ and $\{211\}_\beta$ reflections from the β phase in the sputtered Ti16132 film deposited on Si substrate in logarithm scale. As can be readily seen, the poles characterizing the bcc structure are presented in ring patterns, and an intensified center appears in the $\{110\}_\beta$ pole figure, showing the in plane polycrystalline microstructure and the $\langle 110 \rangle_\beta$ fiber texture of the β grains in our Ti16132 film.

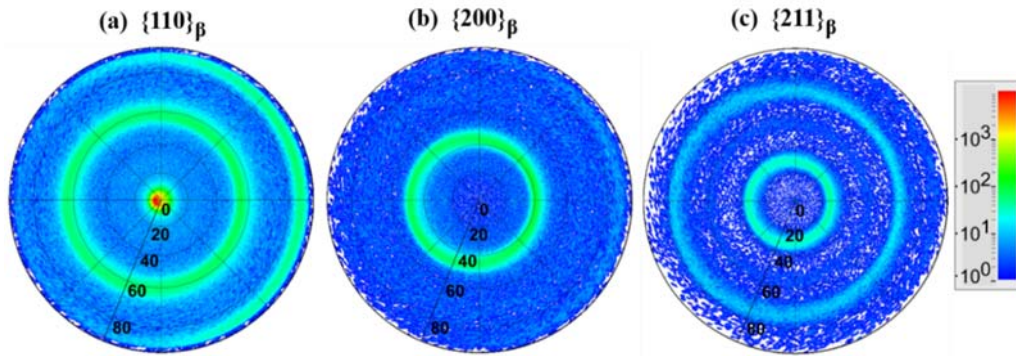


Fig. IV-5 In-plane pole figures in the Ti16132 film: (a) $\{110\}_\beta$, (b) $\{200\}_\beta$, (c) $\{211\}_\beta$.

Fig. IV-6 shows the $\{021\}_{\alpha''}$ in-plane pole figure measurement for which $2\theta_{\{021\}}$ angle was fixed at 41.5° . Results confirm the co-existence of α'' phase in the film and the randomly in plane orientation of the α'' crystals in the film.

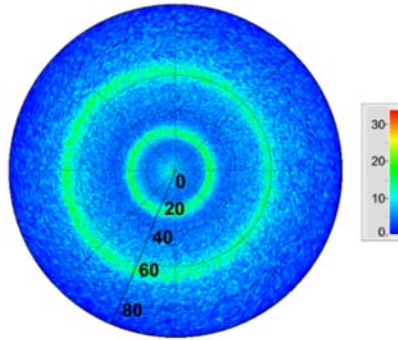


Fig. IV-6 In-plane pole figures of $\{021\}_{\alpha''}$ planes of α'' phase in the Ti16132 film in linear scale.

Fig. IV-7 shows the bright-field (BF) and high resolution (HR) TEM images from the plane-view specimen (~ 30 nm thick) deposited on TEM Cu grid. The BF-TEM image revealed nanosized grains typically less than twenty nanometer diameter. The selected area electron diffraction (SAED) pattern associated to the BF-TEM image and inserted in the corner of Fig. IV-7a, displayed continuous diffraction rings corresponding to the bcc- β phase and indicated the random orientation of the β grains in the planes parallel to the substrate surface and the polycrystalline nature of β phase in the film. $(110)_\beta$ planes were indexed according to the measured interplanar distance from the observable lattice fringes in the HR-TEM image (Fig. IV-7b). No other diffraction ring, besides those indexed as β phase, has been observed from the plane view TEM observations.

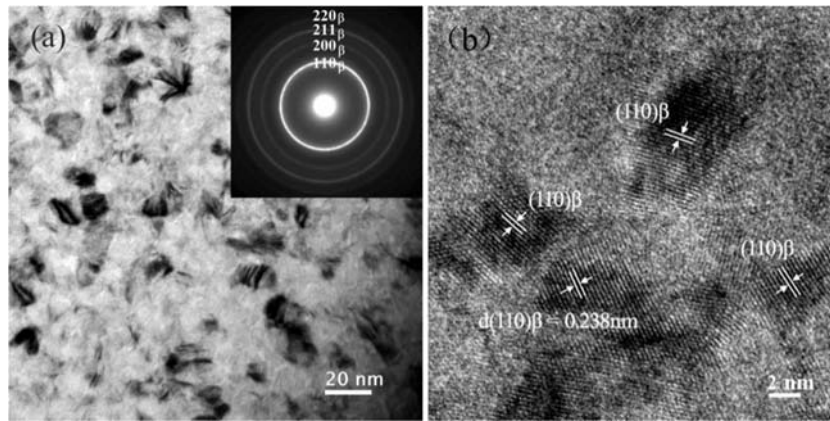


Fig. IV-7 TEM micrographs of the plane view specimen (30 nm thick) deposited on TEM Cu grid: (a) bright-field (BF-TEM) image with the corresponding SAED pattern and (b) high-resolution (HR-TEM) image.

Cross sectional TEM observations of Ti16132 film are shown in Fig. IV-8. The TEM-BF images show the general microstructure throughout the entire thickness layer consisting of fine columns. The diameter of columns progressively expands with the deposition thickness as confirmed by the variations of SAED patterns taken from different thickness positions. The SAED pattern taken from the position close to the substrate interface shows discontinuous $(110)_\beta$ diffraction ring (Fig. IV-8b). In contrast, the SAED pattern taken from the position close to the film surface shows separately diffraction arcs (Fig. IV-8c). This phenomenon that the SEAD pattern evolves from the discontinuous ring shape to independent diffraction arcs arises from the number of columns participating in the SAED pattern and the associated size of the columns. The finer the column size is, the higher the number of participating columns, and thus more approaching ring shape. Besides, the average column diameter estimated from the diffraction contrast TEM images is ~ 10 nm near the substrate interface, and ~ 50 nm near the external surface, respectively. Thus, it is acceptable to conclude that the diameter of the β crystalline columns increases with the deposition thickness.

It is noteworthy that since the SAED pattern is contributed by more than one column, the pattern is indexed by circles, rather than the vectors. Considering the $\{110\}_\beta$ diffraction ring, higher intensity is observed for the circle arcs in the surface normal direction as marked by arrows in Figs. IV-8b and 8c, which indicates a strong $\{110\}_\beta$ fiber texture of the β nanograined columns with the preferential orientation of the $\{110\}_\beta$ crystal planes parallel to the substrate surface. TEM observations confirmed that the film presented a characteristic growth of zone II of the structure zone diagram (SZD) proposed by Thornton [44] and improved by Anders [45] with a preferential growth on the densest $\{101\}$ planes for the β grains.

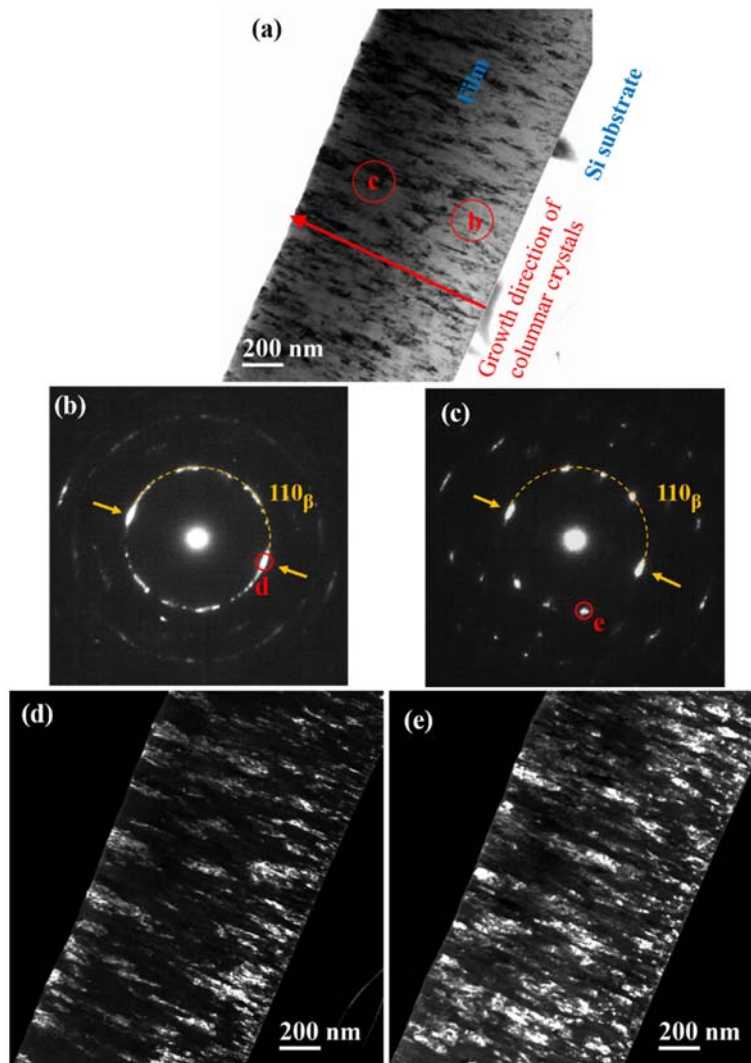


Fig. IV-8 (a) Cross sectional BF TEM image, (b, c) SAED patterns taken from the corresponding marked regions in (a), and (d, e) DF TEM images taken from the circled reflections in (b, c).

At first sight, α'' phase has not been confirmed from our TEM analysis. It is suggested that the TEM specimen preparation could contribute to the destabilization of the martensite phase leading to its disappearance (for example during ion milling bombardment). This has been also frequently observed for TEM preparations of superelastic bulk alloys. For the plane view TEM specimen (~ 30 nm thick) which has been directly observed, the following question remains: Does martensite form since the beginning of the film growth? It may be supposed that martensite formation occurs later when the stress state of the film tends to reach a more constant and stabilized regime.

IV.3.2 Superelastic properties

Fig. IV-9 shows four sets of $F-h$ curves obtained from nanoindentations of Ti16132 film at three selected maximum depth h_m of ~ 110 nm, ~ 200 nm and ~ 280 nm and for the three

spherical indenters Sp10, Sp50 and Sp200 and for the Bkv indenter.

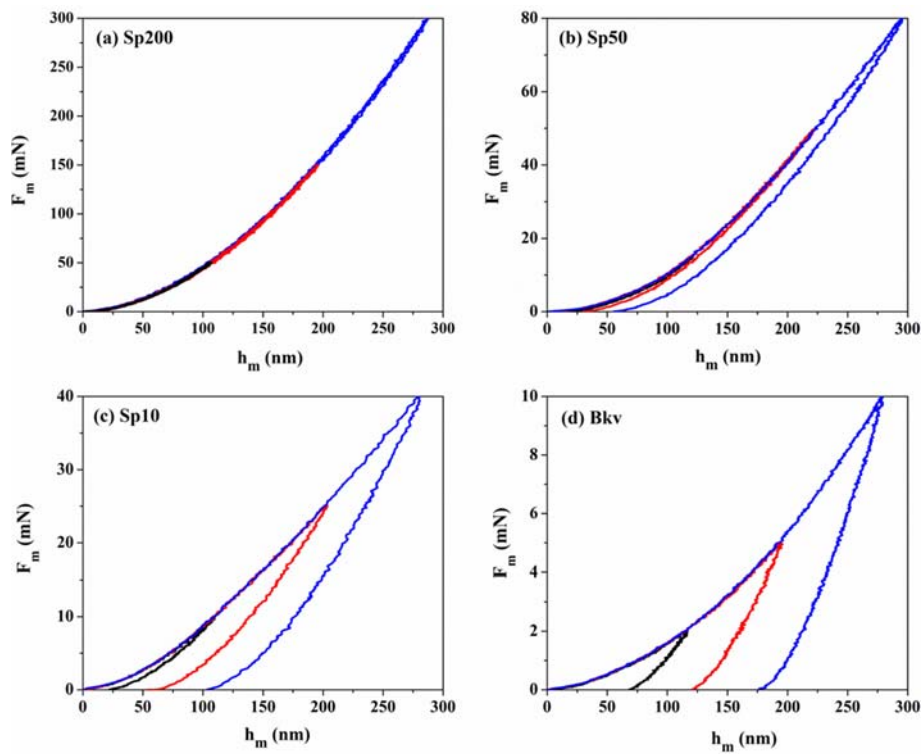


Fig. IV-9 Load-displacement (F - h) curves obtained during nanoindentations carried out at three different maximum depths h_m of ~ 110 nm (in black), ~ 200 nm (in red) and ~ 280 nm (in blue) using spherical indenters with different radii: (a) Sp200; (b) Sp50; (c) Sp10 and (d) Bkv indenter.

Normalized F - h curves (Fig. IV-10) were obtained from raw F - h curves (Fig. IV-9) by scaling the load and depth by their respective maximum load F_m and maximum indentation depth h_m . Thus, the non-dimensional F - h representation gives more sensitivity to unloading curves and allows a direct reading for η_h ratio as shown in Fig. IV-10d. Normalized F - h curves allow to emphasize the depth dependence of η_h and η_w ratios.

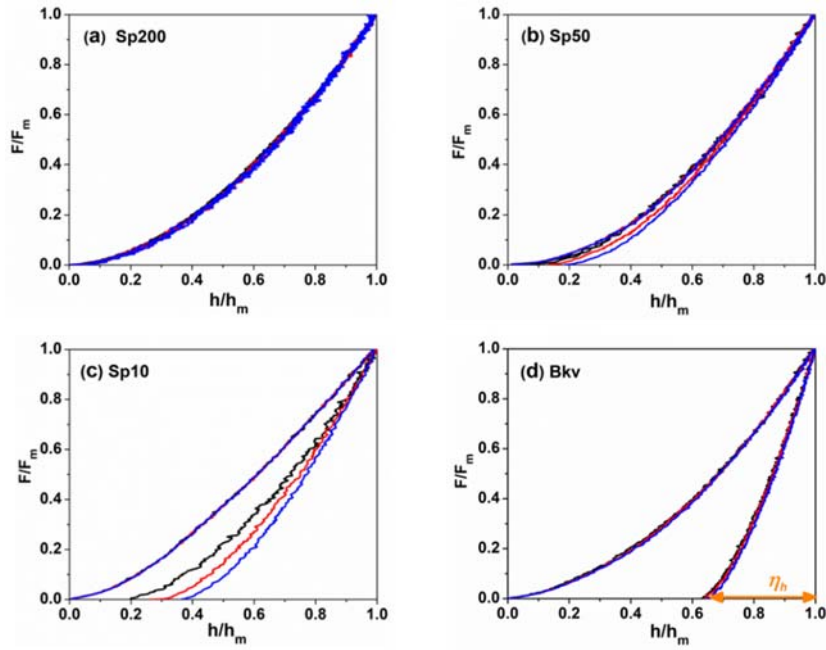


Fig. IV-10 Normalized load-displacement ($F-h$) curves corresponding to the $F-h$ curves in Fig. IV-9. Nanoindentations were conducted at three different maximum depths h_m of ~ 110 nm (in black), ~ 200 nm (in red) and ~ 280 nm (in blue) using spherical indenters with different radii: (a) Sp200); (b) Sp50; (c) Sp10 and (d) Bkv indenter.

The normalized $F-h$ curves for Sp200 indenter (Fig. IV-10a) show that nearly complete recoveries were achieved whatever the maximum penetration depth indicating that elastic deformation of parent β phase predominates under these loading conditions. It may also indicate that the large radius of Sp200 tip is rather unwieldy that cannot stimulate and probe superelasticity in the film. When the intermediate (Sp50) and small (Sp10) spherical indenters were used, the normalized $F-h$ curves (Fig. IV-10b and 10c) showed large recovery and depth dependence which is a characteristic of the occurrence of superelastic deformation. As mentioned earlier, for spherical indentations at equivalent penetration depths, the representative strain increases with the narrowness of the tip, and more accurately, it increases continuously with the area of contact between the tip and the film (Eq. (4)). The different tip radii offer the opportunity to vary the magnitude and the spatial distribution of the stress and strain fields for equivalent h_m . Moreover, it is recognized that superelastic performance is very sensitive to the applied strain level. The highest superelastic recovery strain in a given material is generally obtained for a narrow range of applied strain [9]. Those aspects confirm that nanoindentation equipped with appropriate indenters is a promising method for revealing whether or not the material can exhibit superelastic deformation and recovery.

For Bkv indentations, relatively limited recovery and very little depth dependence of normalized $F-h$ curves were observed (Fig. IV-10d). This is attributed to the fact that the indentation response is dominated by the high strain immediately developed beneath the Bkv

tip even at low applied loads, which is well beyond the strain levels that can be accommodated by superelastic deformation [27]. A sharp indenter will induce a fixed and large strain, which is independent of the depth of penetration (Eq. (3)). Under such condition, superelasticity is not expected to be possible.

The phase transformation behavior occurring during nanoindentation at nanometer scales is strongly dependent on local microstructural variations such as grain boundaries and crystal orientation [30]. In our nanocrystalline film, grain sizes are relatively small compared to the indent size and β grains have the unique and common $[110]_{\beta}$ orientation along the loading direction. Therefore, indentation responses of all indents presented in this work are supposed to be equally affected by grain boundaries and crystal orientation. In this way, mechanical features of our film were obtained from a very small and locally homogenized volume at microscale.

To further investigate the influence of indenter geometry and penetration depth h_m on the superelastic responses, a series of nanoindentation experiments at various h_m ranging from 50 nm to 330 nm were performed on Ti16132 film with the three spherical indenters Sp200, Sp50, Sp10 and with the Bkv indenter. The depth recovery η_h and work recovery η_w ratios were calculated as described earlier (Eqs. (1) and (2) from section IV.2.2) and plotted in Fig. IV-11 as a function of h_m for the four indenters.

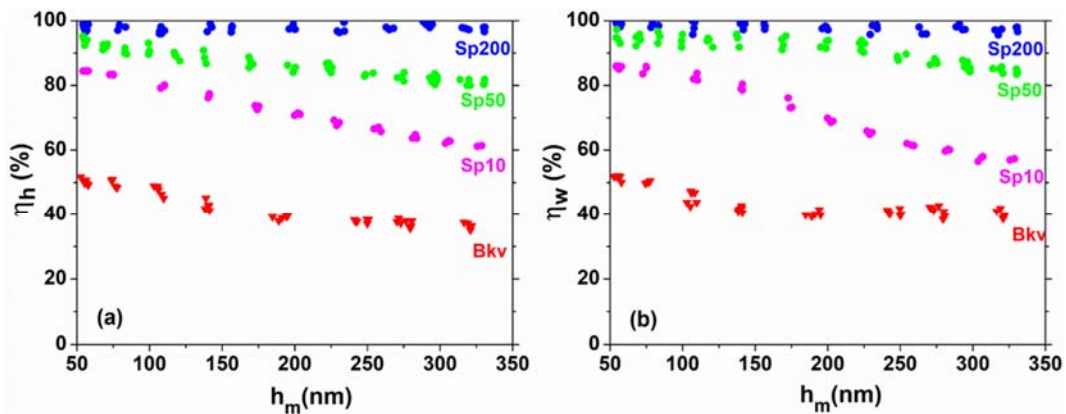


Fig. IV-11 Recovery ratios versus maximum indentation depth h_m for the three spherical indenters Sp200, Sp50 and Sp10 and for the Bkv indenter: (a) depth recovery ratio η_h and (b) work recovery ratio η_w .

For a given h_m , Ti16132 film exhibited higher depth and work recovery ratios under spherical indenters compared to those measured under Bkv indenter. The highest η_h and η_w ratios were observed with the Sp200 indenter, indeed values were nearly 100% for all h_m . In contrast, the decline in η_h and η_w ratios with h_m was more marked for Sp50 and Sp10 indenters. Recovery ratios range from 95% to 81% with Sp50 and from 85% to 60% with Sp10 for h_m

ranging from 50 nm to 330 nm. Such depth dependence of recovery ratios was also reported for spherical indentations of superelastic NiTi alloys using FEM modeling and nanoindentation experiments [29, 46]. As expected, the highest recovery values were obtained for the larger tip since the strain generated beneath spherical tip decreases with increasing tip radius. For Bkv indenter, η_h and η_w ratios are far below the values measured for spherical indenters. Recovery ratios remain below 50% and stabilize at 37% and 40% for η_h and η_w respectively when h_m exceeds 140 nm. Indeed, the high strain levels generated immediately beneath the Bkv tip even at low applied loads promote dislocations through conventional plastic deformation which in exchange limit the formation of martensite upon loading and inhibit its reversion upon unloading. Ni and al. already observed that recovery ratios of Bkv indentations at various h_m are depth independent [29]. The slightly higher values of recovery ratios measured at shallow depths during Bkv indentation can be attributed to a tip bluntness effect owing to the spherical end of the Bkv indenter tip [47]. The actual end shape of the Bkv indenter is not an ideally sharp triangular pyramid but typically exhibits a spherical end shape with a radius of curvature generally valued at around 100-150 nm [47, 48] and the repeated use aggravates the bluntness effect. Thus, when indentation depth is quite small and comparable to the tip radius of the apex, Bkv indentation closely approaches the spherical indentation in nature, demonstrating a depth dependence of recovery ratios as spherical indentations do. However, when the indentation depth exceeds the tip radius of the apex of Bkv indenter, the tip bluntness effect becomes insignificant and Bkv indentation retrieve the sharp indenter properties with constant recovery ratios.

IV.4 Discussion

The different nanoscale indentation responses obtained from the various tip geometries and at various h_m can be discussed in terms of imposed strain levels beneath the indenters. For that, the representative strain ε_r introduced into the film was calculated for each indenter used in this work using the formulae introduced earlier (Eq. (3) and Eq. (4) in section IV-2.2) and was plotted as a function of h_m in Fig. IV-12.

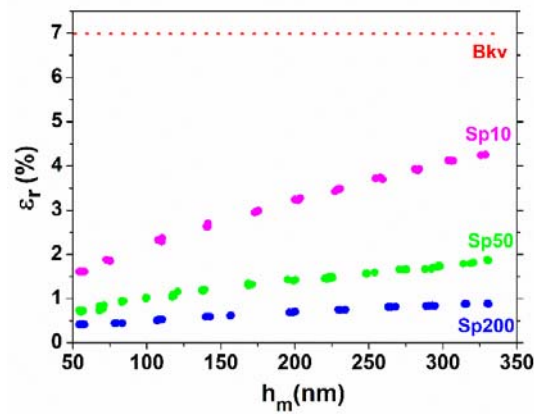


Fig. IV-12 Plot of the representative strain ϵ_r as a function of h_m for the three spherical indenters Sp200, Sp50, Sp10 and for the Bkv indenter.

The plot illustrates that ϵ_r depends greatly on the tip geometry. The sharper tip, the higher ϵ_r , which is also consistent with the predicted strain fields calculated from FEM simulations [27]. The bluntest Sp200 indenter generates the lowest ϵ_r from 0.4% to 0.9% for h_m ranging from 50 nm to 330 nm, followed by the intermediate Sp50 indenter and the small Sp10 indenter for which ϵ_r values range from 0.7% to 1.9% and from 1.6% to 4.3%, respectively, for h_m ranging from 50 nm to 330 nm. It can be seen that the ϵ_r under spherical indenters is far lower than that under ideally sharp Bkv indenter for which ϵ_r is considered depth independent and estimated to be around 7%. As mentioned above, actual Bkv indenter typically exhibits a spherical end tip with a radius of approximately 100-150nm, which represents the smallest and the sharpest tip radius when compared with those of the three spherical indenters used in this study. In this case, it is reasonable to conclude that ϵ_r is much higher under the sharp Bkv tip. Moreover, calculation of ϵ_r is, in some way, an average value of the imposed strain beneath the indenter tip and it is also well established that the spatial distribution of stress and strain fields in the material underneath a sharp indenter such as the Bkv tip is much steeper than in the case of spherical indenters [27]. Therefore, it is generally considered that Berkovich geometry produces very localized high stress and high strain regions within the material underneath the tip. Using FEM modeling, Ni and al. [29] showed that the maximum equivalent plastic strain under ideally sharp pyramidal indenter is approximately three times higher than that under spherical indents at equivalent ϵ_r of 8%. Considerable differences exist in the magnitude and spatial distribution of stress and strain fields between the spherical and pyramidal geometries [27]. In selecting different indenter shape and size, it is possible to investigate the nanoscale indentation behavior of small volumes of material over a wide range of representative strains (from 0.4% to 7% in the present work).

Fig. IV-13 presents the measured η_h and η_w recovery ratios as a function of the calculated

ε_r . It is evident that recovery ratios decrease with the strain level. For small strains, $\varepsilon_r \leq 1\%$, nearly 100% recoveries were obtained during spherical indentations with Sp200 indenter. As ε_r increases, recovery ratios decrease continuously from 95% to 60% for ε_r between 1% and 4.3% during spherical indentations with Sp50 and Sp10 indenters, and even decrease to 40% for ε_r of 7% during Bkv indentations. One can note the break on the X-axes of Fig. IV-13 to place the recovery ratios measured with Bkv indenter.

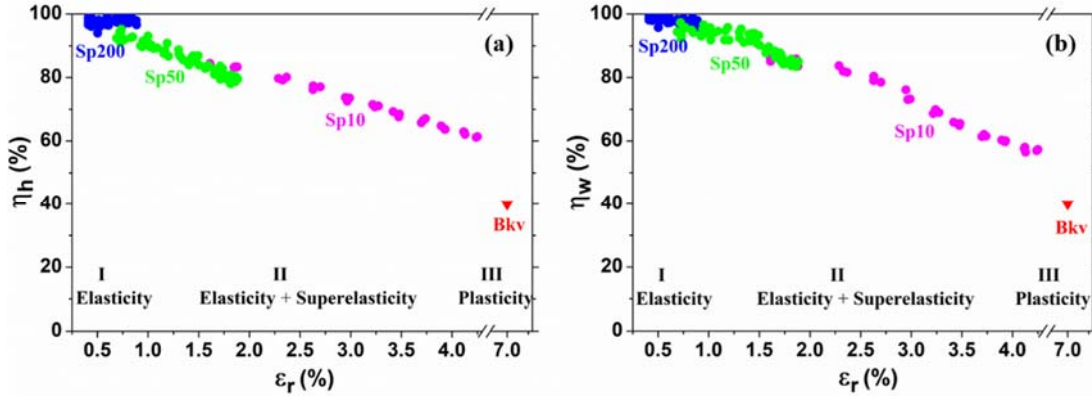


Fig. IV-13 Plots of the recovery ratios as a function of the calculated ε_r for the three spherical indenters Sp200, Sp50 and Sp10 and for the Bkv indenter: (a) η_h and (b) η_w .

Owing to the various indenters used in this work, ε_r was varying continuously from 0.4% to 4.3%, and thereafter up to 7%, allowing the study of the indentation response of our film through different deformation regimes. Results may be described in a three-stage evolution: (I) elastic regime; (II) elasto-plastic regime for which the response of the superelastically deformed region predominates; and (III) elasto-plastic regime with prominent plastic deformation. At low strain state ($\varepsilon_r \leq 1\%$), the imposed strain was fully accommodated by the elastic deformation of the matter underneath the Sp200 tip as illustrated by the complete indent recovery upon unloading shown in Fig. IV-14b, on the AFM image after Sp200 indentation at $h_m = 280$ nm. As the imposed strain was increased ($1\% \leq \varepsilon_r \leq 4.3\%$), relatively large recovery ratios were observed ranging from 95% to 60%. Plastic deformation appeared to occur progressively leading to the continuous decrease of η_h and η_w ratios during Sp50 and Sp10 indentations.

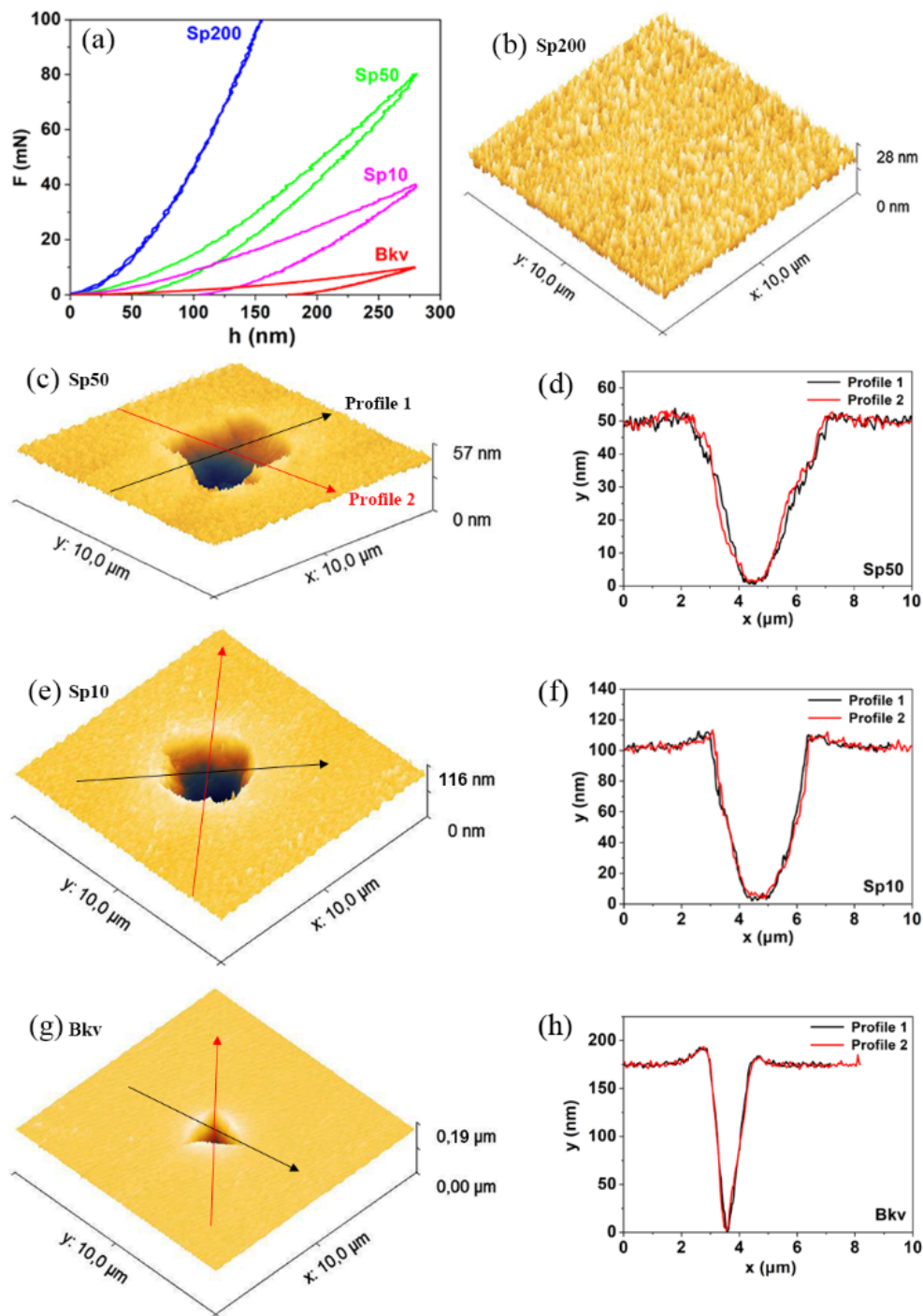


Fig. IV-14 (a) F-h nanoindentation curves obtained for fixed maximum penetration depth ($h_m = 280$ nm) using the three spherical indenters Sp200, Sp50 and Sp10 and the Bkv indenter. And the corresponding recoveries of indentation depths (after indentation at $h_m = 280$ nm) observed using AFM: (b) for the Sp200 indenter, $\varepsilon_r = 0.8\%$; (c) for the Sp50 indenter, $\varepsilon_r = 1.7\%$ and (d) the corresponding depth profiles; (e) for the Sp10, $\varepsilon_r = 3.9\%$ and (f) the corresponding depth profiles; (g) for the Bkv indenter, $\varepsilon_r = 7\%$ and (h) the corresponding depth profiles.

Figs. IV. 14c - 14e display nanoindentation imprints after Sp50 indentation ($\varepsilon_r = 1.7\%$) and after Sp10 indentation ($\varepsilon_r = 3.9\%$) with both at $h_m = 280$ nm and their corresponding depth cross-sectional profiles evidencing that for a fixed h_m , the permanent indent depth, h_p , has

increased progressively with the imposed strain. It may be noted here that h_p was 50 nm for the Sp50 indentation at $\varepsilon_r = 1.7\%$ and h_p was 104 nm for the Sp10 indentation at $\varepsilon_r = 3.9\%$. In this way, plastic deformation still remains the minor mechanism while superelastic deformation with reversible and stress-induced martensitic transformation is supposed to be the predominant deformation mechanism for ε_r between 1% and 4.3%. Subsequently, the increasing amount of dislocations has restricted additional formation of martensite upon loading and impeded the reverse transformation of the existent martensite upon unloading since the high density of dislocations stabilized both the parent β phase and the existent martensite [49]. When the local stress exceeds the yield stress of martensite, permanent deformation occurs leading to the stabilization of martensite. The stress relaxation arising from plastic deformation also reduces the driving force for phase transformation. Thus, the increasing imposed strain reduces progressively the superelastic response due to an increased volume fraction of dislocations and stabilized martensite. When ε_r was increased to $\sim 7\%$ during Bkv indentations, immediate plastic deformation of parent β phase was supposed to occur beneath the tip and large permanent depths persisted upon unloading as shown in Figs. IV.14g-14h for which a very high residual depth of 176 nm was observed still for the same maximum depth h_m of 280 nm. The 37% of η_h and the 40% of η_w measured for Bkv indentations were contributed by the elastic strain relaxation of mainly parent β phase and some martensite from the outer region.

Until now, discussion was focused on differences in the unloading data including calculation of the recovery ratios for the various indenter geometries. Indeed, unloading curves reflect contribution of the lattice relaxation and contribution of the reverse martensitic transformation. Nevertheless, there were also significant differences in the loading portions of the raw $F-h$ curves depending on the indenter geometry. Fig. IV-14a displays the raw $F-h$ curves measured at $h_m = 280$ nm for the three Sp10, Sp50 and Sp200 spherical indenters and for the Bkv indenter. One can note that only the front end of the $F-h$ curve for the Sp200 indenter is visible at the selected scale. This plot displays a clear divergence between the loading behaviors depending on the indenter geometry. Loading curves reflect accommodation of the imposed deformation primarily through elastic strains and then through phase transformation (martensite formation) and through plastic process (dislocation motion). In this way, three indentation regimes may be reappointed: (i) prominent elastic deformation of β phase with the Sp200 indenter; (ii) mainly elastic and superelastic deformations with Sp50 and Sp10 indenters; and (iii) predominant plastic deformation with Bkv indenter.

Interpreting the measured indentation response which is as such difficult for conventional

elasto-plastic materials due to the complex loading conditions imposed during nanoindentation experiment involving inhomogeneous distribution of stress and strain fields underneath the indenter tip and the constantly evolving probing volume, becomes even more complex when simultaneous superelastic deformation (i.e. phase transformation) occurs in conjunction with elastic and plastic deformation. Many efforts have been made to depict the deformation process during nanoindentation. Fischer-Cripps [50] introduced the normalized contact stress distribution to quantitatively determine the deformation characteristics and showed that the severe stress concentration beneath the sharp Berkovich indenter results in larger plastic zone than under spherical indenter. The stress-affected indentation volume has approximately a spherical shape whatever the tip geometry and the affected volume under spherical indenter is significantly greater than that for Berkovich indenter at the same penetration depth [51]. Crone et al. [52] firstly illustrated the deformation process occurring beneath the indenter tip for superelastic NiTi films by a series of three concentric shells: a plastic deformation region, a stress-induced martensitic transformation region and an elastic deformation region as the stress level decays further away from the tip. Maletta et al. [53] and Kan et al. [54] carried out FEM simulations to investigate the microstructural evolution due to the phase transition in the indentation region by comparing the Von Mises equivalent stress with the characteristic transformation stresses (see section I.3.1) of superelastic alloys. They described the deformation process occurring beneath the indenting tip as a series of four concentric shells: a fully transformed martensite zone plastically deformed in the region nearest the indenter tip, a fully transformed and reversible martensite region further from the indenter tip, a partial transformation zone still further away from the indenter tip and a fully untransformed parent β phase zone. It has been shown that the magnitude and spatial distribution of the evolving strain field in the indentation region is strongly affected by the indenter geometry [27, 29]. The present study used four indenters with different geometries to investigate the contribution of the superelastic response over a large range of representative strain. Fig. IV-15 presents an overview of our measurements coupled with a schematic representation of the evolution of the predominant deformation mechanisms with respect to the representative strain imposed and to the indenter geometry.

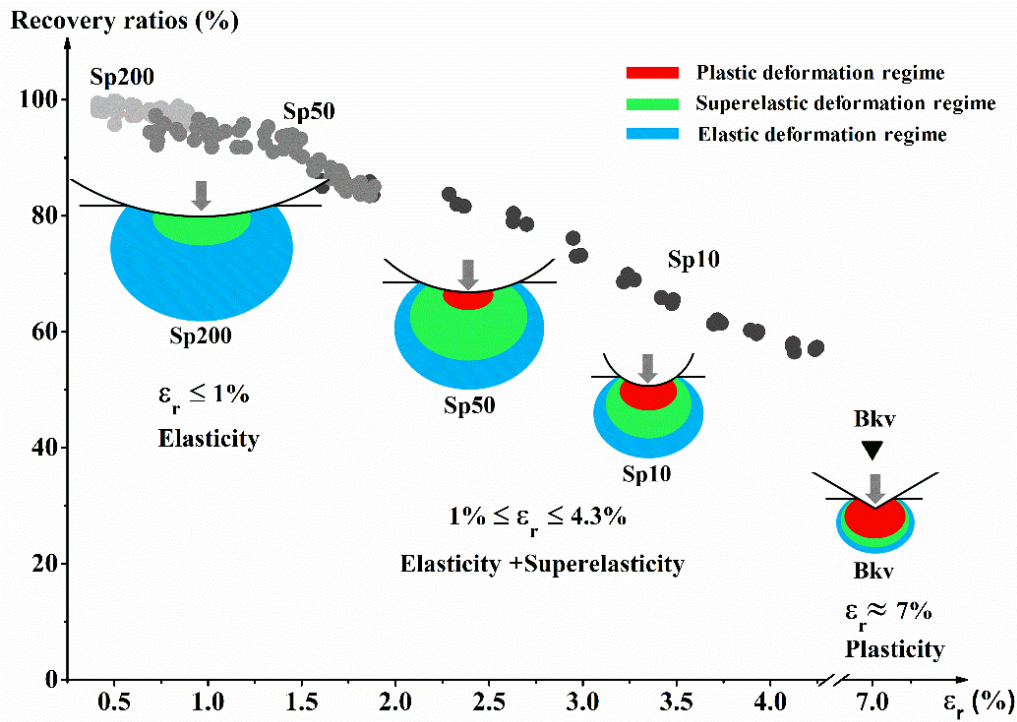


Fig. IV-15 Schematic representation of the prominent deformation mechanisms occurring underneath the indenter tip as the load is applied to the film surface with respect to the representative strain ϵ_r and to the indenter geometry.

Results showed the importance of selecting the appropriate representative strain window to reveal superelasticity. Under Bkv indenter, the response of the material is dominated by regions of high strains generated immediately under the tip and for which strain levels exceed those which can be accommodated by elastic and superelastic deformations leading to the large predominance of the plastic deformation during Berkovich indentation. Using a large spherical tip, such as the Sp200 indenter, it does not seem the most appropriate to deal with superelasticity due to the expanded strain field beneath the tip which is of considerably lower level and promotes the prevalence of the conventional elastic deformation of the parent β phase. Indenting with intermediate spherical tip, such as Sp50 and Sp10 indenters, is a viable strategy to reveal the superelasticity of materials at micro- and nano-meter length scales by ensuring that the straining is in the competitive regime between superelastic and plastic deformations.

IV.5 Conclusion

A new quaternary Ti-16Zr-13Nb-2Sn (at.%) film was elaborated by magnetron sputtering at room temperature from a single alloyed target. The film displays nanograined microstructure with relatively compact and smooth morphology. The films were composed of mainly metastable β phase with preferential growth orientation along [110] direction and of some α'' martensite phase. The lattice parameters for β and α'' phases were calculated as: a_β

$=3.39 \text{ \AA}$; $a_{\alpha''} = 3.29 \text{ \AA}$, $b_{\alpha''} = 4.88 \text{ \AA}$ and $c_{\alpha''} = 4.78 \text{ \AA}$. In-plane pole figure measurements for the bcc β structure are presented in ring patterns, and an intensified center appears in the $\{110\}_{\beta}$ pole figure, showing the in plane polycrystalline microstructure and the $\langle 110 \rangle_{\beta}$ fiber texture of the β grains in the our Ti16132 film.

The superelastic response of the Ti16132 film was examined in light of nanoindentation experiments by measuring the depth and work recovery ratios from the load-displacement curves for various penetration depths. Results were discussed with regard to the calculation of the representative strain (ϵ_r). Owing to the four different indenters employed in this work, representative strain was varying continuously from 0.4% to 4.3% using three spherical indenters with tip radii of 200 μm (Sp200), 50 μm (Sp50) and 10 μm (Sp10), and thereafter up to 7% with the Berkovich (Bkv) indenter. The nanoscale indentation behavior of Ti16132 film was significantly affected by the indenter geometry due to the large differences in the magnitude and spatial distribution of the strains developed beneath each indenter tip.

Using the Bkv indenter, almost no depth dependence of recovery ratios was observed. The constant and high representative strain ($\epsilon_r \sim 7\%$) imposed whatever the applied loads was beyond the level that can be accommodated by superelastic deformation leading to restricted recovery ratio measurements as low as 40%. Such conditions promote plastic deformation resulting in high density of dislocations which contribute to both limit the formation of martensite and inhibit its subsequent reversion to the parent β phase.

In contrast, the representative strain imposed during spherical indentations is depth dependent with respect to the indenter radius allowing to encompass the different deformation regimes from elastic to elasto-plastic regimes. Nearly 100% recovery ratios were measured with the large radius spherical indenter (Sp200) which imposed relative low representative strain ($0.4\% \leq \epsilon_r \leq 1\%$) and probed predominately elastic deformation. Large recovery ratios ranging from 95% to 60% were measured with Sp50 and Sp10 indenters for ϵ_r between 1% and 4.3%. Plastic deformation is then still the minor mechanism while superelastic deformation with reversible and stress-induced martensitic transformation is the predominant deformation mechanism. Indenting with intermediate spherical tips, such as Sp50 and Sp10 indenters, is a viable strategy to reveal the superelastic response of materials in the micro- and nano-meter length scales by ensuring that the straining is in the competitive regime between superelastic and plastic deformations.

The present work shows the importance of considering the appropriate indentation depth window associated to the indenter tip radius to reveal the superelastic behavior of materials

on the nanoscale. Superelastic performance is very sensitive to the applied strain level and spherical indentations offer the opportunity to determine at the local scale the strain levels under which small volumes of material would perform local superelastic deformation and recovery.

References:

- [1] P. Castany, A. Ramarolahy, F. Prima, P. Laheurte, C. Curfs, T. Gloriant, In situ synchrotron X-ray diffraction study of the martensitic transformation in superelastic Ti-24Nb-0.5 N and Ti-24Nb-0.5 O alloys, *Acta Materialia*, 88 (2015) 102-111.
- [2] Y. Hao, S. Li, S. Sun, R. Yang, Effect of Zr and Sn on Young's modulus and superelasticity of Ti-Nb-based alloys, *Materials Science and Engineering: A*, 441 (2006) 112-118.
- [3] Y. Hao, S. Li, S. Sun, C. Zheng, R. Yang, Elastic deformation behaviour of Ti-24Nb-4Zr-7.9 Sn for biomedical applications, *Acta Biomaterialia*, 3 (2007) 277-286.
- [4] Y. Yang, P. Castany, M. Cornen, F. Prima, S. Li, Y. Hao, T. Gloriant, Characterization of the martensitic transformation in the superelastic Ti-24Nb-4Zr-8Sn alloy by in situ synchrotron X-ray diffraction and dynamic mechanical analysis, *Acta Materialia*, 88 (2015) 25-33.
- [5] J. Fu, A. Yamamoto, H.Y. Kim, H. Hosoda, S. Miyazaki, Novel Ti-base superelastic alloys with large recovery strain and excellent biocompatibility, *Acta Biomaterialia*, 17 (2015) 56-67.
- [6] S. Li, Y.-w. Kim, M.-s. Choi, T.-h. Nam, Superelastic Ti-18Zr-12.5 Nb-2Sn (at.%) alloy scaffolds with high porosity fabricated by fiber metallurgy for biomedical applications, *Intermetallics*, 115 (2019) 106631.
- [7] J. Gao, I. Thibon, P. Castany, T. Gloriant, Effect of grain size on the recovery strain in a new Ti-20Zr-12Nb-2Sn superelastic alloy, *Materials Science and Engineering: A*, (2020) 139878.
- [8] L.L. Pavón, H.Y. Kim, H. Hosoda, S. Miyazaki, Effect of Nb content and heat treatment temperature on superelastic properties of Ti-24Zr-(8-12) Nb-2Sn alloys, *Scripta Materialia*, 95 (2015) 46-49.
- [9] S. Li, T.-h. Nam, Superelasticity and tensile strength of Ti-Zr-Nb-Sn alloys with high Zr content for biomedical applications, *Intermetallics*, 112 (2019) 106545.
- [10] S. Miyazaki, A. Ishida, Martensitic transformation and shape memory behavior in sputter-deposited TiNi-base thin films, *Materials Science and Engineering: A*, 273 (1999) 106-133.
- [11] H. Rumpf, T. Walther, C. Zamponi, E. Quandt, High ultimate tensile stress in nano-grained superelastic NiTi thin films, *Materials Science and Engineering: A*, 415 (2006) 304-308.
- [12] X.-G. Ma, K. Komvopoulos, Pseudoelasticity of shape-memory titanium-nickel films subjected to dynamic nanoindentation, *Applied Physics Letters*, 84 (2004) 4274-4276.
- [13] K. Li, Y. Li, K. Yu, C. Liu, D. Gibson, A. Leyland, A. Matthews, Y.Q. Fu, Crystal size induced reduction in thermal hysteresis of Ni-Ti-Nb shape memory thin films, *Applied Physics Letters*, 108 (2016) 171907.
- [14] S. Achache, S. Lamri, M.A.P. Yazdi, A. Billard, M. François, F. Sanchette, Ni-free superelastic binary Ti-Nb coatings obtained by DC magnetron co-sputtering, *Surface and Coatings Technology*, 275 (2015) 283-288.
- [15] X.L. Meng, B. Sun, J.Y. Sun, Z.Y. Gao, W. Cai, L.C. Zhao, Microstructure and shape memory behavior of Ti-Nb shape memory alloy thin film, *Shape Memory and Superelasticity*, 3 (2017) 230-237.
- [16] M. Baatarsukh, J. Bae, S. Huh, H. Jeong, B. Choi, G. Cho, T. Nam, J. Noh, Composition Dependence of the β Phase Stability and Mechanical Properties of Ti-Nb Thin Films, *Journal of Nanoscience and Nanotechnology*, 19 (2019) 3627-3630.
- [17] J. Yang, M. Baatarsukh, J. Bae, S. Huh, H. Jeong, B. Choi, T. Nam, J. Noh, Phase stability and properties of Ti-Nb-Zr thin films and their dependence on Zr addition, *Materials*, 11 (2018) 1361.

- [18] S. Achache, S. Lamri, A. Alhoussein, A. Billard, M. François, F. Sanchette, Gum Metal thin films obtained by magnetron sputtering of a Ti-Nb-Zr-Ta target, *Materials Science and Engineering: A*, 673 (2016) 492-502.
- [19] N.T.P. D. Photiou, L. Koutsokeras, G.A. Evangelakis, G. Constantinides Microstructure and nanomechanical properties of magnetron sputtered Ti-Nb film, *Surface & Coatings Technology* 302 (2016) 310–319, (2016).
- [20] J. Málek, V. Starý, The correlation between substrate and deposited biocompatible layer microstructures on different substrates, *Applied Surface Science*, 459 (2018) 114-119.
- [21] C.R.M.A. E.D. Gonzalez, Pedro A.P. Nascente, Influence of Nb content on the structure, morphology, nanostructure, and properties of titanium-niobium magnetron sputter deposited coatings for biomedical applications, *Surface & Coatings Technology* 326 (2017) 424–428, (2017).
- [22] D. Tallarico, A. Gobbi, P. Paulin Filho, M.M. da Costa, P. Nascente, Growth and surface characterization of TiNbZr thin films deposited by magnetron sputtering for biomedical applications, *Materials Science and Engineering: C*, 43 (2014) 45-49.
- [23] E. Frutos, M. Karlík, J.A. Jiménez, H. Langhansová, J. Lieskovská, T. Polcar, Development of new β/α Ti-Nb-Zr biocompatible coating with low Young's modulus and high toughness for medical applications, *Materials & Design*, 142 (2018) 44-55.
- [24] X.-H. Yan, J. Ma, Y. Zhang, High-throughput screening for biomedical applications in a Ti-Zr-Nb alloy system through masking co-sputtering, *SCIENCE CHINA Physics, Mechanics & Astronomy*, 62 (2019) 996111.
- [25] J. Musil, A. Bell, J. Vlček, T. Hurkmans, Formation of high temperature phases in sputter deposited Ti-based films below 100 C, *Journal of Vacuum Science & Technology A: Vacuum, Surfaces, and Films*, 14 (1996) 2247-2250.
- [26] M.F. Ijaz, H.Y. Kim, H. Hosoda, S. Miyazaki, Effect of Sn addition on stress hysteresis and superelastic properties of a Ti-15Nb-3Mo alloy, *Scripta Materialia*, 72 (2014) 29-32.
- [27] A.M. Wood, T. Clyne, Measurement and modelling of the nanoindentation response of shape memory alloys, *Acta materialia*, 54 (2006) 5607-5615.
- [28] R. Liu, D. Li, Y. Xie, R. Llewellyn, H. Hawthorne, Indentation behavior of pseudoelastic TiNi alloy, *Scripta Materialia*, 41 (1999) 691-696.
- [29] W. Ni, Y.-T. Cheng, D.S. Grummon, Microscopic shape memory and superelastic effects under complex loading conditions, *Surface and Coatings Technology*, 177-178 (2004) 512-517.
- [30] H. Jabir, A. Fillon, P. Castany, T. Gloriant, Crystallographic orientation dependence of mechanical properties in the superelastic Ti-24Nb-4Zr-8Sn alloy, *Physical Review Materials*, 3 (2019) 063608.
- [31] V. Shastry, U. Ramamurty, Simultaneous measurement of mechanical and electrical contact resistances during nanoindentation of NiTi shape memory alloys, *Acta Materialia*, 61 (2013) 5119-5129.
- [32] Y. Zhou, A. Fillon, H. Jabir, D. Laillé, T. Gloriant, Investigation of the superelastic behavior of a Ti-16Zr-13Nb-2Sn sputtered film by nanoindentation, *Surface and Coatings Technology*, (2020) 126690.
- [33] K.L. Johnson, K.L. Johnson, *Contact mechanics*, Cambridge university press, 1987.
- [34] D. Tabor, *The hardness of metals*, Oxford university press, 2000.
- [35] L. Min, C. Wei-Min, L. Nai-Gang, W. Ling-Dong, A numerical study of indentation using indenters of different geometry, *Journal of Materials Research*, 19 (2004) 73-78.

- [36] W.C. Oliver, G.M. Pharr, An improved technique for determining hardness and elastic modulus using load and displacement sensing indentation experiments, *Journal of Materials Research*, 7 (1992) 1564-1583.
- [37] S. Habib, A. Rizk, I. Mousa, Physical parameters affecting deposition rates of binary alloys in a magnetron sputtering system, *Vacuum*, 49 (1998) 153-160.
- [38] Y. Yamamura, H. Tawara, Energy dependence of ion-induced sputtering yields from monatomic solids at normal incidence, *Atomic data and nuclear data tables*, 62 (1996) 149-253.
- [39] X. Feng, G. Tang, M. Sun, X. Ma, L. Wang, K. Yukimura, Structure and properties of multi-targets magnetron sputtered ZrNbTaTiW multi-elements alloy thin films, *Surface and Coatings Technology*, 228 (2013) S424-S427.
- [40] F. Sanchette, L. Tran Huu, A. Billard, C. Frantz, Structure—properties relationship of metastable Al-Cr and Al-Ti alloys deposited by r.f. magnetron sputtering: role of nitrogen, *Surface and Coatings Technology*, 74-75 (1995) 903-909.
- [41] J. Pelleg, L. Zevin, S. Lungo, N. Croitoru, Reactive-sputter-deposited TiN films on glass substrates, *Thin Solid Films*, 197 (1991) 117-128.
- [42] B. Rauschenbach, J. Gerlach, Texture development in titanium nitride films grown by low-energy ion assisted deposition, *Crystal Research and Technology: Journal of Experimental and Industrial Crystallography*, 35 (2000) 675-688.
- [43] E. Frutos, M. Karlík, J.A. Jiménez, H. Langhansová, J. Lieskovská, T. Polcar, Development of new β/α'' -Ti-Nb-Zr biocompatible coating with low Young's modulus and high toughness for medical applications, *Materials & Design*, 142 (2018) 44-55.
- [44] J.A. Thornton, Influence of apparatus geometry and deposition conditions on the structure and topography of thick sputtered coatings, *Journal of Vacuum Science and Technology*, 11 (1974) 666-670.
- [45] A. Anders, A structure zone diagram including plasma-based deposition and ion etching, *Thin Solid Films*, 518 (2010) 4087-4090.
- [46] Y. Zhang, Y.-T. Cheng, D.S. Grummon, Finite element modeling of indentation-induced superelastic effect using a three-dimensional constitutive model for shape memory materials with plasticity, *Journal of Applied Physics*, 101 (2007) 053507.
- [47] G.A. Shaw, D.S. Stone, A.D. Johnson, A.B. Ellis, W.C. Crone, Shape memory effect in nanoindentation of nickel–titanium thin films, *Applied Physics Letters*, 83 (2003) 257-259.
- [48] J. Čech, P. Haušild, O. Kovářik, A. Materna, Examination of Berkovich indenter tip bluntness, *Materials & Design*, 109 (2016) 347-353.
- [49] J. Anuja, R. Narasimhan, U. Ramamurty, Effects of superelasticity and plasticity on the spherical indentation response of shape memory alloys: a finite element analysis, *Smart Materials and Structures*, 28 (2019) 035028.
- [50] A.C. Fischer-Cripps, *Introduction to contact mechanics*, Springer, 2007.
- [51] V. Králík, J. Němeček, Comparison of nanoindentation techniques for local mechanical quantification of aluminium alloy, *Materials Science and Engineering: A*, 618 (2014) 118-128.
- [52] W. Crone, G. Shaw, D. Stone, A. Johnson, A. Ellis, Shape recovery after nanoindentation of NiTi thin films, in: *Proceedings of the SEM Annual Conference on Experimental Mechanics*, Citeseer, 2003.

[53] C. Maletta, F. Furgiuele, E. Sgambitterra, M. Callisti, B. Mellor, R. Wood, Indentation response of a NiTi shape memory alloy: modeling and experiments, *Frattura ed Integrità Strutturale*, 6 (2012) 5-12.

[54] Q. Kan, W. Yan, G. Kang, Q. Sun, Oliver–Pharr indentation method in determining elastic moduli of shape memory alloys—A phase transformable material, *Journal of the Mechanics and Physics of Solids*, 61 (2013) 2015-2033.

**Chapter V: Microstructure and local
mechanical properties in superelastic Ti-
24Nb-4Zr-8Sn film**

V.1 Introduction

Metastable β -Ti alloys only composed of biocompatible β -stabilizer elements have demonstrated outstanding superelastic behavior in recent studies [1-4]. Biocompatible alloys with specific functionalities such as superelasticity are highly required for the fabrication of biomedical devices such as cardiovascular stents, heart valves, blood filters, and guide wires for catheters, orthodontic arch wires, rod and screw fixations... The superelasticity is a visually striking phenomenon whereby a material is able to recover its initial shape after significant deformation and through subsequent unloading. The superelastic effect involves a solid-state phase transition known as reversible and stress-induced martensitic (SIM) transformation between the parent β phase (bcc structure) and the α'' martensite phase (orthorhombic structure).

The metastable β Ti-24Nb-4Zr-8Sn (wt. %; abbreviated as Ti2448) alloy primarily designed by Hao et al [5, 6] for biomedical applications, is a low Young's modulus (42 GPa), high strength (>800 MPa), good corrosion and high recoverable strain (3.3%) alloy [7-11]. In terms of the superelasticity of the solution treated Ti2448 alloys, Yang et al. [7] characterized the martensitic transformation by *in situ* synchrotron X-ray diffraction during tensile tests and by dynamic mechanical analysis and have highlighted the reversible SIM Transformation occurring in this bulk alloy. In another work, Yang et al. [12] showed that the $\langle 110 \rangle_{\beta}$ Ti2448 single crystal exhibited a maximum recoverable strain of 4.2% at the applied tensile strain of 4.5% and revealed the sequence of deformation in this single crystal as following: (i) during loading, the β phase firstly transforms into α'' martensite; (ii) when this transformation was fully accomplished, $\{110\} \langle 110 \rangle_{\alpha''}$ twins were formed in the α'' martensite during subsequent plastic deformation, as well as dislocation slip occurs; (iii) when the stress was removed from the plastic deformation range, the reverse transformation from α'' to β phase occurred; (iv) the α'' martensite twins thus reversed into a deformation band exhibiting a $\{112\} \langle 111 \rangle_{\beta}$ twinning relationship; (v) a thin layer of ω phase lying along the twin boundary is also formed in order to relax the compressive stress accompanying this reverse transformation. Yang et al. [13] recently reported that the main plastic deformation mechanism in the solution-treated Ti2448 polycrystalline alloy was hierarchical and nano-sized martensitic twinning complementing the conventional dislocation slip.

The increasing demands for the development of thin film micro-devices have stimulated the research activities related to the mechanical properties and deformation behavior of

superelastic films, mainly in NiTi-based films [14-16]. Research has demonstrated that the crucial factors which determine the applicability of these alloy films are the transformation temperature and the amount of recoverable strain, both are strongly dependent on metallurgical factors such as alloy composition [17], thermal treatment [16, 18, 19], deposition parameters (pressure, target power, substrate temperature, bias, etc.) [20].

Nanoindentation has emerged as a convenient technique for the local characterization of mechanical properties of thin films at small length scale. Specifically, this technique can reveal the superelasticity in functional materials when an appropriated stress-strain condition is applied by choosing suitable indenter geometry and penetration depth window, as discussed in chapters III and IV. In the present study, the nanoscale deformation behavior of Ti2448 films was investigated through a large range of stress-strain levels using four different indenters, i.e., Berkovich tip and 200-, 50-, and 10- μm radius spherical tip. The instrumented nanoindentation digitally records forces and displacements during the indentation process. Many information can be extracted from the force-displacement ($F-h$) curves, such as contact stiffness S , indentation hardness H_{IT} and elastic modulus E_{IT} through Oliver and Pharr model [21, 22]. Since the nanoindentation instrument is associated to an accurate X-Y motorized table, large regular indentation arrays were performed for different maximum loads and maximum penetration depths.

The depth-dependency of indentation hardness H_{IT} is a well-known and active research topic for which some questions still remain open. In literature, experimental results show that the indentation hardness measured using Bkv indenter increases with decreasing indentation load, known as indentation size effect (ISE). Fleck *et al.* [23] pointed out that this phenomenon can be explained by a strain localization theory. Nix and Gao [24] used the simple model of geometrically necessary dislocations to describe the depth dependency of indentation hardness and to explain the ISE in crystalline materials. This model leads to a characteristic relation for the depth dependence of hardness: $H_{IT}/H_0 = \sqrt{1 + h^*/h_m}$, where H_{IT} is the indentation hardness for a given indentation depth h_m , H_0 is the hardness in the limit of infinite depth and h^* is a characteristic length. Rewriting this equation as: $H_{IT}^2 = H_0^2 (1 + h^*/h_m)$, a linear relationship would be found in a plot of H_{IT}^2 vs. h_m^{-1} . This relation is well-obeyed on most ductile metallic materials where plasticity is the dominant deformation mechanism, i.e., copper [25, 26]. However, for superelastic materials that can react to mechanical loads through solid-state phase transition, the occurrence of the phase transformation during indentation may have substantial effects on the measurements of indentation hardness, resulting in a large

deviation from the phenomena in ordinary ductile materials. Animi *et al.* [27] conducted the measurements on the hardness-depth relationship of superelastic NiTi with spherical indenter. The spherical hardness (H_{IT-sph}) increased with depths. This behavior is contrary to the decrease in the Bkv hardness H_{IT-Bkv} with depths and the depth-insensitive H_{IT-sph} in ordinary ductile metals [28]. The indentation hardness of materials involving phase transitions is not only an indicator of the resistance to plastic deformation, but also an indicator of the resistance to phase transition [29].

Elastic modulus E_{IT} can be calculated from the unloading part of the nanoindentation curve. In most ductile materials, the Oliver and Pharr analysis allows the evaluation of E_{IT} based on the assumption that during unloading the response is entirely elastic. However, this assumption is not valid for superelastic materials, since reversible SIM transformation can be activated during unloading.

This provides the basics for a challengeable and interesting subject to analyze the influence of phase transition (the stress-induced martensitic transformation in the present work) on the measurement of E_{IT} and H_{IT} . To our knowledge, the nanoscale indentation behavior of metastable β -Ti films has not been systematically investigated. Particularly, an in-depth understanding of the underlying deformation mechanisms that are responsible for the depth-dependent behaviors of indentation hardness H_{IT} and elastic modulus E_{IT} in metastable β -Ti films subjected to nanoindentations with various indenters has not been obtained yet.

In the present study, metastable β -Ti2448 film was elaborated by magnetron sputtering at room temperature and its microstructural properties were studied. Nanoindentation measurements were performed using spherical tips with different radii and Berkovich tip at various applied loads to systematically characterize SIM transformation in the Ti2448 film at the nanoscale. The depth dependences of the indentation depth-, work-recovery ratios, indentation hardness and elastic modulus were investigated in the metastable β -Ti2448 film with a specific attention to the phase transition, with the aim of providing a better understanding of the mechanisms that govern the functional properties of metastable β Ti-based superelastic films.

V.2 Experimental protocol

Quaternary Ti-24Nb-4Zr-8Sn (wt. %) films were deposited on Si (100) substrates by RF magnetron sputtering from a single Ti-24Nb-4Zr-8Sn alloy target prepared from a hot-forged slice after multi-pass cold rolling and resurfacing. The chemical compositions of targets and

films were measured by EDS coupled with the SEM operated at 10 kV.

A Rigaku SmartLab X-ray Diffractometer was used to perform XRD analyses (phase identification, structure and texture) with Cu K α radiation ($\lambda=1.5406 \text{ \AA}$), operating at a combination of voltage and current of 40 kV and 50 mA respectively. The XRD patterns were fitted and refined using Smartlab Studio II analysis software, to determine the phase nature and positions for deconvoluted individual peaks. A pseudo-Voigt function was chosen for peak shapes in the profile fitting procedure. CelRef software package was used for XRD data refinement. Refinement analyses were carried out using space groups and crystallographic information to identify the multiple reflections contributing to peak overlap of Ti phases and to fit and refine the lattice parameters of each phase present in the film. The film texture was analyzed through in-plane pole figure measurements.

Nanoindentation technique was used to evaluate the superelastic recovery ratios (η_h, η_w), the contact stiffness S , the indentation hardness H_{IT} and the elastic modulus E_{IT} of Ti2448 film. Extensive examinations were conducted on Ti2448 film using one Bkv indenter and 3 spherical Sp10, Sp50 and Sp200 indenters, in order to compare the mechanical responses under different stress-strain conditions and to study the deformation mechanisms induced under the different indenter tips. Each indenter was calibrated by analyzing indentations performed in fused silica. At least 5 indents were made for each load, and the indents were placed far enough apart to avoid interferences. For the nanoindentation experiments on the Ti2448 film, the indentation depth did not exceed 10% of the film thickness, thus avoiding a major contribution from the substrate [30]. The indentation $\eta_h, \eta_w, S, E_{IT}$ and H_{IT} were calculated as described in Chapter II section II.2.2.2.

V.3 Results and discussion

V.3.1 Microstructural analyses

V.3.1.1 Chemical composition

The chemical compositions of the quaternary Ti2448 alloy target and the as-deposited alloy film are presented in Table V-1. The concentrations of Nb, Zr and Sn elements in the film are slightly lower than that in the sputtering target. The deviation of the stoichiometric composition between target and film is frequently attributed to the preferential sputtering effect [31]. The preferential sputtering phenomenon is commonly observed whenever an alloy

target is subjected to ion bombardment. It may arise from the difference in the kinetic energy transfer to the constituents due to different kinematic factors and in the interatomic collision potentials between incident ions and target constituents due to the mass difference [32]. Lighter components are prone to be preferentially sputtered, resulting in higher sputtering yield (the number of sputtered atoms per incident ion) and thus higher concentration is expected in the film. The analysis is consistent with the experimental results that the lighter Ti atoms are preferentially sputtered showing a higher concentration in the film while heavier atoms of Nb, Zr and Sn exhibit lower concentration.

Table V-1 Chemical compositions of the Ti2448 alloy target and the as-deposited Ti2448 film

Elements (wt.%)	Nb	Zr	Sn	Ti
Target	23.5	3.8	8.2	-
Film	21.6	3.3	7.8	-

It is worth noting that collisions between sputtered species and Ar ions and atoms should be also considered during the transport. Nevertheless, as it will be discussed in the next section, considering our deposition conditions, it seems that this effect is not the predominant mechanism affecting the film concentration.

V.3.1.2 Morphology

Fig. V-1 shows the film morphology observed by SEM. The film exhibits high compactness with a measured thickness of 3.3 μm from the cross-sectional SEM image. The film surface is smooth and homogeneous with no discernible morphological features, which is corroborated by the nanometric roughness with a root mean square (RMS) roughness of 1.5 nm measured by AFM imaging in a $10\mu\text{m} \times 10\mu\text{m}$ area (the image is not shown here).

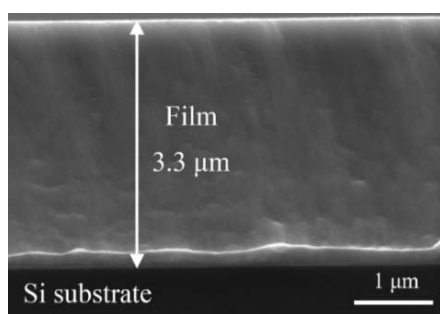


Fig. V-1 SEM images of cross-sectional view of Ti2448 alloy film deposited on Si (100) substrate.

The formation of dense and smooth film by magnetron sputtering is favored by the deposition conditions of low working pressure (0.2 Pa), high sputtering power (300 W) and small target-substrate distance (5.5 cm) because under these conditions sputtered atoms reach the substrate surface with high kinetic energy, resulting in relative strong atomic bombardments on the growing surface and high mobility of surface adatoms so as to increase the crystallization and density of films [33]. It is worthy note that the effect of working pressure on the film microstructure is associated to the extent of collisions among energetic particles in the plasma and has been described by the relationship [34, 35]:

$$\lambda = 2.330 \times \frac{T}{(P\delta_m^2)} \times 10^{-20}$$

where λ (cm) is the mean free path, T (K) is the temperature, P (Torr) is the working pressure and δ_m (cm) is the molecular diameter of the sputtering gas, which is 3.76 Å for Ar calculated from the van der Waals radius. According to the equation above, for our aforementioned deposition conditions, the mean free path was calculated to be 3.3 cm, which is long so that the sputtered atoms undergo less collisions before arriving at the substrate surface. As a result, the sputtered atoms have less possibility of agglomerating to increase the particle size, and hence decrease in surface roughness of the films. Besides, a high sputtering power and less collisions of sputtered atoms contribute to high adatom mobility, which facilitates the nucleation and growth of crystallites, and thus results in dense film with the fine crystalline structure.

V.3.1.3 Phase composition

The identification of crystalline phases present in the sputtered Ti2448 film was performed from XRD patterns. Fig. V-2a shows the XRD pattern (θ - 2θ scan) of the film, with the measured intensities shown in square root scale. Attention should be paid on the indexation of the peaks in the 2θ range from 36° to 40° , since multiple reflections of Ti phases including $(002)_{\alpha''}$, $(110)_\beta$, $(020)_{\alpha''}$ and $(111)_{\alpha''}$ may contribute to a overlapped peak in this range. Therefore, a detailed analysis in fitting and refinement procedures has been focused on the reflections in the 2θ range of 32° - 44° . The profile fitting and the deconvolution analysis were performed using pseudo-Voigt function, in order to obtain the positions of constructive peaks, as the detailed close-up view shown in Fig. V-2b. It is observed that the film is fully crystallized and consists of β -Ti phase (bcc structure) mixed with α'' martensitic phase (orthorhombic structure).

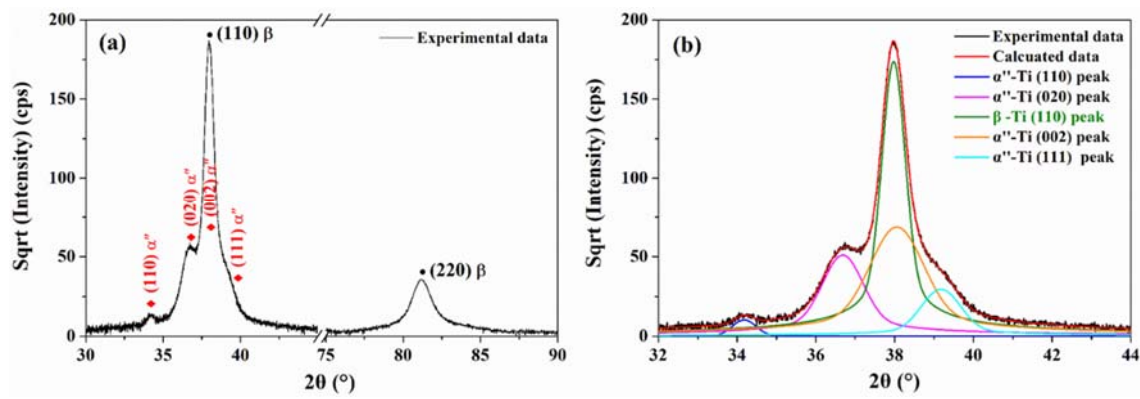


Fig. V-2 (a) XRD pattern in θ - 2θ scan of the Ti2448 film deposited on Si (100) substrate, and (b) deconvolution of XRD pattern showing the individual peaks corresponding to the 2θ range from 32° to 44° . The intensities are shown in square root scale.

The formation of metastable β -Ti alloy film at room temperature is attributed to three causes: (i) the energy for the formation of the high-temperature β -Ti phase is from the high energy delivered to the growing surface by particle bombarding; (ii) the particle bombarding is an extremely non-equilibrium heating process occurring at an atomic level, which is followed by the fast energy dissipation of condensing atoms onto the substrate, resulting in the rapid cooling of the β -Ti phase in a metastable state; and (iii) at room temperature, the metastable β -Ti phase could be retained during the whole deposition because of relatively limited atomic mobility [36]. The presence of α'' martensitic phase in the as-deposited film is possible due to that less β -stabilizer Nb and Zr elements in the film leads to the martensitic start (M_s) temperature higher than room temperature as compared to the case of counterpart bulk with exactly Ti2448 (wt.%) concentration. Hao *et al.* [37] similarly reported that phase constitutions of as-quenched Ti-Nb-Zr-Sn bulk alloys depended on the concentration of the β stabilizer elements and a reduction in the Nb or Zr content favor the stabilization of martensite in the bulk alloy. It is also suggested that martensite formation may be promoted by the development of intrinsic stress during film growth. Frutos *et al.* [38] showed that β/α'' volume ratios can be designed by controlling the sputtering process. Besides, the phase formation in the sputtered films is also determined by a combined effect of the reduced surface energy of the film and the interfacial energy between different phases [39].

Table V-2 presents the peak positions of β -Ti and α'' -Ti phases and the refined lattice parameters for both phases, and lattice parameters for Ti2448 bulk alloys in the literature measured by in situ tensile tests. It shows that the set of lattice parameters for β -Ti and α'' -Ti phases are evidently dependent on the stress state of the specimen.

Table V-2 Peak positions and lattice parameters of β -Ti and α'' -Ti phases for the Ti2448 film in the present work, and lattice parameters for Ti2448 bulk alloys from the literature.

Peaks	$(110)\alpha''$	$(020)\alpha''$	$(110)\beta$	$(002)\alpha''$	$(111)\alpha''$	$(220)\beta$
2θ ($^\circ$)	34.2	36.61	37.934	38.39	39.34	81.095
Lattice parameters	a_β (\AA)	$a_{\alpha''}$ (\AA)	$b_{\alpha''}$ (\AA)	$c_{\alpha''}$ (\AA)		
Present work	3.351	3.097	4.905	4.685		
Yang <i>et al.</i> [12]	3.298	3.260	4.865	4.851		
Liu <i>et al.</i> [40]	3.298	3.222	4.788	4.667		

The extended diffractogram (not entirely shown in Fig. V-2a) measured for 2θ ranging from 30° to 120° revealed only two reflections for the β -Ti phase in the Ti2448 film, the first diffraction order of $(110)_\beta$ plane and of the second diffraction order of $(220)_\beta$ indicating that the bcc structure of β phase grows with a preferred orientation of $\{110\}_\beta$ plane parallel to the substrate surface. The texture was further investigated through in-plane pole figure measurement presented in the following section V.3.1.4.

V.3.1.4 Texture analysis

Fig. V-3 shows the in-plane pole figures of $\{110\}_\beta$, $\{200\}_\beta$ and $\{211\}_\beta$ reflections from the β phase existing in the sputtered Ti2448 film deposited on Si substrate. Note that the intensities of pole figures are represented in logarithm scale. As one can be readily see, the poles are presented in the ring patterns, such as the rings observed at $\alpha = 60^\circ$ and 90° for $\{110\}_\beta$ reflection, at $\alpha = 45^\circ$ for $\{200\}_\beta$ reflection, and at $\alpha = 30^\circ, 54.74^\circ, 73.22^\circ$ and 90° for $\{211\}_\beta$ reflection. It is also observed that a pole maximum is positioned at the center of the $\{110\}_\beta$ pole figure. It suggests that the β phase present in Ti2448 film exhibits a $\langle 110 \rangle_\beta$ fiber texture whereby the $\langle 110 \rangle_\beta$ crystallographic axis of crystallites is aligned parallel to the sample surface normal direction and the azimuthal angle direction around the $\langle 110 \rangle_\beta$ fiber axis is randomly distributed.

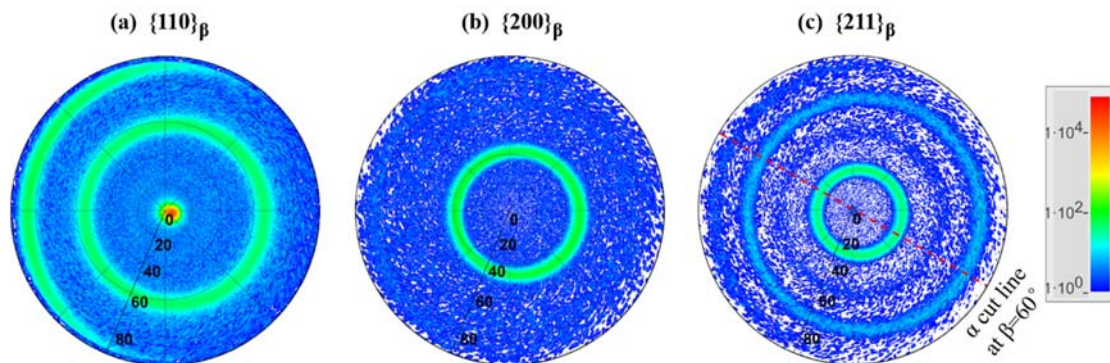


Fig. V-3 In-plane pole figures of the Ti2448 film: (a) $\{110\}_\beta$, (b) $\{200\}_\beta$, (c) $\{211\}_\beta$.

It is common to observe that bcc films grown by physical vapor deposition generally develop a $\langle 110 \rangle$ fiber texture. The well-established mechanism for the formation of fiber texture in films is the evolutionary selection model. That is, the fiber texture results from the growth preference associated to the thermodynamic preference of deposited atoms to condense on low-energy surfaces so as to minimize the surface energy [41]. The low-energy crystal faces grow fast and survive, while the slow-growing crystal faces with high energy terminate in the blanks between the fast-growing crystals. This is in agreement with our observation that β phase develops a fiber texture along $\{110\}_\beta$ planes of the highest atomic density, reducing the surface energy.

Besides, it is worth noting that the reflection of the single-crystal Si(400) substrate is observed on the $\{211\}_\beta$ pole figure because the Si(400) plane at $2\theta = 69.13^\circ$ and $\alpha = 0^\circ$ satisfies the diffraction conditions, resulting in a high reflection intensity. Fig. V-4 shows the α cut line at $\beta=60^\circ$. The extremely sharp and narrow peak in the center is contributed by the Si(400) reflection, showing the intensity as high as approximately 25000 cps in Fig. V-4a. To protect the detector from the possible damage of high intensity Si (400) diffraction, the $\{211\}_\beta$ pole figure was measured with the K_β filter.

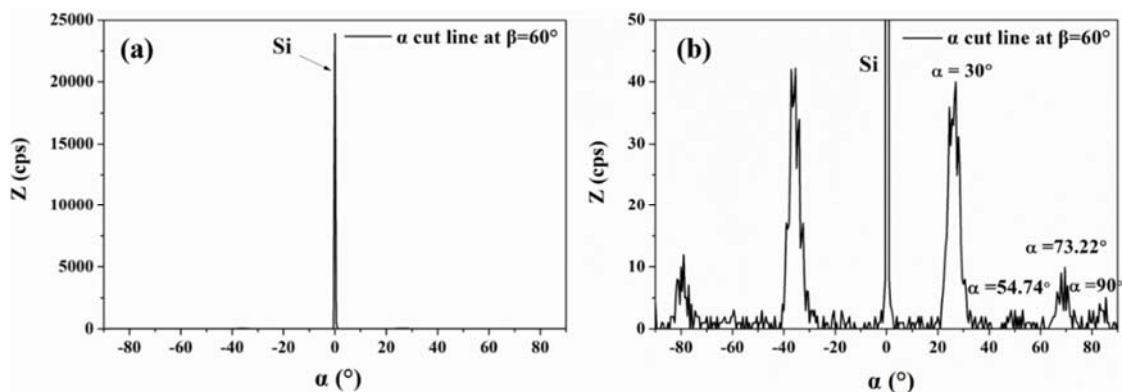


Fig. V-4 (a) α cut line at $\beta=60^\circ$ in $\{211\}_\beta$ pole figure in Fig. V-3, and (b) a zoomed view of (a).

Omega scan is a useful way to study the misorientation of the planes. During the measurement, the X-ray tube and detector are fixed at the positions of expected Bragg reflection $2\theta_{hkl}$, and the sample is tilted, so as to detect the $\{h k l\}$ planes not exactly parallel to the sample surface. An omega scan X-ray diffraction for $(110)_\beta$ planes shows that there is a shift of 5.6° between the peak position ($\omega = 13.326^\circ$) measured from the omega scan in Fig. V-5 and the $\theta_{110\beta}$ ($(2\theta_{110\beta})/2 = 18.97^\circ$) calculated from θ - 2θ symmetric scan in Fig. V-2a, suggesting the presence of misorientation in the $(110)_\beta$ planes and that $(110)_\beta$ planes are not strictly parallel to the film surface. This can explain why the maximum pole in the $\{110\}_\beta$ pole figure and diffraction rings are not centered (Fig. V-3).

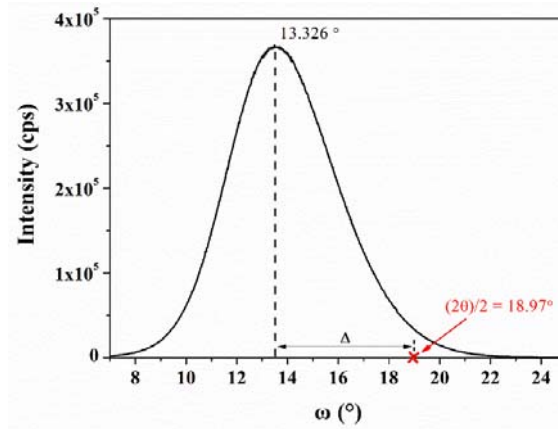


Fig. V-5 X-ray diffraction pattern in omega scan with $2\theta_{110\beta}$ maintained at 37.934° .

We also would like to go further with martensitic phase and investigate reflections from martensite planes. Using the martensite lattice parameters previously determined in Table V-2, the 2θ peak positions of martensite reflections which satisfied the X-ray diffraction conditions were calculated by CelRef software, and presented in sequences according to their relative intensities in the first two columns of Table V-3, as marked in blue color.

As seen from the classic XRD pattern in θ - 2θ scan in Fig. V-2, $(110)_{\alpha''}$, $(020)_{\alpha''}$, $(002)_{\alpha''}$, and $(111)_{\alpha''}$ diffraction peaks were detected. Stereographic projections of $(110)_{\alpha''}$, $(020)_{\alpha''}$, $(002)_{\alpha''}$, and $(111)_{\alpha''}$ were used to provide the χ angle (α angle) and φ angle (β angle) for each type of reflections over a half hemisphere, which predicts the pole positions of the reflections appearing in the pole figures. It means that by setting the detector at the $2\theta_{hkl}$ angle of the diffraction signal to be measured, such as $2\theta_{021\alpha''} = 41.522^\circ$, when the scanning reaches to the (χ, φ) combination of $(28.13^\circ, 104.87^\circ)$ corresponding to $(021)_{\alpha''}$ planes in $(020)_{\alpha''}$ stereographic projection, Bragg's law is satisfied and the diffraction occurs. The diffracted signal is recorded by the detector, thus a $(021)_{\alpha''}$ pole appears in the pole figure. As such, the pole figure can be connected with the stereographic projection. That is, the pole figure is displayed by compositing the diffraction intensity distribution of poles with the stereographic projection.

It is worth noting that since the Ti2448 sputtered film is polycrystalline with a fiber texture, the pole figures are expected in ring patterns, and the ring position is only related to the χ angle, independent of φ angle. Therefore, only the χ angles were reported for each type of reflections in the columns 3-6 of Table V-3. The last column in yellow color in Table V-3 shows the diffraction conditions for the pole figures of β phase, providing the references to be avoided when choosing the measurement conditions for α'' phase, in order to distinguish the α'' -Ti phase from the β -Ti phase in Ti2448 film. The χ angles for α'' phase marked in grey color in the columns 3-6 of Table V-3 are close to χ angles for β -Ti phase as marked with

underlines. To put it in another way, under those diffraction conditions marked in grey color, α'' -Ti phase is not distinguishable from the β -Ti phase. Therefore, the χ angles uncovered by grey color can be used to detect the α'' phase, without diffraction contribution from β -Ti phase.

Table V-3 Diffraction conditions to distinguish the α'' phase from the β phase.

Planes	2 θ -CeIRef (Relative Int.)	Stereographic projections				Diffraction conditions
		(020) $_{\alpha''}$	(002) $_{\alpha''}$	(111) $_{\alpha''}$	(110) $_{\alpha''}$	
(111) $_{\alpha''}$	39.339° (100%)	$\chi = 62.9^\circ$	$\chi = 60.84^\circ$	$\chi = 0^\circ$	$\chi = 29.16^\circ$	2 $\theta_{110\beta} = 37.934^\circ$ $\chi = \underline{0^\circ}, \underline{60^\circ}, 90^\circ$
(021) $_{\alpha''}$	41.522° (80%)	$\chi = 28.13^\circ$	$\chi = 61.87^\circ$	$\chi = 50.83^\circ$	$\chi = 62.6^\circ$	2 $\theta_{110\beta} = 37.934^\circ$ $\chi = 0^\circ, \underline{60^\circ}, 90^\circ$
(022) $_{\alpha''}$	54.102° (80%)	$\chi = 46.91^\circ$	$\chi = 43.09^\circ$	$\chi = 48.15^\circ$	$\chi = 69.12^\circ$	2 $\theta_{200\beta} = 54.73^\circ$ $\chi = \underline{45^\circ}, 90^\circ$
(020) $_{\alpha''}$	36.60° (60%)	$\chi = 0^\circ$	$\chi = 90^\circ$	$\chi = 62.89^\circ$	$\chi = 58.54^\circ$	2 $\theta_{110\beta} = 37.934^\circ$ $\chi = \underline{0^\circ}, \underline{60^\circ}, \underline{90^\circ}$
(002) $_{\alpha''}$	38.415° (60%)	$\chi = 90^\circ$	$\chi = 0^\circ$	$\chi = 60.84^\circ$	$\chi = 90^\circ$	2 $\theta_{110\beta} = 37.934^\circ$ $\chi = \underline{0^\circ}, \underline{60^\circ}, \underline{90^\circ}$
(200) $_{\alpha''}$	59.517° (60%)	$\chi = 90^\circ$	$\chi = 90^\circ$	$\chi = 41.85^\circ$	$\chi = 31.4^\circ$	2 $\theta_{200\beta} = 54.73^\circ$ $\chi = 45^\circ, \underline{90^\circ}$
(113) $_{\alpha''}$	70.095° (60%)	$\chi = 74.48^\circ$	$\chi = 30.85^\circ$	$\chi = 29.99^\circ$	$\chi = 59.15^\circ$	- 2 $\theta_{004Si} = 69.13^\circ$ - 2 $\theta_{211\beta} = 68.52^\circ$ $\chi = \underline{30^\circ}, 54.74^\circ,$ $\underline{73.22^\circ}, 90^\circ$
(110) $_{\alpha''}$	34.155° (50%)	$\chi = 58.84^\circ$	$\chi = 90^\circ$	$\chi = 29.16^\circ$	$\chi = 0^\circ$	
(131) $_{\alpha''}$	67.725° (50%)	$\chi = 33.07^\circ$	$\chi = 72.62^\circ$	$\chi = 29.82^\circ$	$\chi = 34.22^\circ$	- 2 $\theta_{004Si} = 69.13^\circ$ - 2 $\theta_{211\beta} = 68.52^\circ$ $\chi = \underline{30^\circ}, 54.74^\circ,$ $\underline{73.22^\circ}, 90^\circ$

Fig. V-6 presents the XRD profiles in θ - 2θ scan with χ fixed at 29.16° and 58.54° , respectively. In Fig. V-6a, three deconvoluted individual peaks after fitting were identified as $(110)_{\alpha''}$, $(111)_{\alpha''}$ and $(021)_{\alpha''}$ reflections with 2θ positions at 34.14° , 39.33° and 41.52° , respectively. In Fig. V-6b, the peak profile was indexed as $(110)_{\alpha''}$, $(020)_{\alpha''}$ and $(110)_{\beta}$. Among the martensitic peaks, $(021)_{\alpha''}$ reflection exhibits the highest intensity. The α'' -Ti phase is textured, but not as textured as β -Ti phase in the film.

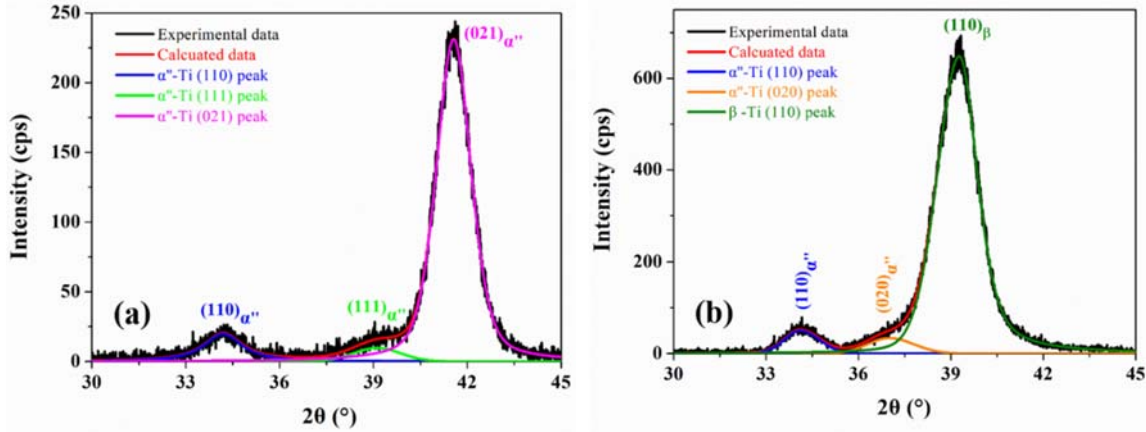


Fig. V-6 θ - 2θ scanning profile with χ fixed at: (a) 29.16° and (b) 58.54° .

After much consideration, the $(021)_{\alpha''}$ in-plane pole figure has been successfully obtained with 2θ fixed at 41.52° , as shown in Fig. V-7. The ring pattern shows no preferential orientation for the azimuthal angle directions of $[021]_{\alpha''}$ directions.

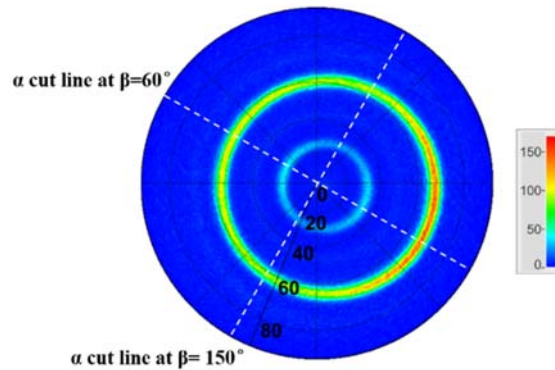


Fig. V-7 In-plane pole figure of $\{021\}_{\alpha''}$ in Ti2448 film.

The α cut lines performed at $\beta = 60^\circ$ and $\beta = 150^\circ$ in perpendicular in Fig. V-8 indicate that the ring pattern is axisymmetric approximately along the α cut lines performed at $\beta = 60^\circ$, possible due to the presence of misorientation of the planes parallel to the film surface.

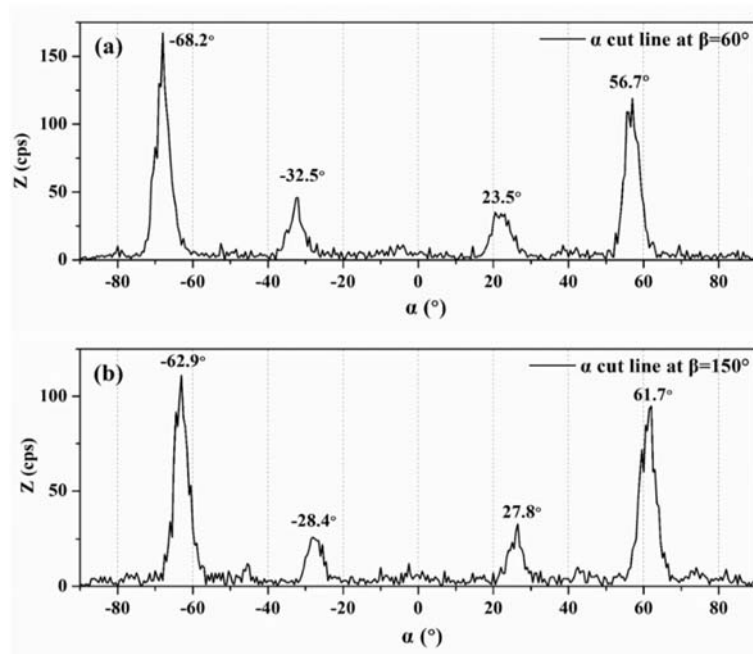


Fig. V-8 α cut lines in $\{021\}_{\alpha''}$ pole figure: (a) at $\beta = 60^\circ$ and (b) at $\beta = 150^\circ$.

V.3.1.5 TEM observations

The film microstructure was observed by TEM on plane and cross-sectional view. Fig. V-9 shows TEM BF image and the corresponding SAED pattern of the Ti2448 film. The grains represent the cross sections of the columns with a size of approximately 21.9 ± 5.5 nm, and the intercolumnar boundaries are tight without visible voids or grooves. The presence of both bcc β -Ti phase and orthorhombic α'' martensite phase were confirmed from the SAED pattern, and the ring character revealed the polycrystalline microstructure of the film.

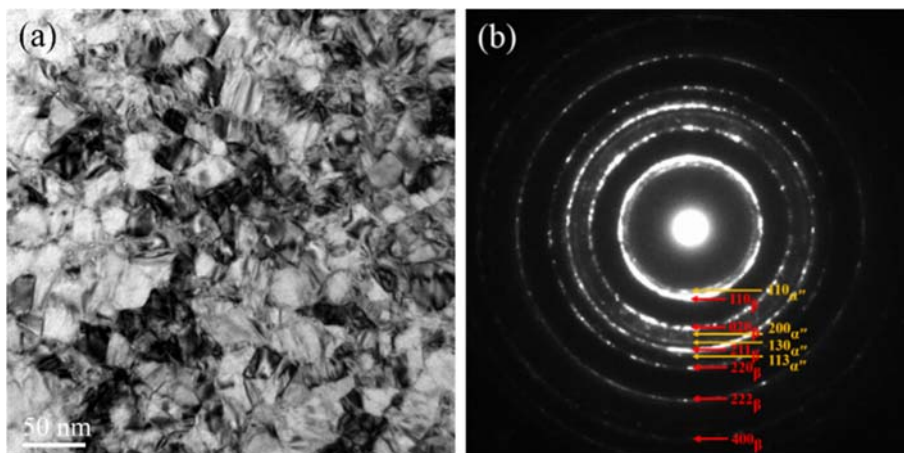


Fig. V-9 Plane-view TEM micrographs for the Ti2448 film: (a) DF image, and (b) SAED pattern.

Fig. V-10 shows the BF and DF TEM images and SAED patterns taken from the cross-sectional TEM specimen. The Ti2448 film demonstrates typical columnar crystals with growth

direction perpendicular to the substrate surface. SAED patterns taken from the regions of near-substrate, middle and near-surface along the film thickness made it possible to investigate the evolution of the microstructure and texture. Considering the diffraction information provides from more than one columnar grain, the SAED patterns were indexed using rings instead of vectors. The coexistence of β -Ti and martensitic α'' -Ti phases in Ti2448 film is also revealed by SAED patterns taken from cross-sectional TEM specimen, in agreement with the XRD analysis (Fig. V-2) and the SAED pattern taken from the plane-view (Fig.V-9). Besides, the changes in the SAED patterns from ring shaped pattern at near-substrate domain to spot shaped pattern at the upper part of the film indicate the widening and coarsening of the columns with increasing deposition thickness, suggesting a thickness-dependence of the column diameter. This can be corroborated by the observations in the DF TEM images in Figs. V-10 b and c which were taken from the $[110]_{\beta}$ reflection. The columnar crystals near the substrate interface are fine with a column diameter of approximately 20 nm, while with increasing thickness the column diameter increases to approximately 60 nm. The development of column diameter with the film thickness has also been reported in TiN films grown by magnetron sputtering [42]. The observation that the columnar grains oriented in $\langle 110 \rangle_{\beta}$ is perpendicular to the substrate surface throughout the entire film thickness is in agreement with the XRD results that the film exhibits a strong $\langle 110 \rangle_{\beta}$ fiber texture. Figs. V-10 d and e present the traces of martensitic α'' -Ti phases in the Ti2448 films. The nanosized α'' -Ti crystallites are randomly distributed in the β matrix. It has been proposed in the literature that the grain boundaries impose constraints on the growth of the martensite and confine the transformed volume fraction in nanocrystalline structure [43]. A martensite plate nucleated within a grain will be stopped at the grain boundaries acting as obstacles for martensite growth. To propagate the transformation, the plate has to exert stresses that are sufficient to stimulate nucleation and growth of favorable martensite variants in the adjacent grains.

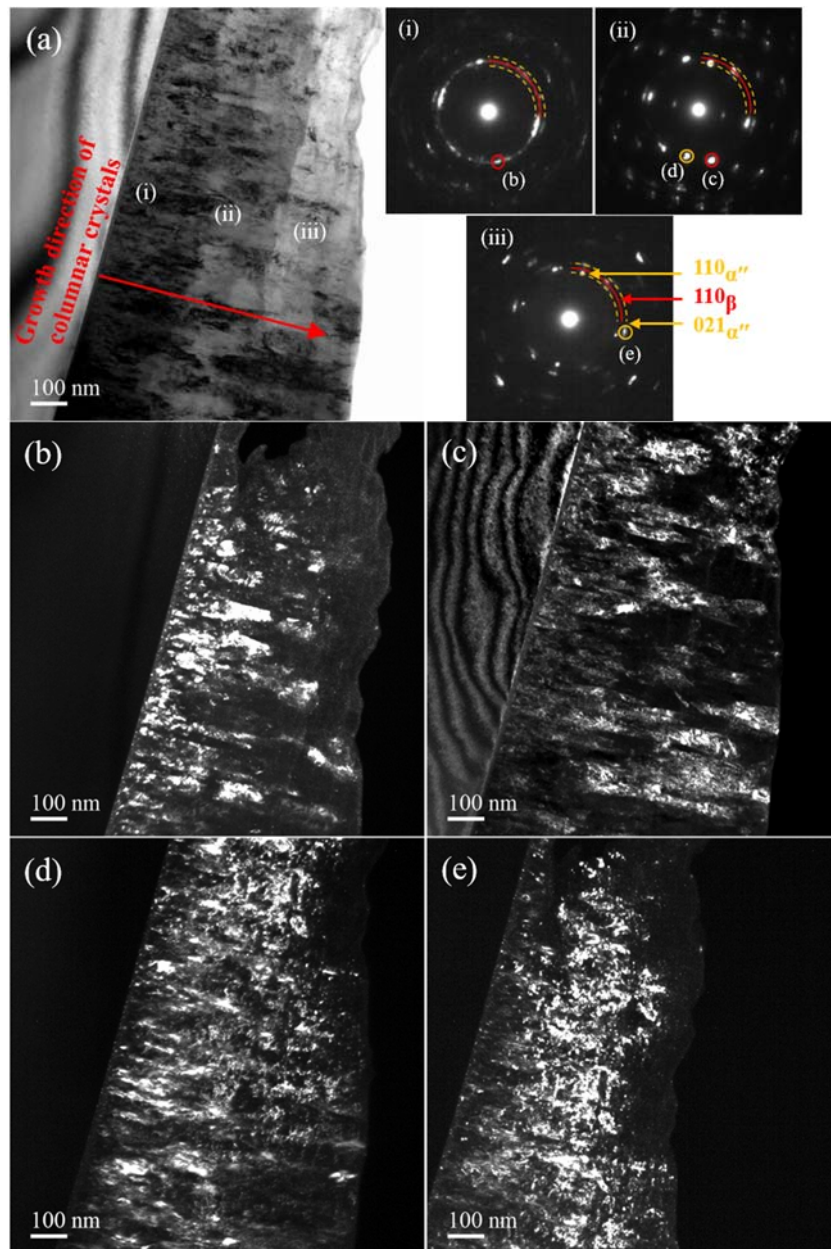


Fig. V-10 (a) Cross sectional BF TEM image, (i-iii) SEAD patterns taken from the corresponding marked regions in (a), and (b-e) DF TEM images taken by the $[110]_{\beta}$ reflection in (i), $[110]_{\alpha'}$ and $[110]_{\beta}$ reflections in (ii), and $[021]_{\alpha'}$ reflection in (iii), respectively.

V.3.2 Characterization of the superelastic response

Different from elastic-plastic materials, superelastic materials can reversibly accommodate external loads through SIM transformation. When subjected to indentation, and depending on indentation conditions (strain/stress states), superelastic materials may simultaneously undergo recoverable deformation via elasticity and SIM transformation, and irrecoverable plastic deformation. The elastic deformation and plastic deformation can take place in either parent or martensitic phases. Therefore, the intricate deformation modes make

it complex to interpret the indentation responses of superelastic materials.

Spherical indenters of different tip radii R of $10\mu\text{m}$ (Sp10), $50\mu\text{m}$ (Sp50) and $200\mu\text{m}$ (Sp200) and Berkovich indenter (Bkv, with an equivalent blunt tip estimated at $100\text{-}300\text{ nm}$ in diameter) were used in this study. The different indenters make it possible to discriminate the superelastic behavior of the Ti2448 film by comparing the measurements with each other.

V.3.2.1 Depth recoverability and work recoverability

To investigate the indentation behavior of superelastic Ti2448 film, nanoindentation experiments were performed at maximum indentation loads F_m in the ranges of $1\text{-}15\text{ mN}$, $3\text{-}45\text{ mN}$, $5\text{-}100\text{ mN}$ and $30\text{-}300\text{ mN}$ for Bkv, Sp10, Sp50 and Sp200 indenters, respectively, which correspond to maximum penetration depth h_m varying between $50\text{-}330\text{ nm}$.

The microstructure of Ti2448 film is composed mainly of metastable β -phase, thus superelastic effect is expected when the film is subjected to nanoindentation. The depth recovery ratio η_h and work recovery ratio η_w were calculated, and plotted with respect to h_m for the four indenters in Fig. V-11. In these curves, each point is the result of one complete load-unload indentation test. It is shown that the η_h and η_w values measured with Sp200 indenter over the entire range of investigated depths, remain above 92% and 99% for η_h and η_w respectively suggesting that the indents are nearly fully recovered upon unloading. In the case of Sp50 and Sp10 indenters, η_h and η_w decrease remarkably with increasing depth, from 98% to 68% for Sp50 indenter, and from 85% to 50% for Sp10 indenter, while indenting with Bkv indenter, recovery ratios are relatively low at approximately 30% .

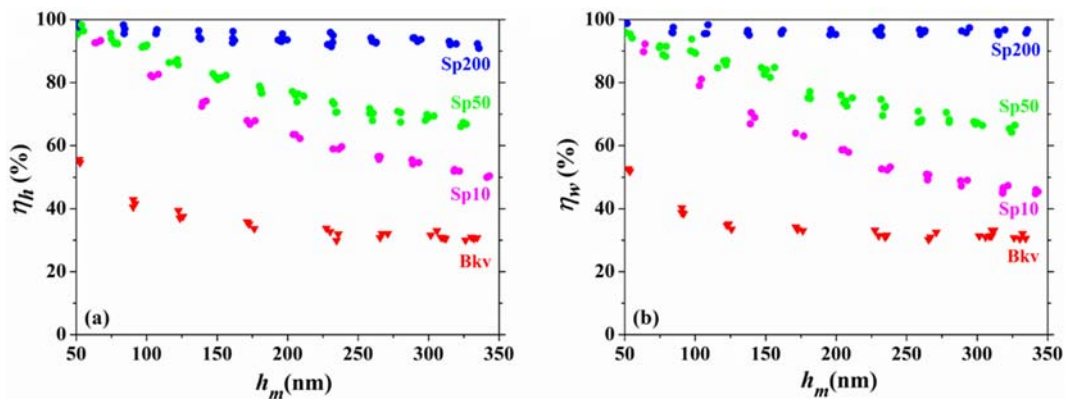


Fig. V-11 Variation of recovery ratios with maximum indentation depth h_m for the three spherical indenters Sp200, Sp50 and Sp10 and for the Bkv indenter: (a) depth recovery ratio η_h and (b) work recovery ratio η_w .

Nanoindentation and AFM were coupled to investigate the residual imprints produced by

the four tips indenting to a maximum depth h_m of approximately 290 nm. The four $F-h$ curves are shown in Fig. V-12a. It is observed that indenting with Sp200 exhibits almost a full recovery, resulting in no visible imprint remained from the AFM image taken after indentation (Fig. V-12b), while indenting with Sp50, Sp10 and Bkv, the residual depths measured from the corresponding AFM surface profiles are 75 nm, 130 nm, and 200 nm, respectively. The AFM surface profiles corresponding to each indentation imprints are displayed in the same axes scales, which shows that the indentation imprint gets narrow and steep from Sp50 to Sp10 further to Bkv indenter. It is obvious that the indenter geometry is responsible for the changes in the residual imprint profiles.

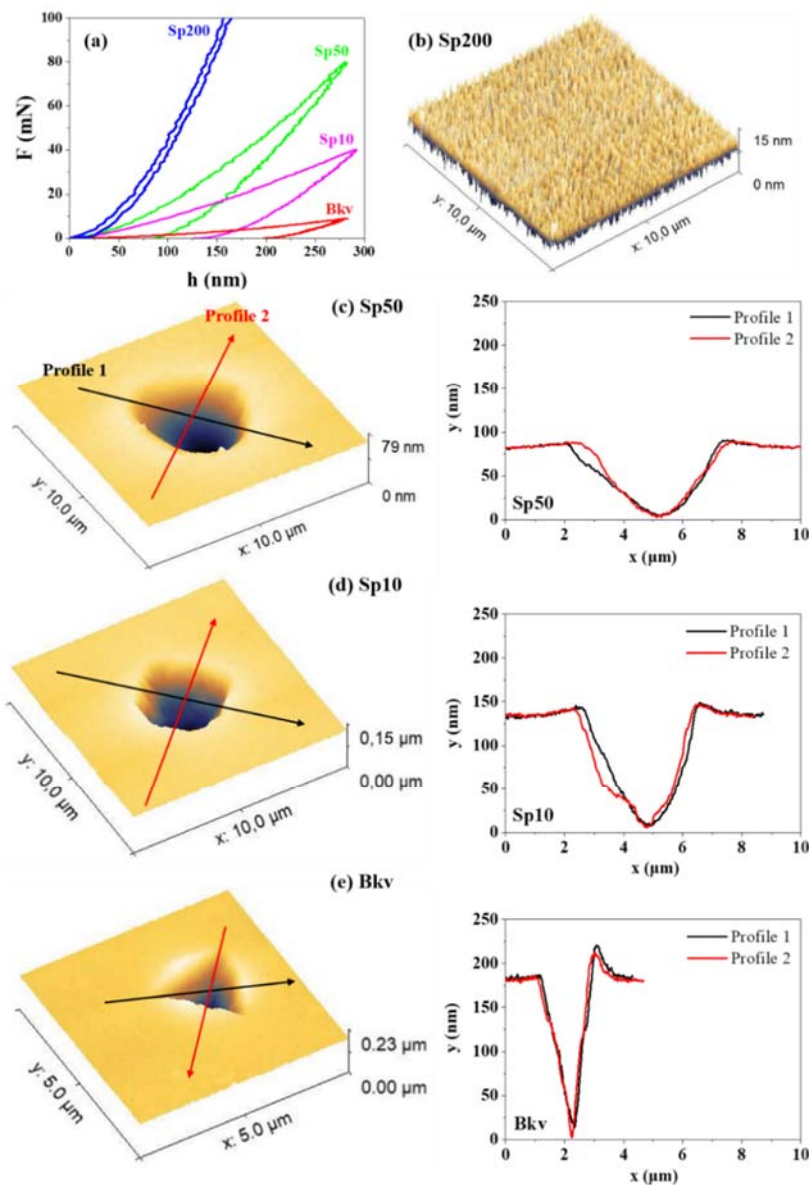


Fig. V-12 Nanoindentation $F-h$ curves obtained with the four indenters indenting to a maximum depth h_m of approximately 290 nm (a), and AFM images of the residual imprints after nanoindentation and the corresponding surface profiles of the imprints: with Sp200 indenter (b), Sp50 indenter (c), Sp10 indenter (d) and Bkv indenter (e).

V.3.2.2 Strain and Stress distributions under tips

It is observed in Fig. V-11 that for equivalent h_m , the recovery ratios when indenting with spherical indenters are higher than those with the Bkv indenter. This phenomenon can be explained by the difference in strain fields or stress fields developed underneath each indenter.

V.3.2.2.1 Strain fields

During indentation, a progressive strain field is applied to the material. The Tabor approach is used to transfer the complex strain field underneath the indenter in a uniaxial strain field using a representative strain ε_r . The material is thus treated as a so-called representative strain ε_r , which does depend on the total included angle of the indenter. For sharp indenter, the representative strain is defined independently of indentation depth, as $\varepsilon_r = 0.2 \cot\beta$. For a Bkv indenter, $\beta = 70.3^\circ$ fixing the evaluation of ε_r to $\sim 7\%$. For spherical indenters, the representative strain is defined as $\varepsilon_r = 0.2 a_c/R$, where a_c is the contact radius, $a_c = \sqrt{(2hcR - h_c^2)}$ and R is the tip radius. Thus the representative strain for spherical tips is depth-dependent via the contact radius a_c . This indicates that spherical ε_r can be varied depending on the indenter geometry and the indentation depth. The ε_r for the three spherical indenters were calculated and plotted as a function of h_m in the range of 50-300 nm in Fig. V-13. It shows that the calculated ε_r increases with increasing h_m . The largest radius indenter Sp200 indenter generates the lowest ε_r (from 0.4% to 0.8%), followed by the intermediate Sp50 indenter (0.7% - 1.9%), and then the smallest Sp10 indenter (1.7% - 4.3%), which are much lower than that for the Bkv indenter (7%). It is reasonable to conclude that the sharper tip, the higher ε_r .

It is worth noting that ε_r are only averaged values of the evaluated strains. Indeed, a gradient distribution must be considered along the radial distance from the indenter tip [44]. According to Tymiak *et al.* [45], the smaller radii tips have the largest strain gradients. There is a strain singularity for the Bkv indenter tip for which the maximum strain (of the order of a few tens of percentage) exists exactly at the apex of the tip. Such high strain causes substantial plastic flow in the region underneath the Bkv tip, and the formed dislocations can stabilize the stress-induced martensite preventing its reversion to parent β phase when the load is released.

Unlike the case of Bkv indenter, the strain field under spherical indenters is more homogeneous and smoother. Thus, the strain generated by spherical indenters can be more easily controlled to activate the stress-induced martensitic transformation avoiding too much plasticity to allow its reversion in the parent β phase when the load is released [46].

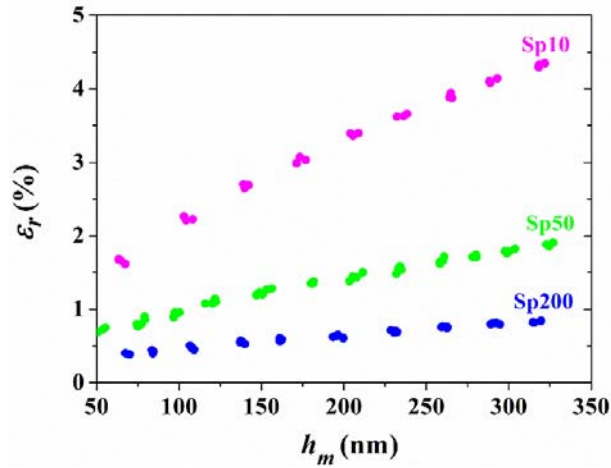


Fig. V-13 Representative strain ϵ_r for three spherical indenters.

V.3.2.2.2 Stress fields

Studying the stress distribution developed underneath the indenter also makes it possible to understand the different behaviors obtained during spherical and Bkv indentations. According to Fischer-Cripps [47], the distribution of normalized contact pressure σ_z/P_m under spherical and Bkv indenters was given as follows:

$$\text{for spherical indenter: } \frac{\sigma_z}{P_m} = -\frac{3}{2} \left(1 - \frac{r^2}{a_c^2}\right)^2, \quad r \leq a_c$$

$$\text{for Bkv indenter: } \frac{\sigma_z}{P_m} = -\cosh^{-1} \frac{a_c}{r}, \quad r \leq a_c$$

where σ_z is the normal stress along indenter symmetric axis, P_m is the mean contact pressure, a_c is the contact radius at peak load, r is the radial coordinate denoting the radial distance from the center of the contact circle, as illustrated in Fig. V-14a. p_m , a_c and r are positive quantities whereas the stress σ_z is a negative value indicating a compression state. Fig. V-14b shows the distributions of normalized contact pressure σ_z/P_m and the normalized contact profiles z/h_m for spherical and Bkv indenters. z is the coordinate along the indenter symmetric axis denoting the distance between the initial surface and the indenter tip, with positive z corresponding to the direction from the surface towards the inside of the material.

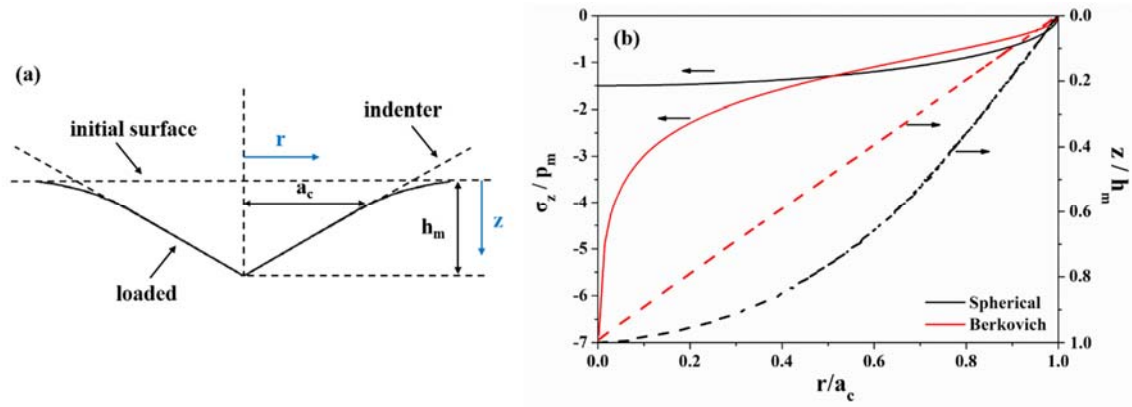


Fig. V-14 (a) Illustration of indentation parameters under load, (b) normalized contact pressure distribution σ_z/p_m and normalized contact profiles z/h_m under load as a function of r/a_c for spherical and Bkv indenters.

It is observed from Fig. V-14 that for both spherical and Bkv indenters, the normalized contact pressure reaches a maximum right beneath the tip at $z = h_m$ and then falls to zero at the edge of the contact circle at $z = 0$. However, for spherical indenter, there is few stress concentration was observed as compared to Bkv indenter for which the stress increases dramatically as r approaches zero. This is in agreement with the observation that the contact profile for the spherical indenter at the center is a smooth transition while that of the Bkv indenter is steep and sharp. It is due to the severe stress concentration that occurs beneath the sharper Bkv indenter, resulting in larger plastic zone as compared to the case of spherical indenter. Consequently, more residual deformation will remain after releasing the load in the case of Bkv indentations.

V.3.2.3 Microstructure evolutions during indentation process

It is also observed in Fig. V-11 that η_h and η_w values decrease with h_m . It can be explained by the microstructure evolutions upon loading illustrated in Fig. V-15. The deformation modes for different zones underneath the indenter tip are determined by comparing the von Mises equivalent stress σ with the critical stresses, i.e., martensitic start transformation stress σ_{Ms} , martensitic finish transformation stress σ_{Mf} and the martensitic yielding stress $\sigma_{y^{\alpha'}}$ [48, 49]. The magnitude of the stress under the indenter tip depends on the depth to which the tip is indented. It is worth noting that the illustrated zone boundaries in Fig. V-15 represent average estimates of predominant deformation regions and are not realistic.

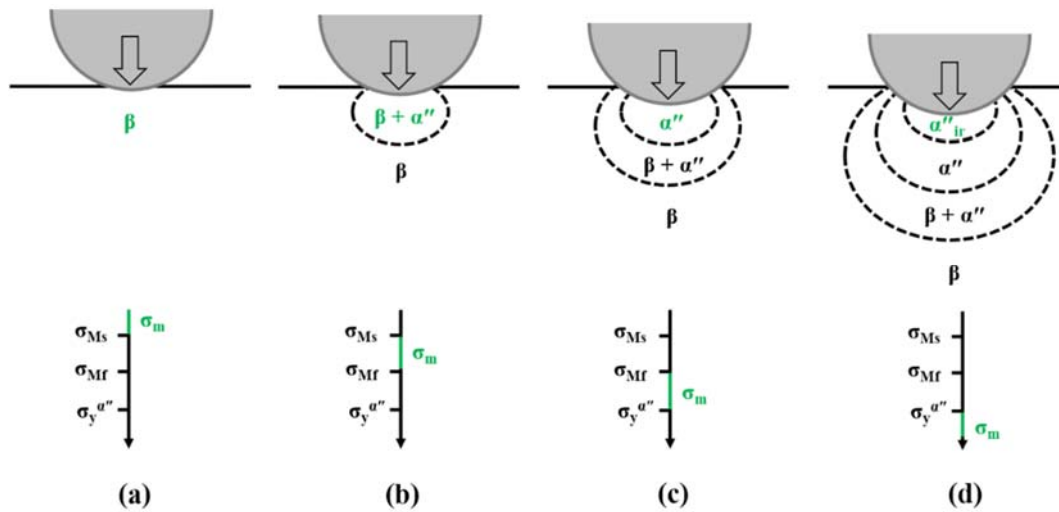


Fig. V-15 Schematics of microstructure evolutions with increasing penetration depth in four stages: (a) pure parent β phase; (b) a partial transformed zone with mixed $\beta + \alpha''$ phases enclosed by β phase and (c) a fully transformed and reversible martensite α'' zone, mixed phase zone and pure β phase zone; (d) a fully transformed and irreversible martensite α''_{ir} zone, a fully transformed and reversible martensite α'' zone, a partial transformation zone and a fully untransformed parent β phase zone.

When initially indenting in a shallow depth, the von Mises equivalent stress under the tip is lower than the martensitic start transformation stress, $\sigma < \sigma_{Ms}$, so the film is elastically deformed and a pure β phase zone still remains (Fig. V-15a). As the stress σ of the region nearest to the tip increases with increasing depth to $\sigma_{Ms} < \sigma < \sigma_{Mf}$, β phase is partially transformed into α'' phase, thus a partial transformation zone consisting of mixed $\beta + \alpha''$ phases surrounded by β phase in outer region is correspondingly observed (Fig. V-15b). Further increase in the depth results in a fully martensitic transformation zone where the stress is higher than σ_{Mf} . However, in the region of $\sigma_{Mf} < \sigma < \sigma_{y^{\alpha''}}$, the β phase is fully transformed into martensite which is reversible (Fig. V-15c) while in the region where the local stress exceeds the yield stress of the martensite, i.e., $\sigma > \sigma_{y^{\alpha''}}$, a fully transformed and irreversible martensitic α''_{ir} zone is formed, since the martensite is stabilized due to the plastic deformation and cannot revert back to parent β phase upon unloading (Fig. V-15d). Once the plastically deformed zone is formed, not only the irreversible martensite in such zone is not recovered, it may also constrain the recovery from the zones below, such as the recovery that would have obtained through the reversible martensite transforming back to β phase and the elastic recovery from the β phase. Therefore, due to the formation of plastically deformed and irreversible martensitic zone, the recoverability will decrease by increasing such plastic volume with increasing indentation depths.

In summary, considering the combined effect of the recovery behaviors and the evolution

of stress/strain states underneath the four indenters, it is noteworthy that the sharp Bkv indenter of equivalent blunt tip of diameter $\sim 100\text{-}200$ nm is not appropriate to assess the superelastic behavior of the film since indentation volume is dominated by the dislocation mediated plasticity. These dislocations impede the reversible phase transformation i.e. SIM transformation in superelastic Ti2448 film. However, such recoverable superelastic behavior can be better appreciated using spherical indenters with a comparatively blunt tip of diameter around two orders of magnitude higher than that of Bkv indenter tip. The large spherical indenter Sp200 mainly reveals the elasticity of the parent β phase in the film, and intermediate Sp50 or Sp10 indenter is a more feasible option to evaluate the superelasticity of the film, owing to that the strain field is in the range where martensitic transformation competes with plastic deformation and prevails.

V.3.3 Mechanical properties

This part examines the elastic modulus E_{IT} and indentation hardness H_{IT} their distributions through indentation depth are of special significance. The procedure used to evaluate H_{IT} and E_{IT} is based on the unloading processes and it is necessary to measure and calculate four principal parameters: the maximum load F_m , the maximum penetration depth h_m , the final or permanent depth h_p , and the contact stiffness. F_m and h_m can be measured directly from the indentation curve, however, S and h_p need to be determined using the Oliver-Pharr method which has been mainly used for instrumented indentation analysis by the majority of researchers. A complete study of the influence of superelastic behavior of the Ti2448 film on the E_{IT} and H_{IT} will be developed in this section.

V.3.3.1 Elastic modulus

Oliver and Pharr demonstrated that unloading curves are not well represented by a linear fit. In the Oliver and Pharr method, unloading curves are properly approximated by a power law relationship $F = \alpha (h - h_p)^m$, where α and m are power law fitting constants. This method can be extrapolated to a diversity of axisymmetric indenter geometries such as sphere and pyramids [22]. Oliver and Pharr did a broad study over different materials and proved that the variation of the power law exponent remains in the range of $1.2 \leq m \leq 1.6$, which discards the flat punch approximation ($m = 1$) and approaches instead to a paraboloid of revolution ($m = 1.5$).

Contact stiffness S is defined as the slope of the upper portion (from 98% of F_m to 40%

of F_m) of power law fit of unloading curve. Fig. V-16 shows the variation of contact stiffness S as a function of h_m for the four indenters. It is observed that in all cases S increases with increasing h_m , and indenting with Sp200 exhibits the highest value at a fixed h_m .

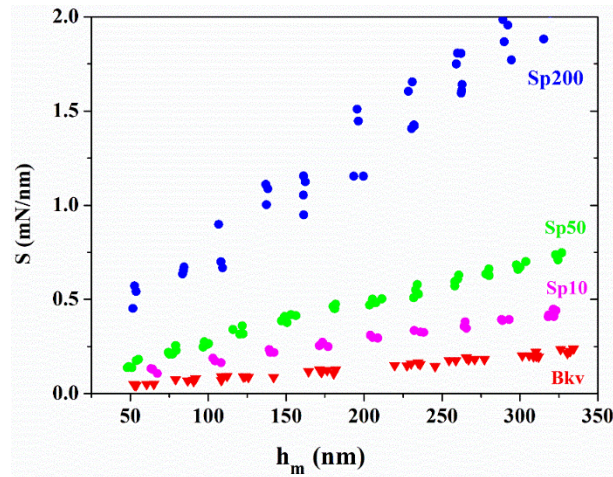


Fig. V-16 Variation of the contact stiffness S as a function of h_m for Sp200, Sp50, Sp10 and Bkv indenters.

The depth dependence of indentation modulus E_{IT} has been rarely reported in literature. Fig. V-17 shows the variation of E_{IT} as a function of maximum indentation depth h_m indenting with Bkv and spherical indenters. It is likely that the measured E_{IT} depends not only on the indentation depth but also on the indenter tip radius. The indentation elastic modulus measured with Bkv tip, E_{IT-Bkv} , decreases firstly with the increase of the maximum indentation depth and eventually approaches a constant, while indentation moduli measured with spherical tips E_{IT-sph} exhibits a contrary tendency, showing an increase in the indentation modulus values with increasing the maximum penetration depth. It is also observed that at fixed h_m , Sp200 probes the highest E_{IT} among spherical indentations. It is important to understand that E_{IT} of superelastic Ti2448 film is an apparent modulus which depends on the transformed volume fraction between β and α'' phases which varies as the function of the loading conditions. It is worth noting that SIM transformation in Ti2448 film occurs at a stress level reaching the critical value σ_s when the specimen is subjected to indentation, which provides the basis for a more comprehensive analysis of the influence of the deformation mode on the E_{IT} measurements. The volume fraction of phases is primarily associated with the strain gradient within the indentation volume as explained through section V.3.2. Hence, mixture of phases is expected to exist within the indentation volume at any instance.

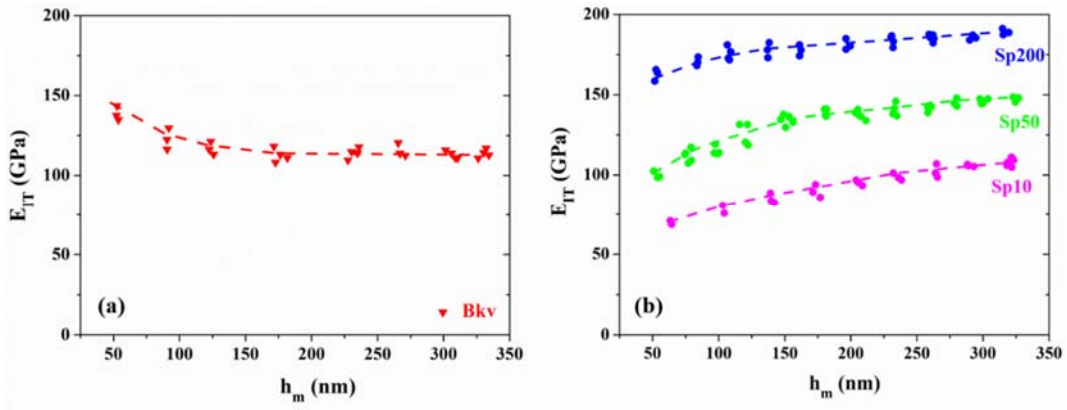


Fig. V-17 Evolution of indentation elastic modulus E_{IT} as a function of maximum penetration depth h_m measured with Bkv indenter (a) and with Sp10, Sp50 and Sp200 indenters (b).

It is interesting to notice that as plotting E_{IT} as a function of contact radius a_c for the three spherical tips, the dependence of E_{IT} on tip radius R is evidently observed in Fig. V-18a. Probing over the same range of h_m , the indenter with larger R generates larger a_c , corresponding to higher E_{IT} . Over a large range of a_c , E_{IT} increases successively from small radius Sp10, to intermediate Sp50, and further to large Sp200. Since E_{IT} is deduced from the indentation measurements, it is definitely related to the indentation process, the indenters, as well as the indented materials. Different indentation responses derive from the different strain states under different indenters. For Ti2448 film involving phase transition during indentation, the microstructure evolution is sensitive to the strain states developed under the indenting tips, and therefore, the measured E_{IT} is a mixture product contributed by β and α'' phases. E_{IT} is plotted as a function of representative strain ε_r , as shown in Fig. V-18b. It is obviously observed that the values of E_{IT} is significantly influenced by the indenter configuration. Therefore, the indenter used must be pointed out when comparing the elastic properties from different measurements.

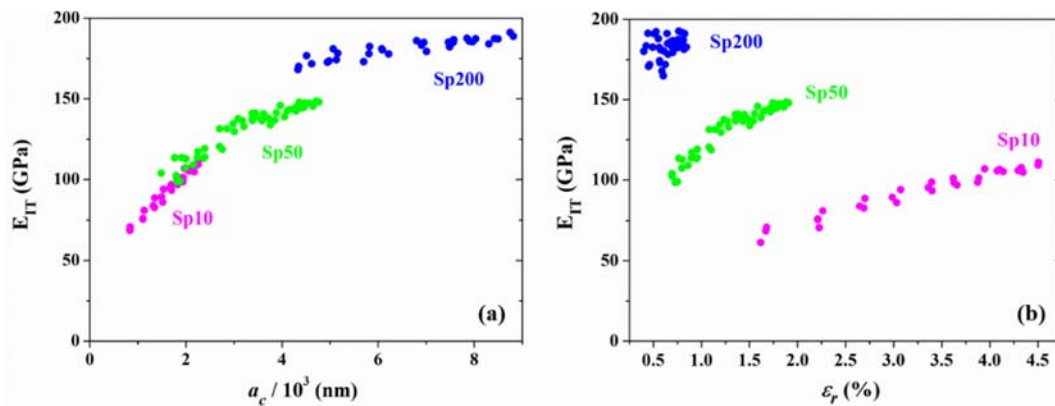


Fig. V-18 Variation of elastic modulus E as a function of thousand times the contact radius a_c (a) and as a function of the representative strain ε_r (b).

The measured E_{IT} provides information about the elastic moduli of the β and α'' phases and about the propagation of the phase transformation in the indenting volume. Fig. V-19 presents the variation of E_{IT} with respect to the depth recovery ratio η_h which represents the degree of depth recoverability during indentation experiment, and thus, is also an indicator on the magnitude of the superelastic response. For Sp50 and Sp10 indenters, E_{IT} evolves with the η_h value, and the film has lower E_{IT} values as it exhibits better superelasticity, while for Bkv indenter, E_{IT} is not sensitive to η_h with a constant value of approximately 110 GPa, and for Sp200 indenter, E_{IT} is clustered at around 180 GPa. The additional superelastic recovery decreases the slope of the unload curve and, thus, decreases the E_{IT} .

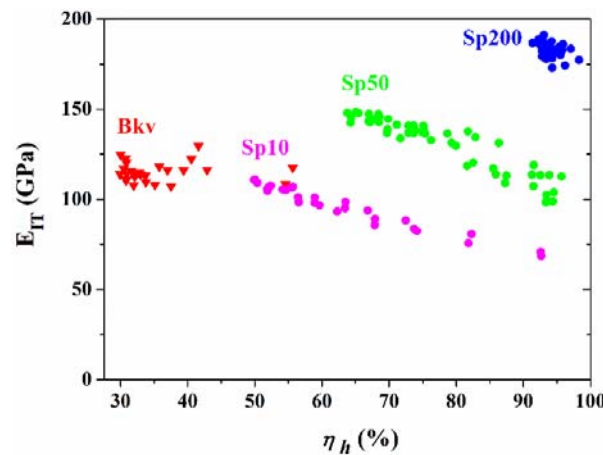


Fig. V-19 Influence of recoverability degree on elastic modulus E_{IT} .

It is concluded that the E_{IT} measured in our superelastic Ti2448 film is determined by the indentation depth, the indenter shape and tip radius, and the phase fractions associated with the SIM transformation.

V.3.3.2 Indentation hardness

The indentation hardness H_{IT} is calculated as the ratio of maximum applied load F_m to the projected contact area A_p at F_m . Fig. V-20 shows the relation of h_m versus F_m for the four different tips. At a fixed F_m , the four indenters penetrate into relatively different depths, suggesting the difference in indentation hardness.

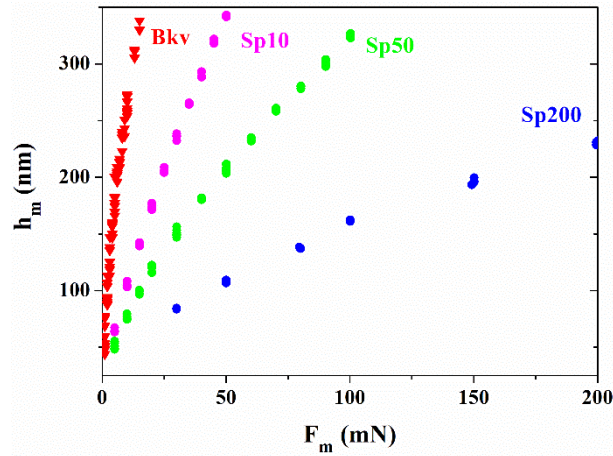


Fig. V-20 Maximum indentation depth h_m versus maximum indentation load F_m with different tips.

Here, the term “hardness” should be stressed. If hardness is understood in terms of resistance to plastic deformation, the condition of a full plastic regime should be met. However, in the present work, the indentation hardness H_{IT} is calculated as the ratio of F_m to the projected contact area A_p at F_m , which indicates that H_{IT} is a quantity measured in a loading state simultaneously involving elastic, superelastic and plastic deformation regions, rather than from a measurement using the residual imprint area after complete release of the load. Therefore, the interpretation for the variation of indentation hardness H_{IT} should take account of the role of elasticity and superelasticity in accommodating indentation induced deformation.

It is seen from Fig. V-21 that the indentation hardness H_{IT} displays opposite dependence on the indentation depth h_m when compared measurements with the Bkv indenter and those with spherical indenters, decreasing and increasing, respectively, with increasing h_m . It is also observed that indentation hardness measured with spherical tips increases with the decreasing indenter tip radius. Tymiak et al. [45] reported similar observations during sphero-conical (commonly known as spherical) indentations with nominal tip radii of 0.5, 1, 5 and 20 μm : hardness values increased with decreasing indenter tip radius.

Xue et al. [50] developed an indentation model based on the theory of mechanism-based strain gradient (MSG) plasticity to study the effect of indenter tip radius, and proposed that the opposite depth dependence between Berkovich and spherical indenters results from the different distribution of strain and strain gradient underneath a sharp indenter and a spherical indenter. Nix and Gao [24] developed a model to estimate the density of geometrically necessary dislocations (GNDs) underneath a sharp and conical indenter, while Swadener et al. [28] and Tymiak et al. [45] extended the model for a spherical indenter. These models predict different dependence of the density of GNDs on the indentation depth, which may shed light

on understanding the opposite depth dependence of indentation hardness measured during Bkv and spherical indentation experiments.

In MSG theory, the indentation hardness H_{IT} is expressed as:

$$\text{for sharp Bkv indenter: } H_{MSG} = 3\sigma_{ref} \sqrt{c_1^{2N} \tan^{2N} \theta + \frac{l c_1 \tan^2 \theta}{h_m}}, \quad (\text{V-1})$$

$$\text{for spherical indenter: } H_{MSG} = 3\sigma_{ref} \sqrt{\left(\frac{a_c}{5R}\right)^N + \frac{l}{5R}}, \quad (\text{V-2})$$

where σ_{ref} is a reference stress in uniaxial tension, and N is the plastic work hardening exponent ($0 \leq N < 1$), l is the intrinsic material length in strain gradient plasticity, the constant c_1 is on the order of 1, θ is the equivalent semi-apex angle for Bkv indenter, a_c is the contact radius, R is the radius of spherical indenter. Here, $a_c = \sqrt{2hcR - h_c^2}$, and h_c is the contact depth, $h_c = h_m - 0.75(F_m/S)$.

The equation (V-1) predicts that the Berkovich hardness H_{IT-Bkv} decreases with the increasing indentation depth h_m . The evolution of the measured H_{IT-Bkv} presented in Fig. V-21a is in agreement with predictions from equation (V-1). Such a trend, increasing hardness with decrease in indentation depth, is considered as the ISE as described earlier in section V.1. On indenting the specimen surface, GNDs are generated within the indentation volume beneath the indenter tip. For a self-similar Bkv indenter tip with sharp tip geometry, the strain generated under the tip appears almost constant, suggesting that smaller the indentation depth, larger is the strain gradient and hence larger is the density of GNDs. Such high dislocation density leads to enhanced hardening at smaller indentation depths [51].

The equation (V-2) predicts that for a fixed indenter tip radius R , spherical hardness H_{IT-sph} increases with the indentation depth h_m through a_c , which is consistent with the evolution of the measured H_{IT-sph} presented in Fig. V-21b. Taking account of the phase transformation involved during indentation experiment, many interpretations have been made in literature. The depth dependence of H_{IT-sph} has also been observed in NiTi alloys by Li et al. [52]. They proposed that the increase in the H_{IT-sph} with indentation depth is attributed to the increase in the transformed region and plastic deformation during loading. Amini et al. [27] explained the spherical hardness behavior with the well-known Hertz's theory. According to the Hertz's theory for a purely elastic contact of a material with no phase transition, the H_{IT-sph} is expressed as:

$$H_{IT} = \frac{4}{3\pi} \frac{E_{IT}}{1 - \nu^2} \sqrt{\frac{h_m}{R}} \quad (V-3)$$

where E_{IT} is the elastic modulus, ν is the Poisson's ratio, R is the spherical tip radius and h_m is the indentation depth. It clearly indicates that the spherical hardness increases with the square root of h_m for a purely linear elastic material. Although the square-root law in equation (V-3) cannot be completely applied to materials with phase transition, the tendency that H_{IT-sph} increases with depth still can be obtained. This is confirmed by the spherical hardness measured in NiTi bulk alloys which increases with h_m [27].

Nix and Gao [24] proposed a relation between H_{IT} and h_m as following:

$$\frac{H_{IT}}{H_0} = \sqrt{1 + \frac{h^*}{h_m}} \quad (V-4)$$

H_0 is the hardness at infinite indentation depth. In other words, H_0 is the hardness that would arise from merely the statistically stored dislocations (SSDs), in the absence of any GNDs. h^* is a length that characterizes the depth dependence of hardness. It is noted that h^* is not a constant for a given material and indenter geometry, and it depends on the SSDs through H_0 . A higher value of H_0 signifies higher hardness at infinite depth, and a higher value of h^* signifies stronger depth dependence of hardness.

To carefully assess the ISE in superelastic Ti2448 film, a plot of square of hardness versus reciprocal of indentation depth is presented in Fig. V-21c. Quantification of ISE is further performed on the basis of the curve. The value of H_0 is obtained from the square root of the intercept of the linear variation with its ordinate. The slope of the line signifies $H_0^2 \cdot h^*$. The values are presented at the inset of Fig. V-21c. The linear nature of the variation of H_{IT}^2 versus h_m^{-1} for the Ti2448 film does signify that indentation size effect is active for this material. This linear relation is also well-obeyed in NiTi alloys [51]. Due to the availability of different tip size indenters in the present study, spherical indentations with a wide range of spherical contact radii have been evaluated in Fig. V-21d. According to equation (V-2), at a fixed contact radius a_c , the smaller radius indenters lead to higher indentation hardness, which is consistent with the measurements for spherical indenters in Fig. V-21d.

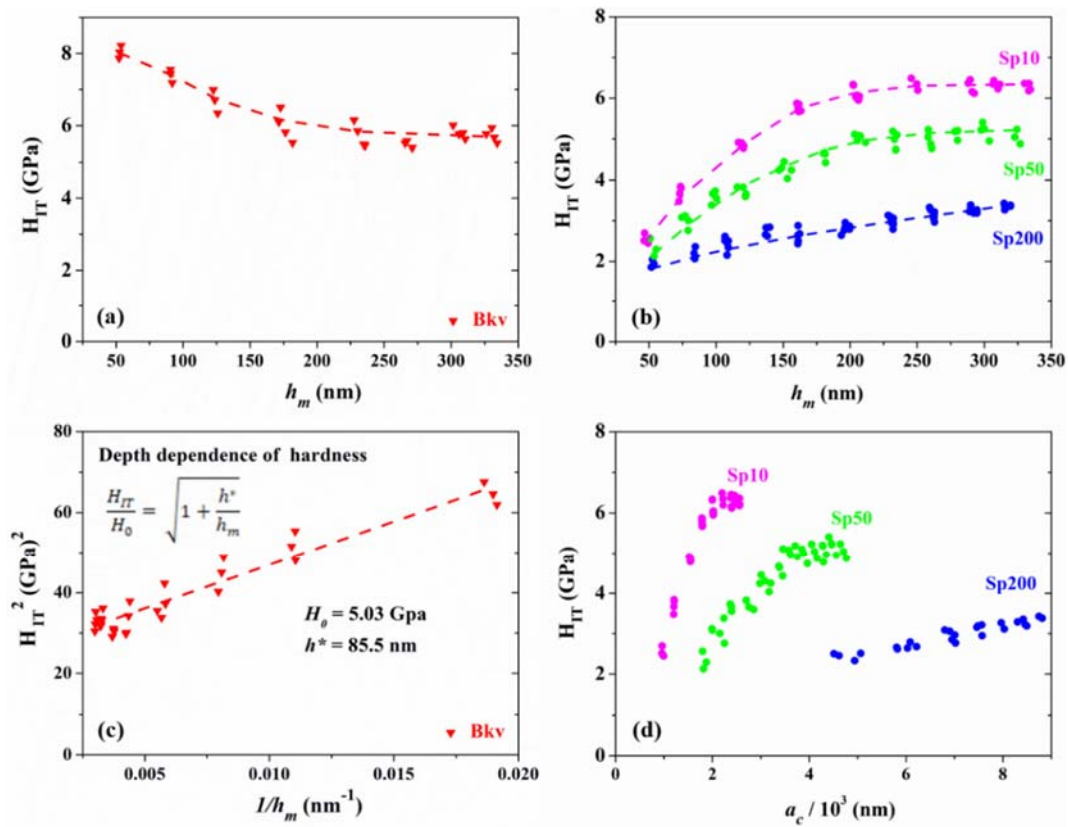


Fig. V-21 Variation of indentation hardness H_{IT} as a function of maximum penetration depth h_m measured with Bkv indenter (a) and with Sp10, Sp50 and Sp200 indenters (b). (c) Variation of the square of Bkv hardness (H_{IT}^2) with respect to the inverse of depth of penetration (h_m^{-1}). The values of H_0 and h^* were estimated from the fitting of the linear curve. (d) Variation of spherical H_{IT} as a function of contact radius a_c .

Tabor [53] pointed out that an equivalence existed between conventional stress-strain curves and that generated by plotting hardness versus contact radius divided by indenter radius (a_c/R). Fig. V-22 shows the variation of H_{IT} as a function of representative strain, $\epsilon_r = 0.2a_c/R$. The three indenters employed induced very different strain levels into the indentation area, and provoked different mechanical phenomena associated with the elasticity, superelasticity and plasticity in our superelastic Ti2448 film. Martinez et al. [54] similarly reported that results obtained from nanoindentation measurements on Cr coating using four indenters, i.e., 100- and 5- μm -radius diamond spheres, Berkovich and cube-corner diamond pyramids, demonstrated a complete mechanical characterization of thin films in the elastic, elastoplastic, plastic and fracture deformation regimes in sequence, presenting in an indentation stress-strain diagram. Note that indentation hardness H_{IT} and indentation stress are meaningfully equivalent, a measurement of pressure on a given area. The indentation experiments on copper by Lim et al. [38, 39], and subsequently on iridium by Swadener et al. [17] show that there is a size effect for spherical indentations, depending on the tip radius, a small tip radius exhibiting a higher hardness. Other groups, like He et al. [55] have confirmed this observation.

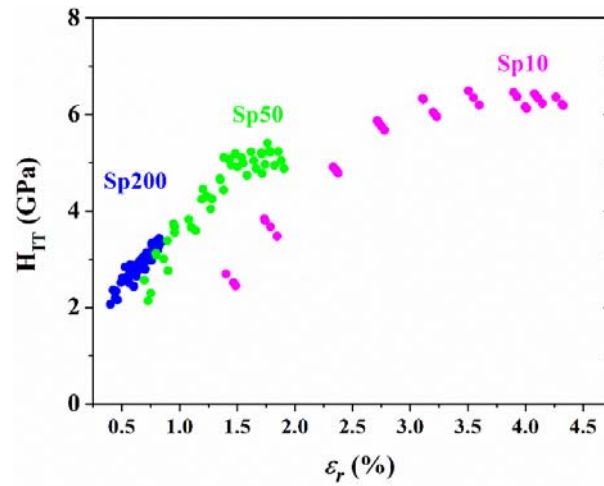


Fig. V-22 Variation of indentation hardness H_{IT} as a function of representative strain ϵ_r for the three spherical tips.

According to Gall *et al.* [56], the hardness for shape memory alloys, such as NiTi, depends on the resistance of deformation due to dislocation motion and phase transformation. The hysteresis area between the loading and unloading curves quantifies the dissipated work, which is due to dislocation activity and martensitic transformation. Therefore, the hardness is related to the irrecoverably dissipated work. Work recovery ratio η_w contains the information of dissipated work, and also can reflect the superelasticity in film. Fig. V-23 shows the indentation hardness H_{IT} as a function of η_w , in order to investigate the role of the martensitic transformation (superelasticity) in the variation of H_{IT} . It is evidently shown that the larger η_w , the lower H_{IT} . The combined effect of elastic deformation and phase transformation phenomenon makes the material soft and increases the indentation depth by a stress relaxation underneath the tip. Larger transformation zone leads to a lower H_{IT} . This is confirmed by numerical studies that larger phase transition strains lead to a lower spherical hardness under the same indentation depth in NiTi [57].

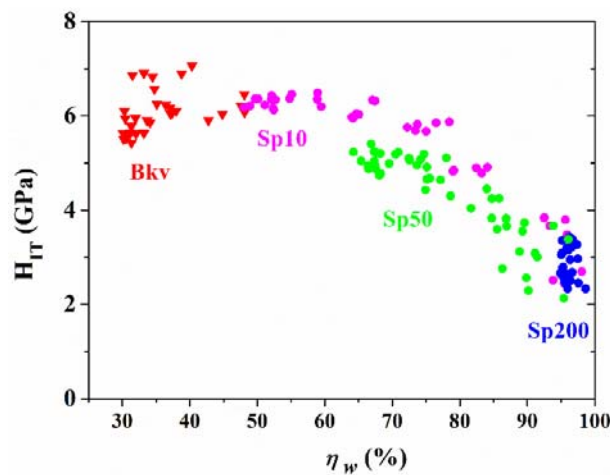


Fig. V-23 Influence of recoverability degree on indentation hardness H_{IT} .

The finding is useful in hardness measurements of materials involving solid-state phase transition. This study enriches our knowledge on the basic concept of hardness, and initiates a new approach towards the hardness measurement for materials with solid-state phase transitions under different indenters at nanoscales.

V.4 Conclusion

Ti2448 superelastic film was elaborated by magnetron sputtering at room temperature. The microstructure, superelasticity and mechanical properties have been characterized. Results are summarized as follows:

The film consists of a mixture of β -Ti phase and α'' -Ti phase. The lattice parameters were calculated: $a_{\beta} = 3.351 \text{ \AA}$ for the β -Ti phase, and $a_{\alpha''} = 3.097 \text{ \AA}$, $b_{\alpha''} = 4.905 \text{ \AA}$ and $c_{\alpha''} = 4.685 \text{ \AA}$ for the α'' -Ti phase. Ti2448 film exhibits a $\langle 110 \rangle_{\beta}$ fiber texture, or $(110)_{\beta}$ preferred growth direction. The α'' -Ti nanocrystallites are randomly distributed in the β matrix from the cross sectional TEM observations. The α'' -Ti does not show strong texture as confirmed by the presence of various martensite reflections observed from the classical symmetric θ - 2θ scan and by the ring character of the $\{021\}_{\alpha''}$ pole figure.

The superelasticity of the film has been revealed by nanoindentation, comparing the responses to spherical and Berkovich indentations. The strain and stress distributions underneath the indenter tips determine the indentation behavior of the film. Under a sharp Bkv indenter, the film deforms predominantly plastically. Large Sp200 indenter mainly reveal the elasticity of parent β phase in the film. Indenting with intermediate Sp50 or Sp10 indenter is a feasible option to evaluate the superelasticity of the Ti2448 film.

The depth dependence of indentation hardness H_{IT} and elastic modulus E_{IT} has been studied and the influence of martensitic transformation on the variation of H_{IT} and E_{IT} has been investigated in superelastic Ti2448 film. The analysis of the F - h dataset for different tips result in different H_{IT} and E_{IT} values. H_{IT} and E_{IT} exhibit depth-dependency, that is, decrease with depths in case of Bkv indenter and increase with depths in case of spherical indenters. Besides, H_{IT} and E_{IT} values are also dependent on the indenter tip radius. H_{IT} increases with increasing indenter tip radius, “the smaller tip, the stronger”, while E_{IT} decreases with decreasing indenter tip radius, “the larger tip, the stiffer”. The phase transformation phenomenon makes the material apparently softer and favors the stress accommodation underneath the tip, resulting in a lower E_{IT} .

References:

- [1] H.Y. Kim, S. Hashimoto, J.I. Kim, H. Hosoda, S. Miyazaki, Mechanical properties and shape memory behavior of Ti-Nb alloys, *Materials Transactions*, 45 (2004) 2443-2448.
- [2] J.I. Kim, H.Y. Kim, H. Hosoda, S. Miyazaki, Shape memory behavior of Ti-22Nb-(0.5-2.0) O (at%) biomedical alloys, *Materials Transactions*, 46 (2005) 852-857.
- [3] M.F. Ijaz, H.Y. Kim, H. Hosoda, S. Miyazaki, Superelastic properties of biomedical (Ti-Zr)-Mo-Sn alloys, *Materials Science and Engineering: C*, 48 (2015) 11-20.
- [4] F. Sun, Y.L. Hao, S. Nowak, T. Gloriant, P. Laheurte, F. Prima, A thermo-mechanical treatment to improve the superelastic performances of biomedical Ti-26Nb and Ti-20Nb-6Zr (at.%) alloys, *Journal of the Mechanical Behavior of Biomedical Materials*, 4 (2011) 1864-1872.
- [5] Y.L. Hao, S.J. Li, S.Y. Sun, C.Y. Zheng, Q.M. Hu, R. Yang, Super-elastic titanium alloy with unstable plastic deformation, *Applied Physics Letters*, 87 (2005) 091906.
- [6] Y.L. Hao, S.J. Li, S.Y. Sun, C.Y. Zheng, R. Yang, Elastic deformation behaviour of Ti-24Nb-4Zr-7.9Sn for biomedical applications, *Acta Biomaterialia*, 3 (2007) 277-286.
- [7] Y. Yang, P. Castany, M. Cornen, F. Prima, S.J. Li, Y.L. Hao, T. Gloriant, Characterization of the martensitic transformation in the superelastic Ti-24Nb-4Zr-8Sn alloy by in situ synchrotron X-ray diffraction and dynamic mechanical analysis, *Acta Materialia*, 88 (2015) 25-33.
- [8] J. Coakley, D. Isheim, A. Radecka, D. Dye, H.J. Stone, D.N. Seidman, Microstructural evolution in a superelastic metastable beta-Ti alloy, *Scripta Materialia*, 128 (2017) 87-90.
- [9] Y. Yang, P. Castany, M. Cornen, I. Thibon, F. Prima, T. Gloriant, Texture investigation of the superelastic Ti-24Nb-4Zr-8Sn alloy, *Journal of Alloys and Compounds*, 591 (2014) 85-90.
- [10] H. Jabir, A. Fillon, P. Castany, T. Gloriant, Crystallographic orientation dependence of mechanical properties in the superelastic Ti-24Nb-4Zr-8Sn alloy, *Physical Review Materials*, 3 (2019) 063608.
- [11] Y.W. Zhang, S.J. Li, E.G. Obbard, H. Wang, S.C. Wang, Y.L. Hao, R. Yang, Elastic properties of Ti-24Nb-4Zr-8Sn single crystals with bcc crystal structure, *Acta Materialia*, 59 (2011) 3081-3090.
- [12] Y. Yang, P. Castany, E. Bertrand, M. Cornen, J.X. Lin, T. Gloriant, Stress release-induced interfacial twin boundary ω phase formation in a β type Ti-based single crystal displaying stress-induced α' martensitic transformation, *Acta Materialia*, 149 (2018) 97-107.
- [13] Y. Yang, P. Castany, Y. Hao, T. Gloriant, Plastic deformation via hierarchical nano-sized martensitic twinning in the metastable β Ti-24Nb-4Zr-8Sn alloy, *Acta Materialia*, 194 (2020) 27-39.
- [14] H. Rumpf, T. Walther, C. Zamponi, E. Quandt, High ultimate tensile stress in nano-grained superelastic NiTi thin films, *Materials Science and Engineering: A*, 415 (2006) 304-308.
- [15] X.G. Ma, K. Komvopoulos, In situ Transmission Electron Microscopy and Nanoindentation Studies of Phase Transformation and Pseudoelasticity of Shape-memory Titanium-nickel Films, *Journal of Materials Research*, 20 (2005) 1808-1813.
- [16] K.S.S.E. Raju, S. Bysakh, M.A. Sumesh, S.V. Kamat, S. Mohan, The effect of ageing on microstructure and nanoindentation behaviour of dc magnetron sputter deposited nickel rich NiTi films, *Materials Science and Engineering: A*, 476 (2008) 267-273.
- [17] S. Sanjabi, Y.Z. Cao, S.K. Sadrnezhaad, Z.H. Barber, Binary and ternary NiTi-based shape memory films

deposited by simultaneous sputter deposition from elemental targets, *Journal of Vacuum Science & Technology A*, 23 (2005) 1425-1429.

[18] A. Ishida, M. Sato, A. Takei, S. Miyazaki, Effect of heat treatment on shape memory behavior of Ti-rich Ti-Ni thin films, *Materials Transactions, JIM*, 36 (1995) 1349-1355.

[19] A. Ishida, M. Sato, A. Takei, K. Nomura, S. Miyazaki, Effect of aging on shape memory behavior of Ti-51.3 At. pct Ni thin films, *Metallurgical and Materials Transactions A*, 27 (1996) 3753-3759.

[20] A. Ishida, A. Takei, S. Miyazaki, Shape memory thin film of Ti-Ni formed by sputtering, *Thin Solid Films*, 228 (1993) 210-214.

[21] W.C. Oliver, G.M. Pharr, An improved technique for determining hardness and elastic modulus using load and displacement sensing indentation experiments, *Journal of Materials Research*, 7 (1992) 1564-1583.

[22] W.C. Oliver, G.M. Pharr, Measurement of hardness and elastic modulus by instrumented indentation: Advances in understanding and refinements to methodology, *Journal of Materials Research*, 19 (2004) 3-20.

[23] N.A. Fleck, G.M. Muller, M.F. Ashby, J.W. Hutchinson, Strain gradient plasticity: Theory and experiment, *Acta Metallurgica et Materialia*, 42 (1994) 475-487.

[24] W.D. Nix, H. Gao, Indentation size effects in crystalline materials: a law for strain gradient plasticity, *Journal of the Mechanics and Physics of Solids*, 46 (1998) 411-425.

[25] Y. Liu, A.H.W. Ngan, Depth dependence of hardness in copper single crystals measured by nanoindentation, *Scripta Materialia*, 44 (2001) 237-241.

[26] K. McElhane, J.J. Vlassak, W.D. Nix, Determination of indenter tip geometry and indentation contact area for depth-sensing indentation experiments, *Journal of Materials Research*, 13 (1998) 1300-1306.

[27] A. Amini, C. Cheng, Nature of hardness evolution in nanocrystalline NiTi shape memory alloys during solid-state phase transition, *Scientific Reports*, 3 (2013) 2476-2476.

[28] J.G. Swadener, E.P. George, G.M. Pharr, The correlation of the indentation size effect measured with indenters of various shapes, *Journal of the Mechanics and Physics of Solids*, 50 (2002) 681-694.

[29] L. Qian, X. Xiao, Q. Sun, T. Yu, Anomalous relationship between hardness and wear properties of a superelastic nickel-titanium alloy, *Applied Physics Letters*, 84 (2004) 1076-1078.

[30] J. Stinville, C. Tromas, P. Villechaise, C. Templier, Anisotropy changes in hardness and indentation modulus induced by plasma nitriding of 316L polycrystalline stainless steel, *Scripta Materialia*, 64 (2011) 37-40.

[31] S. Habib, A. Rizk, I. Mousa, Physical parameters affecting deposition rates of binary alloys in a magnetron sputtering system, *Vacuum*, 49 (1998) 153-160.

[32] S. Berg, I.V. Katardjiev, Preferential sputtering effects in thin film processing, *Journal of Vacuum Science & Technology A*, 17 (1999) 1916-1925.

[33] S.V. Ketov, R. Joksimovic, G. Xie, A. Trifonov, K. Kurihara, D. Louzguine-Luzgin, Formation of nanostructured metallic glass thin films upon sputtering, *Heliyon*, 3 (2017) e00228.

[34] V. Chawla, R. Jayaganthan, A.K. Chawla, R. Chandra, Microstructural characterizations of magnetron sputtered Ti films on glass substrate, *Journal of Materials Processing Technology*, 209 (2009) 3444-3451.

[35] R. Chandra, A.K. Chawla, D. Kaur, P. Ayyub, Structural, optical and electronic properties of nanocrystalline TiN films, *Nanotechnology*, 16 (2005) 3053-3056.

- [36] G. Liu, Y. Yang, N. Jin, X. Luo, B. Huang, P. Li, Z. Kou, The structural characterizations of Ti-17 alloy films prepared by magnetron sputtering, *Applied Surface Science*, 427 (2018) 774-781.
- [37] Y. Hao, S. Li, S. Sun, R. Yang, Effect of Zr and Sn on Young's modulus and superelasticity of Ti–Nb-based alloys, *Materials Science and Engineering: A*, 441 (2006) 112-118.
- [38] E. Frutos, M. Karlík, J.A. Jiménez, H. Langhansová, J. Lieskovská, T. Polcar, Development of new β/α'' -Ti-Nb-Zr biocompatible coating with low Young's modulus and high toughness for medical applications, *Materials & Design*, 142 (2018) 44-55.
- [39] G. Liu, Y. Yang, X. Luo, B. Huang, P. Li, The phase, morphology and surface characterization of Ti–Mo alloy films prepared by magnetron sputtering, *RSC Advances*, 7 (2017) 52595-52603.
- [40] J.P. Liu, Y.D. Wang, Y.L. Hao, H.L. Wang, Y. Wang, Z.H. Nie, R. Su, D. Wang, Y. Ren, Z.P. Lu, J.G. Wang, X.D. Hui, R. Yang, High-energy X-ray diffuse scattering studies on deformation-induced spatially confined martensitic transformations in multifunctional Ti–24Nb–4Zr–8Sn alloy, *Acta Materialia*, 81 (2014) 476-486.
- [41] F. Ying, R. Smith, D.J. Srolovitz, The mechanism of texture formation during film growth: The roles of preferential sputtering and shadowing, *Applied Physics Letters*, 69 (1996).
- [42] A. Ehiasarian, A. Vetushka, Y.A. Gonzalvo, G. Sáfrán, L. Székely, P.B. Barna, Influence of high power impulse magnetron sputtering plasma ionization on the microstructure of TiN thin films, *Journal of Applied Physics*, 109 (2011) 104314.
- [43] A. Kumar, D. Singh, D. Kaur, Grain size effect on structural, electrical and mechanical properties of NiTi thin films deposited by magnetron co-sputtering, *Surface and Coatings Technology*, 203 (2009) 1596-1603.
- [44] G. Pan, Z. Cao, J. Shi, M. Wei, L. Xu, X. Meng, Different mechanical response of TiNi film induced by the shape of indenter during nanoindentation, *Sensors and Actuators A: Physical*, 217 (2014) 75-80.
- [45] N.I. Tymiak, D.E. Kramer, D.F. Bahr, T.J. Wyrobek, W.W. Gerberich, Plastic strain and strain gradients at very small indentation depths, *Acta Materialia*, 49 (2001) 1021-1034.
- [46] A.M. Wood, J.-H. You, T. Clyne, Nanoindentation response of superelastic materials, in: *Smart Materials III*, International Society for Optics and Photonics, 2004, pp. 216-223.
- [47] A.C. Fischer-Cripps, *Introduction to contact mechanics*, Springer, 2007.
- [48] C. Maletta, F. Furgiuele, E. Sgambitterra, M. Callisti, B. Mellor, R. Wood, Indentation response of a NiTi shape memory alloy: modeling and experiments, *Frattura ed Integrità Strutturale*, 6 (2012) 5-12.
- [49] Q. Kan, W. Yan, G. Kang, Q. Sun, Oliver–Pharr indentation method in determining elastic moduli of shape memory alloys—A phase transformable material, *Journal of the Mechanics and Physics of Solids*, 61 (2013) 2015-2033.
- [50] Z. Xue, Y. Huang, K. Hwang, M. Li, The influence of indenter tip radius on the micro-indentation hardness, *J. Eng. Mater. Technol.*, 124 (2002) 371-379.
- [51] S. Kumar S, L. Marandi, V.K. Balla, S. Bysakh, D. Piorunek, G. Eggeler, M. Das, I. Sen, Microstructure – Property correlations for additively manufactured NiTi based shape memory alloys, *Materialia*, 8 (2019) 100456.
- [52] P. Li, H.E. Karaca, Y.-T. Cheng, Spherical indentation of NiTi-based shape memory alloys, *Journal of Alloys and Compounds*, 651 (2015) 724-730.
- [53] D. Tabor, *The hardness of metals*, Oxford university press, 1951.

-
- [54] E. Martinez, J. Romero, A. Lousa, J. Esteve, Nanoindentation stress–strain curves as a method for thin-film complete mechanical characterization: application to nanometric CrN/Cr multilayer coatings, *Applied Physics A*, 77 (2003) 419-426.
- [55] L.H. He, N. Fujisawa, M.V. Swain, Elastic modulus and stress–strain response of human enamel by nano-indentation, *Biomaterials*, 27 (2006) 4388-4398.
- [56] K. Gall, K. Juntunen, H.J. Maier, H. Sehitoglu, Y.I. Chumlyakov, Instrumented micro-indentation of NiTi shape-memory alloys, *Acta Materialia*, 49 (2001) 3205-3217.
- [57] W. Yan, A. Amini, Q. Sun, On anomalous depth-dependency of the hardness of NiTi shape memory alloys in spherical nanoindentation, *Journal of Materials Research*, 28 (2013) 2031-2039.

General conclusion

In the present work, Ti-20Zr-3Mo-3Sn (Ti2033, at.%), Ti-16Zr-13Nb-2Sn (Ti16132, at.%) and Ti-24Nb-4Zr-8Sn (Ti2448, wt.%) biomedical alloys were synthesized into bulk alloys and into magnetron-sputtered films. The investigations were focused on the characterization of the microstructure and the mechanical properties with special attention paid to the superelastic properties which have more particularly been probed at the local scale by nanoindentation using four types of indenters: three spherical diamond indenters with tip radii of 10 μm (Sp10), 50 μm (Sp50) and 200 μm (Sp200) and the modified Berkovich diamond tip (Bkv).

To confirm the feasibility of the nanoindentation technique to characterize the superelastic property induced by a reversible martensitic transformation, nanoindentation responses in Ti2033 bulk alloy was carried out and the results obtained are presented and discussed in chapter III. The study in chap. III combined nanoindentation and EBSD to examine the crystallographic anisotropy of the indentation response at the scale of individual grains in Ti2033 polycrystalline alloy. The numerous measurements such as indentation hardness H_{IT} , indentation modulus E_{IT} , depth recovery ratio η_h and work recovery ratio η_w carried out on a large range of crystallographic directions allowed an investigation through the entire fundamental crystallographic orientation triangle of the β phase with a good statistic. The results, judiciously presented as inverse pole figure distribution maps: $\eta_h - IPF$, $\eta_w - IPF$, $E_{IT} - IPF$ and $H_{IT} - IPF$, showed that values of η_h and η_w were strongly affected by the loading direction and reached a maximum along the $\langle 001 \rangle_\beta$ direction and a minimum along the $\langle 111 \rangle_\beta$ direction. The η_h - and η_w - IPF distributions were in good agreement with the IPF distribution of compressive lattice distortions $\varepsilon_{\beta \rightarrow \alpha}^{(Vi)}$ calculated from the crystallographic model of martensitic transformation, which evidenced that anisotropy of indentation recovery ratios arose from the superelastic nature of our alloy. It was also shown that spherical nanoindentation is more appropriate for probing crystallographic anisotropy of the superelasticity, due to the strain distribution field generated under the Sp50 indenter which is smoothly distributed and more favorable to the reversion of the martensitic transformation compared to the case of the sharp Bkv indenter. Besides, orientation dependence in E_{IT} was observed, and the $E_{IT} - IPF$ distribution was qualitatively similar to the one predicted by calculations of Young's modulus from the measured elastic constants. No crystallographic anisotropy of H_{IT} was detected, due to multiple slip systems activated in the bcc β crystal.

Therefore, it can be concluded that the crystallographic anisotropy of the nanoindentation

responses was governed by anisotropy of elastic and superelastic responses in our metastable β Ti2033 alloy and in contrast, orientation dependence was lost when plasticity took place. Nanoindentation technique is thus capable of detecting the superelasticity at the local scale, and can be practically employed in the characterization of superelastic films.

In the chapter IV, a new quaternary Ti16132 film was elaborated by magnetron sputtering at room temperature from a single alloyed target. TEM observations and XRD analyses reveal that the film consists of a nanograined microstructure composed of the metastable β phase but some α'' martensitic nanodomains are also detected. In-plane pole figure measurements for the bcc β structure are presented in ring patterns, and an intensified center appears in the $\{110\}_\beta$ pole figure, showing the in plane polycrystalline microstructure and the $\langle 110 \rangle_\beta$ fiber texture of the β grains in the Ti16132 film.

The superelastic response of the Ti16132 film was examined in light of nanoindentation experiments by measuring the depth and work recovery ratios (η_h and η_w) from the load-displacement curves for various penetration depths. Results were discussed with regard to the calculation of the representative strain (ϵ_r). Owing to the four different indenters employed in this work, representative strain was varying continuously from 0.4% to 4.3% using three spherical indenters with tip radii of 200 μm (Sp200), 50 μm (Sp50) and 10 μm (Sp10), and thereafter up to 7% with the Berkovich (Bkv) indenter. The nanoscale indentation behavior of Ti16132 film was significantly affected by the indenter geometry due to the large differences in the magnitude and spatial distribution of the strains developed beneath each indenter tip. Using the Bkv indenter, almost no depth dependence of recovery ratios was observed. The constant and high representative strain ($\epsilon_r \sim 7\%$) imposed whatever the applied loads was beyond the level that can be accommodated by superelastic deformation leading to restricted recovery ratio measurements as low as 40%. Such conditions promote plastic deformation resulting in high density of dislocations which contribute to both limit the formation of martensite and inhibit its subsequent reversion to the parent β phase. In the case of spherical indentations, the representative strain imposed by the spherical indenter is depth dependent with respect to the indenter radius allowing to encompass the different deformation regimes from elastic to elasto-plastic regimes. Nearly 100% recovery ratios were measured with the large radius spherical indenter (Sp200) which imposed relative low representative strain ($0.4\% \leq \epsilon_r \leq 1\%$) and probed predominately elastic deformation. Large recovery ratios ranging from 95% to 60% were measured with Sp50 and Sp10 indenters for ϵ_r between 1% and 4.3%. Plastic deformation is then still the minor mechanism while superelastic deformation with reversible and stress-induced martensitic transformation is the predominant deformation mechanism.

Indenting with intermediate spherical tips, such as Sp50 and Sp10 indenters, is a viable strategy to reveal the superelastic response of materials in the micro- and nano-meter length scales by ensuring that the straining is in the competitive regime between superelastic and plastic deformations.

The work in chapter IV signifies the importance of considering the appropriate indentation depth window associated to the indenter tip radius to reveal the superelastic behavior of materials at the local scale. Superelastic performance is very sensitive to the applied strain level and spherical indentations offer the opportunity to determine at the local scale the strain levels under which small volumes of material would perform local superelastic deformation and recovery.

The study in chapter V is on the magnetron-sputtered Ti2448 thin films. The microstructure, superelasticity and mechanical properties have been characterized. Microstructural analyses showed that the film consisted of β and α'' phases. Ti2448 film exhibited a $\langle 110 \rangle_{\beta}$ fiber texture with α'' nanodomains randomly distributed in the β matrix.

The superelasticity of the Ti2448 film has been revealed by nanoindentation, and the indentation responses underneath different indenters have been explained with the aid of the calculations of representative strain ε_r and normalized contact pressure distribution σ_z/p_m . It has been observed that the smaller radius of the indenter tip, the higher ε_r . The normalized contact pressure reaches a maximum at the contact center and then falls gradually to zero at the edge of the contact circle for both spherical and Bkv indenters. However, a relatively low stress concentration was observed compared to Bkv indenter, for which the stress is particularly high at the center of the imprint. The severe stress concentration occurring beneath the sharp Bkv indenter results in a larger plastic zone compared to the case of spherical indenters and a greater residual deformation remains after releasing the load. The deformation modes for different zones underneath the indenter tip are determined and discussed by comparing the von Mises equivalent stress with the critical stresses inducing the martensitic transformation.

The depth dependence of the indentation hardness H_{IT} and the elastic modulus E_{IT} and the influence of the superelastic recovery on H_{IT} and E_{IT} have been investigated in the present Ti2448 film. It was observed that the values of H_{IT} and E_{IT} were not constant. Indeed, H_{IT} and E_{IT} exhibit a depth dependence which decreases with depths in the case of the Bkv indenter and increases with depth in the case of the spherical indenters. On the other hand, the H_{IT} and E_{IT} values were also observed to depend on the indenter tip radius. H_{IT} increases with the

decrease in the radius of the indenter tip, “the smaller, the stronger”, while E_{IT} increases with the increase in the radius of the indenter tip, “the larger, the stiffer”. The combined effect of elastic deformation and martensitic transformation phenomenon made the material soft and promoting stress relaxation underneath the tip resulting in a lower E_{IT} .

As a general summary, microstructure, superelasticity, elastic modulus and hardness were investigated in superelastic titanium-based films after magnetron sputtering depositions. The films exhibited nanosized columnar β grains microstructure showing a strong $\langle 110 \rangle_{\beta}$ fiber texture in the growth direction. Superelasticity associated with the stress-induced martensitic transformation has been systematically studied by nanoindentation using the four different indenters. The indentation hardness H_{IT} , the indentation modulus E_{IT} , the depth recovery ratio η_h , the work recovery ratio η_w and their crystallographic anisotropy were studied from the indentation load-displacement curves obtained for different penetration depths and for the four different indenters. The deformation mechanisms have been elucidated with the aid of the analytical calculations of the stress and strain fields generated underneath the tips, and the illustration of microstructural evolution during indentation. The different deformation regimes (elastic, superelastic, plastic) have been discriminated. This study demonstrates the importance of determining the appropriate indentation depth window associated with the penetrator tip radius to reveal superelastic behavior at the local scale.

The quaternary films elaborated in this thesis work demonstrate superelasticity. Concentrations of the films were selected on the base of the superelastic performances measured in their bulk counterparts. It is well-known that the phase stability observed in bulk alloys can be different from that in films. The reversible and stress-induced martensitic transformation arises from the mechanical instability of the metastable β -Ti phase. As regards the perspective work, it would be interesting to investigate the effect of the concentration of the alloying elements (β -stabilizers and neutral elements) on the superelastic response and on the mechanical properties of the Ti-Zr-Nb-Sn and Ti-Zr-Mo-Sn films. Moreover, because magnetron sputtering is a flexible deposition technique offering various deposition parameters (pressure, bias voltage, target-substrate distance,...) that may affect the stress development in films, it would be very interesting to investigate the influence of the deposition parameters on the stress development in the growing film in regards to the phase stability and superelastic properties. Other future work might address the challenging target of observing the stress-induced martensitic transformation in superelastic films using in situ TEM or in situ synchrotron XRD. This would clearly allow to further understand the martensitic transformation in superelastic films and to explore their deformation behaviors. Furthermore,

other perspective work might focus on the characterization of the tribological properties and fatigue properties of these functional films in view of their applications.

AVIS DU JURY SUR LA REPRODUCTION DE LA THESE SOUTENUE

Titre de la thèse:

Characterization by nanoindentation of the local mechanical properties of superelastic titanium-based magnetron-sputtered films in connection to their microstructures

Nom Prénom de l'auteur : ZHOU YING

Membres du jury :

- Monsieur RENAULT Pierre Olivier
- Monsieur SANCHETTE Frédéric
- Monsieur GLORANT Thierry
- Monsieur PATOOR Etienne
- Madame FILLON Amélie

Président du jury :

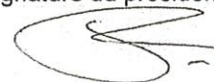
Date de la soutenance : 05 Juillet 2021

Reproduction de la these soutenue

- Thèse pouvant être reproduite en l'état
 Thèse pouvant être reproduite après corrections suggérées

Fait à Rennes, le 05 Juillet 2021

Signature du président de jury



Le Directeur,



Abdellatif MIRAOUI



Titre : Caractérisation par nanoindentation des propriétés mécaniques locales de films superélastiques à base de titane obtenus par pulvérisation magnétron en lien avec leurs microstructures.

Mots clés : Alliages de Titane, Pulvérisation Magnétron, Microstructures, Nanoindentation, Superélasticité, Transformation Martensitique, Anisotropie Mécanique.

Résumé : Dans ce travail de thèse, des alliages biomédicaux du type β métastable et de compositions Ti-20Zr-3Mo-3Sn (Ti2033, at.%), Ti-16Zr-13Nb-2Sn (Ti16132, at.%) et Ti-24Nb-4Zr-8Sn (Ti2448, mass.%), ont été synthétisés en alliages massifs par fusion et en couches minces par pulvérisation magnétron. Les investigations se sont focalisées sur leurs caractérisations microstructurales et leurs propriétés mécaniques avec une attention particulière portée sur leurs propriétés superélastiques qui ont été sondées à l'échelle locale par nanoindentation en utilisant quatre types d'indenteurs: trois indenteurs sphériques de rayons 10 μm (Sp10), 50 μm (Sp50) et 200 μm (Sp200) et la pointe diamantée Berkovich (Bkv). Les microstructures des films ont été analysées par diffraction des rayons X et observées en microscopie électronique en transmission afin de déterminer les phases en présence et les textures de croissance.

Les réponses superélastiques des films ont été sondées par nanoindentation pour évaluer la dureté d'indentation H_{IT} , le module d'indentation E_{IT} , le taux de recouvrement en profondeur η_h , le taux de recouvrement du travail η_w et leur anisotropie à partir des courbes charge-déplacement obtenues pour différentes profondeurs de pénétration et pour les quatre différentes pointes. Les propriétés superélastiques étant très sensibles au niveau de déformation appliqué, les réponses mécaniques d'indentation ont été corrélées aux calculs des déformations représentatives et des distributions de pressions de contact normalisées évaluées sous indenteurs. Ainsi, les différents régimes de déformation sous pointe (élastique, superélastique, plastique) ont pu être discriminés. Cette étude montre l'importance de déterminer la fenêtre de profondeur d'indentation appropriée associée au rayon de la pointe du pénétrateur pour révéler le comportement superélastique à l'échelle locale.

Title : Characterization by nanoindentation of the local mechanical properties of superelastic titanium-based magnetron-sputtered films in connection to their microstructures.

Keywords : Ti alloys, Magnetron Sputtering, Microstructures, Nanoindentation, Superelasticity, Martensitic Transformation, Mechanical Anisotropy.

Abstract : In the present work, Ti-20Zr-3Mo-3Sn (Ti2033, at.%), Ti-16Zr-13Nb-2Sn (Ti16132, at.%) and Ti-24Nb-4Zr-8Sn (Ti2448, wt.%) biomedical alloys were synthesized into bulk alloys and into magnetron-sputtered thin films. The investigations were focused on the characterization of the microstructure and the mechanical properties with special attention paid to the superelastic properties which have more particularly been probed at the local scale by nanoindentation using four types of indenters: three spherical diamond indenters with tip radii of 10 μm (Sp10), 50 μm (Sp50) and 200 μm (Sp200) and the modified Berkovich diamond tip (Bkv). The microstructures of the films were analyzed by X-ray diffraction and observed by transmission electron microscopy in order to determine the phase constitution and the growth textures.

The superelastic responses of the films were probed by nanoindentation to assess the indentation hardness H_{IT} , the indentation modulus E_{IT} , the depth recovery ratio η_h , the work recovery ratio η_w and their crystallographic anisotropy from the load-displacement curves obtained for different penetration depths and for the four different indenters. Since superelastic properties are very sensitive to the level of strain applied, the mechanical indentation responses have been correlated with calculations of representative strains and normalized contact pressure distributions evaluated under indenters. Thus, the different deformation regimes (elastic, superelastic, plastic) could be discriminated. This study demonstrates the importance of determining the appropriate indentation depth window associated with the penetrator tip radius to reveal superelastic behavior at the local scale.